



Pennsylvania Department of Transportation
Bureau of Planning and Research Project
Contract No. 355I01 / Project No. 070202

Inspection Methods & Techniques to Determine Non Visible Corrosion of
Prestressing Strands in Concrete Bridge Components

Task 2 - Assessment of Candidate NDT Methods

June 2010

By

Lawrence Jones

Stephen Pessiki, Ph.D.

Clay Naito, Ph.D., P.E.

Ian Hodgson, S.E.

ATLSS REPORT NO. 09-09

**ATLSS is a National Center for Engineering Research
on Advanced Technology for Large Structural Systems**

**117 ATLSS Drive
Bethlehem, PA 18015-4729**

**Phone: (610)758-3525
Fax: (610)758-5902**

**www.atlss.lehigh.edu
Email: inatl@lehigh.edu**

Abstract

Catastrophic failures of non-composite prestressed precast concrete adjacent-box beam bridges have occurred in several states due to corrosion of the prestressing steel. These failures have highlighted the need to improve methods used to detect corrosion damage and subsequently load rate the damaged members. In light of this, PennDOT initiated a research program aimed at improving inspection techniques through evaluation of off-the-shelf non-destructive testing (NDT) technologies and correlation of surface conditions with non-visible strand corrosion. Funding for the project was provided by the departments of transportation of Pennsylvania (the lead agency), New York, and Illinois.

Currently, inspection of concrete box girder sections relies on visual methods which correlate longitudinal and transverse cracking, spalling, and exposed strands with the rated level of performance of the member. While the visual method provides a qualitative estimate of the amount of damage, the specific location along a strand and the amount of damage to the strands is not clearly defined. As a result, the assessment of the condition of the bridge could in some cases result in an un-conservative or overly-conservative estimate of remaining strength. Furthermore, without a high level of accuracy in locating damage to the strands, remediation and rehabilitation is difficult to accomplish. To improve on the current inspection techniques the visual inspection requirements are revisited through an extensive destructive evaluation study. In addition NDT methods are evaluated and compared with actual damage present in a group of 40-50 year old box beams removed from service. The goal of this project is to determine if visual inspection techniques or currently available NDT technologies will allow for accurate identification of non-visible corrosion of prestressing strands.

To perform this evaluation, seven non-composite adjacent prestressed box beam segments were procured. The beams were recovered from three decommissioned bridges in the state of Pennsylvania. The beams selected were chosen to have variety of different construction details and levels of damage to provide a spectrum of corrosion conditions.

Six NDT experts evaluated the beams prior to destructive evaluation. Each team compiled their data and reported their findings for comparison with the in-house destructive evaluation. This report presents the background of each NDT method used and discusses the accuracy and feasibility of using the method for field inspection of prestressed concrete bridge components. Based on the results of the study it was found that Magnetic Flux Leakage and Remnant Magnetism evaluation methods are potentially viable for the detection of non-visible corrosion of prestressing strands. Ground penetrating radar techniques may also be viable with improvements in the resolution of the hardware. The results produced by Line Scanning Thermography, Electromagnetic Corrosion Detection, Galvanostatic Pulse Corrosion, and Ultrasonic Shear Wave Testing do not provide better accuracy than visual observation techniques.

The accuracy and reliability of two methods were examined more thoroughly. Magnetic Flux Leakage and Remnant Magnetism were re-evaluated using a series of manufactured test slabs. The results of this study indicated that both methods are capable of detecting section loss in strands with good accuracy.

Table of Contents

1. Introduction.....	9
1.1. Bridges Involved in Study	9
1.2. NDT Contractors Involved in Study.....	12
2. NDT Methods and Findings.....	14
2.1. Contractor #1: Dr. Al Ghorbanpoor.....	14
2.1.1. Summary of Methods Deployed	14
2.1.2. Summary of Results	15
2.2. Contractor #2: Infrasense Radar	19
2.2.1. Summary of Methods Deployed	19
2.2.2. Summary of Results	21
2.3. Contractor #3: Dr. Bernd Hillemeier	26
2.3.1. Summary of Methods Deployed	26
2.3.2. Summary of Results	28
2.4. Contractor #4: Physical Acoustics Corporation.....	31
2.4.1. Summary of Methods Deployed	31
2.4.2. Summary of Results	32
2.5. Contractor #5: LIMCMT, Inc. with David L. Gress & Associates.....	37
2.5.1. Summary of Methods Deployed	38
2.5.2. Summary of Results	40
2.6. Contractor #6: Dynasty Group.....	44
2.6.1. Summary of Methods Deployed	44
2.6.2. Summary of Results	49
3. Accuracy Non-Destructive Testing Methods.....	54
3.1. Assessment of Accuracy Method #1: Magnetic Flux Leakage	56
3.2. Assessment of Accuracy Method #2: Ground Penetrating Radar	57
3.3. Assessment of Accuracy Method #3: Remnant Magnetization.....	58
3.4. Assessment of Accuracy Method #4: Line Scanning Thermography	58
3.5. Assessment of Accuracy Method #5: Electromagnetic Corrosion Detection.....	59
3.6. Assessment of Accuracy Method #6: IE/UST/GPR Methods	59
4. Summary and Ranking of Candidate NDT Methods	63
5. Additional Evaluation of Magnetic NDE Methods	65

5.1. Experimental Design & Construction.....	65
5.2. Flaw Locations.....	68
5.3. Results and Analysis of Additional Inspections	73
6. 3D Laser Scanning Methods.....	78
6.1. Sample Application.....	78
6.2. Commercial Equipment	79
7. Summary and Conclusions	80
8. References.....	82
9. Appendix.....	83

List of Figures:

Figure 2-1: MFL Testing Apparatus 14

Figure 2-2: MFL Graph Indicating No Corrosion 14

Figure 2-3: MFL Graph Indicating Corrosion 15

Figure 2-4: MFL Scan Results for Beam CC3..... 16

Figure 2-5: MFL Scan Results for Beam CC4..... 16

Figure 2-6: MFL Scan Results for Beam LV7..... 16

Figure 2-7: MFL Scan for Beam LV7 17

Figure 2-8: MFL Scan Results for Beam LVD16..... 17

Figure 2-9: MFL Scan Results for Beam LVD19..... 18

Figure 2-10: MFL Scan Results for Beam MS2 18

Figure 2-11: MFL Scan Results for Beam MS3 18

Figure 2-12: GPR Data Collection System..... 19

Figure 2-13: Sample Transverse Scan 20

Figure 2-14: Sample Longitudinal Scan 20

Figure 2-15: Transverse Scan Showing Reduced Reflection Amplitude, Indicating Corrosion .. 21

Figure 2-16: Grid Layout for GPR Scans 21

Figure 2-17: Strand Reflection Amplitude Contour Plot for LVD16..... 22

Figure 2-18: GPR Contour Plot Superimposed on Surface for Beam LV16..... 22

Figure 2-19: Strand Reflection Amplitude Contour Plot for LV19 23

Figure 2-20: GPR Contour Plot Superimposed on Surface for Beam LV19 23

Figure 2-21: Strand Reflection Amplitude Contour Plot for CC4..... 24

Figure 2-22: Contour Plot Superimposed on Surface for Beam CC4..... 24

Figure 2-23: Strand Reflection Amplitude Contour Plot for CC3..... 24

Figure 2-24: Contour Plot Superimposed on Surface for Beam CC3..... 25

Figure 2-25: Strand Reflection Amplitude Contour Plot for MS3 25

Figure 2-26: Contour Plot Superimposed on Surface for Beam CC3..... 25

Figure 2-27: RM Scanning Apparatus 26

Figure 2-28: RM Measurement in the Active Field (No Fractures) 27

Figure 2-29: RM Measurement in the Remanent Field (No Fractures)..... 27

Figure 2-30: RM Measurement in the Active Field w/ Fracture 28

Figure 2-31: RM Measurement in the Remanent Field w/ Fracture..... 28

Figure 2-32: RM Scan Results for Beam CC3.....	29
Figure 2-33: RM Scan Results for Beam CC4.....	29
Figure 2-34: RM Scan Results for Beam LV16.....	30
Figure 2-35: RM Scan Results for Beam LV19.....	30
Figure 2-36: RM Scan Results for Beam MS2.....	31
Figure 2-37: RM Scan Results for Beam MS3.....	31
Figure 2-38: LST Apparatus.....	32
Figure 2-39: Thermal Images Produced from LST.....	32
Figure 2-40: LST Scan 1 of Beam MS3.....	33
Figure 2-41: LST Scan 2 of Beam MS3.....	34
Figure 2-42: LST Scan 3 of Beam MS3.....	34
Figure 2-43: LST Scan 1 of Beam CC3.....	35
Figure 2-44: LST Scan 2 of Beam CC3.....	35
Figure 2-45: LST Scan 3 of Beam CC3.....	36
Figure 2-46: LST Scan 1 of Beam CC4.....	36
Figure 2-47: LST Scan 2 of Beam CC4.....	37
Figure 2-48: LST Scan 3 of Beam CC4.....	37
Figure 2-49: Typical Resonance Junction (No Corrosion).....	38
Figure 2-50: Non-Linear Resonance Junction (Corrosion).....	38
Figure 2-51: Galvanostatic Pulse Corrosion Rate Test Equipment.....	39
Figure 2-52: Typical Corrosion Rate Potential Map.....	40
Figure 2-53: EMCD Results for Beam CC3.....	41
Figure 2-54: EMCD Results for Beam LV7.....	41
Figure 2-55: EMCD Results for Beam LV19.....	41
Figure 2-56: EMCD Results for Beam MS3.....	42
Figure 2-57: Corrosion Rate Potential (i_{corr}) for Top Mat of MS3.....	42
Figure 2-58: Corrosion Rate Potential (i_{corr}) for Bottom Mat of MS3.....	42
Figure 2-59: Corrosion Rate Potential (i_{corr}) for Top Mat of CC3.....	43
Figure 2-60: Corrosion Rate Potential for Bottom Mat of CC3.....	43
Figure 2-61: Corrosion Rate Potential for Top Mat of LV7.....	43
Figure 2-62: Corrosion Rate Potential for Top Mat of LV19.....	44
Figure 2-63: IE Testing Device.....	44
Figure 2-64: IE Test Method Theory.....	45

Figure 2-65: Time and Frequency Domain Responses for an Area with No Anomalies	45
Figure 2-66: Time and Frequency Domain Responses for an Area with an Anomaly.....	46
Figure 2-67: UST Polygon Device	46
Figure 2-68: UST Monolith Device.....	47
Figure 2-69: Sample of Results Produced by the UST Polygon Device	47
Figure 2-70: Sample of Results Produced by the UST Monolith Device.....	48
Figure 2-71: 3D Laser Scanning Device and Governing Point Cloud.....	48
Figure 2-72: 3D Laser Scanning used to Detect and Identify Crack-Width.....	49
Figure 2-73: 3D Laser Scanning Used to Detect and Identify Concrete Spall Geometries.....	49
Figure 2-74: Legend for Superimposed NDT Methodologies	50
Figure 2-75: Combined NDT Results Superimposed on Beam Surface for CC3.....	51
Figure 2-76: Combined NDT Results Superimposed on Beam Surface for CC4.....	51
Figure 2-77: Combined NDT Results Superimposed on Beam Surface for LV16.....	52
Figure 2-78: Combined NDT Results Superimposed on Beam Surface for LV19.....	52
Figure 2-79: Combined NDT Results Superimposed on Beam Surface for MS2	53
Figure 2-80: Combined NDT Results Superimposed on Beam Surface for MS3	53
Figure 3-1: Legend to Identify the Different Types of Corrosive Damage	54
Figure 3-2: Legend to Identify Probable Corrosion Locations by NDT Contractors	54
Figure 3-3: Summary of NDT Findings on Beam CC3	60
Figure 3-4: Summary of NDT Findings on Beam CC4.....	60
Figure 3-5: Summary of NDT Findings on Beam LV16.....	61
Figure 3-6: Summary of NDT Findings on Beam LV19	61
Figure 3-7: Summary of NDT Findings on Beam MS3	62
Figure 5-1: Test Slab #1.....	65
Figure 5-2: Test Slab #2.....	65
Figure 5-3: Test Slab #3.....	66
Figure 5-4: Test Slab #4.....	66
Figure 5-5: Pre-fabricated damage level conditions	67
Figure 5-6: Damage level 1 condition	67
Figure 5-7: Slabs 1 and 2 (left to right) prior to concrete placement.....	68
Figure 5-8: Identification of Small Flaws by Non-Destructive Magnetic Methods	76
Figure 5-9: Identification of Small Flaws with Respect to Clear Cover.....	77
Figure 6-1: 3D Laser Scanning Device and Governing Point Cloud.....	78

List of Tables:

Table 1-1: Acquired Beam Data	9
Table 1-2: In-Situ Beam Condition.....	10
Table 2-1: Summary of Findings for MFL	15
Table 2-2: Summary of Findings for RM:	28
Table 2-3: Corrosion Rate Values.....	39
Table 2-4: Contractor #5 Findings Summary	40
Table 3-1: Overlay of NDT Contractor Results w/ Damage Profile on Beam Surface	55
Table 3-2: Accuracy of MFL Findings	56
Table 3-3: Accuracy of GPR Findings.....	57
Table 3-4: Accuracy of RM Findings	58
Table 3-5: Accuracy of EMCD Findings.....	59
Table 4-1: Accuracy of NDT methods.....	63
Table 4-2: Accuracy and Pricing of NDT Methods.....	63
Table 5-1: Flaw Data for Slab #1 – Reinforced with #4 bars	68
Table 5-2: Flaw Data for Slab #2 – Reinforced with #3 bars	69
Table 5-3: Flaw Data for Slab #3 – Reinforced with ½” strand	71
Table 5-4: Flaw Data for Slab #4 – Reinforced with 3/8” strand	72
Table 5-5: Flaw Identifications with Respect to Each Method and Slab.....	73
Table 5-6: Successful Flaw Identification Rates by Method and Slab	74
Table 5-7: Average Wire Strength Due to Corrosion	77
Table 6-1: Laser Scanning Product Specifications	79

1. Introduction

After several catastrophic failures of adjacent prestressed precast box beam bridges due to corrosion of the prestressing steel a research program was initiated by the Pennsylvania Department of Transportation. The goal of the research program is to examine if viable non-destructive testing methods for assessment of non-visible corrosion exist. Six commercially available techniques were assessed for accuracy in locating non-visible corrosion damage. These testing methods were used on seven prestressed concrete box beams removed from three different decommissioned bridges in the state of Pennsylvania. This report compares the various testing methods and discusses the accuracy of each method in identifying corrosion of prestressing steel within the precast concrete beams.

1.1. *Bridges Involved in Study*

Three bridges were selected for forensic and non-destructive evaluation. The details of the bridges and shop drawings for each bridge type were provided by the respective PennDOT district offices. The beams were chosen to represent different fabricators, different ages, and a variety of damage conditions. Beams from three decommissioned bridges were procured for further inspection and evaluation. The bridges included Clearfield Creek (CC), Lakeview Drive (LV), and Main Street (MS). A summary of the beams is listed below and in Table 1-1. The section size, length and general condition is included.

- Bridge 1 (CC): Clearfield Creek Bridge Cambria County PA
Type: Three Span Adjacent PS Box Beam Bridge
Feature Intersected: Clearfield Creek (One span over creek and two spans over flood plain)
Bridge ID: 11102101801351
Year Built: 1956
Beam Manufacturer: New Enterprise Stone and Lime Company
- Bridge 2 (LV): Lakeview Drive Bridge Washington County, PA
Type: Four Span Adjacent PS Box Beam Bridge
Feature Intersected: Interstate 70 (two spans over traffic and two approaches)
Bridge ID: 62101400500000
Year Built: 1960
Beam Manufacturer: Spancrete
- Bridge 3 (MS): Main Street Bridge Washington County, PA
Type: Four Span Adjacent PS Box Beam Bridge
Feature Intersected: Interstate 70 (two spans over traffic and two approaches)
Bridge ID: 62404900301265
Year Built: 1961
Beam Manufacturer: Spancrete

Bridge (ID)	Beam	Span	Section Length	Cross Section [in.]	Condition Description:
Clearfield Creek (CC3)	3	1	15ft	42x36 Box	Longitudinal cracking with rust staining.

Table 1-1: Acquired Beam Data					
Bridge (ID)	Beam	Span	Section Length	Cross Section [in.]	Condition Description:
Clearfield Creek (CC4)	4	2	15ft	42x36 Box	Large longitudinal crack with spalling visible.
Lakeview Drive (LV7)	7	1	15ft	48x27 Box	Heavily damaged section with spalls and cracks. The section was full of water. Examine potential for delamination
Lakeview Drive (LV16)	16	2	12ft	48x42 Box	No cracking or corrosion visible on section however other areas of beam have significant corrosion.
Lakeview Drive (LV19)	19	3	12ft	48x42 Box	Longitudinal crack with heavier corrosion. Hairline and larger distributed cracks Use for visual assessment.
Main Street (MS2)	2	3	15ft	48x42 Box	Heavy corrosion on bottom flange without longitudinal cracking. Large patches. Determine if corrosion adjacent to patch exists using NDE methods.
Main Street (MS3)	3	3	15ft	48x42 Box	Longitudinal crack with heavy splitting. Examine damage formation and NDE study.

As noted in Table 1-1, the condition of the selected beams varied so as to represent the spectrum of conditions that may be encountered in the field. Table 1-2 provides images of the beam bottom flange (soffit). As shown, the various beam conditions can be ranked as average – minimal cracking and exterior damage in CC3 and CC4, through poor – concrete spalling, large cracks, and rust staining in LV7.

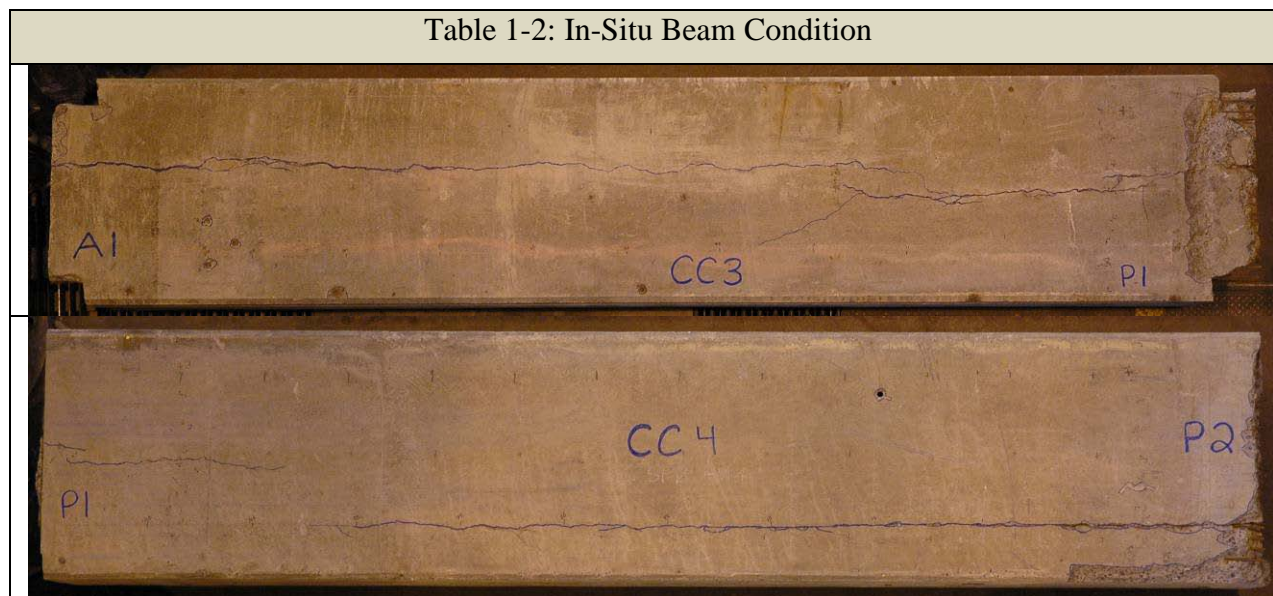


Table 1-2: In-Situ Beam Condition

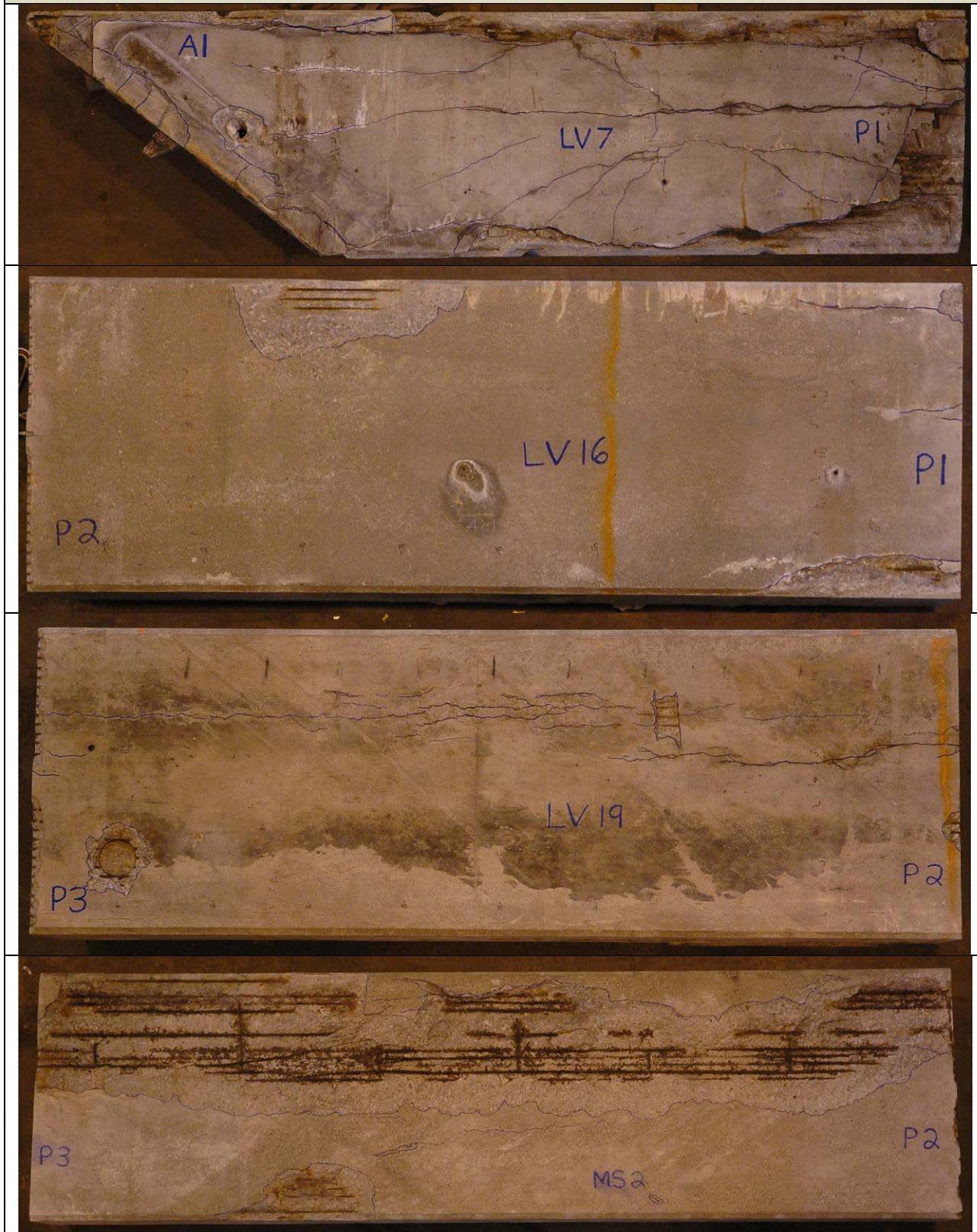
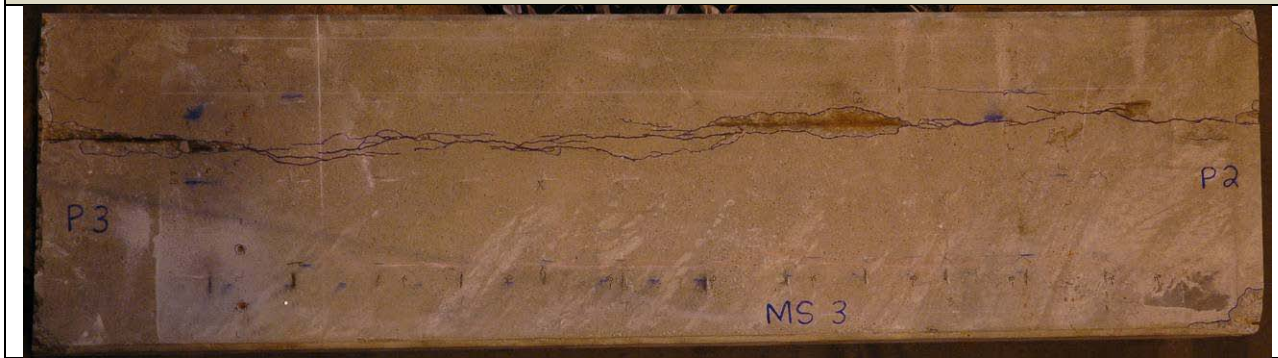


Table 1-2: In-Situ Beam Condition



The seven beam segments, as shown above, were acquired from both PennDOT Districts 9 and 12. The beams were staged and sectioned on site and transported to the ATLSS Center at Lehigh University. The beams were carefully handled to minimize further deterioration or damage to the sections. The beams were staged at Lehigh University within the laboratory. The sections were inverted with the beam soffit facing upward to ease inspection. The goal of the study was to assess the accuracy of the methods and not the ease of use therefore the inverted position was deemed acceptable.

1.2. *NDT Contractors Involved in Study*

Six contractors evaluated the procured beams using Non-Destructive Testing (NDT) methods. Each contractor attempted to detect the presence and location of strand corrosion in the strands of the bottom flange of the box beam section. The contractor and NDT method(s) used by each group are summarized below. A background on each method is presented in Chapter 2. The associated accuracy and feasibility of each method is presented in Chapter 3.

- 1.) Contractor #1: Dr. Al Ghorbanpoor and Mr. Emad Abdelsalam
 - a. Method: Magnetic Flux Leakage (MFL)
- 2.) Contractor #2: Infrasense, Inc.
 - a. Method: Ground Penetrating Radar (GPR)
- 3.) Contractor #3: Prof. Bernd Hillemeier and Andri Walther of Technische Universität Berlin Institute for Civil Engineering in association with Vector Corrosion Technologies
 - a. Method: Remanent Magnetization (RM)
- 4.) Contractor #4: Physical Acoustics Corporation (PAC)
 - a. Method: Line Scanning Thermography (LST)
- 5.) Contractor #5: LIMCMT, Inc. & David L. Gress & Associates
 - a. Method 1: Electromagnetic Corrosion Detection (EMCD)
 - b. Method 2: Galvanostatic Pulse Corrosion Rate (GPCR)
- 6.) Contractor #6: Dynasty Group
 - a. Method 1: Ultrasonic Impact Echo (IE) Test Method
 - b. Method 2: Ultrasonic Shear-Wave Test (UST) Method

- c. Method 3: Ground Penetrating Radar (GPR)
- d. Method 4: 3D Laser Scanning.

2. NDT Methods and Findings

2.1. Contractor #1: Dr. Al Ghorbanpoor

Dr. Al Ghorbanpoor and Mr. Emad Abdelsalam of the University of Wisconsin-Milwaukee performed a series of MFL scans on all seven prestressed concrete beams. Figures and verbage from their report “Magnetic Flux Leakage NDE of Penn-DOT Prestressed Concrete Box Girders” are used within this section. The complete report is presented in the Appendix.

2.1.1. Summary of Methods Deployed

Magnetic Flux Leakage is a method that involves magnetizing the steel strands through the concrete surface and searching for changes in the magnetic field which is an indicator of corrosion. The apparatus used to do this can be seen in Figure 2-1. It is important to note that this MFL system needs a smooth concrete surface to operate on, therefore it is impractical to use this on beams with severe concrete spalling.

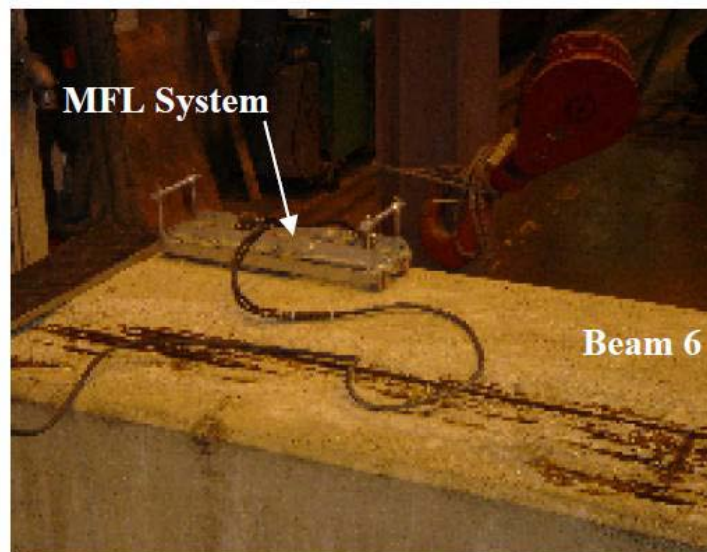


Figure 2-1: MFL Testing Apparatus

This MFL system consists of two strong magnets and a number of Hall-Effect sensors contained on a sled with a width of 8 inches. There is also an encoder device within the system that detects traveled distance. The graphs produced by this method display relative magnetic field amplitude versus traveled distance. An example MFL graph can be seen in Figure 2-2. The red lines indicate detected locations of transverse steel reinforcement.

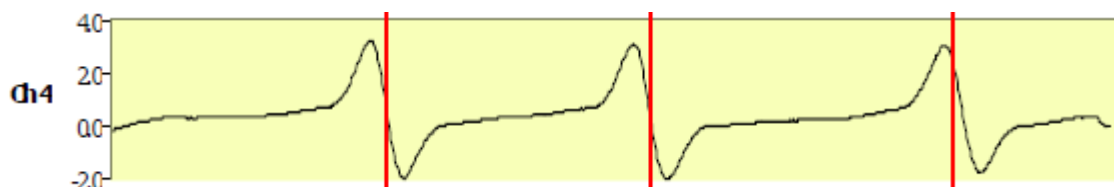


Figure 2-2: MFL Graph Indicating No Corrosion

The tests are performed by running the MFL system along the length of the beam above the strands. Doing this in a series of lines allows for complete scanning of each concrete beam

surface. If corrosion is present, the measured magnetic flux leakage becomes erratic and will become evident on the graphical results.

One sweep of the machine above an area with no corrosion can be seen in Figure 2-2. It is important to notice the smooth lines between successive peaks. If corrosion is present in a sweep of the MFL system, a graph such as one seen in Figure 2-3 is produced. Here we can see the changes in the magnetic field due to the presence of corrosion on the steel strands. The lines in between peaks are no longer smooth, indicative of an erratic magnetic flux leakage and an area where corrosion is likely.

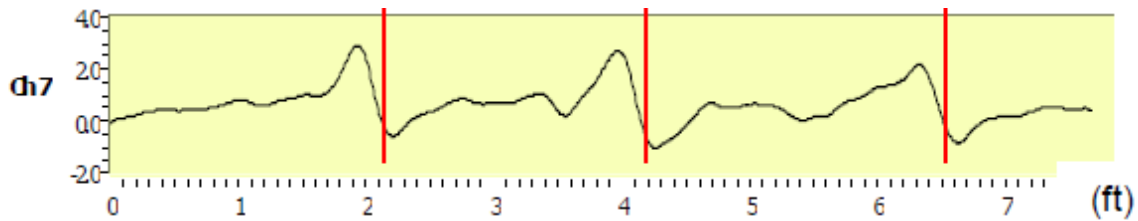


Figure 2-3: MFL Graph Indicating Corrosion

2.1.2. Summary of Results

MFL scans were performed on all seven beams. To scan each beam fully, several sweeps along the length of each beam were taken, each with a width of eight inches. The method results were presented as either “Local Steel” such as chairs, “Corrosion”, “Bumps,” or “Anomaly.” The corrosion information from the report is reproduced in Table 2-1.

Beam ID:	Ref. Pier End:	Start Scan Dist: (in)	End Scan Dist: (in)	Find?	Scan Line:	Start Location: (in)	End Location: (in)
CC3	P1	24	168	Local steel	Track 3	84	120
				Corrosion/bumps	Track 2	144	168
CC4	P2	17.5	155.5	No	N/A	N/A	N/A
LV7	P1	39	99	No	N/A	N/A	N/A
LV16	P1	23.5	119.5	Anomaly	Track 1	100	100
LV19	P2	22	106	Corrosion	Track 2	28	43
				Corrosion	Track 2	50.8	66.4
				Corrosion	Track 2	77.2	92.8
MS2	P2	24	144	Corrosion	Track 4	90	132
				Corrosion	Track 5	90	132
				Corrosion	Track 6	90	132
MS3	P2	29	149	Corrosion	Track 4	29	53
				Corrosion	Track 5	29.8	53
				Corrosion	Track 5	78.8	101

The suspected corrosion locations were overlaid on images of each beam surface. In each figure, the transverse solid white lines indicate the distance along the beams length that was scanned, the longitudinal solid white lines indicate tracks along which the centerline of the scanning apparatus was passed, and the purple markings are indicators of suspected corrosion locations.

For Beam CC3, major findings were limited to a location along track 3 – which is called out as a concentration of local steel – and a location along track 4 – which is described as “corrosion or bumps”. A plot of the findings on the beams surface is shown below in Figure 2-4.

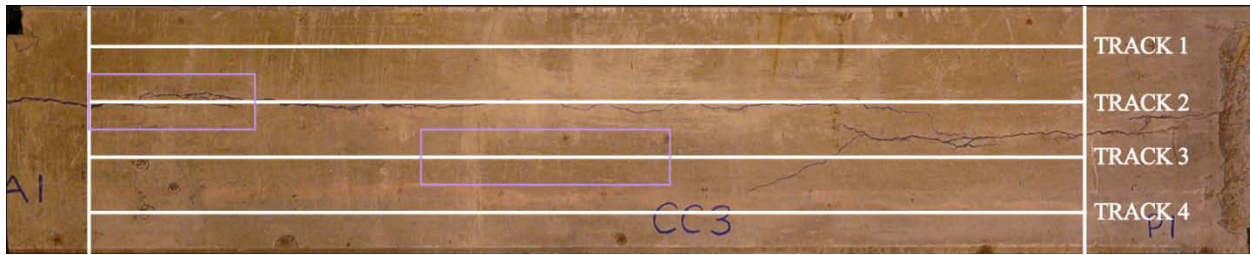


Figure 2-4: MFL Scan Results for Beam CC3

Beam CC4 had no major findings, as shown in Figure 2-5, indicating that no serious cases of corrosion within that particular specimen were found.

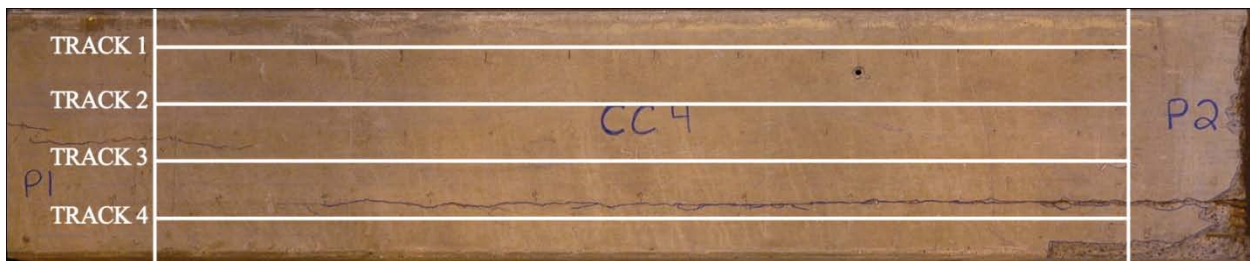


Figure 2-5: MFL Scan Results for Beam CC4

No regions of corrosion were found on Beam LV 7 as shown in Figure 2-6. The locations of transverse reinforcement were accurately identified as illustrated in Figure 2-7.

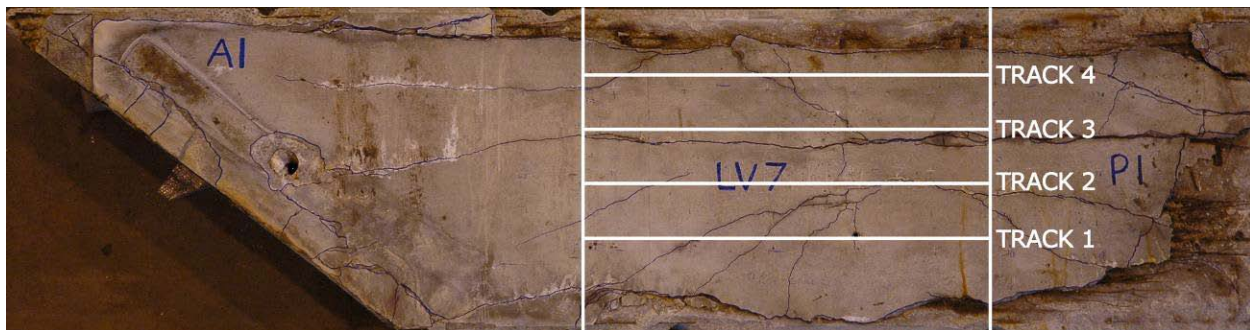


Figure 2-6: MFL Scan Results for Beam LV7

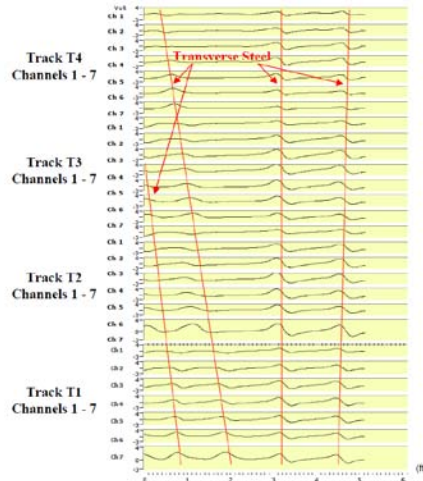


Figure 2-7: MFL Scan for Beam LV7

In Beam LV16, an anomaly was detected in track 1 near a spalled area of concrete by the MFL scans. This can be seen in Figure 2-8. It was noted that the contractor was uncertain what may lie beneath the concrete in this area.

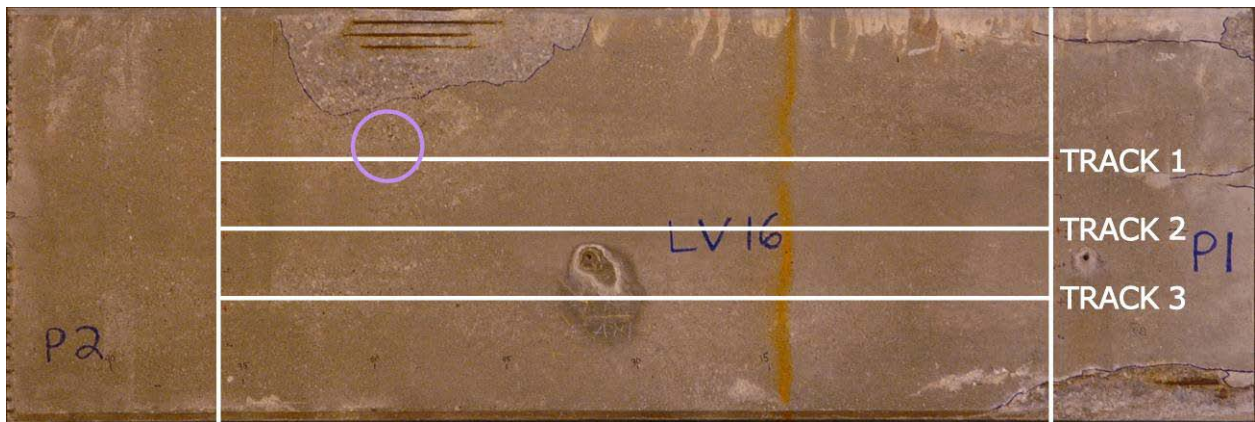


Figure 2-8: MFL Scan Results for Beam LVD16

Beam LV19 has several possible corrosion locations, all of which lie along track 2. Coincidentally, track 2 lies almost directly under the longitudinally cracked region of the beam. This can be seen in Figure 2-9.

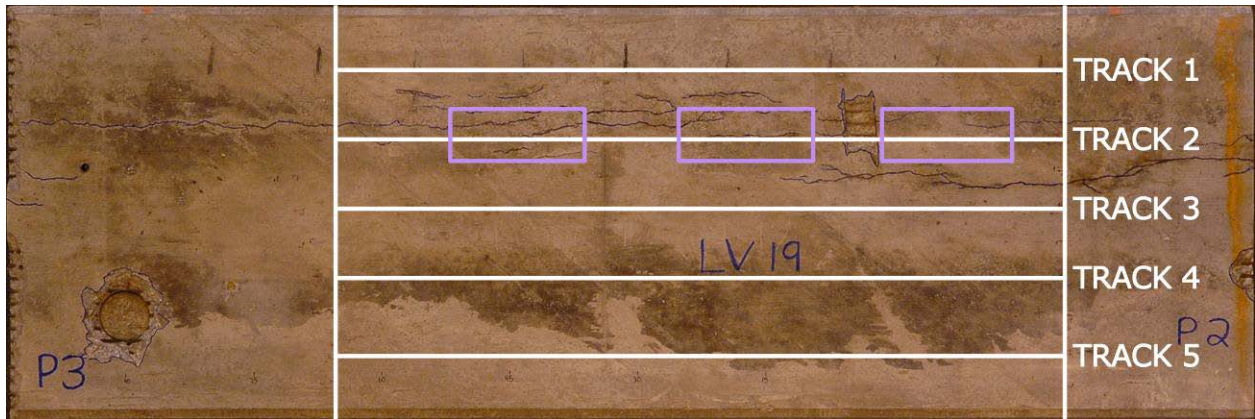


Figure 2-9: MFL Scan Results for Beam LVD19

Beam MS2 has several possible corrosion locations, one each on tracks 4, 5, and 6. This can be seen in Figure 2-10. The spalled top half of the beam was inspected, despite the apparatus' ineffectiveness on uneven surfaces. A smooth surface was created by filling in the uneven spalled area with wood chips. The area was then covered with plastic tape. It is of importance to note that this method detected the corrosion in the prestressing strands underneath the added material.

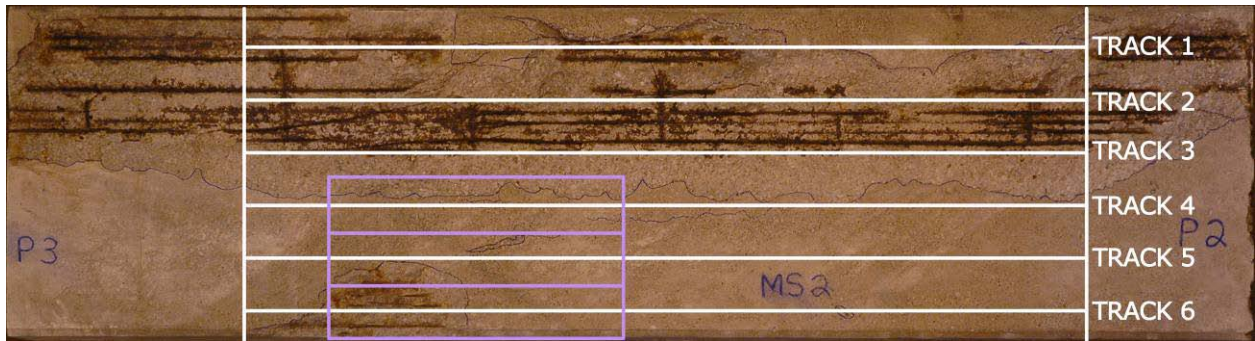


Figure 2-10: MFL Scan Results for Beam MS2

Beam MS3 has several potential corrosion locations, two on track 5 and one on track 4. This can be seen in Figure 2-11. The detected corrosion locations lie along the longitudinal crack on the beam surface.

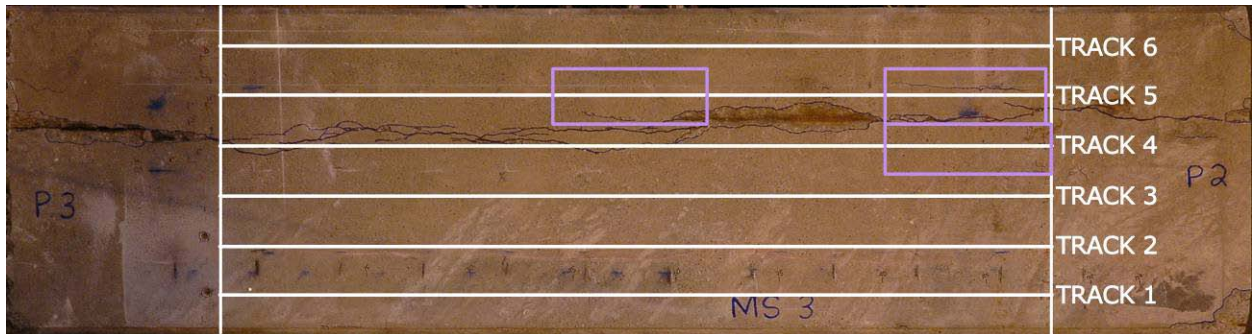


Figure 2-11: MFL Scan Results for Beam MS3

It should be noted that the MFL scans can detect, and correspondingly locate, the transverse steel reinforcement.

2.2. Contractor #2: Infrasense Radar

Infrasense, Inc. performed Ground Penetrating Radar tests on five of the seven beams; MS2 and LV7 were not examined. Figures from their report “Laboratory Evaluation of Subsurface Corrosion in Box Beam Prestressing Strands using Ground Penetrating Radar” are used within this report. The entire report is given in the Appendix.

2.2.1. Summary of Methods Deployed

Ground Penetrating Radar (GPR) is a method in which an antenna sends short pulses of radio waves into the surface of the concrete structure. Dielectric discontinuities, such as the reinforcing steel, reflect the waves back to the antenna. The collected data can then be processed. This NDT method has been used to detect reinforcing steel within concrete structures, to detect delaminations in the concrete, and to detect deteriorated conditions within the concrete.

There are two main principles applied in the use of GPR for detecting corrosion: (1) corroded reinforcement will produce a reduced GPR reflection; and (2) the moisture condition in the concrete that produced the corrosion will alter the GPR reflection. The latter principle cannot be accounted for in this study due to the fact that the beam moisture were kept within the lab and are not representative of field conditions. The beams remained dry during testing, and therefore GPR could not pick up any moisture-related effects.

A 2.6 GHz antenna was used for this study. This is the highest frequency antenna available commercially. The need for such a high frequency comes from the fact that prestressing steel is spaced more closely and has a smaller diameter than conventional steel reinforcement. The antenna is rolled along the surface of the beam. One of the wheels has a rotary encoder which tracks the position of the antenna. The entire data collection system is as shown in Figure 2-12.

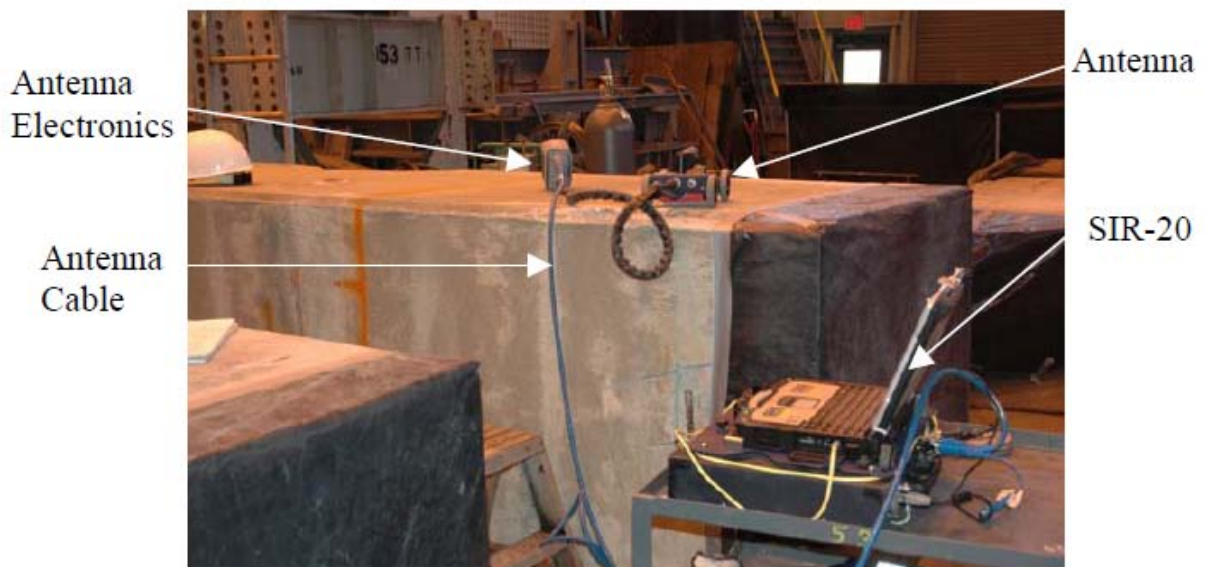


Figure 2-12: GPR Data Collection System

Scans of each beam surface were made in both the transverse and longitudinal directions. In transverse scans, (e.g., Figure 2-13), the prestressed strands reflect the waves back to the antenna. In longitudinal scans, (e.g., Figure 2-14), the waves can penetrate the concrete to a

greater depth and reveal the interior of the bottom flange of the box beam as well as the transverse steel.

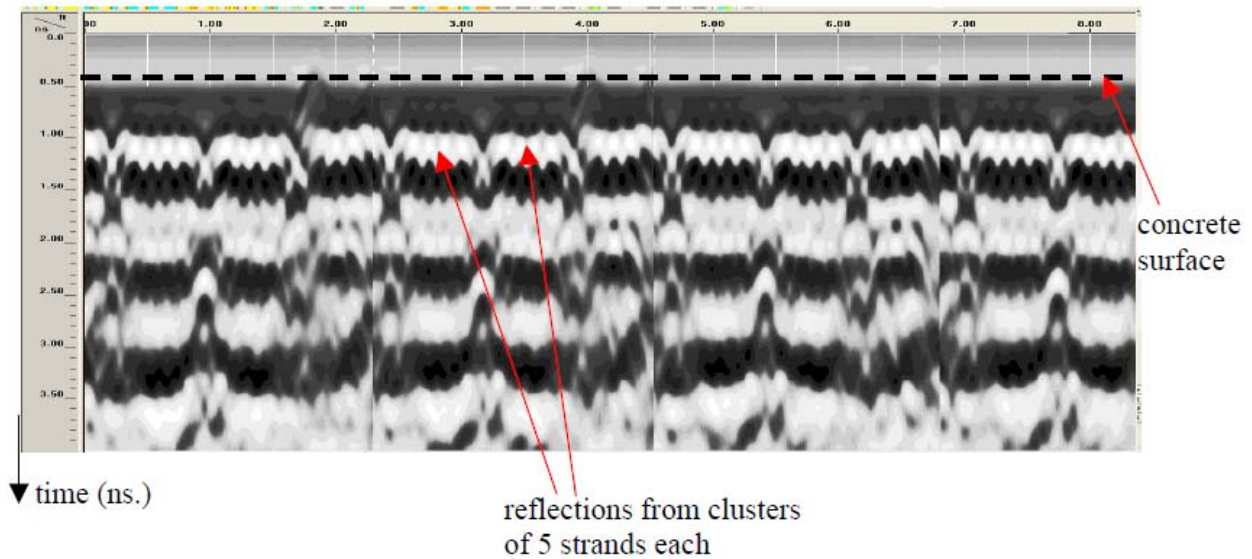


Figure 2-13: Sample Transverse Scan

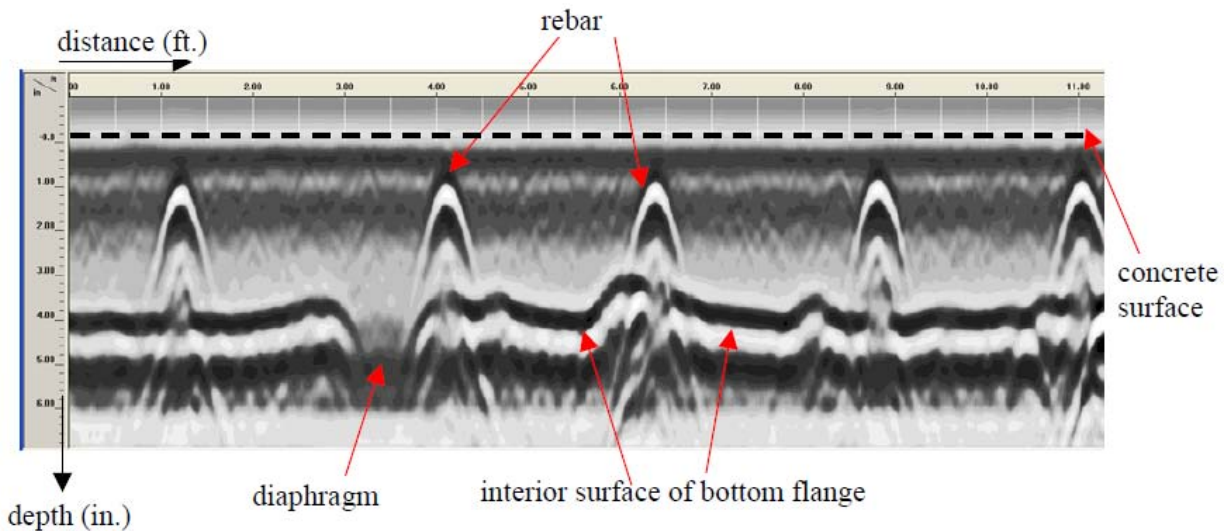
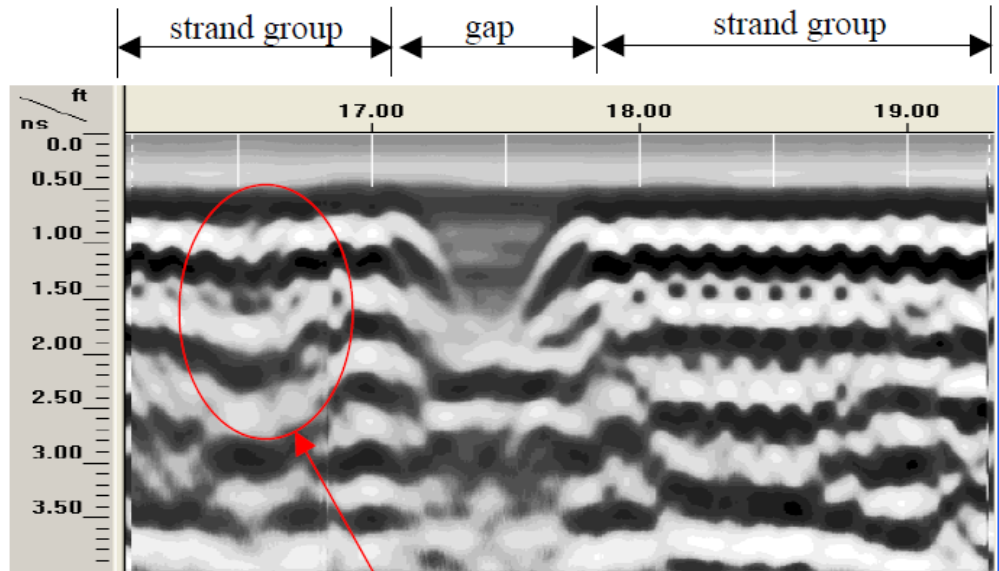


Figure 2-14: Sample Longitudinal Scan

The transverse scans also allow the user to detect corrosion within the strands. As mentioned above, corrosion will produce a reduced GPR reflection, as shown in Figure 2-15. The strength of the colors indicates the quality of the GPR reflection. If strands are corroded, a blurry weak vision is shown, such as in the left strand group.



diminished reflection amplitude

Figure 2-15: Transverse Scan Showing Reduced Reflection Amplitude, Indicating Corrosion

2.2.2. Summary of Results

GPR was used to test five of the seven beams at the ATLSS Research Center. The basic layout used for testing is as indicated in Figure 2-16. Scans were taken by rolling the antenna over the grid lines. For beams with a width of 48 in. the longitudinal passes were performed at 12 inches. For beams with a width of 36 inches the longitudinal passes were performed at 9 inches. It should be noted that the antenna needed to rest fully on the girder before scans could begin. Therefore, each transverse scan was approximately 8 inches less than the width of the girder. The first transverse scan is offset 12 inches from each beam end.

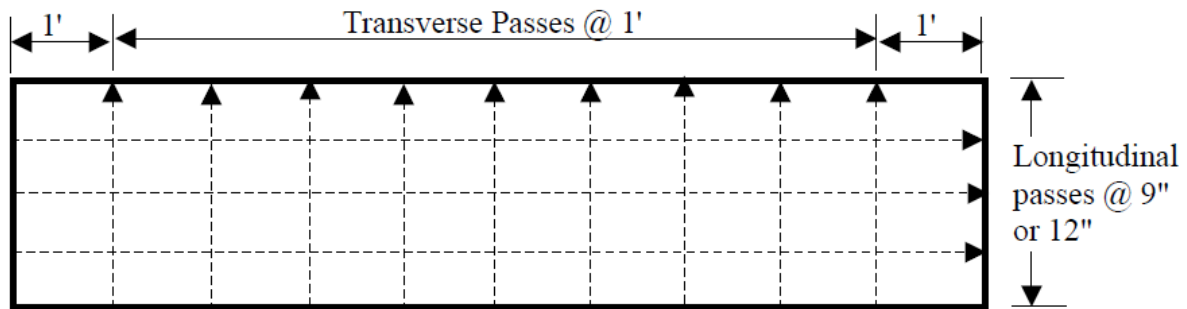


Figure 2-16: Grid Layout for GPR Scans

The saved data is converted into a quantitative analysis using Infrasense's automated GPR analysis software winDecar. A color contour plot is displayed, indicating areas with reduced reflection amplitude and therefore possible areas of corrosion. Green shaded regions indicate high amplitude reflections, red shaded regions indicate low amplitude reflections, and yellow/orange shaded regions fall in between. Below a certain value, the color is set to white; indicating regions with no prestressing strands. The graphs for the five tested beams can be seen below.

The strand reflection amplitude contour plot for LV16, Figure 2-17, shows diminished amplitude around the area of the spall indicating that this is a possible area of corrosion. Along the North edge of the beam, east of the spall, low reflection amplitudes exist. Regions of low reflection amplitude also exist along the south edge of the beam, from approximately five to ten feet.

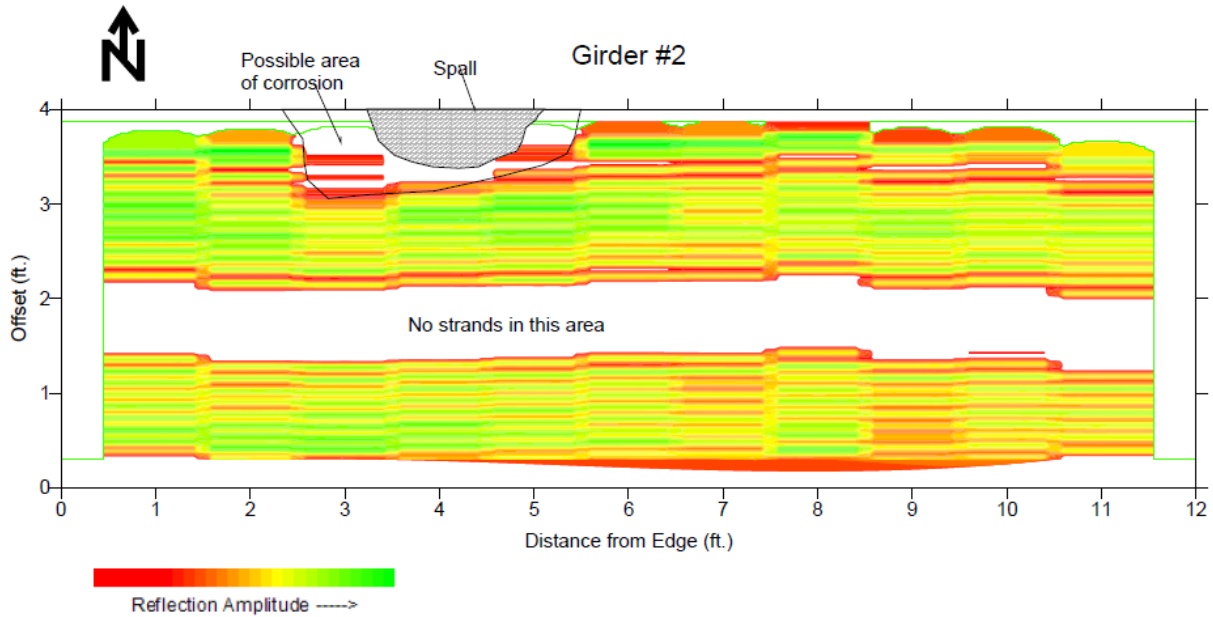


Figure 2-17: Strand Reflection Amplitude Contour Plot for LVD16

The GPR contour plot was superimposed over the beams surface. The corrosion locations are surrounded with a white box (see Figure 2-18).

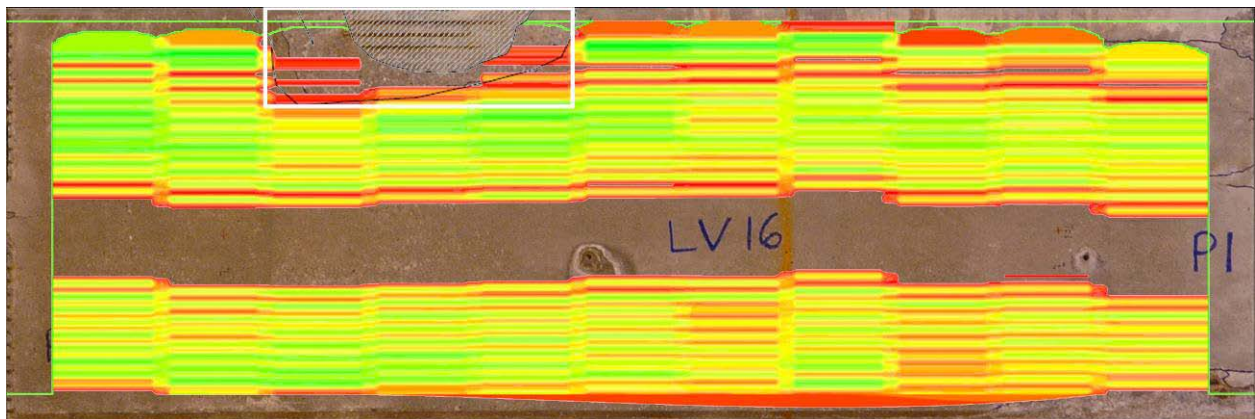


Figure 2-18: GPR Contour Plot Superimposed on Surface for Beam LV16

The strand reflection amplitude contour plot for LV19 (see Figure 2-19) indicates a large possible area of corrosion on the bottom half of the beam. Some of the areas appear white, indicating that no strands were found. Isolated strands can be found in the top half of the beam indicating low reflection amplitude.

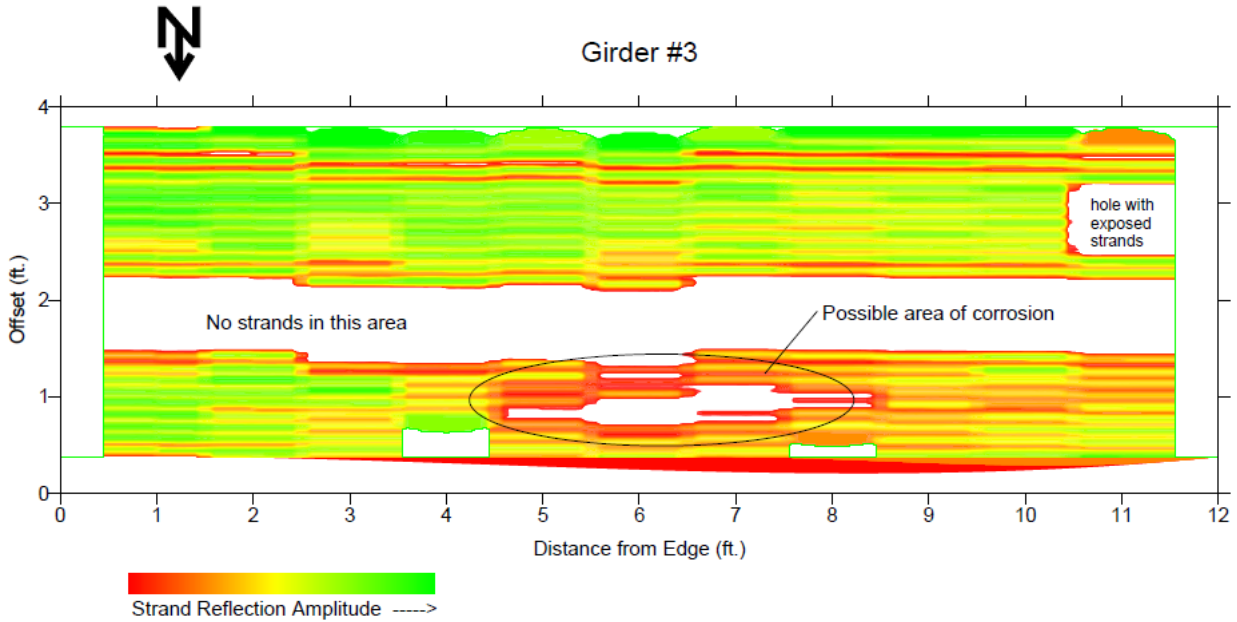


Figure 2-19: Strand Reflection Amplitude Contour Plot for LV19

The GPR contour plot was then superimposed over an image of the beam surface. Potential corrosion locations were surrounded with a white box (see Figure 2-20).

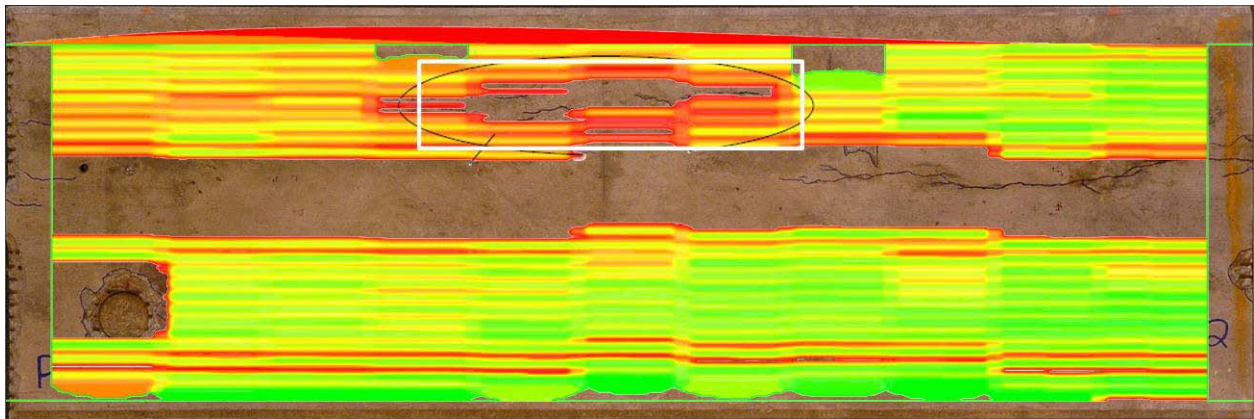


Figure 2-20: GPR Contour Plot Superimposed on Surface for Beam LV19

The strand reflection amplitude contour plot for CC4, Figure 2-21, shows minimal areas of low reflection amplitude. Two areas are called out as having possible corrosion along individual strands.

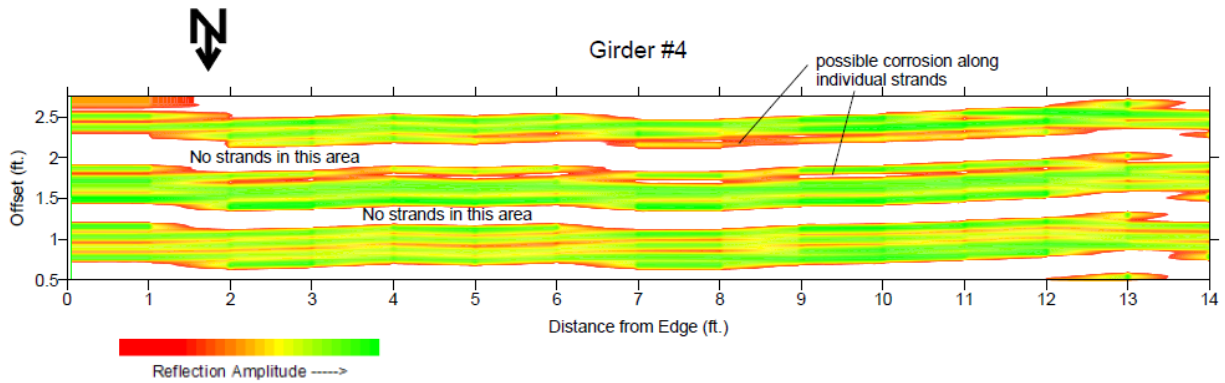


Figure 2-21: Strand Reflection Amplitude Contour Plot for CC4

The GPR contour plot was superimposed over an image of the beam surface. No areas of corrosion were identified. It is indicated, however, that corrosion may lie along the strand under the crack (see Figure 2-22).

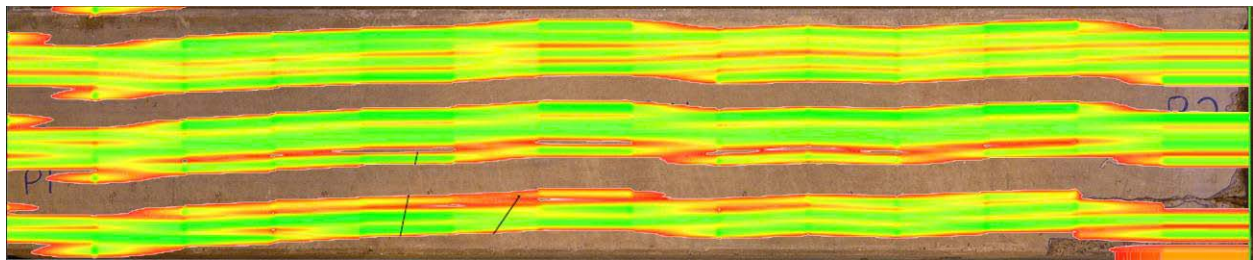


Figure 2-22: Contour Plot Superimposed on Surface for Beam CC4

The strand reflection amplitude contour plot for CC3, Figure 2-23, indicates erratic strand placement and several strands that indicate low reflection amplitude along the entire length. However, no areas of potential corrosion are explicitly identified by the Infrasense, Inc. team.



Figure 2-23: Strand Reflection Amplitude Contour Plot for CC3

The GPR contour plot was superimposed over an image of the beam surface. Again, no areas of potential corrosion were identified (see Figure 2-24).

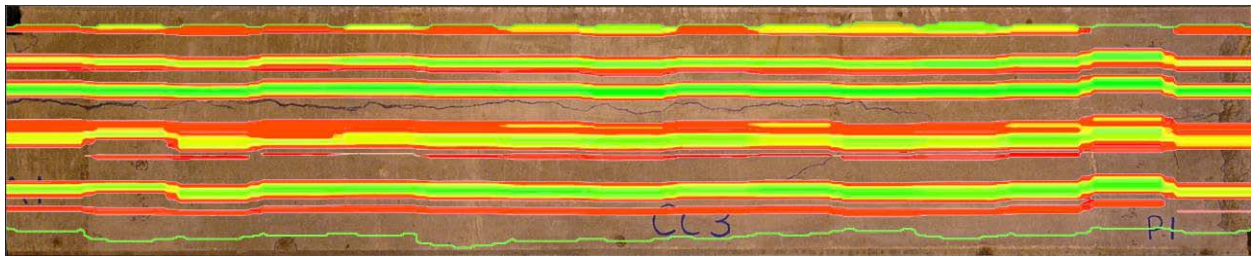


Figure 2-24: Contour Plot Superimposed on Surface for Beam CC3

The strand reflection amplitude contour plot for MS3, Figure 2-25, indicates two possible areas of corrosion on the beam, both on the top half of the beam. There are many strands within this beam that indicate low reflection amplitudes along their length.

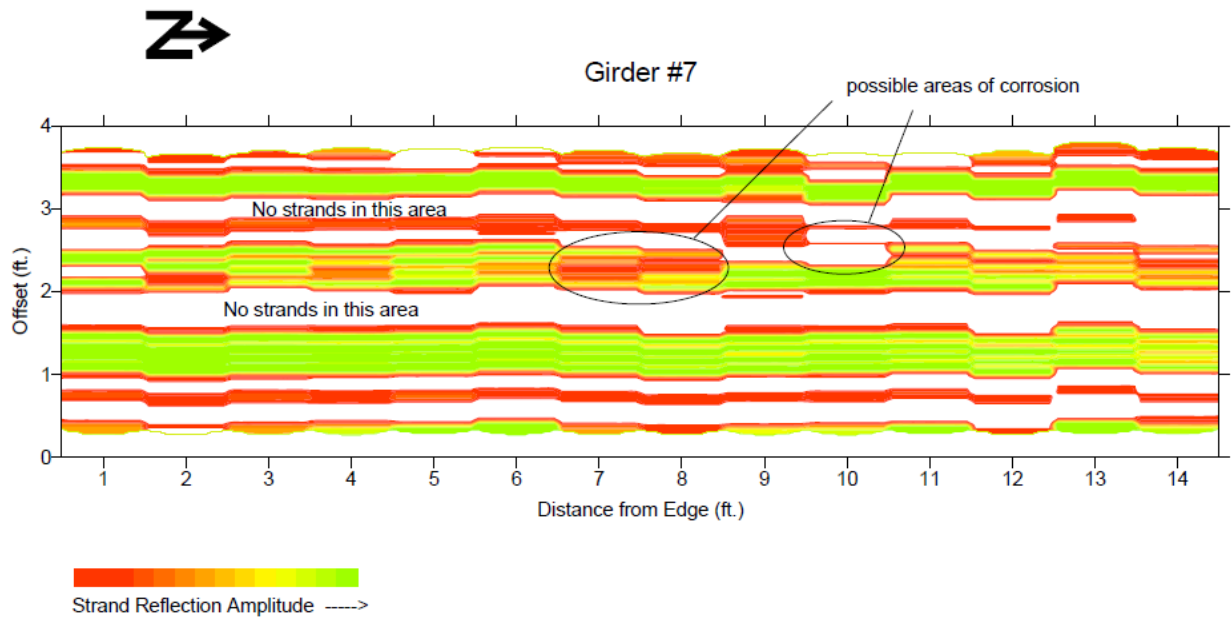


Figure 2-25: Strand Reflection Amplitude Contour Plot for MS3

The GPR contour plot was superimposed over an image of the beam surface. Two potential areas of corrosion were identified by reduced GPR readings (see Figure 2-26).

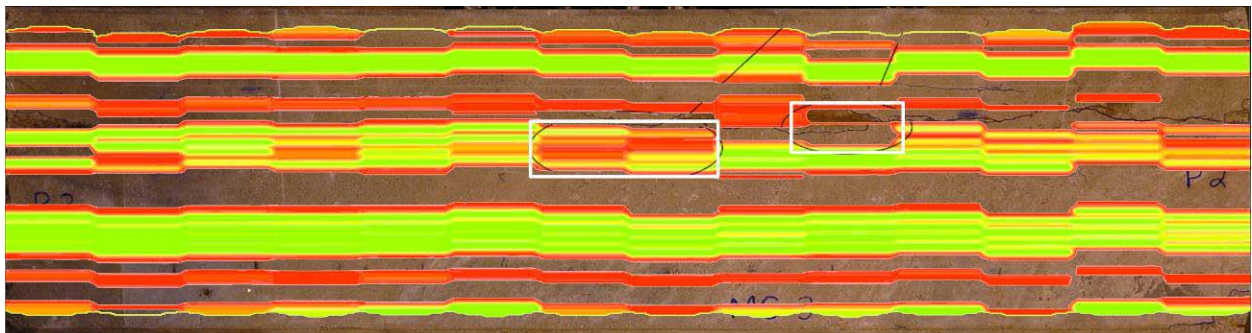


Figure 2-26: Contour Plot Superimposed on Surface for Beam CC3

2.3. Contractor #3: Dr. Bernd Hillemeier

Dr. Bernd Hillemeier and Andrei Walther of the Technische Universität (TU) Berlin Institute for Civil Engineering performed a series of Remanent Magnetization scans on six of the acquired beams (all but LV7); which were performed in association with Vector Corrosion Technologies Ltd. located in the USA. All measurements were completed within one day. Figures from their report “The Remanent Magnetization Method (RM-Method) Applied for the Localization of Fractures in Pretensioned Strands in Box Girders of 3 Bridges at Lehigh University, Bethlehem, PA” are used within this report. The complete report is provided in the Appendix.

2.3.1. Summary of Methods Deployed

The Remanent Magnetization (RM) Method involves pre-magnetizing the steel strands with an electromagnet and measuring the magnetic field of the tendons at the concrete surface. If a fracture is present in the strand, magnetic leakage will occur. This will be picked up by the scanning machine which can be seen in Figure 2-27. The beam must be scanned several times across its length using the apparatus to inspect all the strands.



Figure 2-27: RM Scanning Apparatus

This machine measures the magnetization in two fields, namely (1) the remanent field and (2) the active field. Figure 2-28 shows an example of RM measurements in the active field where no damage was present. The signals caused by the stirrups show up very clearly in this field. Figure 2-29 displays an example of RM measurements in the remanent field.

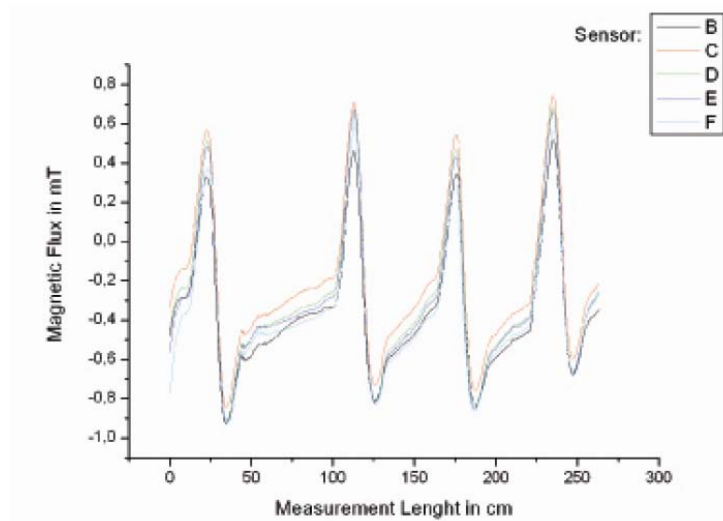


Figure 2-28: RM Measurement in the Active Field (No Fractures)

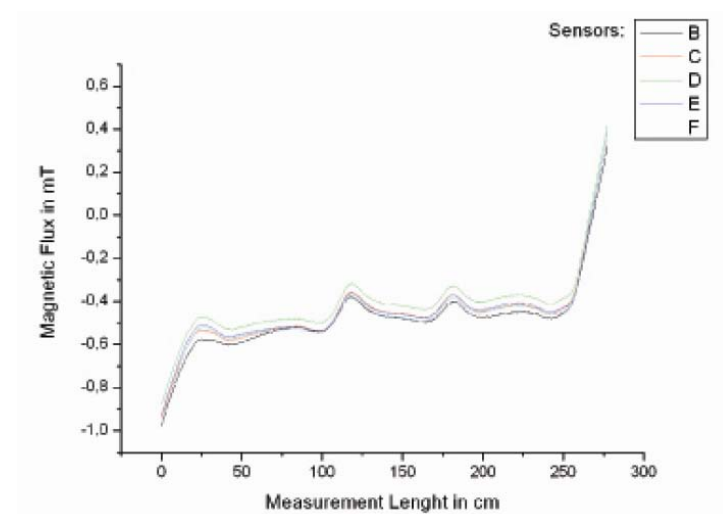


Figure 2-29: RM Measurement in the Remanent Field (No Fractures)

As mentioned, fractures will become evident through assessment of the RM measurements in both fields. In Figure 2-30, the magnetic flux in the active field is plotted against beam distance. In this example, a fracture is located toward the end of the scan. Figure 2-31 shows the remnant field magnetic flux plotted against beam distance; again, the fracture is located toward the end of the scan.

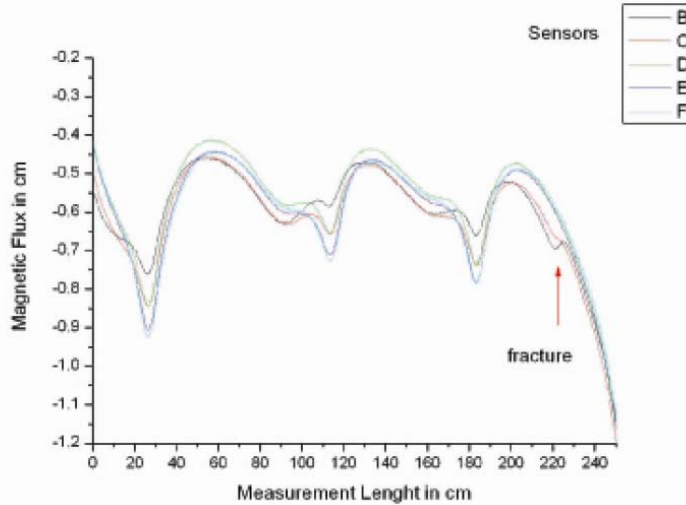


Figure 2-30: RM Measurement in the Active Field w/ Fracture

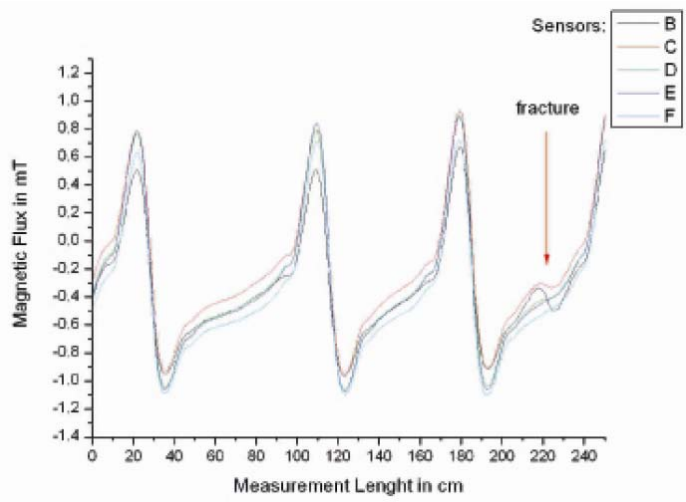


Figure 2-31: RM Measurement in the Remanent Field w/ Fracture

2.3.2. Summary of Results

Each beam was scanned with the RM apparatus, and locations of tentative fractures have been identified. This data is compiled in Table 2-2. It is important to note that the start and end distances were not reported and are consequently approximated in the following table. The potential corrosion locations may be off by several inches.

Table 2-2: Summary of Findings for RM:				
Beam ID:	Track #:	Start (in):	End (in):	Condition:
CC3	Track 4	102.36	106.30	Possible Fracture
CC4	N/A	-	-	-
LV16	Track 1	15.75	19.69	Corrosion
	Track 3	7.87	11.81	Possible Fracture
	Track 4	84.65	88.58	Fracture in Strand 17/18
	Track 5	84.65	88.58	Fracture in Strand 17/18
	Track 6	84.65	88.58	Corrosion
LV19	Track 4	68.90	72.83	Fracture in Strand 15

Table 2-2: Summary of Findings for RM:				
Beam ID:	Track #:	Start (in):	End (in):	Condition:
	Track 5	35.43	47.24	Possible Fracture
	Track 5	68.90	72.83	Fracture
MS2	Track 1	29.53	33.46	Fracture
	Track 1	84.65	88.58	Possible Fracture
	Track 1	112.20	116.14	Fracture
	Track 2	86.61	94.49	Possible Fracture
	Track 4	25.59	29.53	Fracture
	Track 4	57.09	61.02	Fracture
	Track 4	76.77	80.71	Fracture
MS3	Track 4	82.68	86.61	Possible Fracture
	Track 4	92.52	96.46	Fracture
	Track 4	112.20	116.14	Possible Fracture
	Track 5	41.34	45.28	Fracture
	Track 5	68.90	72.83	Possible Fracture

Information from the above table was assessed and then plotted over images of the beam surfaces. In the figures below, the transverse solid white lines indicate the extent of the beam length that was scanned, the longitudinal solid white lines indicate tracks along which the centerline of the scanning apparatus was passed, and the pink markings identify locations of suspected corrosion damage.

The RM scan results for beam CC3, shown in Figure 2-32, indicate one suspected area of wire fracture along track 4. No surface indicators of corrosion are present at this location.

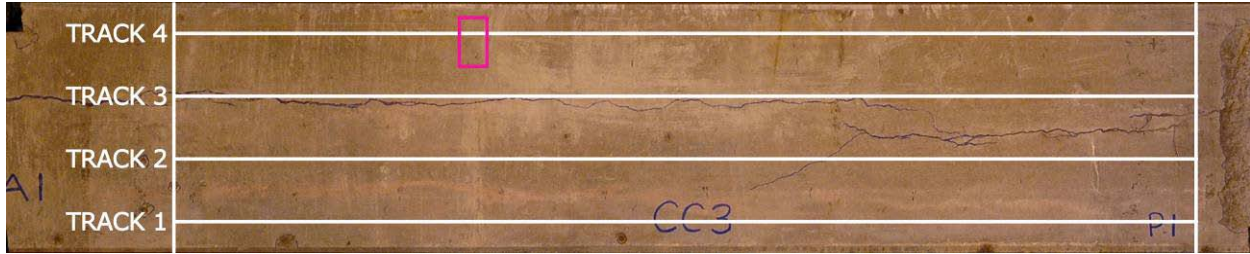


Figure 2-32: RM Scan Results for Beam CC3

The RM scan results for beam CC4, shown in Figure 2-33, indicate no suspected areas of wire fracture throughout this member despite the large longitudinal crack present along nearly the entire length of the beam.



Figure 2-33: RM Scan Results for Beam CC4

The RM scan results for beam LV16, shown in Figure 2-34, indicate five suspected areas of wire fracture throughout this member. It is important to note that the scans along tracks 4 and 5 picked up the same anomaly: a fracture in a particular strand. The suspected corrosion location

along track 6 can be identified as visually correct since it is located over a spalled section of concrete where heavily corroded steel reinforcement is exposed. The region identified along track 3 is located above a drainage hole and the region identified along track 1 is near a spalled section of concrete with cracking.



Figure 2-34: RM Scan Results for Beam LV16

The RM scan results for beam LV19, shown in Figure 2-35, indicate three suspected areas of wire fracture throughout this member all of which are near the various longitudinal cracks just north of the beam centerline.

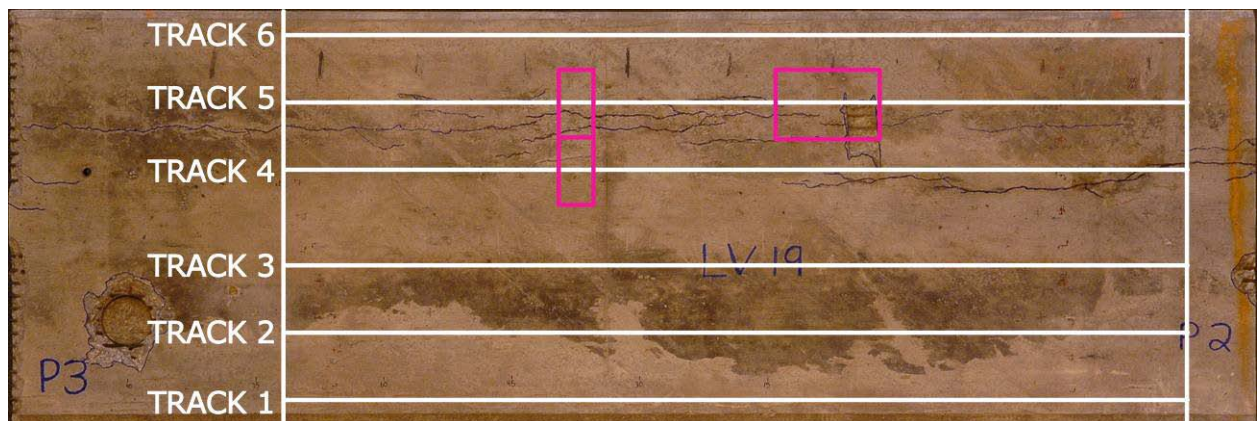


Figure 2-35: RM Scan Results for Beam LV19

The RM scan results for beam MS2, shown in Figure 2-36, indicate four suspected areas of wire fracture throughout this member. The first suspected area from the P3 side of track 1 is visually identifiable. It is located over a spalled section of concrete where the reinforcing steel is exposed and clearly corroded. The other three suspected fracture locations show no visible signs of strand damage on the concrete surface.

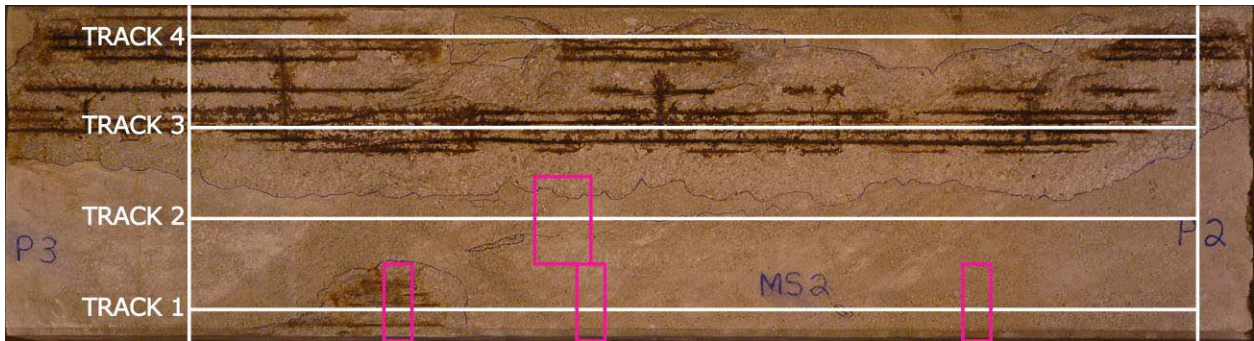


Figure 2-36: RM Scan Results for Beam MS2

The RM scan results for beam MS3, shown in Figure 2-37, indicate five suspected areas of wire fracture throughout this member all of which lie along the longitudinal crack detected during the visual inspection.

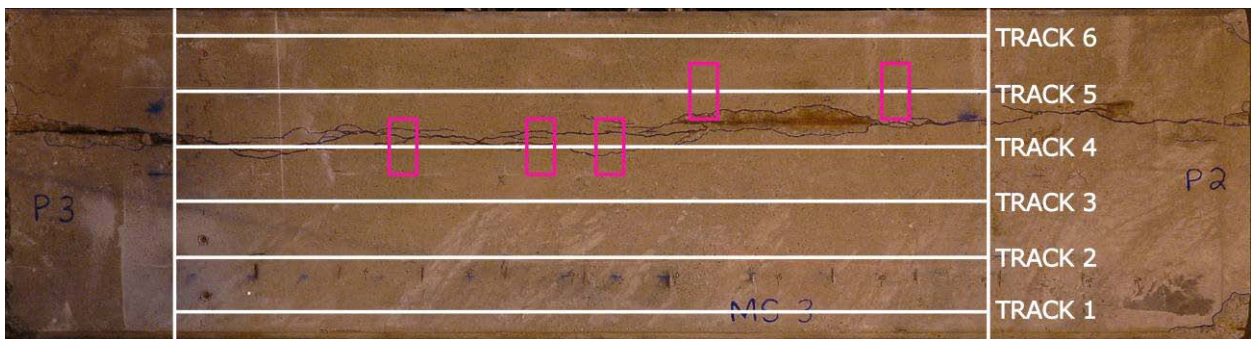


Figure 2-37: RM Scan Results for Beam MS3

2.4. Contractor #4: Physical Acoustics Corporation

Physical Acoustics Corporation examined the beams. Figures from their summary report “Feasibility of using Line Scanning Thermography for the Inspection of Concrete Structures with Embedded Rebar” are used within this report. The full report is included in the Appendix.

2.4.1. Summary of Methods Deployed

Line Scanning Thermography (LST) is a process in which a line heat source of finite width sweeps across the surface of a specimen at a constant speed. It is coupled with an Infrared Camera – or Microbolometer - to read the temperature changes in the surfaces during the test. An example of the testing machinery can be seen below in Figure 2-38.

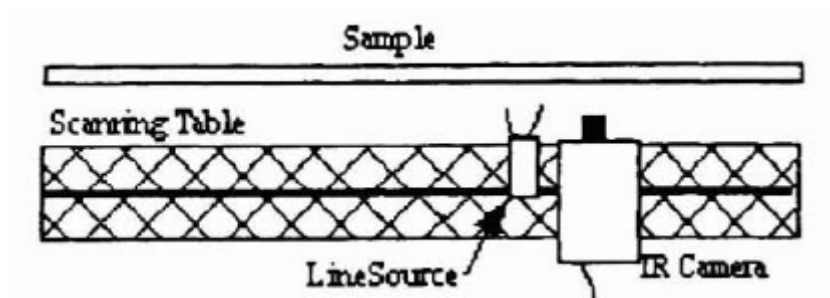


Figure 2-38: LST Apparatus

The IR Camera picks up the thermal response of the specimen and an analysis program (ThermoWin) compiles the data into a thermal map of the scanned subject. For the tests conducted at Lehigh University, the speed of the Thermography assembly ranged from 0.25 in./sec to 0.5 in./sec.

LST scans were to be performed and those thermal maps were to be analyzed to determine if the thermography assembly could pick up the location of strands and any defects due to corrosion. The LST assembly was placed 24 in. above the face of the scanned beams. Three scans were performed at the same location at varying times after the beam was heated; approximately 5, 20, and 42 seconds. The heating intensity was chosen to be 90 W/in. A sample of the produced thermal images can be found below in Figure 2-39.

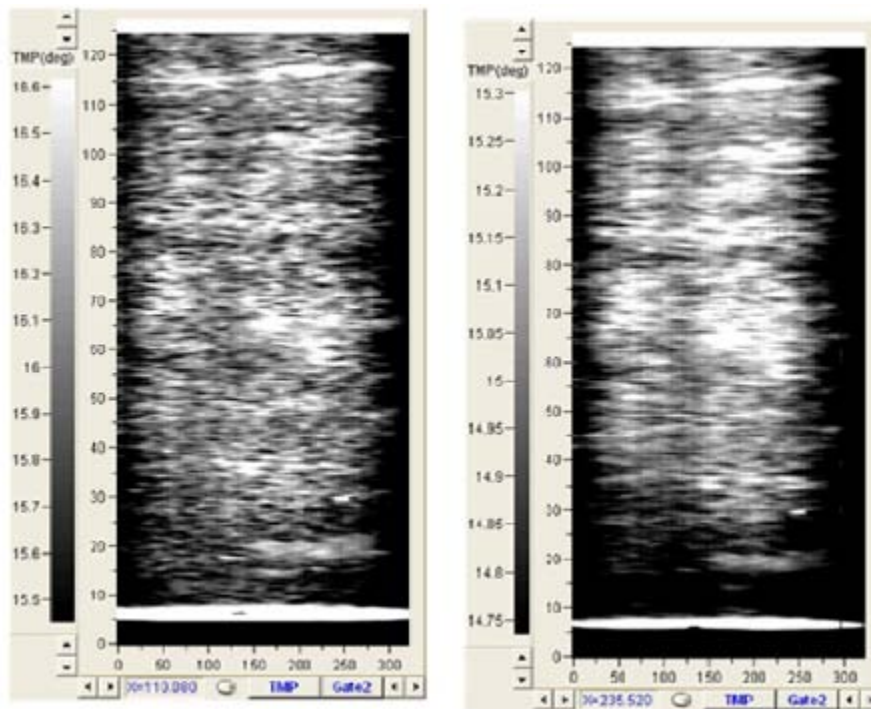


Figure 2-39: Thermal Images Produced from LST

2.4.2. Summary of Results

Physical Acoustics Corporation (PAC) tested three beams – MS3, CC3, and CC4 – using Thermography to try to identify corrosion in the strands. Each beam was divided into three sections along a particular length, and scanned three times after the heat source was applied at

approximately 5, 20, and 42 seconds. The aforementioned times correspond to Gate 220, Gate 120, and Gate 5 respectively as noted in the figures below. The average scan length was 120 inches and started from 25 to 35 inches from the end of each structure.

Beam MS3 was scanned in three strips, starting from the P3 end. The first scan represents the bottom third of the beam as shown in the picture of MS3 in Table 1-2. Accordingly, scan two represents the middle third of the beam and scan three represents the top third of the beam in that table. Scan 1, Scan 2, and Scan 3 for beam MS3 can be seen in Figure 2-40, Figure 2-41, and Figure 2-42, respectively. Scans 2 and 3 show the longitudinal crack on the surface of the beam detected during the visual inspection. The strands are not identifiable in the following figures. Consequently, it appears that identification of corrosion is not feasible with this method.

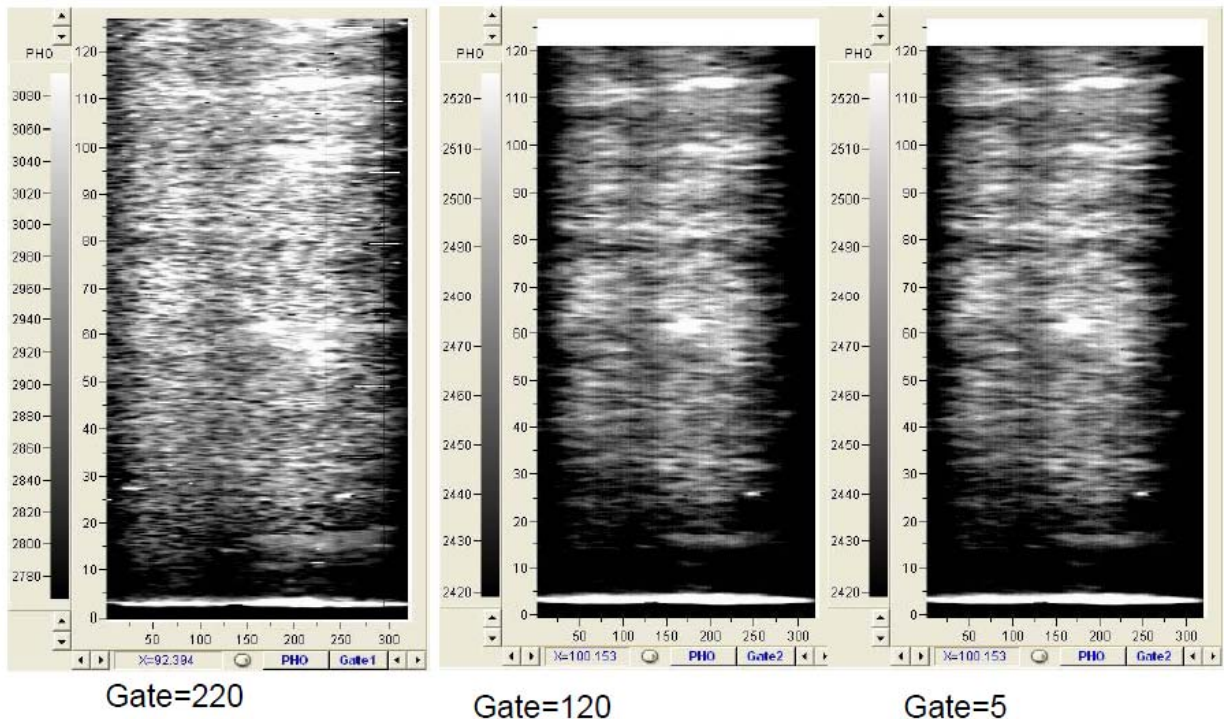
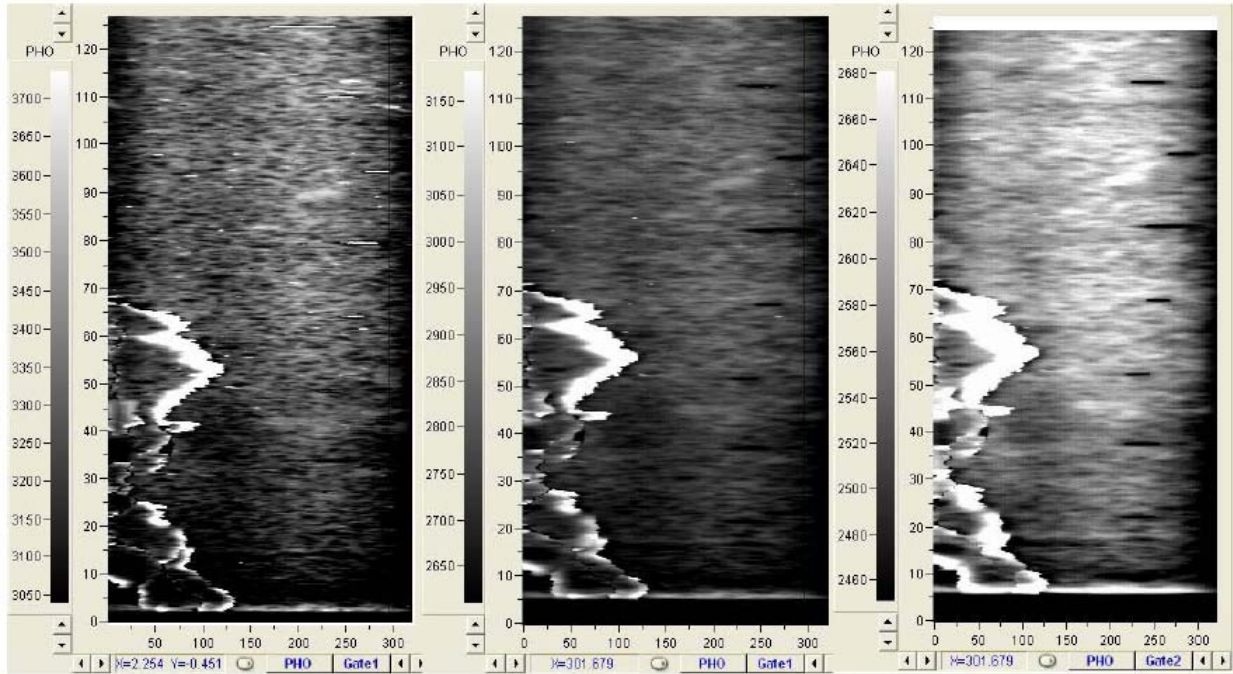


Figure 2-40: LST Scan 1 of Beam MS3

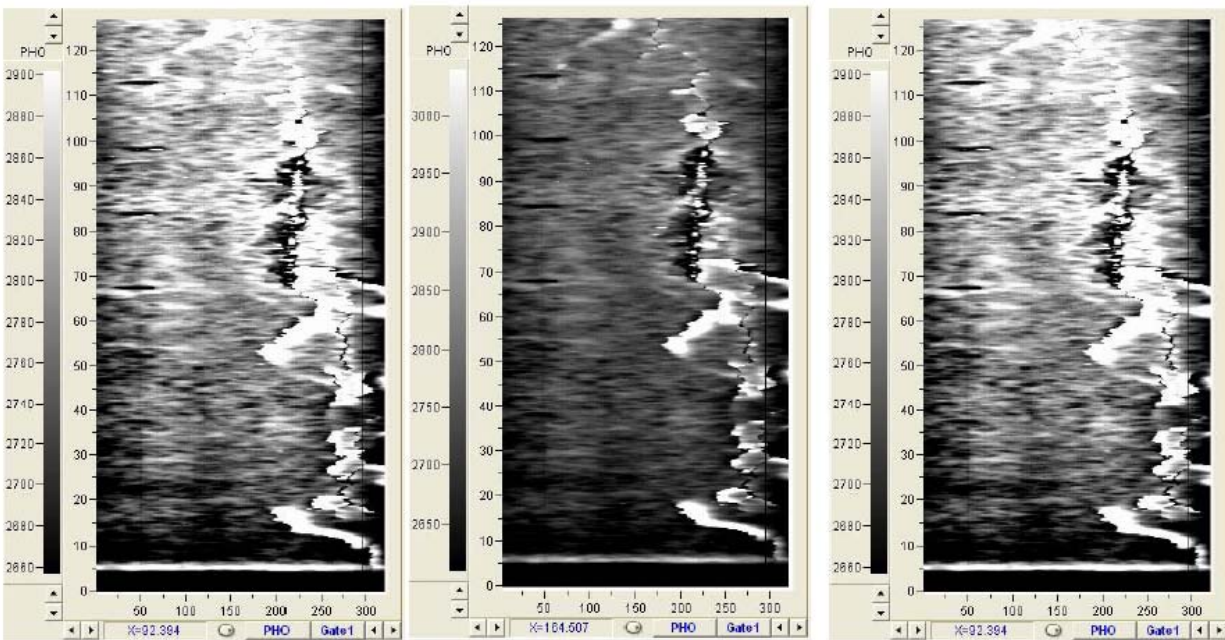


Gate=220

Gate=120

Gate=5

Figure 2-41: LST Scan 2 of Beam MS3



Gate=220

Gate=120

Gate=5

Figure 2-42: LST Scan 3 of Beam MS3

Beam CC3 was scanned in three strips starting from the P1 end. Scan 1, Scan 2, and Scan 3 for beam CC3 can be seen in Figure 2-43, Figure 2-44, and Figure 2-45, respectively. In the three scans, the longitudinal cracks along the center of the beam appear to be identified. The strands however are not discernable. Consequently, corrosion locations cannot be identified.

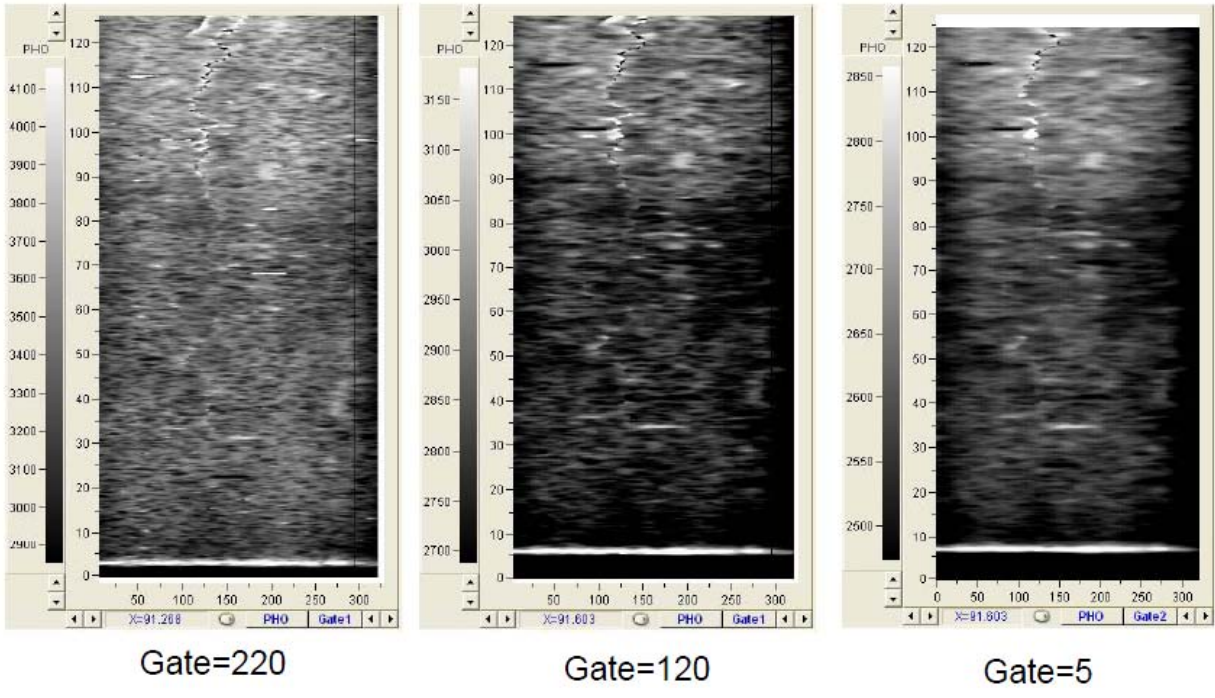


Figure 2-43: LST Scan 1 of Beam CC3

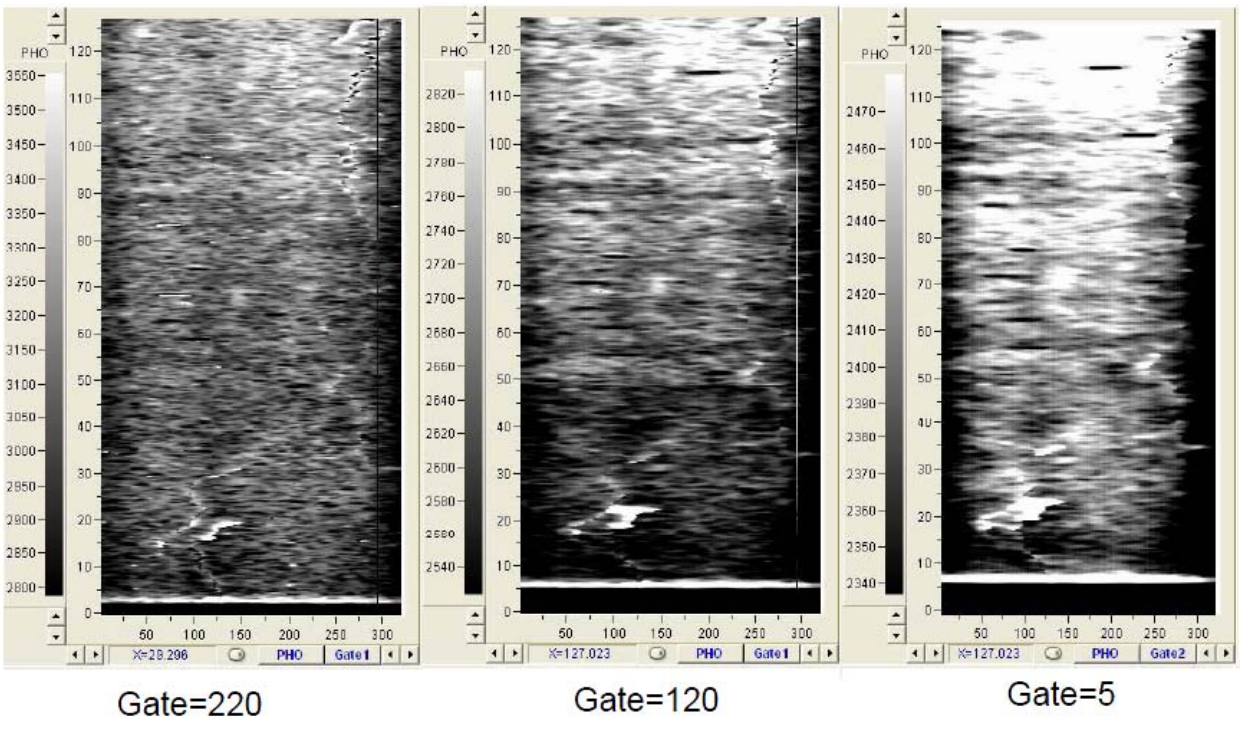


Figure 2-44: LST Scan 2 of Beam CC3

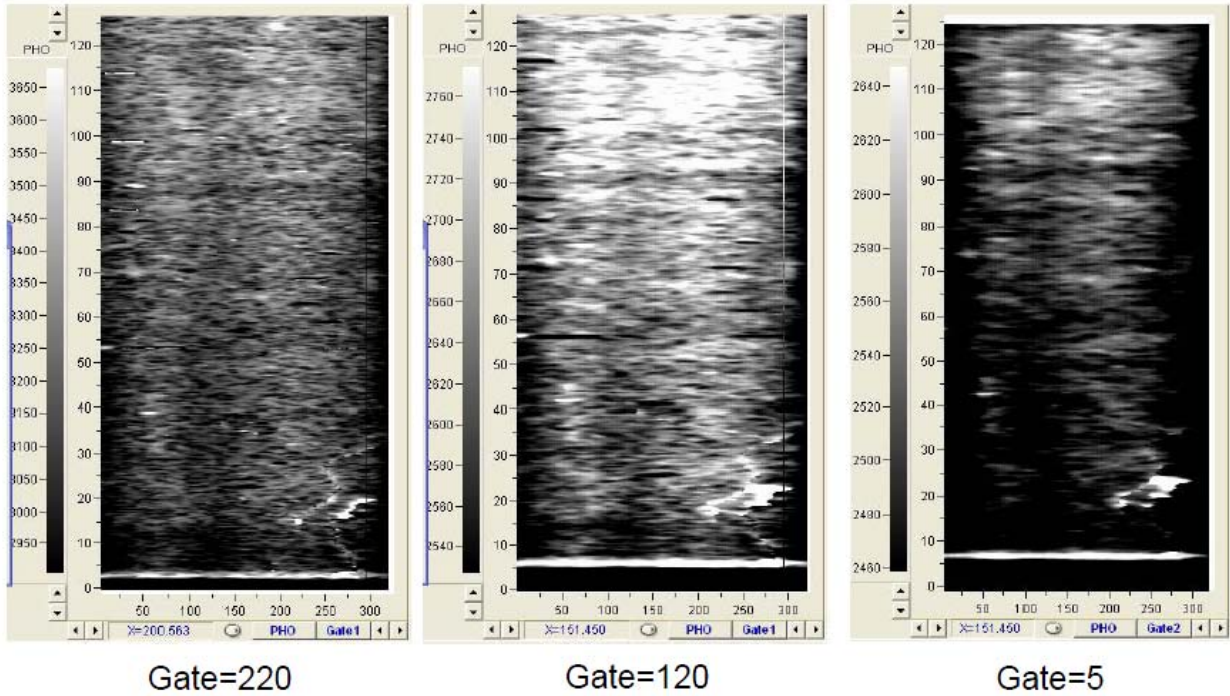


Figure 2-45: LST Scan 3 of Beam CC3

Beam CC4 was scanned in three strips, starting from the P2 end. Scan 1, Scan 2, and Scan 3 for beam CC4 can be seen in Figure 2-46, Figure 2-47, and Figure 2-48, respectively. Throughout the three scans, the longitudinal crack detected during the visual inspection cannot be located. The strands cannot be located in the following figures. Consequently, corrosion locations cannot be identified.

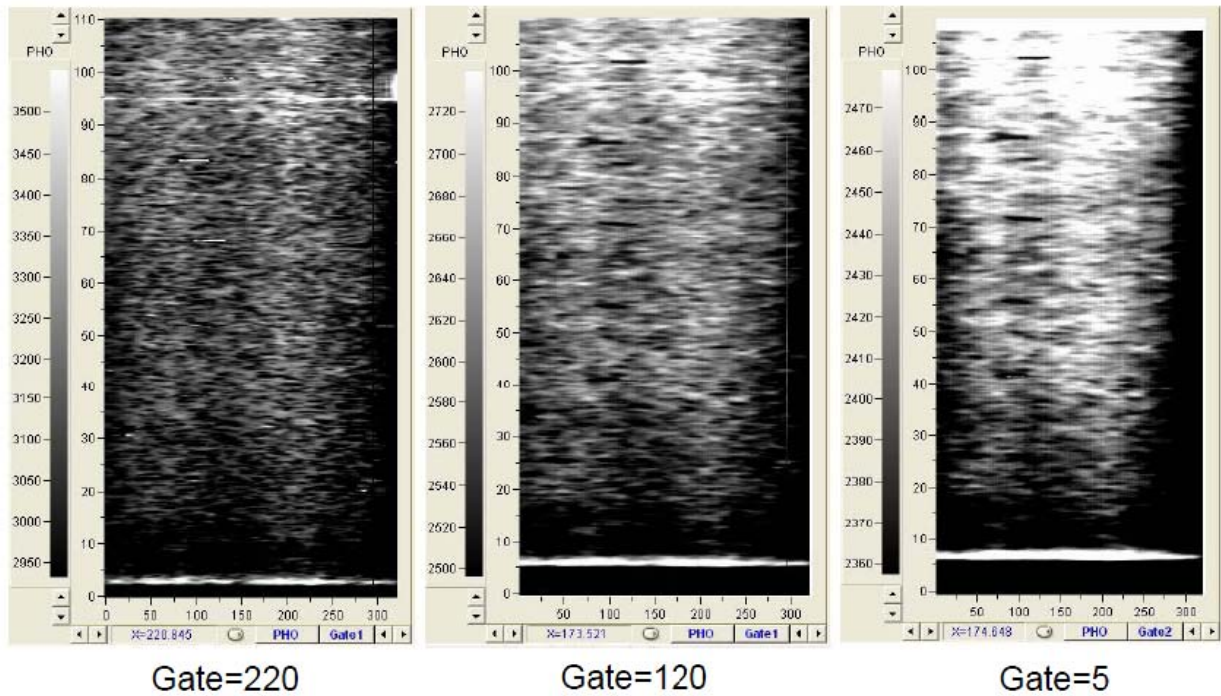


Figure 2-46: LST Scan 1 of Beam CC4

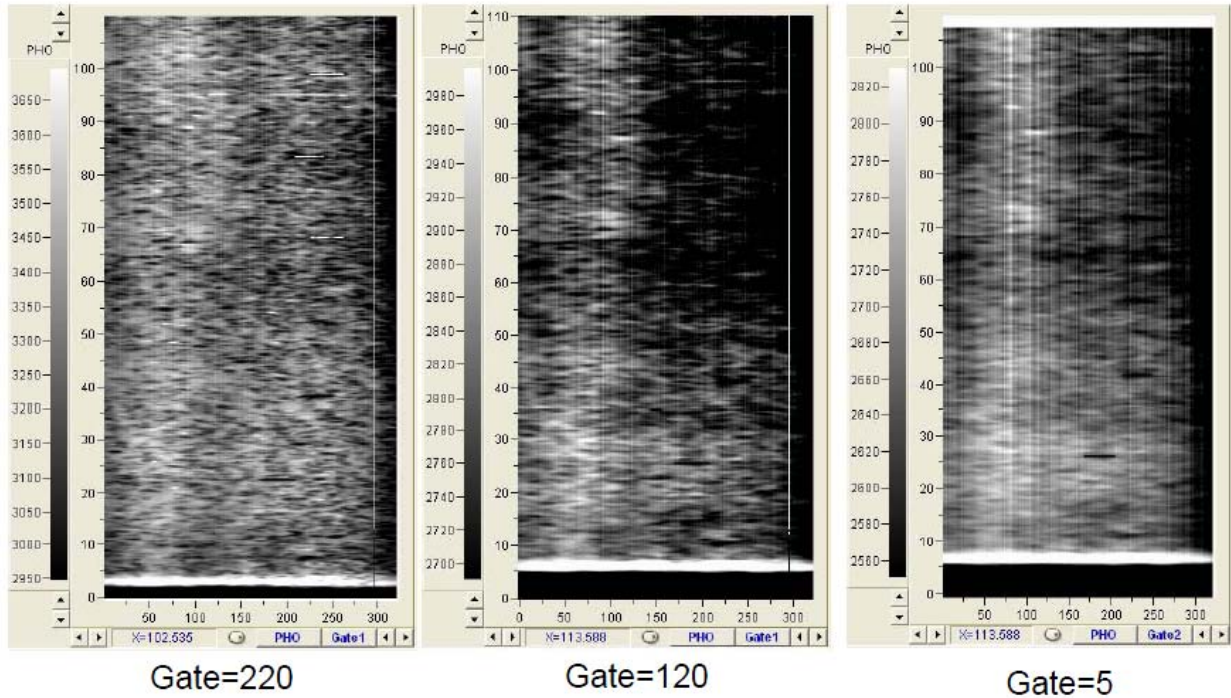


Figure 2-47: LST Scan 2 of Beam CC4

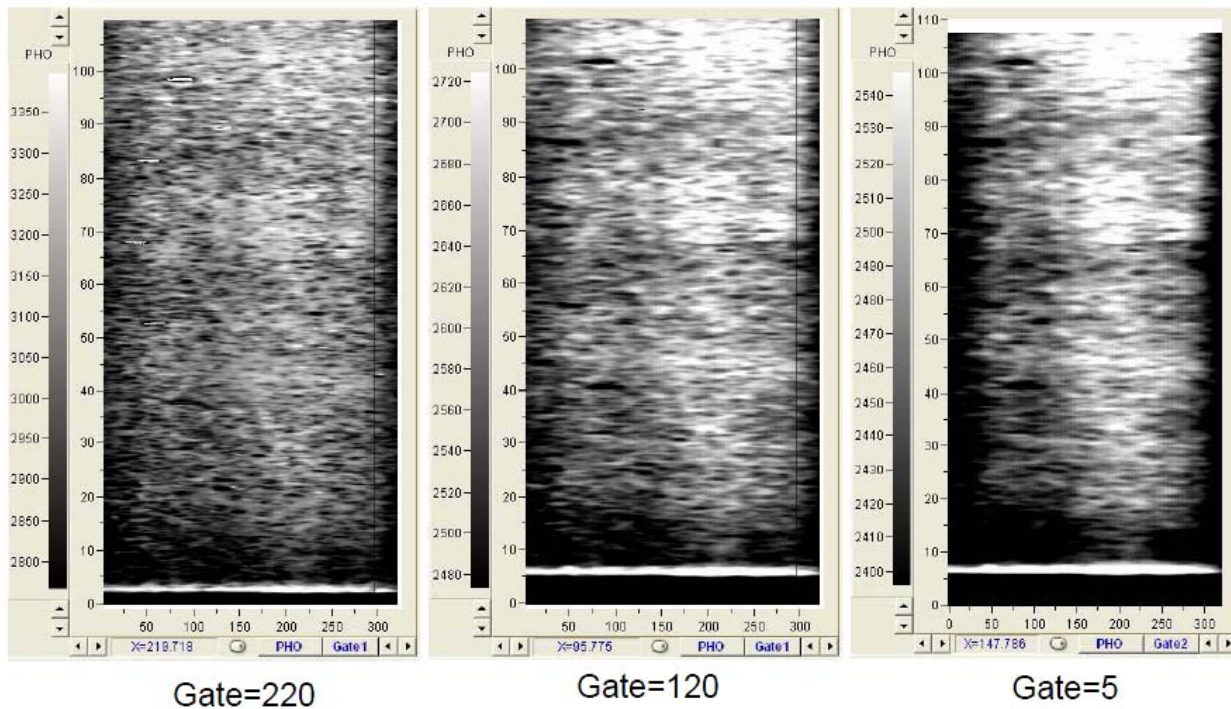


Figure 2-48: LST Scan 3 of Beam CC4

2.5. Contractor #5: LIMCMT, Inc. with David L. Gress & Associates

Mr. Malcolm Lim, Dr. David Gress, and Mr. Adam Perkins performed two types of tests on the beam specimens, namely (1) Electromagnetic Corrosion Detection (EMCD) and (2) Galvanostatic Pulse Corrosion Rate (GPCR). Figures from their report “Study to Identify

Inspection Methods and Techniques to Determine Non-Visible Corrosion of Pre-Stressing Strands in Concrete Bridge Components” are used within this section. The complete report is included in the Appendix.

2.5.1. Summary of Methods Deployed

Electromagnetic Corrosion Detection (EMCD) is a technique in which radio frequency excitations are imposed on a conductor (the steel strands in this case) to cause sympathetic re-radiation at specific frequencies. Re-radiation may cause non-linear junctions in the frequency whereby the signal re-radiates at multiple frequencies, changing the fundamental frequency. This can be more easily illustrated through the following figures.

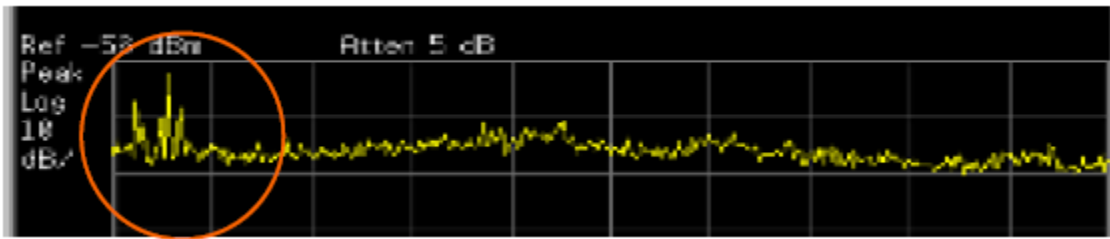


Figure 2-49: Typical Resonance Junction (No Corrosion)

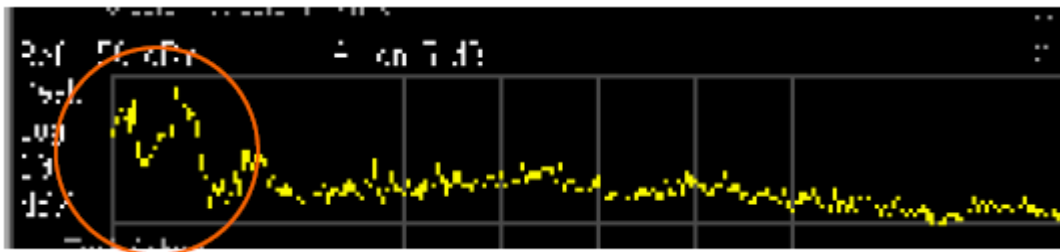


Figure 2-50: Non-Linear Resonance Junction (Corrosion)

Figure 2-49 shows a common resonance junction with no corrosion present and no spurious emissions. This figure was obtained by sweeping the frequency generator and antenna across a strand. As this is occurring the response is monitored on a spectrum analyzer.

Figure 2-50 shows a non-linear resonance junction, which is indicative of corrosion by-products. As mentioned previously, the presence of a non-linear junction results in the radiation of spurious emissions. These signals mix and alter the fundamental frequency, most often creating a rise in the initial amplitude. Generally, non-linear junctions occur within the frequency bandwidth of 0 to 1.5 GHz.

Galvanostatic Pulse Corrosion Rate (GPCR) is a testing method that allows the estimation of the corrosion rate of the reinforcing steel. The testing apparatus can be seen below in Figure 2-51.



Figure 2-51: Galvanostatic Pulse Corrosion Rate Test Equipment

The guard ring on the end of the apparatus has a counter electrode directly behind it. This produces an anodic current pulse in an attempt to polarize the steel reinforcement. The steel reinforcement is easier to polarize when in a passive state since corrosion has not started yet. If corrosion is present, the polarized potential is lowered and a different current reading is obtained. The suggested values for different corrosion rates are listed in Table 2-3:

Table 2-3: Corrosion Rate Values	
Corrosion Current Density (i_{corr}):	Corrosion Rate:
$10 < i_{\text{corr}} \leq 100$	Very High
$1.0 < i_{\text{corr}} < 10$	High
$0.1 < i_{\text{corr}} < 1.0$	Low/Moderate
$i_{\text{corr}} \leq 0.1$	Negligible

To perform the Galvanostatic Pulse Corrosion Rate tests, a grid was laid out on each beam; readings were obtained for each grid intersection point. A connection had to be made to each strand to establish a closed circuit and obtain correct readings. The surface of the beams had to be wet upon time of the test. The top and bottom mat of strands were tested, and corrosion potential maps were created as seen in Figure 2-52.

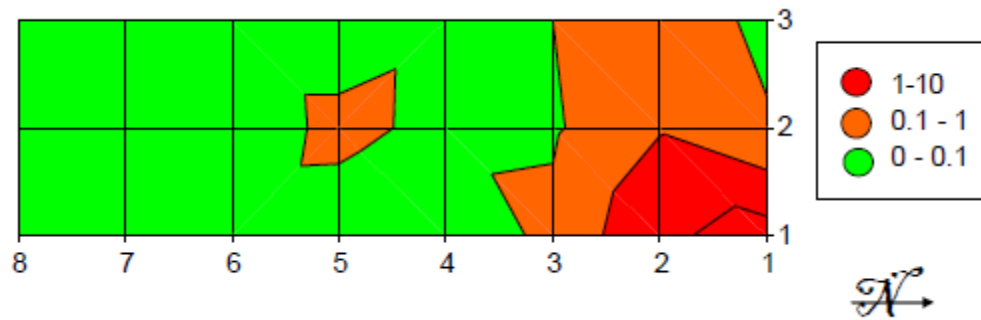


Figure 2-52: Typical Corrosion Rate Potential Map

2.5.2. Summary of Results

Electromagnetic Corrosion Detection was used in conjunction with Galvanostatic Pulse Corrosion Rate to attempt to detect non-visible corrosion on beams CC3, LVD7, and MS3. Results are as indicated below in Table 2-4. The identification of non-linear junctions – supposed corrosion locations – were only identified at grid points for the Galvanostatic Pulse Corrosion Rate Test.

Beam ID:	Ref. Pier End:	X Grid:	Y Grid:	X Dist (in):	Y Dist (in):
CC3	P1	1	1	6	6
		1	2	6	18
		6	3	66	30
		8	3	90	30
		9	2	102	18
		5	1	54	6
LVD7	P1	10	1	114	6
		1	1	6	12
MS3	P2	7	3	78	36
		5	2	54	24
		5	3	54	36
		6	3	66	36
		8	3	90	36
		9	3	102	36
		2	2	18	24

Information from the above table was assessed and then plotted over an image of the respective beam surface. The figures below display the suspected corrosion locations identified by blue circles over a grid intersection.

The findings for beam CC3 indicate corrosion at seven different grid intersection points; as shown in Figure 2-53.

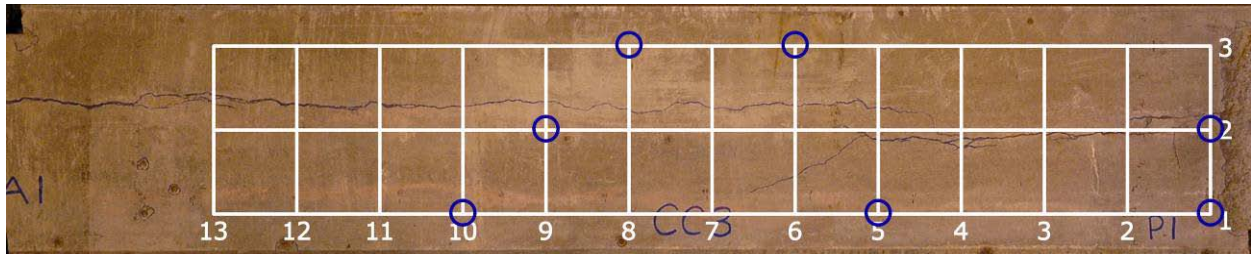


Figure 2-53: EMCD Results for Beam CC3

The findings for beam LVD7 indicate corrosion at two different grid intersection points; as shown in Figure 2-54.

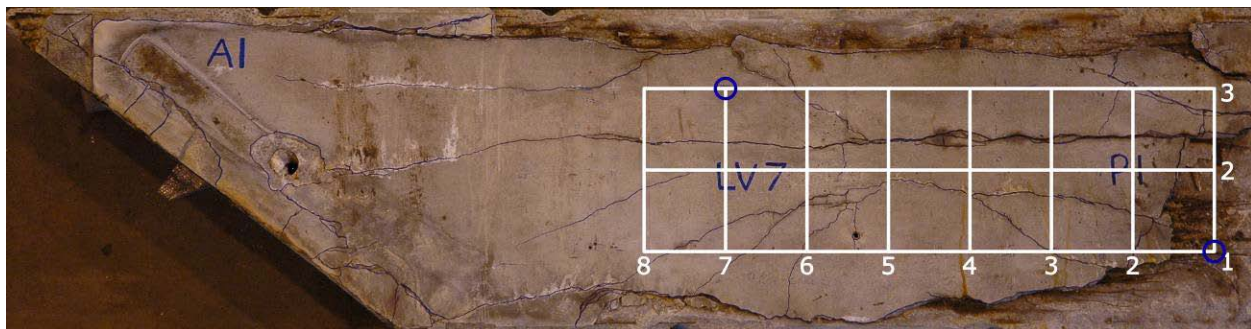


Figure 2-54: EMCD Results for Beam LV7

The EMCD test was not performed for beam LV19; only the GPCR Test was used on this member. To provide more insight to the location of the pulse corrosion rate readings, Figure 2-55 is presented below.

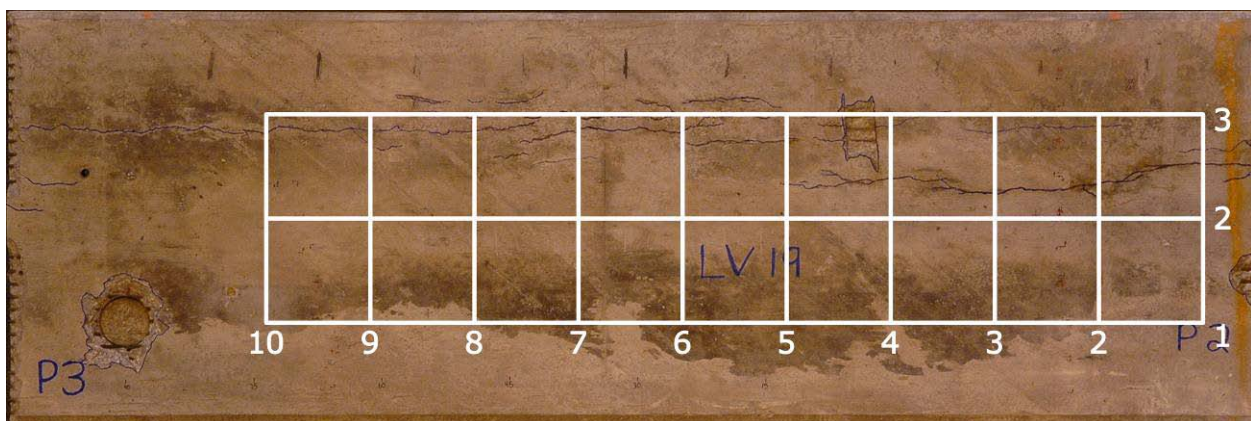


Figure 2-55: EMCD Results for Beam LV19

The findings for beam MS3 indicate corrosion at six different grid intersection points as shown in Figure 2-56. The four points located along the longitudinal line 3 are located near the longitudinal crack detected during the visual inspection.

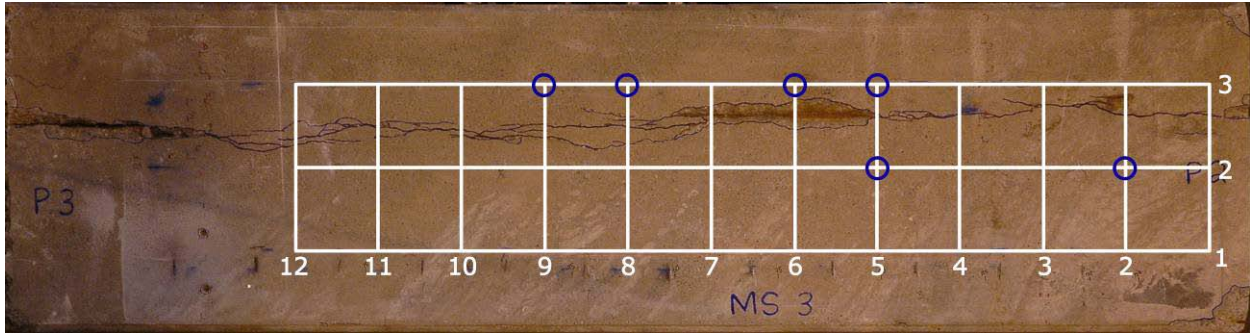


Figure 2-56: EMCD Results for Beam MS3

The Galvanostatic Pulse Corrosion Rate tests led to the development of corrosion potential (equal to i_{corr}) maps. Tests were performed for top and bottom mat reinforcement for beams MS3 and CC3. Only the top mat was tested for LV7 and LV19. The corrosion rate potential maps are presented below, whereby regions shaded red ($1.0 < i_{corr} < 10$) indicate high corrosion rate potential, regions shaded orange ($0.1 < i_{corr} < 1.0$) indicate moderate to low corrosion rate potential, and regions shaded green ($i_{corr} < 0.1$) indicate negligible corrosion rate potential.

Figure 2-57 shows the corrosion rate potential for the bottom strand layer of MS3. It indicates that along the top half of the beam, i_{corr} readings show a likelihood of a high corrosion rate. The bottom half of the beam has i_{corr} readings that indicate a moderate to low corrosion rate.

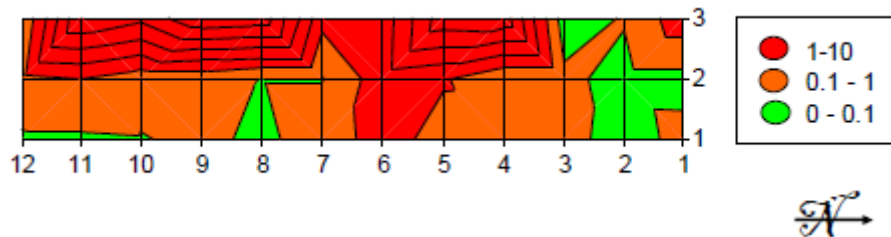


Figure 2-57: Corrosion Rate Potential (i_{corr}) for Top Mat of MS3

Figure 2-58 shows the corrosion rate potential for the bottom strand layer of MS3. It shows that the bottom mat has less corrosion rate potential than the top mat. There is an i_{corr} indication for high corrosion rate potential along the top half of the beam from approximately grid lines 6 through 12.

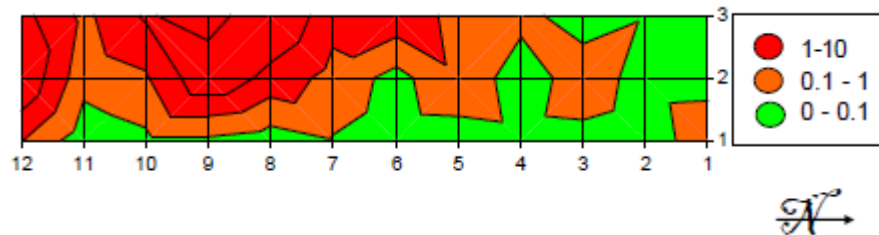


Figure 2-58: Corrosion Rate Potential (i_{corr}) for Bottom Mat of MS3

Figure 2-59 shows the corrosion rate potential for the top mat reinforcement of CC3. The vast majority of the beam has i_{corr} readings in the negligible range. High i_{corr} readings can be found at the grid intersections of 8-3 and 6-3.

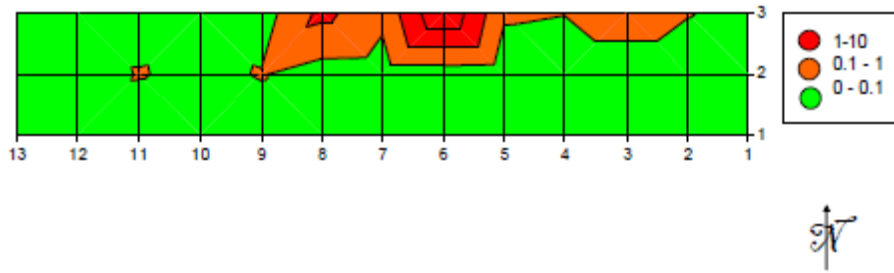


Figure 2-59: Corrosion Rate Potential (i_{corr}) for Top Mat of CC3

Figure 2-60 shows the corrosion rate potential for the bottom mat reinforcement of CC3. Again, the majority of the beam has i_{corr} readings in the negligible range. Locations of high corrosion rate potential can be found at grid intersections 1-1, 4-3, and 8-3.

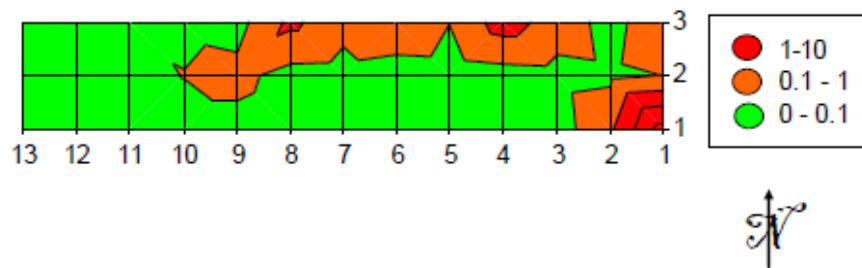


Figure 2-60: Corrosion Rate Potential for Bottom Mat of CC3

Figure 2-61 shows the corrosion rate potential for the top mat reinforcement of LV7. The i_{corr} readings in the lower-right quadrant of the beam indicate the likelihood of a high corrosion rate.

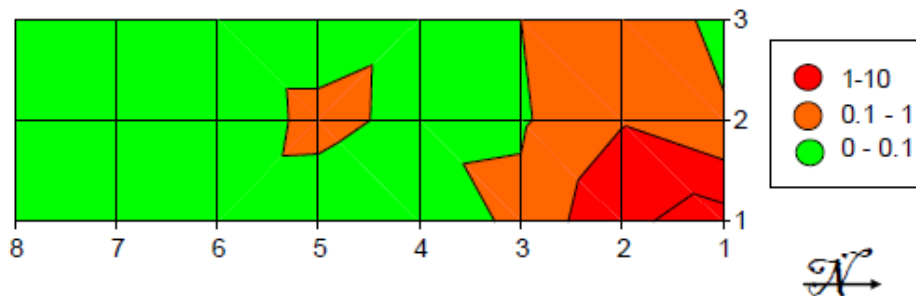


Figure 2-61: Corrosion Rate Potential for Top Mat of LV7

Figure 2-62 shows the corrosion rate potential for the top mat reinforcement of LV19. All areas except grid intersection 7-2 show i_{corr} in the range of low to moderate and negligible corrosion rate potential. Grid intersection 7-2 indicates a high corrosion rate potential.

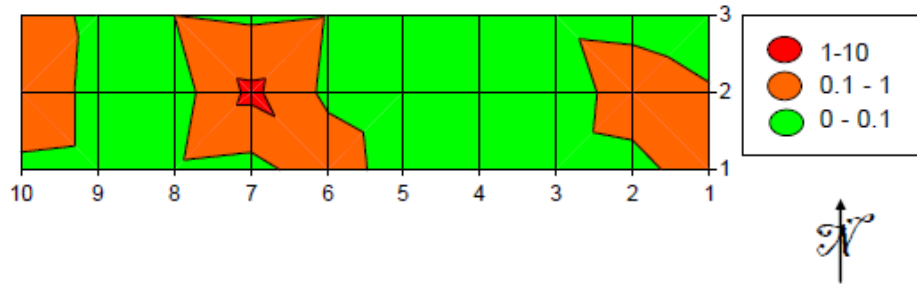


Figure 2-62: Corrosion Rate Potential for Top Mat of LV19

2.6. Contractor #6: Dynasty Group

Mr. Aldo de la Haza, representing the Dynasty Group performed a series of tests on six of the seven prestressed concrete beams (all but LV7). Those tests consisted of (1) Ultrasonic Impact Echo (IE) tests, (2) Ultrasonic Shear Wave tests (UST) using two different devices, (3) Ground Penetrating Radar (GPR), and (4) 3D Laser Scanning. Figures from his report “Report for the Nondestructive Testing of Prestressed Precast Box-Beams” are used within this report. The complete report is given in the Appendix.

2.6.1. Summary of Methods Deployed

The Impact Echo test method can be used to detect internal flaws within concrete materials such as freezing and thawing deterioration, internal voids and cracks, honeycombing, and delaminations in concrete due to corrosion of steel reinforcement. Figure 2-63 displays the IE test apparatus.



Figure 2-63: IE Testing Device

During an IE test, mechanical energy is introduced to the beam at a particular point. This energy creates stress waves which propagate through the concrete at a finite speed. It is theorized that the velocity of the stress waves is related to the material through which it passes. If no internal discontinuities exist the waves will have a higher velocity compared to those with internal discontinuities. The transducer acoustically mounted on the surface receives the reflections created from the energy impact. The amplitude spectrum is then analyzed to determine if any discontinuities are present. This information is reinforced graphically in Figure 2-64.

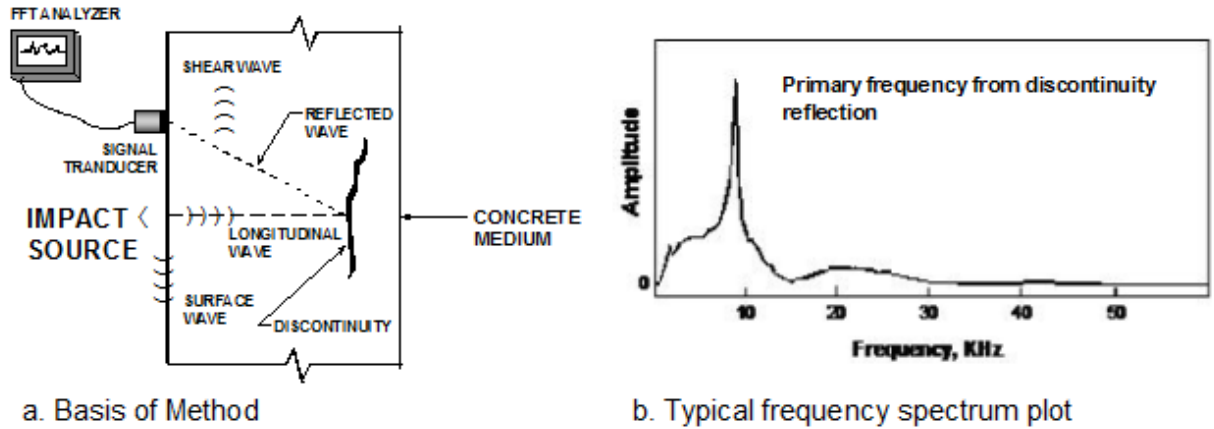


Figure 2-64: IE Test Method Theory

Further, Figure 2-65 and Figure 2-66 provide the time and frequency domain amplitude spectra for an area with no anomalies and anomalies, respectively. The time domain response for an area with no detected anomalies begins when the energy is introduced into the structure and slowly decays with time. This is much different from an area with detected anomalies, where the response is inconsistent.

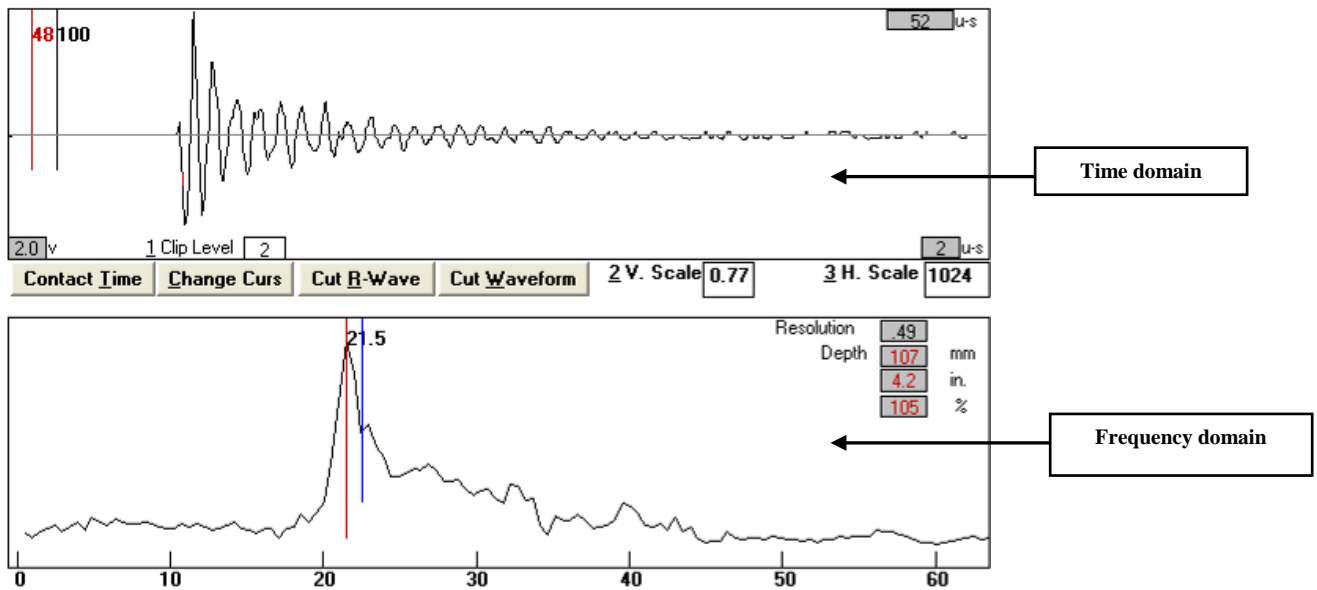


Figure 2-65: Time and Frequency Domain Responses for an Area with No Anomalies

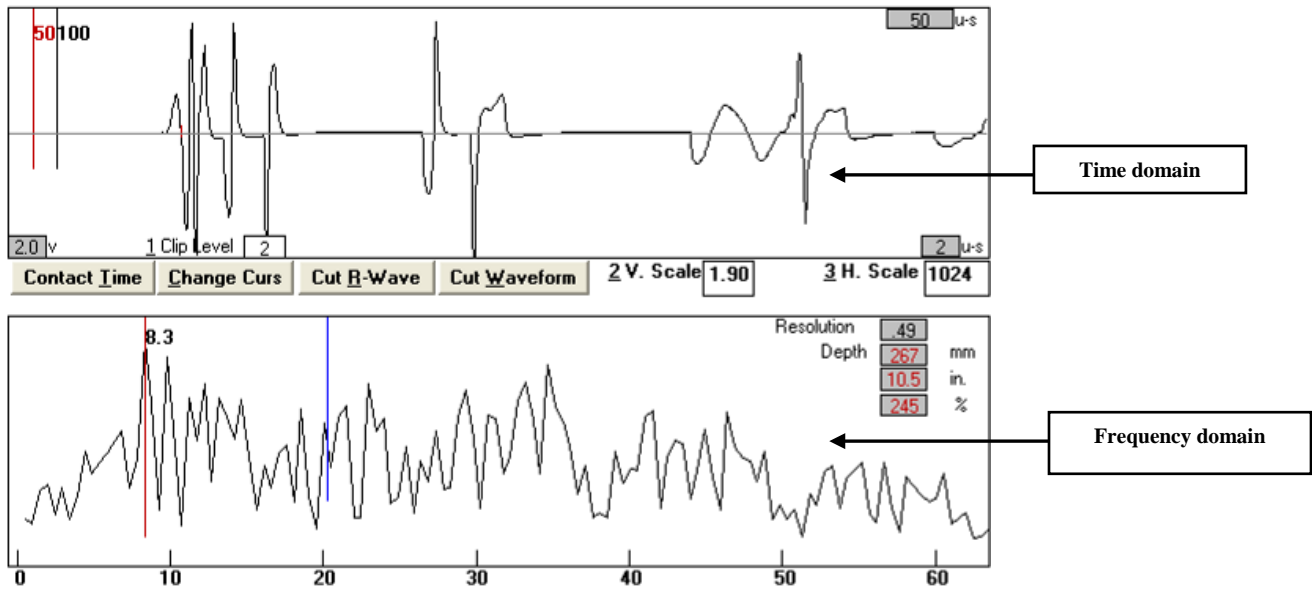


Figure 2-66: Time and Frequency Domain Responses for an Area with an Anomaly

Ultrasonic Shear-Wave Testing (UST) was performed on the bridge members as well. Two devices were used, namely the Monolith Device and the Polygon Device, as shown in Figure 2-67 and Figure 2-68, respectively. UST is commonly used on concrete structures to detect internal flaws such as honeycombing, delaminations, cracks, and poorly consolidated concrete. It is also used to assess the geometrical properties of concrete structures. The principle behind UST – similar to Ultrasonic IE principles – is that as shear-waves are emitted into the structure, they pass through the concrete and are monitored by the receiving unit which then analyzes the data and produces time and frequency domain responses such that internal conditions of the concrete can be assessed.



Figure 2-67: UST Polygon Device



Figure 2-68: UST Monolith Device

The Polygon device produces results as shown in Figure 2-69. The tomographic map produced – which can be displayed in 2D or 3D – indicates reflections from potential internal flaws. Top, longitudinal side, and cross section views of these maps are produced.

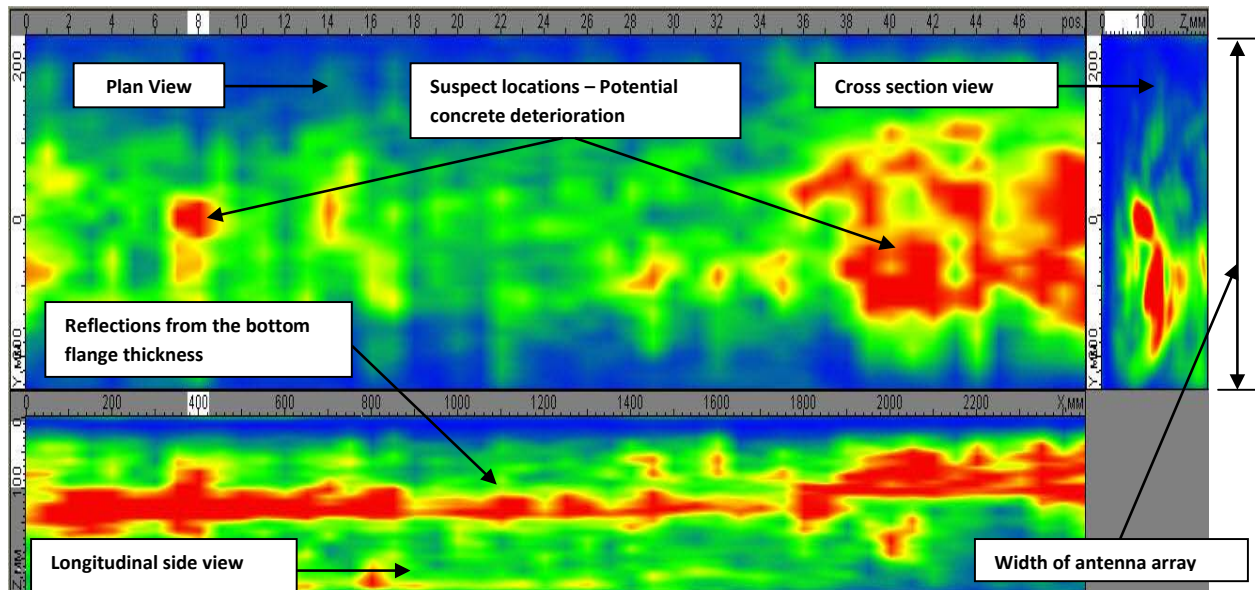


Figure 2-69: Sample of Results Produced by the UST Polygon Device

The Monolith testing device produces results as shown in Figure 2-70. The x-axis represents two-way travel time for the shear waves and the y-axis represents shear-wave amplitude. The wave velocity through a particular material, in this case concrete, is used to calculate the depth of the member or a potential internal flaw.

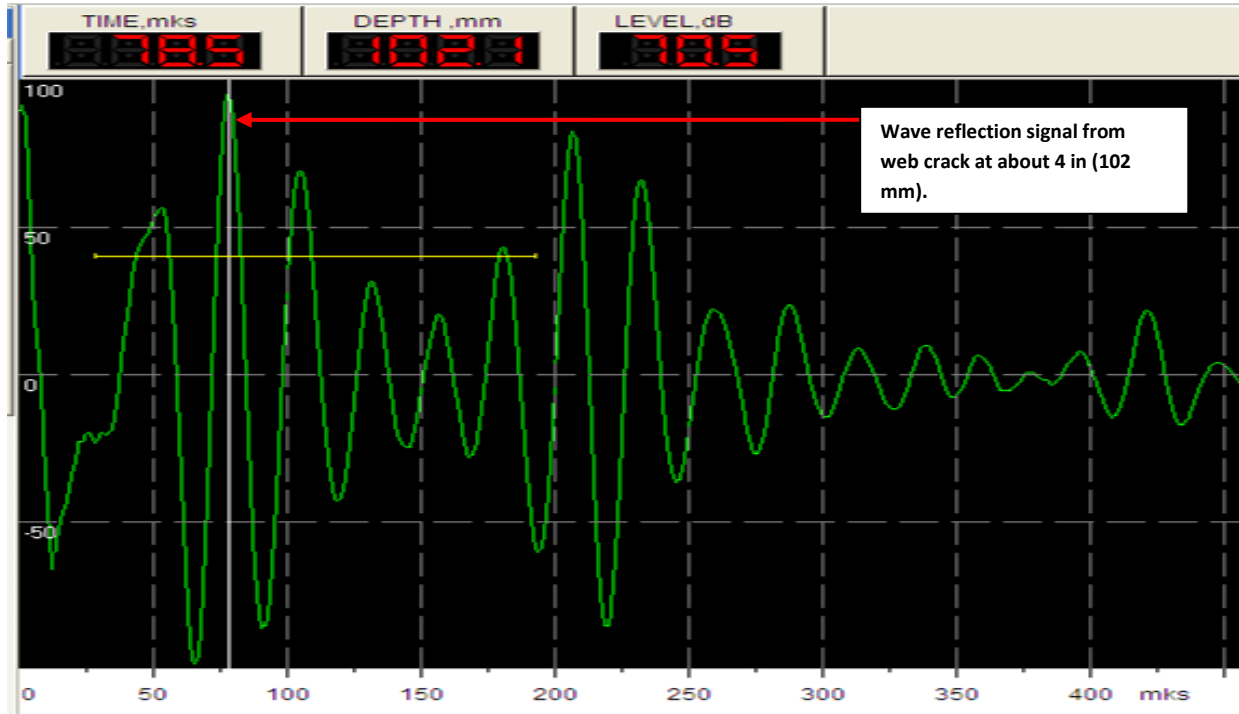


Figure 2-70: Sample of Results Produced by the UST Monolith Device

GPR technology was also utilized by Contractor #6 for these bridge beams. For a review of the methodology, refer to Section 2.2.1. NDT Contractor #6 used the same device as NDT Contractor #2.

3D Laser Scanning was also in an evaluation of the beams by Contractor #6. Through this technology, thousands of measurements are made each second creating an array of points with a specific x, y, and z coordinates relative to the measurement device. A typical scan contains millions of measurements and is visualized as a point cloud. Accurate measurements can be taken from point cloud data, such as concrete spall geometries, crack geometries, etc. The measurement device and governing point cloud are as shown below in Figure 2-71.

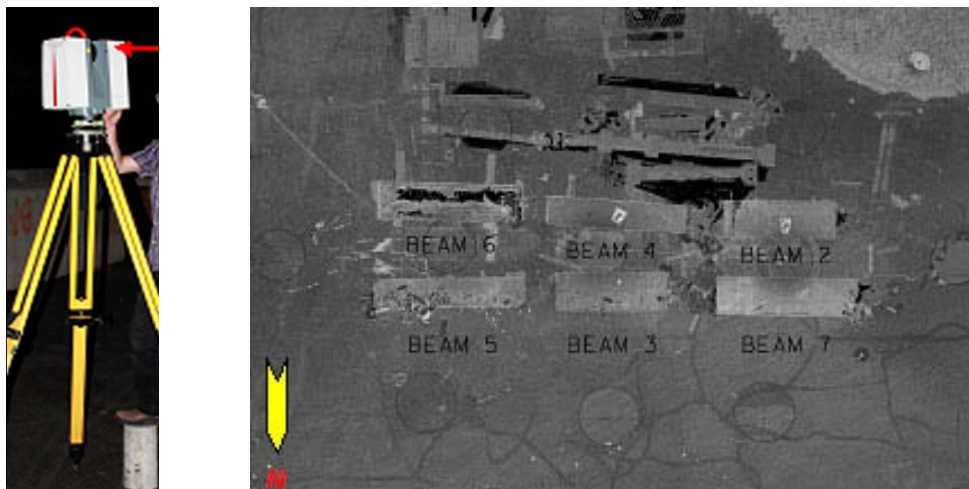


Figure 2-71: 3D Laser Scanning Device and Governing Point Cloud

Shown below, in Figure 2-72 and Figure 2-73, is a comparison of the physical state of a box-girder compared to the 3D Laser Scanning representation.

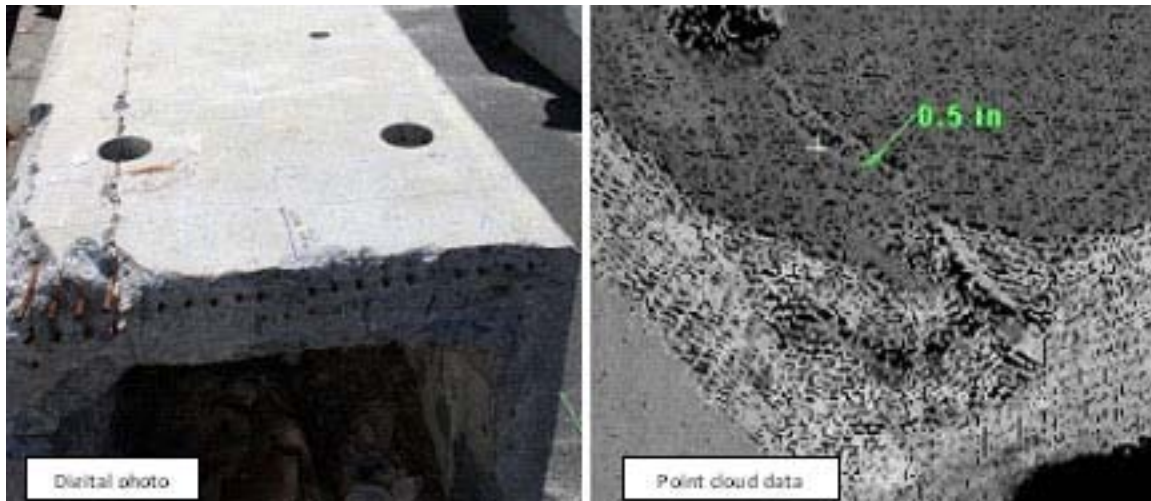


Figure 2-72: 3D Laser Scanning used to Detect and Identify Crack-Width

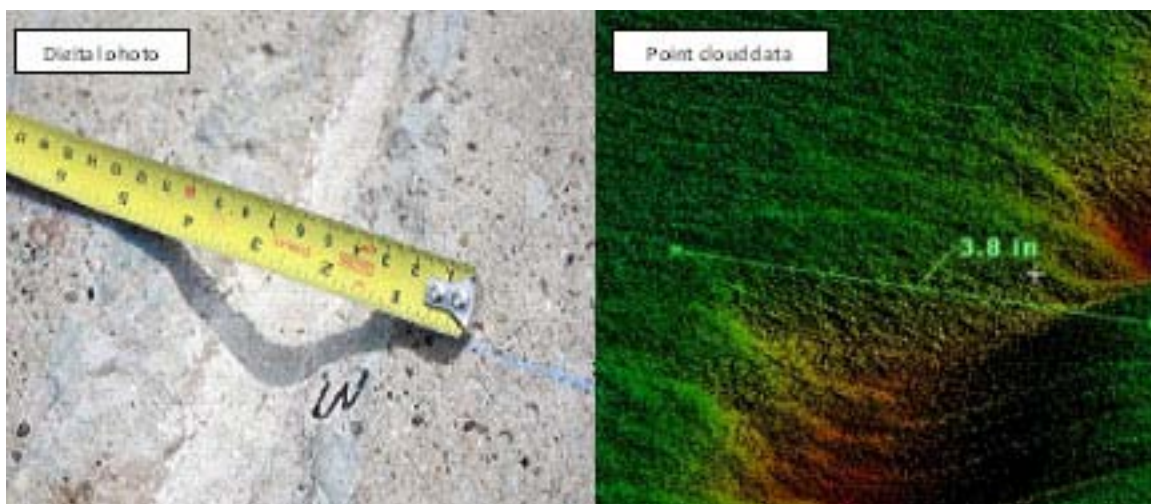


Figure 2-73: 3D Laser Scanning Used to Detect and Identify Concrete Spall Geometries

2.6.2. Summary of Results

As mentioned previously, four different NDT methods were used on these beams by Contractor #6, namely Ultrasonic Impact-Echo Tests, Ultrasonic Shear-Wave Tests, Ground Penetrating Radar, and 3D Laser Scanning. 3D Laser Scanning was used to assess the geometric characteristics, and will not be discussed. A grid was setup for each beam, with transverse lines spaced at 12 inches and longitudinal lines spaced at 6 inches.

The IE tests were performed at every grid intersection point for the following beams: CC3, CC4, LV16, LV16, and MS3. Data for beam MS2 was not recorded due to the uneven concrete surface from spalling. In the superimposed results figures, a full green circle represents a full-flange thickness; no detected internal flaws were recorded at these locations. A full red circle represents the findings of a suspected anomaly such as delaminations, cracks, honeycombing, etc.

Two separate devices were used for the Shear-wave tests: the polygon and the monolith. The polygon is represented in the superimposed results figures as the colored tomographic map on the beam surface. The Polygon machine was used to conduct UST for beams CC3, CC4, LV16, LV19, and MS2; data for beam MS2 was not recorded due to the uneven concrete surface from spalling. The Polygon machine performed an ultrasonic shear-wave test every 2 in. along each beams length. Two lines of scanning were needed to cover the width of the beam. Readings of blue and green represent a stronger reflection of internal conditions versus readings of yellow and red, where potential internal discontinuities may exist. The Monolith device was used to conduct UST for beams CC3 and MS3, as well as a few discrete locations on other beams. The tests for the monolith device were performed at grid intersection points. For the superimposed results figures below, a green open-triangle represents a full thickness reflection from the flange whereas a red open-triangle represents a potential internal discontinuity.

GPR technology was used on the following beams: CC3, CC4, LV16, LV19, MS2, and MS3. The scanning apparatus was used along each transverse and longitudinal grid line. In the superimposed results figures, a yellow box is placed over regions where GPR signal attenuations – indicative of potential corrosion locations – were found.

The findings of all of these NDT methods were combined and superimposed on the beams surface. These figures are displayed in the figures below. The legend for these figures is shown in Figure 2-74.

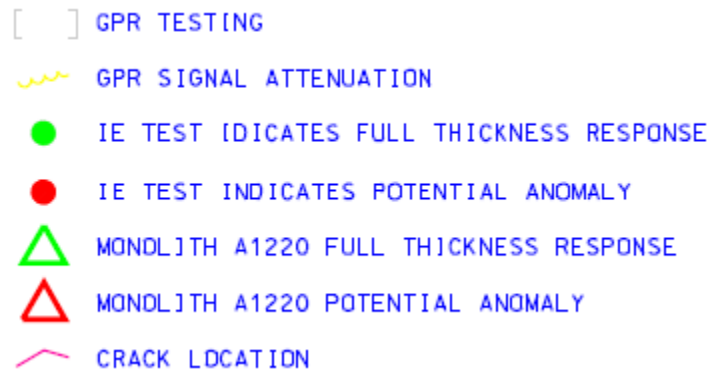


Figure 2-74: Legend for Superimposed NDT Methodologies

Beam CC3 was subjected to a combination of NDT procedures. The results are shown in Figure 2-75. Of the 75 locations tested by the Monolith device, 6 were identified as having potential anomalies. Of the 105 locations tested by the IE method, 13 were identified as having potential anomalies. GPR technology was applied to this beam, but no diminished reflections were identified. The polygon UST results indicate diminished reflections towards the midspan of the beam. Some of the anomalies have been listed as: “Delamination,” “Crack in Web,” and “Reflection from Crack.” It is important to note that the methods also picked up the diaphragm located within the void of the beam.

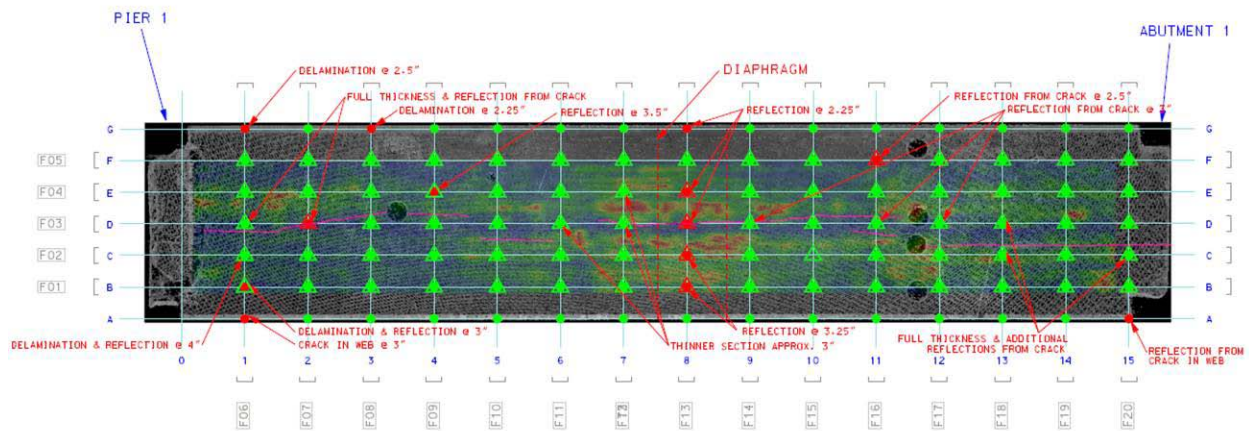


Figure 2-75: Combined NDT Results Superimposed on Beam Surface for CC3

Beam CC4 was subjected to a combination of NDT procedures. The results are shown in Figure 2-76. Of the 96 locations tested by the IE method, 29 were identified as having potential anomalies. GPR technology was applied to this beam, but no diminished reflections were identified. The polygon UST results indicate diminished reflections towards the pier 1 end of the beam. Some of the anomalies have been listed as: “Crack in Web” and “Reflection from Crack.”

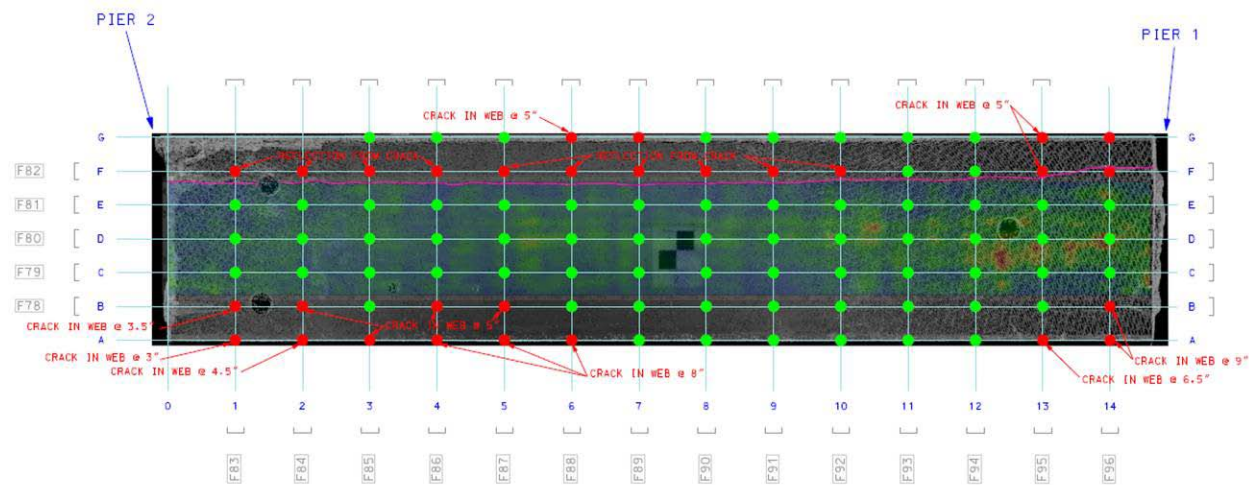


Figure 2-76: Combined NDT Results Superimposed on Beam Surface for CC4

Beam LV16 was subjected to a combination of NDT procedures. The results are shown in Figure 2-77. Of the 89 locations tested by the IE method, 10 were identified as having potential anomalies. GPR technology was applied to this beam, but no diminished reflections were identified. The polygon UST results indicate diminished reflections around the same location as the diaphragm. Some of the anomalies have been listed as: “Crack in Web,” “Crack,” and “Delaminated Concrete.” It is important to note that the methods also picked up the diaphragm located within the void of the beam.

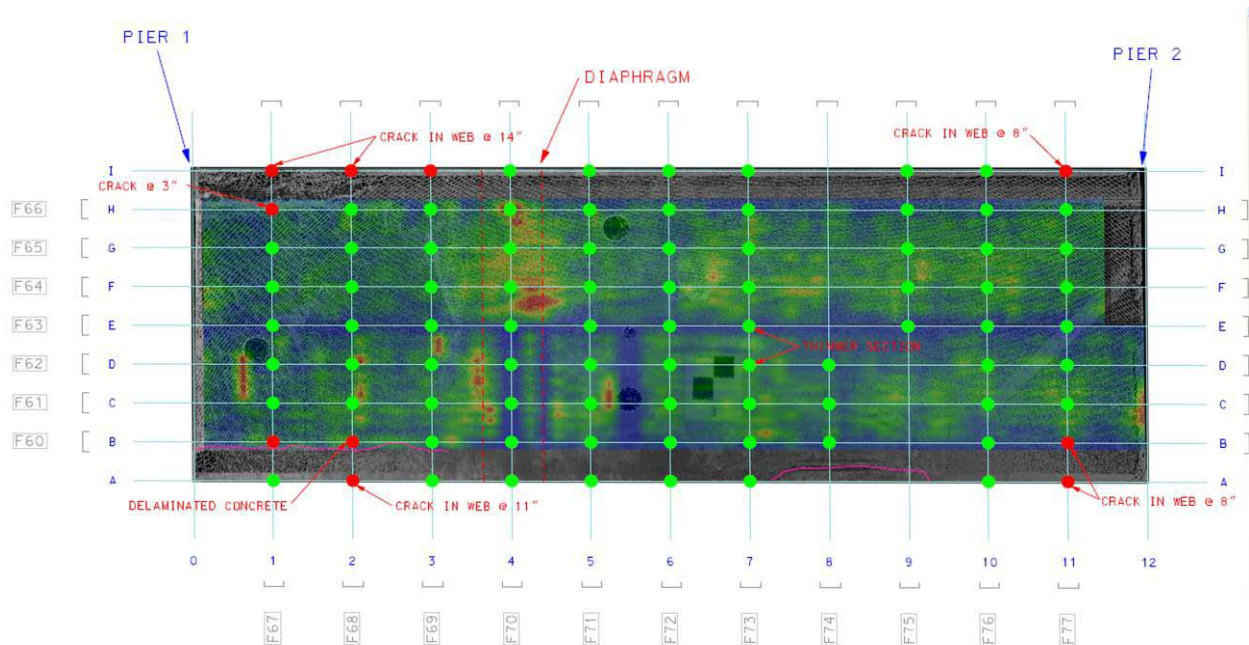


Figure 2-77: Combined NDT Results Superimposed on Beam Surface for LV16

Beam LV19 was subjected to a combination of NDT procedures. The results are shown in Figure 2-78. Of the 90 locations tested by the IE method, 23 were identified as having potential anomalies. GPR technology was applied to this beam, and two areas with diminished reflection are identified, both of which lie above the longitudinal crack present on the beam surface. The polygon UST results indicate diminished reflections around the longitudinal crack. Some of the anomalies have been listed as: “Crack in Web,” “Crack,” and “Delaminated Concrete.”

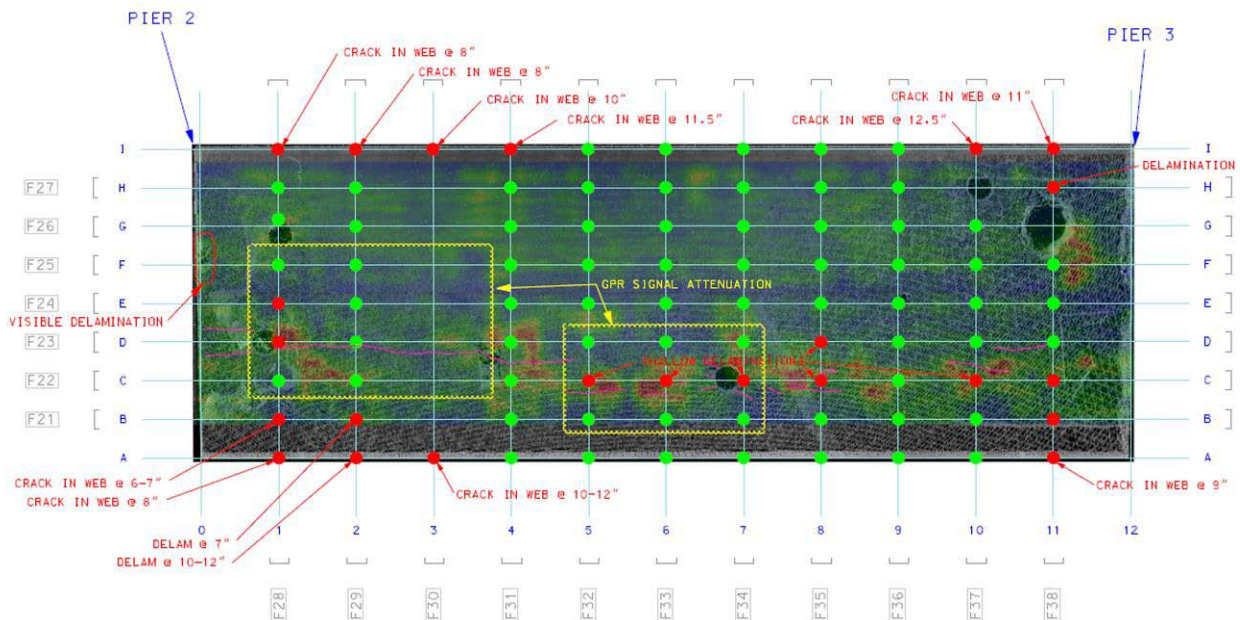


Figure 2-78: Combined NDT Results Superimposed on Beam Surface for LV19

Beam MS2 was subjected to only one NDT procedure. The results are shown in Figure 2-79. GPR technology was applied to this beam, and one large area with diminished reflection is

identified. Almost the entire bottom half of the beam is spalled off, leaving the strands corroded and missing in some spots. Despite the seriously adverse condition of the bottom half of the beam, only a portion is picked up as an attenuated signal by the GPR device. The top half of the beam does not show any attenuated signals.

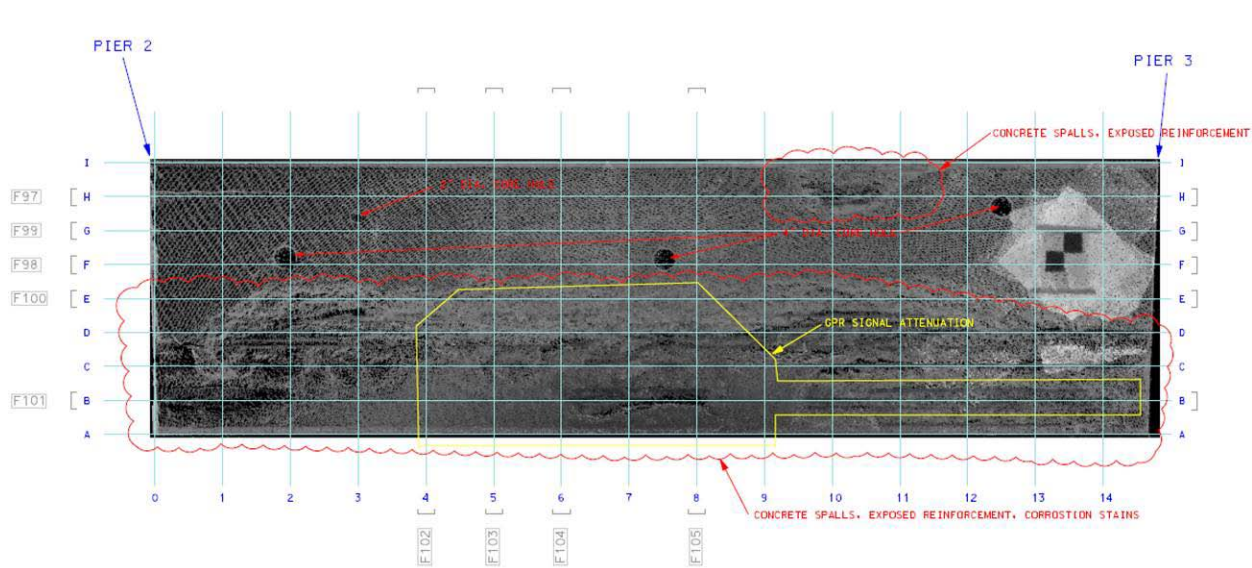


Figure 2-79: Combined NDT Results Superimposed on Beam Surface for MS2

Beam MS3 was subjected to a combination of NDT procedures. The results are shown in Figure 2-80. Of the 68 locations tested by the monolith device (UST), none were identified as having potential anomalies. Of the 126 locations tested by the IE method, 22 were identified as having potential anomalies. GPR technology was applied to this beam, and three areas with diminished reflection are identified, all of which lie above the longitudinal crack present on the beam surface. The polygon UST results indicate diminished reflections around the longitudinal crack. Some of the anomalies have been listed as: “Crack in Web,” “Crack,” “Shallow Delamination,” “Possible Honeycomb,” “Reflection in Web,” “Delamination,” and “Reflection from Crack.”

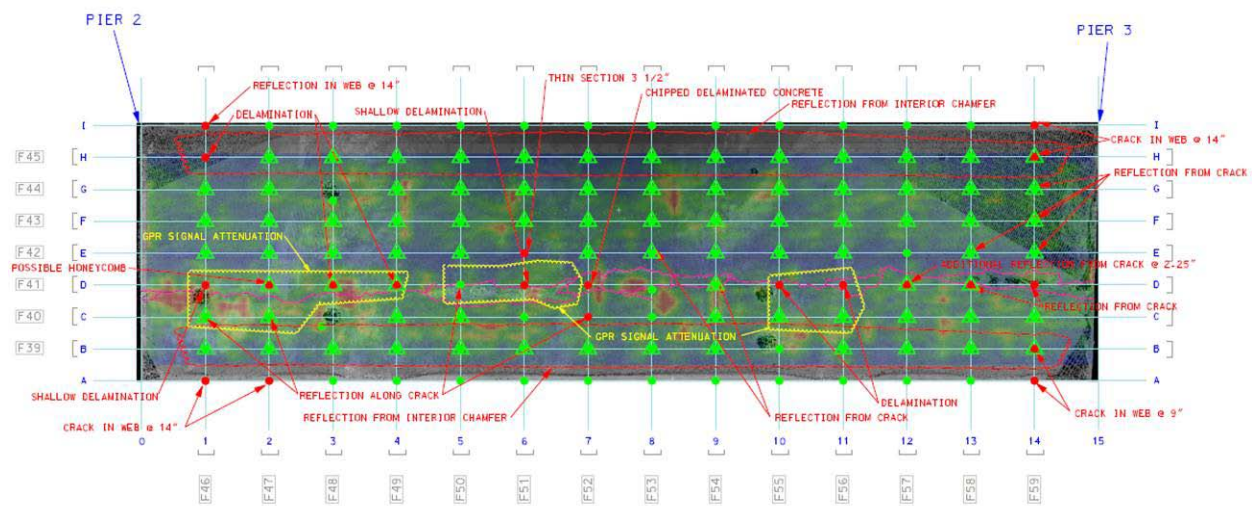


Figure 2-80: Combined NDT Results Superimposed on Beam Surface for MS3

3. Accuracy Non-Destructive Testing Methods

To assess the accuracy of the NDT methods investigated, the results of each testing method were compared to the findings of the destructive evaluation of the seven beams. The external damage of each beam and the internal damage of each strand was measured and recorded. A detailed description of the methods used and the results are presented in Task 2.1 of the project and are summarized in the 2010 report [Naito, Hodgson, and Jones].

The exact location and type of corrosion damage on each beam strand was documented. For each case of corrosion damage, the number of wires damaged and the severity of damage were recorded. Damage was assessed relative to a Damage Index. Six damage indices were used, each representing unique level of damage:

- (0) No corrosion
- (1) Light corrosion – Surface corrosion without significant section loss.
- (2) Pitting – Section loss less than 20% of section due to corrosion.
- (3) Heavy pitting – Section loss greater than 20% of section due to corrosion.
- (4) Wire loss – Complete section loss of wire(s) on strand due to corrosion.
- (5) Wire fracture – Fracture of wire(s) on strand due to combined effects of corrosion and load redistribution due to failure of adjacent wire(s).

Damage was documented in areas where the cover was intact. In areas where the concrete had spalled and strands were exposed or missing the damage was visible and not recorded.

The results of the visual inspection were compiled and summarized [Naito, Hodgson, and Jones 2010]. The results of the study are reproduced here to allow direct comparison with the NDT methods. The legend to identify the different levels of corrosion damage can be seen in Figure 3-1. The damage conditions occurred at specific points and over various lengths along the strand. Consequently these damage locations are illustrated as points or lines on the damage profile overlays that follow.



Figure 3-1: Legend to Identify the Different Types of Corrosive Damage

The results of NDT Contractors 1, 2, 3, and 5 were superimposed on each beam surface with the damage profile. Thus, the accuracy of these various methods can be assessed. NDT Contractor 4, using the method of LST, returned no useful results for this study and has no results to display in the following figures. NDT Contractor 6 will be assessed separately due to the fact that they used three methods of NDT technology. The four methods identified regions on each beam where corrosion may be occurring. The regions are outlined over the actual damage conditions on each beam and outlined with a different color in accordance with the legend shown in Figure 3-2.



Figure 3-2: Legend to Identify Probable Corrosion Locations by NDT Contractors

Table 3-1 presents all seven beams with the damage profile from the destructive evaluation and various NDT Contractor results superimposed on their surface. The black rectangles on beams LV7 and MS2 depict the inspected strand area for corrosion. A thorough discussion on the accuracy of each method is provided in the following sections. For each method the number of regions identified and the accuracy of each method in finding regions of significant damage (heavy pitting, wire fracture, or loss) is tabulated.

Table 3-1: Overlay of NDT Contractor Results w/ Damage Profile on Beam Surface	
<p>AI</p> <p>CC3</p> <p>PI</p>	<p>CC4</p> <p>P2</p> <p>PI</p>
<p>AI</p> <p>LV7</p> <p>PI</p>	
<p>P2</p> <p>LV16</p> <p>PI</p>	<p>PI</p>

Table 3-1: Overlay of NDT Contractor Results w/ Damage Profile on Beam Surface



3.1. Assessment of Accuracy Method #1: Magnetic Flux Leakage

Magnetic Flux Leakage (MFL) was performed on six of the seven beams: CC4, LV7, LV16, LV19, MS2, and MS3. The findings and comparison with the damage profile are shown below in Table 3-2.

Table 3-2: Accuracy of MFL Findings

NDT Contractor:	Method:	Beam ID:	Identified Corrosion Locations:	Corrosion at Identified Locations?	Comments:
1	MFL	CC3	2	1 of 2	Missed cases of HP
		CC4	0	N/A	No Serious Damage on Strands
		LV7	0	N/A	Missed Cases of HP

NDT Contractor:	Method:	Beam ID:	Identified Corrosion Locations:	Corrosion at Identified Locations?	Comments:
		LV16	1	1 of 1	Detected the one case of WL
		LV19	3	3 of 3	Detected WL,HP
		MS2	3	2 of 3	Detected WL,HP; Missed cases of HP
		MS3	3	2 of 3	Detected, WL,HP; Missed one case of WL

The MFL method identified ten regions of damage. Of the twelve regions nine had corrosion damage, thus the method provided a 75% identification success rate. This method successfully identified the severe wire loss in beam LV16 where there were no surface indicators of corrosion. Also, it correctly identified beam CC4 as having no serious damage. This method appears to only pick up heavy corrosion damage in the strands, i.e., corresponding to Heavy Pitting and Wire Loss as identified in the destructive evaluation. Beam CC3 could not be assessed due to a lack of information from NDT Contractor 1.

It appears that interpretation of the results requires additional refinement. For example the region of severe strand loss in beam LV16 was noted as an “Anomaly” by the NDT inspectors. Additionally, the MFL method did not identify numerous regions of wire loss and heavy pitting throughout some of the members. Despite these shortcomings, it appears that this method could be used successfully in the field to identify cases of severe corrosion within the prestressing strands of concrete components.

3.2. Assessment of Accuracy Method #2: Ground Penetrating Radar

Ground Penetrating Radar (GPR) was performed on five of the seven beams: CC3, CC4, LV16, LV19, and MS3. The findings and comparison with the damage profile are shown in Table 3-3.

NDT Contractor:	Method:	Beam ID:	Identified Corrosion Locations:	Corrosion at Identified Locations?	Comments:
2	GPR	CC3	0	N/A	Missed some HP
		CC4	0	N/A	No serious damage on strands
		LV16	1	1 of 1	Confirmed Visibly Corroded Strands; missed one case of both WL and HP
		LV19	1	1 of 1	Detected severe cases of WL,HP; missed cases of HP
		MS3	2	2 of 2	Detected cases of WL,HP; missed cases of WL,HP

Of the regions identified, GPR was 100% successful. Unfortunately, the method did not identify the severe wire loss in beam LV16 where there were no surface indicators of corrosion. Furthermore, there were many regions of heavy pitting that were not identified by the GPR contractor. The method, however, did correctly identify beam CC4 as having no serious damage. This method appears to only pick up heavy corrosion damage in the strands: i.e., Heavy Pitting and Wire Loss.

The sections in which NDT Contractor #2 identified corrosion were large. The methodology did not allow for localized identification of corrosion. With more testing and an improvement in the ability to interpret the data, this method may be useful in the field to determine areas of severe corrosion within the prestressing strands of concrete components. Additional information on this NDT method is given in the Appendix.

3.3. Assessment of Accuracy Method #3: Remnant Magnetization

Remnant Magnetization (RM) was performed on six of the seven beams (all but LV7). The findings and comparison with the damage profile are shown below in Table 3-4.

NDT Contractor:	Method:	Beam ID:	Identified Corrosion Locations:	Corrosion @ Identified Locations?	Comments:
3	RM	CC3	1	0 of 1	No Corrosion in Detected Area
		CC4	0	N/A	No serious damage on strands
		LV16	5	3 of 5	Detected the one case of WL; other locations show no corrosion in detected area
		LV19	3	3 of 3	Detected WL,HP; missed cases of HP
		MS2	4	4 of 4	Detected cases of WL,HP,P; missed cases of HP
		MS3	5	4 of 5	Detected cases of WL,HP,P; missed cases of WL,HP

Of the eighteen regions identified, the remnant magnetization method was 82% successful. This method successfully identified the severe wire loss in beam LV16 where there were no surface indicators of corrosion. Also, it correctly identified beam CC4 as having no serious damage. This method appears to only pick up heavy corrosion damage in the strands, i.e., Heavy Pitting and Wire Loss.

The MFL method did not identify numerous regions of wire loss and heavy pitting. It also identified regions where no damage was found. Based on the ability to identify the localized damage in LV16, it appears that this method could be used successfully in the field to determine severe corrosion within the prestressing strands of concrete components.

3.4. Assessment of Accuracy Method #4: Line Scanning Thermography

Line Scanning Thermography was performed on three of the seven beams; CC3, CC4, and MS3. The results are displayed in section 2.4.2. This method was unable to identify the strands,

making the identification of corrosion within the strands impossible. Therefore, the NDT method of LST is currently not applicable towards the identification of corrosion in prestressing strands of concrete structures. For additional information, the full report is given in the Appendix.

3.5. Assessment of Accuracy Method #5: Electromagnetic Corrosion Detection & GPCR

Electromagnetic Corrosion Detection (EMCD) was used along with Galvanostatic Pulse Corrosion Rate to attempt to determine locations of corrosion damage. The study was performed on three of the seven beams: CC3, LVD7, and MS3. The findings and comparison with the damage profile are shown below in Table 3-5.

NDT Contractor:	Method:	Beam ID:	Identified Corrosion Locations:	Corrosion @ Identified Locations?	Comments:
5	EMCD	CC3	7	0 of 7	No Corrosion in detected area
		LV7	2	N/A	Could not be verified
		MS3	6	1 of 6	Detected one case of P; no corrosion in other detected areas

Damage indices were not recorded for the regions of inspection identified in method #5. Consequently, the predicted locations of damage could not be verified on LV7. Considering the data from beams CC3 and MS3, there is an 8.0% identification success rate. The method does not accurately predict corrosion in the prestressing strands of concrete structures.

NDT Contractor 5 also inspected the beams using the method of Galvanostatic Pulse Corrosion Rate. In comparing Figure 2-57 through Figure 2-62 with the damage profiles, it is clear that this particular NDT test does not correlate with the strand damage profiles. Based on the results of this study these methods are not recommended for field identification of corrosion in the prestressing strands of concrete structures.

3.6. Assessment of Accuracy Method #6: IE/UST/GPR Methods

NDT Contractor 6 scanned the beams using several methods: Impact Echo (IE), Ultrasonic Shear-Wave Testing (UST), and Ground Penetrating Radar (GPR). The results from the various methods were compiled and superimposed over the beams surface. The damage profiles were then superimposed over these figures to assess the accuracy of these methods. Figure 3-1 provides the damage profile legend.

Beam CC3 was scanned using the aforementioned NDT procedures and Figure 3-3 was produced. The combination of NDT technologies did not identify the severe cases of wire loss and heavy pitting present in the structure. Two regions were correctly identified as being corroded: a case of pitting at grid intersection 8-C and a case of heavy pitting at grid intersection at 2-D. Of the 19 overall anomalies identified through IE and Monolith UST, corrosion was found at only 4 of them; a 21% success rate. Further, the GPR technology did not detect any instances of deterioration within this beam. The Polygon UST had moderate correlation with strand damage in some locations, and no correlation in other locations.

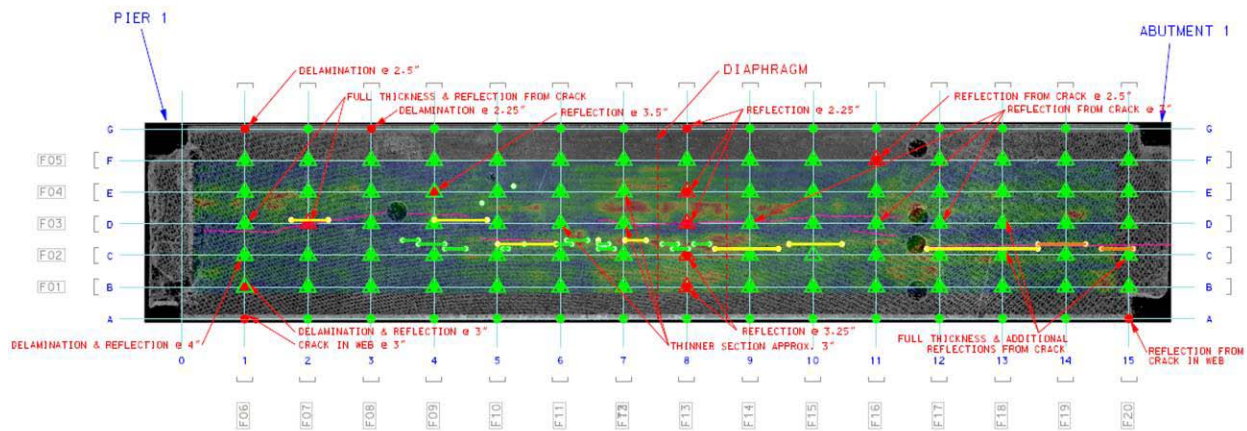


Figure 3-3: Summary of NDT Findings on Beam CC3

Beam CC4 was scanned using the aforementioned NDT procedures and Figure 3-4 was produced. Of the 29 overall anomalies identified through IE, corrosion was found at only 6 of them; a 21% success rate. The GPR accurately showed no signal attenuation. No severe damage (HP and WL) was detected in the strands of this member. The Polygon UST showed no correlation with strand damage.

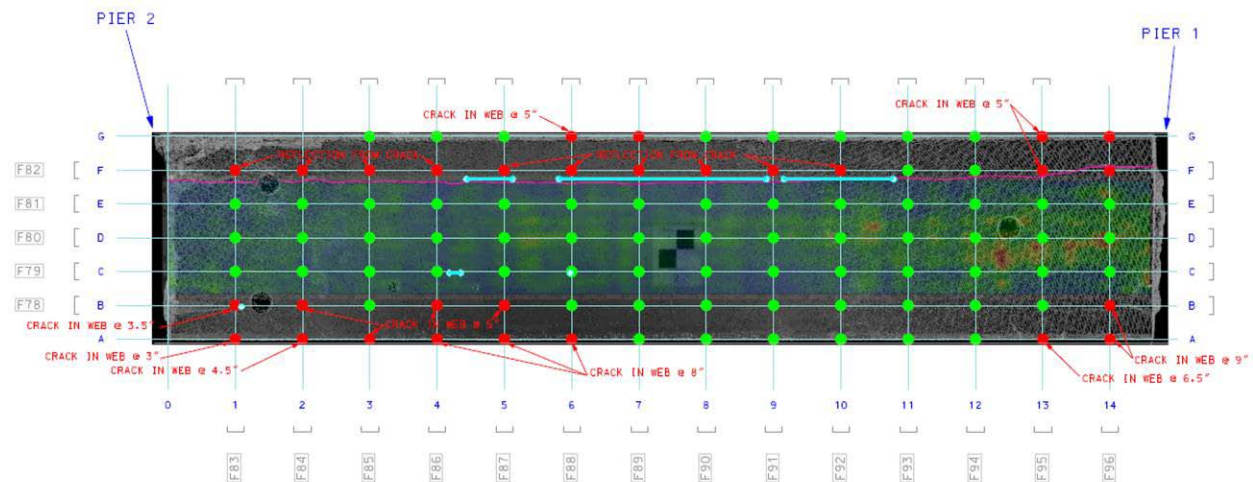


Figure 3-4: Summary of NDT Findings on Beam CC4

Beam LV16 was scanned using the aforementioned NDT procedures and Figure 3-5 was produced. The combination of NDT technologies did not pick up the single case of wire loss or the single case of heavy pitting. Of the 10 overall anomalies identified through IE, corrosion was not found at any location; a 0% success rate. Further, the GPR technology did not detect the single cases of heavy pitting or wire loss. The Polygon UST showed no correlation with strand damage.

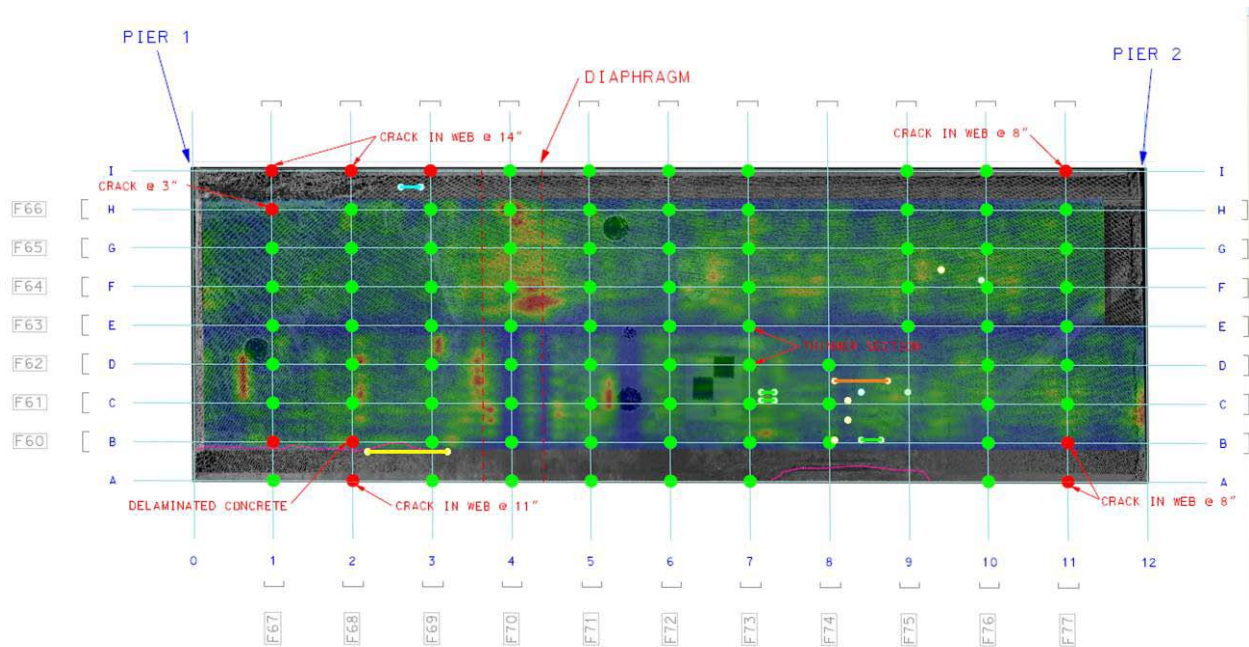


Figure 3-5: Summary of NDT Findings on Beam LV16

Beam LV19 was scanned using the aforementioned NDT procedures and Figure 3-6 was produced. The combination of NDT technologies picked up cases of wire loss and heavy pitting. Of the 23 overall anomalies identified through IE, corrosion was found at six locations; a 26% success rate. The GPR technology had signal attenuations in two areas on the beam surface; both were confirmed to have corrosion in the form of Heavy Pitting and Wire Loss. However, the areas identified with GPR signal attenuation were very large. The Polygon UST had moderate correlation with strand damage in some locations, and no correlation in other locations.

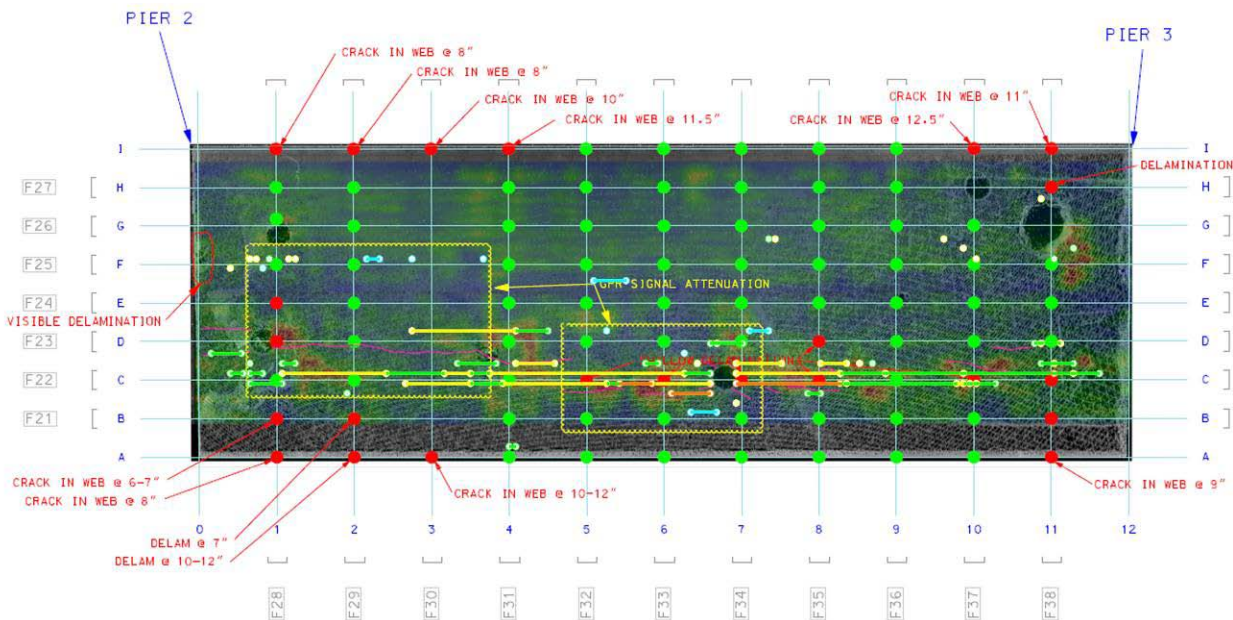


Figure 3-6: Summary of NDT Findings on Beam LV19

Beam MS2 was scanned using the aforementioned NDT procedures. The results of the scan are summarized in Figure 3-7. The combination of NDT technologies picked up cases of wire loss and heavy pitting in some areas, and missed them in other areas. Of the 21 overall anomalies identified through IE and Monolith UST, corrosion was found at 11 locations; a 52% identification success rate. The GPR technology had signal attenuations in three areas on the beam surface, all of which were confirmed to have corrosion in the form of Heavy Pitting and Wire Loss. However, the areas identified as having GPR signal attenuation were very large. The technology was not able to identify corrosion in a more localized area such as a particular strand. The Polygon UST had moderate correlation with strand damage in some locations, and no correlation in other locations.

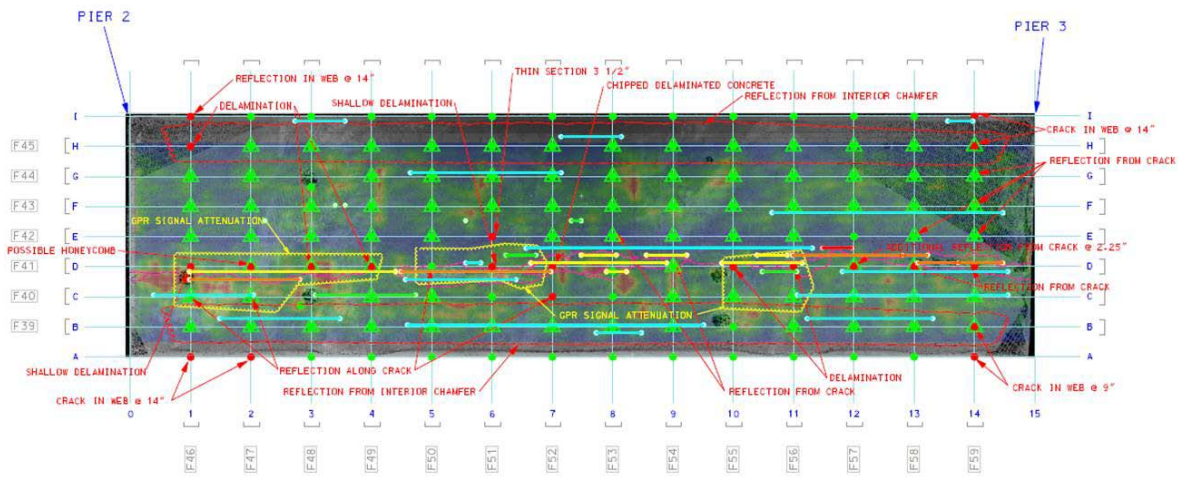


Figure 3-7: Summary of NDT Findings on Beam MS3

4. Summary and Ranking of Candidate NDT Methods

The accuracy of the various NDT methods examined is summarized in this section. The number of regions where corrosion was identified was previously listed in the discussion of each method; the results are reproduced in Table 4-1. In some cases the regions identified were discrete and in other cases a window was identified. This distinction is included in the table. A number of wire loss / strand fractures were identified on the beams. The ability of each method to identify these locations is also tabulated.

The MFL and RM methods are shown to provide the best performance. Both methods provide reasonable accuracy and are capable of identifying the majority of wire loss locations. The GPR appears to have high accuracy however the method identified a few large regions of possible corrosion and did not identify a majority of wire loss locations. The other NDT methods were not accurate in identifying corrosion. The ranking of the methods based on the beam evaluation is included in the table. Due to the poor accuracy of the GPR and other methods they are not viable for detection of non-visible strand corrosion and are not ranked.

Contractor	Method	Ranking	Regions Identified	Corrosion identified correctly	Global /Discrete	Regions of Wire Loss or Fracture Identified
1	MFL	1	12	75%	Global	11 of 15
2	GPR	NA	4	100%	Global	4 of 10
3	RM	2	18	78%	Discrete	7 of 15
4	LST	NA	0	NA	Global	0 of 15
5	EMCD, GPCR	NA	15	6.7%	Discrete	0 of 15
6	IE, UST, GPR	NA	0	NA	Global	5 of 15

To fully assess the practicality of these methods for field use the operating costs and effort involved in each NDT method were summarized. A questionnaire was sent to each NDT vendor with series of questions developed to establish the feasibility of field use and all associated costs for the testing of each method. The complete questionnaire is given in the Appendix. The questionnaire data was sorted and is as shown below in Table 4-2. The questionnaire was completed by all vendors with the exception of Physical Acoustics Corporation (NDT Contractor #4).

NDT Contractor:	Cost of Equipment:	Equipment Use Rate?	Equipment Rental cost/day?	Rate of Concrete Inspection:	Req'd Personnel:	Personnel Rates/hr:	Time to Analyze One Day of Data:
1 - MFL	\$57,000	Not Listed	\$1,200.00	9600 ft ² /day	Laborer/ Technician	\$42.50	3 to 4 hours
					Laborer/ Technician	\$42.50	

Table 4-2: Accuracy and Pricing of NDT Methods							
NDT Contractor:	Cost of Equipment:	Equipment Use Rate?	Equipment Rental cost/day?	Rate of Concrete Inspection:	Req'd Personnel:	Personnel Rates/hr:	Time to Analyze One Day of Data:
					Staff Engineer	\$112.50	
2 - GPR	\$35,000	\$350.00 per day	\$350.00	5000 ft ² /day	GPR Antenna Operator	\$85.00	24 hours
					GPR System Operator	\$100.00	
					GPR Data Analyst	\$110.00	
3 - RM	Not Available for Purchase	Not Listed	\$400.00	1200 ft ² /day	Trained Engineer (2)	\$100.00	8 hours
			\$1,000.00		PhD Analyst	\$125.00	
4 - LST	Data Not Received						
5 - EMCD & GPCR	\$100,000	\$1,000.00 per day	Not Available for Rent	Not Answered	Principal	\$185.00	8 to 12 hours
					2-Man NDT Crew	\$188.00	
					NDT Tech. Specialist	\$85.00	
					CAD Operator	\$65.00	
6 - IE, UST, GPR, & 3LDS	No information available						

If the NDT equipment must be purchased, GPR technology is the most economical at \$35,000. The most expensive technology is that of NDT contractor #5 at \$100,000. The RM technology is currently not for sale but specific inspections can be contracted to Vector Corrosion Technologies. The MFL method has the highest claimed inspection rate by far with 9600 square feet of concrete per day. RM can only accomplish 1200 square feet per day and it requires the installation of supports under the bridge. NDT contractor #2 and the GPR methodology can cover 5000 square feet per day. The MFL method also has the fastest reduction of data, taking approximately 4 hours to reduce one days worth of data (9600 square feet). GPR and NDT contractor #5 take the longest to analyze a day of data collection. Personnel rates are close amongst all NDT contractors.

5. Additional Evaluation of Magnetic NDE Methods

As discussed in section 4, two magnetic Non-Destructive testing methods showed promise in accurately identifying severe corrosion in the strands of the bottom flange of prestressed adjacent concrete box girders. To evaluate these methods further an additional study was conducted on a series of concrete slabs with pre-fabricated levels of damage to the strands. The two methods examined include (1) Magnetic Flux Leakage and (2) Remnant Magnetization. For a background on these methods refer to Sections 2.1. and 2.3. , respectively. Dr. Al Ghorbanpoor of the University of Wisconsin-Milwaukee conducted the MFL examination and Dr. Bernd Hillemeier of the Technische Universitat (TU) Berlin in association with Vector Corrosion Technologies, Ltd performed the Remnant Magnetization examination.

5.1. Experimental Design & Construction

The initial study of the damaged box beams were conducted prior to the forensic evaluation of the beams. The forensic evaluation revealed that the strand consisted of corrosion primarily along the crack locations with only a few regions of heavy corrosion or strand loss. To provide more sensitivity to the assessment a series of slabs were fabricated with various levels of predefined damage. Four reinforced concrete slabs were fabricated, each with its own type of longitudinal reinforcement. Test Slab #1, as shown in Figure 5-1, is reinforced #4 conventional reinforcing bars. Test Slab #2, as shown in Figure 5-2, is reinforced with #3 conventional reinforcing bars. Test Slab #3, as shown in Figure 5-3, is reinforced with ½ in. diameter seven wire strand. Test Slab #4, as shown in Figure 5-4, is reinforced with 3/8 in. diameter seven wire strand. All four of the slabs had a length of 141 inches and a width of 24 inches.

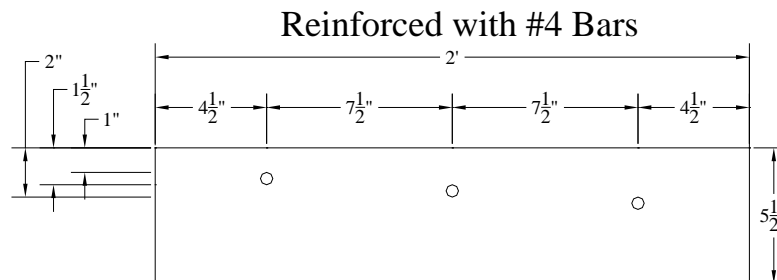


Figure 5-1: Test Slab #1

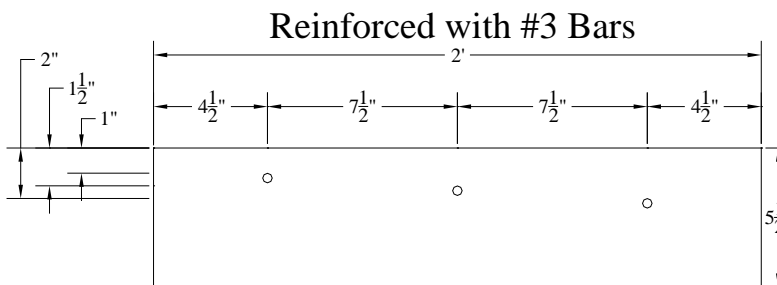


Figure 5-2: Test Slab #2

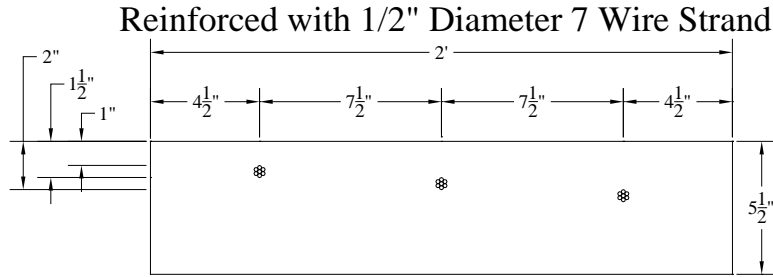


Figure 5-3: Test Slab #3

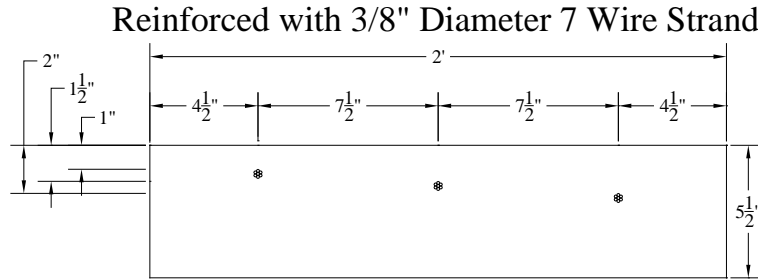


Figure 5-4: Test Slab #4

Each slab contains three longitudinal reinforcement bars, with each with a different amount of clear cover. Clear covers include 1 in., 1.5 in., and 2 in. The degree of damage is varied along each bar/strand; with inflicted section losses of: (1) small with approximately 10% section loss, (2) medium with approximately 20% section loss, (3) heavy with approximately 50% section loss, and (4) full fracture with 100% section loss. The length of each defect was also varied at: (a) 1/2 in., (b) 1 in., and (c) 1.5 in. Additionally, the damage was inflicted to the reinforcement at both the topside and underside; with the underside notation as shown in Figure 5-5. The damage was imposed upon the reinforcement at predetermined locations by fabricating a divot with a grinder. A sample section damage level is presented in Figure 5-6. Note, the conditions created within these test slabs are more significant than a corrosion-induced section loss. Section loss due to corrosion should change the profile however the corroded material will remain within the concrete and thus create less of a change in the magnetic signature. The results generated with this test series represent an upper bound in the capability of the equipment.

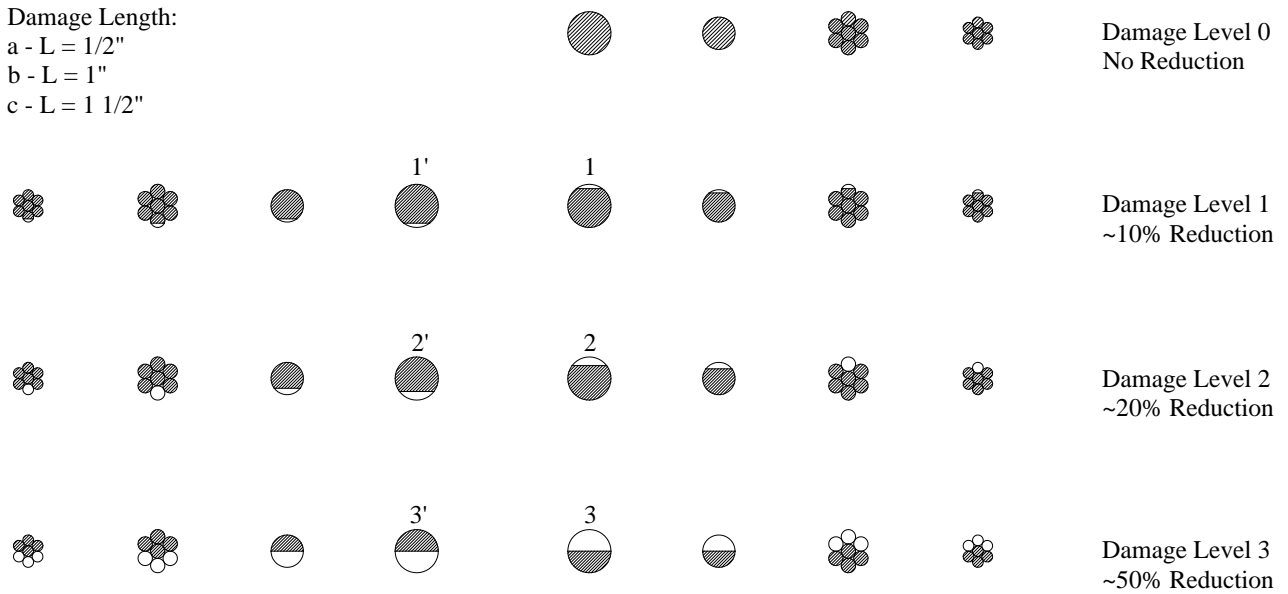


Figure 5-5: Pre-fabricated damage level conditions



Figure 5-6: Damage level 1 condition

Once the defects were made on the longitudinal reinforcement, they were inserted into the slab forms. The reinforcement was tied at three locations along each slabs length with heavy-duty plastic wire to avoid sagging and to minimize the influence on the magnetic signature. An image of Slabs 1 and 2 prior to concrete placement is illustrated in Figure 5-7. The reinforcement extended from the forms at least 6 inches on each end to allow the magnetic NDT contractors to have adequate magnetization of the reinforcement at the edge of the concrete. The location of each damage region were measured and tabulated prior to concrete placement.



Figure 5-7: Slabs 1 and 2 (left to right) prior to concrete placement

5.2. Flaw Locations

Both magnetic NDT methods were conducted on the four fabricated slabs, with the intent of discovering whether these methods could identify the inflicted damage to the steel reinforcement. The locations of the damage on the steel reinforcement are summarized in this section; for defect type notation, refer to Figure 5-5.

As shown in Table 5-1, slab one was reinforced with #4 conventional rebar. It contained 37 different defects along the three strands. There were ten smaller flaws, twelve medium sized flaws, twelve heavy flaws, and three complete fractures. This density of damage regions was typical of all slabs.

Strand #:	Defect ID:	Defect Type:	Defect Length:	Defect Depth:	Distance to Center of Defect from P1:
1	1	1c`	1.5	0.032	10.5
	2	2c	1.5	0.102	30.5
CC	3	2a	0.5	0.110	38.5
@	4	3b	1.0	0.194	58.5
2"	5	3c`	1.5	0.184	66.5
	6	4a	0.5	Fracture	
1	7	1b	1.0	0.048	74.5
	8	1c	1.5	0.054	82.5
CC	9	2b	1.0	0.040	102.5
@	10	2c`	1.5	0.067	110.5
2"	11	3c	1.0	0.135	130.5
	12	3a	0.5	0.157	138.5
2	13	1b	1.0	0.051	10.5

Table 5-1: Flaw Data for Slab #1 – Reinforced with #4 bars					
Strand #:	Defect ID:	Defect Type:	Defect Length:	Defect Depth:	Distance to Center of Defect from P1:
	14	2c`	1.5	0.072	26.5
CC	15	2c	1.5	0.072	34.5
@	16	3c	1.5	0.184	50.5
1.5"	17	3b	1.0	0.196	58.5
	18	4a	0.5	Fracture	
2	19	1c	1.5	0.057	78.5
	20	1c`	1.5	0.048	86.5
CC	21	2a	0.5	0.065	102.5
@	22	2b	1.0	0.074	110.5
1.5"	23	3c`	1.5	0.145	126.5
	24	3a	0.5	0.210	134.5
3	25	1c`	1.5	0.050	10.5
	26	1c	1.5	0.051	18.5
CC	27	2a	0.5	0.078	30.5
@	28	2c`	1.5	0.061	42.5
1"	29	3b	1.0	0.181	50.5
	30	3a	0.5	0.218	58.5
	31	4a	0.5	Fracture	
3	32	1b	1.0	0.034	74.0
	33	1a	0.5	0.048	86.0
CC	34	2c	1.5	0.056	108.0
@	35	2b	1.0	0.056	114.0
1"	36	3c`	1.5	0.131	126.0
	37	3c	1.5	0.145	138.0

As shown in Table 5-2, slab two was reinforced with #3 conventional rebar. It contained 39 different defects along the three strands. There were twelve smaller flaws, twelve medium sized flaws, twelve heavy flaws, and three complete fractures.

Table 5-2: Flaw Data for Slab #2 – Reinforced with #3 bars					
Strand #:	Defect ID:	Defect Type:	Defect Length:	Defect Depth:	Distance to Center of Defect from P1:
1	1	1a	0.5	0.012	14.5
	2	1b	1.0	0.016	18.5

Table 5-2: Flaw Data for Slab #2 – Reinforced with #3 bars					
Strand #:	Defect ID:	Defect Type:	Defect Length:	Defect Depth:	Distance to Center of Defect from P1:
CC	3	2c	1.5	0.048	26.5
@	4	2c'	1.5	0.049	34.5
1"	5	3a	0.5	0.132	54.5
	6	3c	1.5	0.136	62.5
	7	4a	0.5	Fracture	
1	8	1c	1.5	0.020	78.5
	9	1c'	1.5	0.026	90.5
CC	10	2a	0.5	0.054	102.5
@	11	2b	1.0	0.060	110.5
1"	12	3c'	1.5	0.094	126.5
	13	3b	1.0	0.137	134.5
2	14	1a	0.5	0.012	6.0
	15	1b	1.0	0.020	10.0
CC	16	2b	1.0	0.048	26.0
@	17	2c	1.5	0.042	34.0
1.5"	18	3a	0.5	0.180	54.0
	19	3b	1.0	0.164	59.0
	20	4a	0.5	Fracture	
2	21	1c'	1.5	0.018	82.5
	22	1c	1.5	0.023	90.5
CC	23	2a	0.5	0.050	110.5
@	24	2c`	1.5	0.035	114.5
1.5"	25	3c	1.5	0.089	122.5
	26	3c`	1.5	0.086	130.5
3	27	1a	0.5	0.011	6.0
	28	1c	1.5	0.020	14.0
CC	29	2c`	1.5	0.038	26.0
@	30	2b	1.0	0.058	38.0
2"	31	3c`	1.5	0.103	54.0
	32	3c	1.5	0.132	63.0
	33	4a	0.5	Fracture	
3	34	1b	1.0	0.024	79.0
	35	1c`	1.5	0.027	87.0
CC	36	2a	0.5	0.041	103.0

Strand #:	Defect ID:	Defect Type:	Defect Length:	Defect Depth:	Distance to Center of Defect from P1:
@	37	2c	1..5	0.041	107.5
2"	38	3a	0.5	0.146	123.0
	39	3b	1.0	0.153	135.0

As shown in Table 5-3, slab three was reinforced with ½ inch diameter seven wire strands. It contained 35 different defects along the three strands. There were eleven smaller flaws, twelve medium sized flaws, nine heavy flaws, and three complete fractures.

Strand #:	Defect ID:	Defect Type:	Defect Length:	Defect Depth:	Distance to Center of Defect from P1:
1	1	1c	1.5	0.043	2.5
	2	1b	1.0	0.043	6.5
CC	3	2c`	1.5	0.080	22.5
@	4	2b	1.0	0.079	34.5
2"	5	3b	1.0	0.160	50.5
	6	3c`	1.5	0.120	58.5
	7	4a	0.5	Fracture	
1	8	1a	0.5	0.032	93.5
	9	1c`	1.5	0.044	97.5
CC	10	2a	0.5	0.069	109.5
@	11	2c	1.5	0.064	117.5
2"	12	3a	0.5	0.170	129.5
2	13	1a	0.5	0.033	14.0
CC	14	2a	0.5	0.065	31.0
@	15	2c	1.5	0.080	38.0
1.5"	16	3a	0.5	0.140	46.0
	17	3c	1.5	0.140	62.0
	18	4a	0.5	Fracture	
2	19	1c	1.5	0.054	86.0
	20	1c`	1.5	0.034	94.0
CC	21	2b	1.0	0.085	114.0
@	22	2c`	1.5	0.081	122.0
1.5"	23	3b	1.0	0.186	138.0

Table 5-3: Flaw Data for Slab #3 – Reinforced with ½” strand					
Strand #:	Defect ID:	Defect Type:	Defect Length:	Defect Depth:	Distance to Center of Defect from P1:
3	24	1c	1.5	0.050	1.0
	25	1b	1.0	0.043	9.0
CC	26	2c	1.5	0.082	21.0
@	27	2a	0.5	0.082	34.0
1"	28	3c	1.5	0.161	45.0
	29	3b	1.0	0.156	53.5
	30	4a	0.5	Fracture	
3	31	1a	0.5	0.073	80.5
	32	1c`	1.5	0.043	88.5
CC	33	2c`	1.5	0.070	104.5
@	34	2b	1.0	0.066	121.0
1"	35	3c`	1.5	0.167	133.0

As shown in Table 5-4, slab four was reinforced with 3/8 inch diameter seven wire strands. It contained 35 different defects along the three strands. There were ten smaller flaws, twelve medium sized flaws, ten heavy flaws, and three complete fractures.

Table 5-4: Flaw Data for Slab #4 – Reinforced with 3/8” strand					
Strand #:	Defect ID:	Defect Type:	Defect Length:	Defect Depth:	Distance to Center of Defect from P1:
1	1	1c`	1.5	0.019	9.0
	2	2c`	1.5	0.041	21.0
CC	3	2a	0.5	0.055	25.0
@	4	3b	1.0	0.135	49.0
1"	5	3c`	1.5	0.117	57.0
	6	4a	0.5	Fracture	
1	7	1b	1.0	0.032	89.0
	8	1a	0.5	0.034	93.0
CC	9	2c	1.5	0.058	107.0
@	10	2b	1.0	0.050	115.0
1"	11	3c	1.5	0.163	131.0
2	12	1b	1.0	0.035	2.5
	13	1c`	1.5	0.031	6.5

Table 5-4: Flaw Data for Slab #4 – Reinforced with 3/8” strand					
Strand #:	Defect ID:	Defect Type:	Defect Length:	Defect Depth:	Distance to Center of Defect from P1:
CC	14	2c	1.5	0.080	16.5
@	15	2a	0.5	0.083	28.5
1.5"	16	3c`	1.5	0.141	40.5
	17	3a	0.5	0.125	52.5
	18	4a	0.5	Fracture	
2	19	1a	0.5	0.038	80.5
	20	1c	1.5	0.039	92.5
CC	21	2b	1.0	0.066	110.5
@	22	2c`	1.5	0.044	119.0
1.5"	23	3c	1.5	0.141	126.5
	24	3b	1.0	0.137	135.0
3	25	1c	1.5	0.031	8.0
	26	2c	1.5	0.055	18.0
CC	27	2c`	1.5	0.055	33.0
@	28	3a	0.5	0.158	45.5
2"	29	3c`	1.5	0.183	50.0
	30	4a	0.5	Fracture	
3	31	1b	1.0	0.031	79.5
	32	1c`	1.5	0.026	95.5
CC	33	2a	0.5	0.060	106.5
@	34	2b	1.0	0.060	119.0
2"	35	3b	1.0	0.180	126.5

5.3. Results and Analysis of Additional Inspections

The Magnetic Flux Leakage and the Remnant Magnetism Methods were repeated on the test slabs. Data on the damage location and size were provided by the contractors. All testing was conducted by the contractors without prior knowledge of the damage types or locations. The predicted locations of damage provided by the contractors were provided to Lehigh and were compared independent from the contractors. The variation in the predicted and actual flaw locations are summarized to determine accuracy and resolution. Table 5-5 presents the number of flaws per slab and how each method performed. Table 5-6 summarizes the data as a percentage.

Table 5-5: Flaw Identifications with Respect to Each Method and Slab										
Scenario:	All Slabs		Slab #1		Slab #2		Slab #3		Slab #4	
	RM	MFL	RM	MFL	RM	MFL	RM	MFL	RM	MFL

Scenario:	All Slabs		Slab #1		Slab #2		Slab #3		Slab #4	
# of Overall Damage Locations	146		37		39		35		35	
# of Overall Successful Damage IDs	118	135	29	33	29	35	33	34	27	33
# of Incorrect IDs	18	4	5	0	1	1	7	1	5	2
# of Misses of Damage Locations	28	11	8	4	10	4	2	1	8	2
# of Overall Small Damage Locations	43		10		12		11		10	
# of Successful Small Damage IDs	19	31	2	6	3	8	9	9	5	8
# of Overall Medium Damage Locations	48		12		12		12		12	
# of Successful Medium Damage IDs	46	48	12	12	12	12	12	12	10	12
# of Overall Heavy Damage Locations	43		12		12		9		10	
# of Successful Heavy Damage IDs	41	43	12	12	11	12	9	9	9	10
# of Fracture Locations	12		3		3		3		3	
# of Successful Fracture IDs	12	12	3	3	3	3	3	3	3	3

As shown in Table 5-6, the RM method correctly identified 72% of all reinforcement defects and the MFL method correctly identified 90% of all defects. The RM method correctly identified 44.2% of small defects, 95.8% of medium defects, 95.3% of heavy defects, and 100% of fractures. The MFL method correctly identified 74.4% of small defects and 100% of medium defects, large defects, and fractures. Therefore, most of the overall inaccuracy comes from both technologies inability to accurately predict small flaws; with a section loss of approximately 10%. Both methods do a good job of identifying flaws greater than 20% of the cross-section.

Scenario:	All Slabs		Slab #1		Slab #2		Slab #3		Slab #4	
	RM	MFL	RM	MFL	RM	MFL	RM	MFL	RM	MFL
% of Successful IDs	72.0	90.0	69.0	89.2	72.5	87.5	78.6	94.4	67.5	89.2
% of Successful IDs for Small Damage	44.2	74.4	20.0	60.0	25.0	66.7	81.8	81.8	50.0	80.0

Scenario:	All Slabs		Slab #1		Slab #2		Slab #3		Slab #4	
% of Successful IDs for Medium Damage	95.8	100	100	100	100	100	100	100	83.3	100
% of Successful IDs for Heavy Damage	95.3	100	100	100	91.7	100	100	100	90.0	100
% Successful Fracture IDs	100	100	100	100	100	100	100	100	100	100

Overall, both methods were slightly more accurate in correctly identifying flaws in the steel strand versus flaws in the conventional rebar. The MFL method accurately identified 88.3% of flaws in slabs with conventional steel reinforcing; compared to 91.8% of flaws in slabs reinforced with 7-wire strand. The RM method accurately identified 70.7% of flaws in slabs with conventional steel reinforcing; compared to 73.2% of flaws in slabs reinforced with 7-wire strand.

In addition to looking at the ability to correctly identify these flaws, it was also desired to assess how accurate these technologies were at locating the flaw locations. The reported flaw distances from the NDT vendors were compared against the exact physical flaw locations to determine the differential error. For the RM method, the average location differential was approximately 1.8 inches, whereas for the MFL method the average location differential was approximately 1.0 inch.

Due to the fact that both methods had an almost perfect detection rate for medium flaws, large flaws, and fractures, the sensitivity of the equipment to clear cover and damage length is assessed by comparison of the of the small flaws. The effect of varying the damage length at 1.5 in., 1 in., or 0.5 in. can be seen in Figure 5-8. Both methods were better at locating small section flaws with a damage length of 1.5 in. over those that were shorter in length, i.e., 0.5 or 1 in. The MFL method correctly identified the presence of 91.3% of all small flaws with a large damage length of 1.5 in., compared to only 60% correctly identified for those with damage lengths of 1 inch or ½ in. The RM method correctly identified the presence of 56.5% of all small flaws with a damage length of 1.5 in., compared to only 30% correctly identified for those with damage lengths of 1 in. or ½ in.

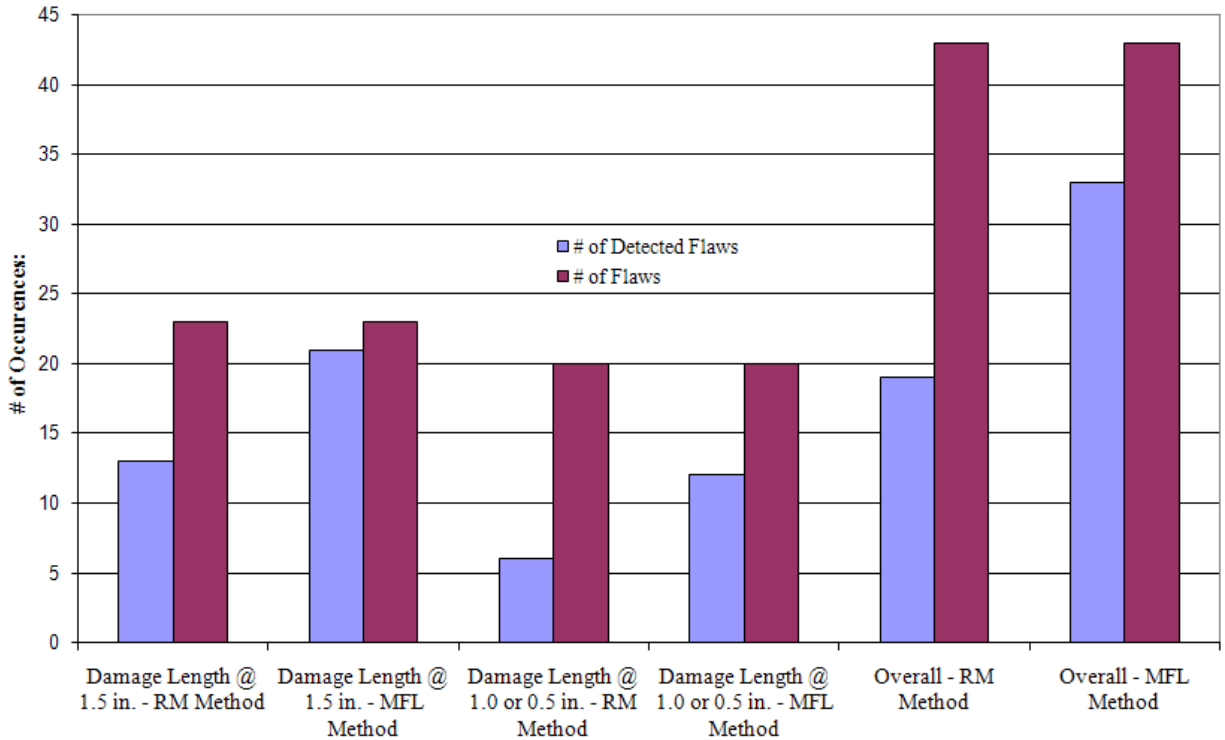


Figure 5-8: Identification of Small Flaws by Non-Destructive Magnetic Methods

The effect of varying the clear cover at 2.0 in., 1.5 in., or 1 in. is illustrated in Figure 5-9. As the clear cover varied, both magnetic methods had a somewhat consistent flaw identification rate with respect to small flaws. The MFL method successfully detected 73.3% of small flaws with 1 inch of clear cover, 78.6% of small flaws with 1.5 in. of clear cover, and 71.4% of small flaws with 2 in. of clear cover. The RM method successfully detected 40% of small flaws with 1 in. of clear cover, 42.9% of small flaws with 1.5 in. of clear cover, and 50% of small flaws with 2 in. of clear cover.

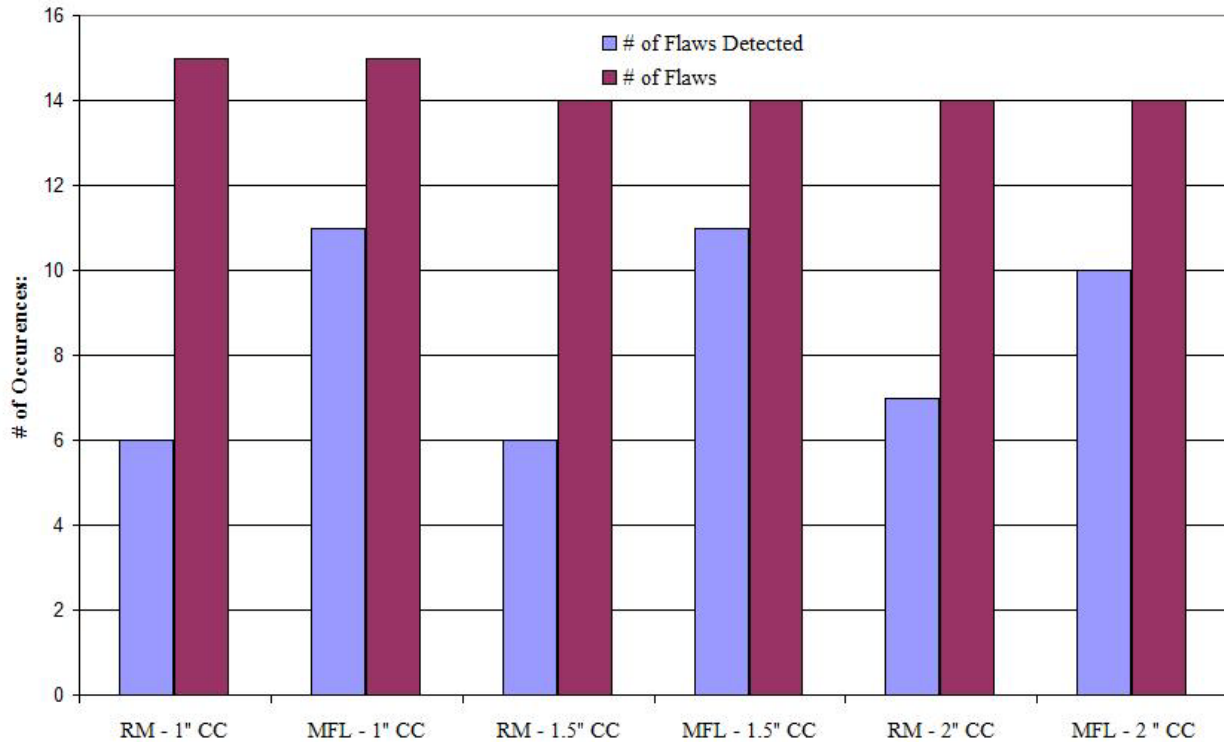


Figure 5-9: Identification of Small Flaws with Respect to Clear Cover

It is important to connect the percentage of section loss to the actual loss of strength in a piece of steel reinforcement. The reduction in strength associated with levels of corrosion (reduced strand cross section) was examined in 2006 [Naito, et. al. 2006]. The results of the study are reproduced in Table 5-7. Based on the findings, light corrosion did not alter the strength of the material. Pitting and heavy pitting resulted in a decrease in the tensile strength due to the reduction in cross-section and stress concentrations generated at the pitted sections. Therefore, if a small flaw (10% section loss) is not detected by these methodologies the reinforcement strength loss is not significant. These NDT technologies have accuracy in excess of 95% for detecting medium flaws, large flaws, and fractures; which correlate with strength losses from 30% to 100%. Based on this assessment both methods are viable and capable of identifying non-visible corrosion of prestressing strand.

Wire Condition:	Strength: [ksi]	COV:	Relative Strength:
Light Corrosion (No Section Loss)	288.0	4.2%	100%
Pitting (10% Section Loss)	230.0	10.6%	79.9%
Heavy Pitting (20% Section Loss)	205.6	10.9%	71.4%

6. 3D Laser Scanning Methods

A 3D laser scanner collects geometric data for a surveyed real-world environment. A digital 3D model can then be produced from that collected data. This method is most often associated with the quality control and inspection of civil structures such as bridges, roadways, foundations, refineries, etc. A 3D scanner captures information relative to a spherical coordinate system; capturing the radial distance, inclination angle, and azimuth angle from the scanning device to each point in the point cloud. It is often necessary to run scans at several locations to capture information about all sides of the subject. Through reconstruction of this data, the 3D model is assembled.

Laser scanning technology lends itself to inspection of adjacent precast box beam bridges. This bridge system consists of a flat bottom section allowing for laser measurement from one location. Furthermore, since the beams are adjacent the construction precludes the possibility of inspection between the beams. A laser system could potentially be stationed at one location and be used to accurately measure crack location, spall location and size, beam sag or loss of camber and beam separation. While these damage conditions are noted as part of a standard inspection they are approximated from a distance. It is likely that the resolution of a field inspection would be +/- 2 in. Use of a laser scanning device will allow for a much more precise measurement (+/- 0.25 in.) and can be executed in a much shorter duration. Furthermore, the level of accuracy in the inspection record can be used to more easily assess changes in the condition of the bridge over the life of the bridge.

6.1. Sample Application

As previously presented in section 2.6. the Dynasty Group used a 3D Laser Scanning device to assess the geometries of several concrete box-girder segments. The scanning device and overall point cloud are illustrated again in Figure 6-1.

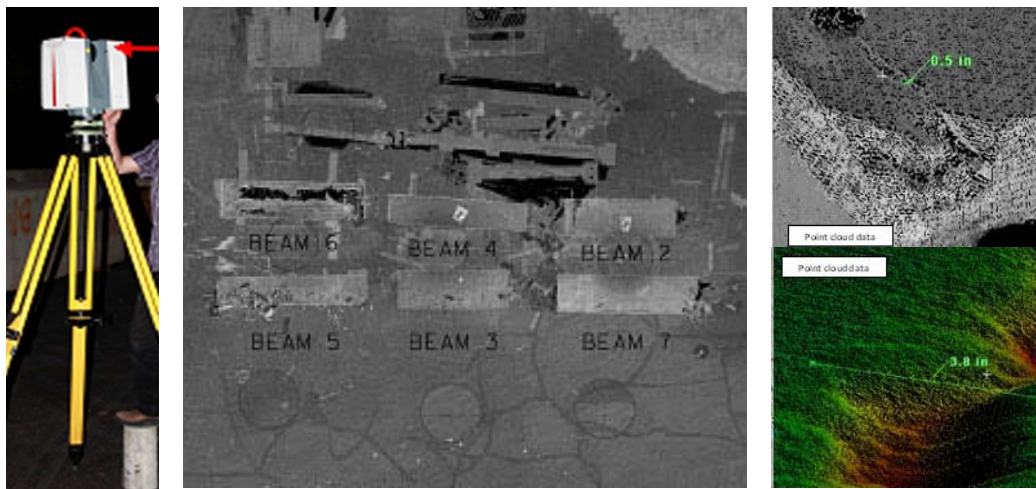


Figure 6-1: 3D Laser Scanning Device and Governing Point Cloud

Using 3D laser scanning methods, accurate structural monitoring can be performed over the life of a structure. This technique would provide crack width, crack length, spall geometry, sag, etc. would change over time. Further evaluation of these techniques are strongly recommended to help ensure the health of the infrastructure.

6.2. Commercial Equipment

PennDOT currently has in their inventory a Cyrax 2500. This system is relatively old but is still capable. The system can scan at a maximum distance of approximately 90 m over a 40-degree field, defects of 3 mm. This level of accuracy is adequate for evaluation and inspection of a conventional adjacent box girder bridge system.

Newer scanning lasers are available at similar resolution to the Cyrax system. The majority of laser scanning equipment available today is produced by Leica. Four different models are currently available. They include the Leica ScanStation C10, Leica ScanStation 2, Leica HDS6100, and Leica HDS4400. Because the HDS4400 was specifically designed for used in Mine Surveying, it is not included in the following discussion.

The Leica ScanStation2 is an entry level scanner, requiring laptop or notebook control. It has comparable specifications with the ScanStation C10, the difference being that the C10 has an onboard computer requiring no external connection. Additionally, the C10 has the most capabilities and best value packed into a single scanning instrument. The HDS6100 is geared towards high-speed and closer range laser scanning. The product specifications of these instruments are shown below in Table 6-1. As noted in the table, all levels of scanners are capable of identifying damage in the form of spalls that are larger than 4mm (0.16 in.). This level of accuracy would allow for identification of large cracks but may not identify hairline cracks. It is likely that the systems may be able to identify smaller discontinuities at closer distances. It is strongly recommended that field trials of this technology be evaluated.

Machine:	HDS6100	ScanStation2	ScanStation C10
Position Accuracy	5 mm - 9 mm	6 mm	6 mm
Distance Accuracy	2 mm - 5mm	4 mm	4 mm
Angle Accuracy	125 μ rad	60 μ rad	60 μ rad
Range	79 m	300 m	300 m
Scan Rate	508000 pts./sec.	50000 pts./sec.	50000 pts./sec.
Horizontal Field of View	360°	360°	360°
Vertical Field of View	310°	270°	270°

7. Summary and Conclusions

A research program was conducted to examine the accuracy of non-destructive testing methods in identifying regions of non-visible corrosion on prestressing strands used in concrete bridge members. Seven box beam sections with varying levels of corrosion damage were acquired from PennDOT. The beams were examined by six NDT vendors and detailed inspection reports were developed. The beams were forensically examined through destructive evaluation and the results of the in-situ level of corrosion were compared with the NDT methods to judge the accuracy of each method. Based on the comparison the following conclusions can be drawn.

- Magnetic Flux Leakage (Contractor #1) and the Remnant Magnetism (Contractor #3) methods provide a relatively accurate means of identifying corrosion of prestressing strand. Neither method correctly identified all locations of corrosion damage; also locations identified did not always contain corrosion. These methods appear to be viable.
- Ground Penetrating Radar (Contractor #2) identified corrosion over large regions. The method was correct in the regions identified, however, the regions were large thus the accuracy was low. The method identified fewer regions of heavy pitting and wire loss than the magnetic methods (MFL and RM). Also, the method does not appear to be able to identify the corrosion damage in a particular strand; instead it gives the damage over a larger area. In its current form the method does not provide improvements over visual observation. Perhaps with improvements in the technology and the interpretation of the results the methodology could be viable.
- Line Scanning Thermography (Contractor #4) was not able to identify the prestressing strands through the concrete cover, making the location of corrosion on the strands impossible. Currently, this method is not viable for identification of corrosion on prestressing strands.
- Electromagnetic Corrosion Detection combined with Galvanostatic Pulse Corrosion Rate (Contractor #5) resulted in an 8% identification success rate. These methods are not currently viable for the identification of corrosion on prestressing strands.
- Impact Echo (Contractor #6) had a low identification success rate, as did Monolith Ultrasonic Shear-Wave Testing. Polygon Ultrasonic Shear-Wave Testing diminished reflections did not correlate well with strand damage. Ground Penetrating Radar picked up some cases of Heavy Pitting and Wire Loss, and missed others. In the case of corrosion identification in prestressed strands of concrete structures, these methods are not viable for accurate detection of corrosion.
- The 3D Laser Scanning techniques used by the contractor could be very useful for rapid inspection of bridges in particular crack mapping, location of delaminations and spalled regions. This technology would be vital for consistent inspections. Commercial systems are readily available and are recommended for bi-annual inspection of box beam bridges.

To further assess the magnetic NDT methods an additional study was conducted on an idealized slab with corrosion flaws manufactured in both steel strand and conventional rebar cast at various depths in concrete slabs. The degree of damage was varied and included: (1) small flaws of 10% section loss, (2) medium flaws of approximately 20% section loss, (3) heavy flaws of approximately 50% section loss, and (4) full fracture with 100% section loss. The length of each

defect varied at: (a) 0.5 in., (b) 1.0 in., and (c) 1.5 in. The following conclusions can be made based on the results:

- The MFL method correctly identified the presence of 90% of all flaws. All of the undetected flaws were of the small variety, with this method correctly identifying approximately 76% of them. The method was able to identify flaws within a region of 1.8 in.
- The RM method correctly identified the presence of 72% of all flaws. The vast majority of the undetected flaws were of the small variety, with this method correctly identifying approximately 44% of them. Additionally, this method picked up over 95% of all medium and heavy flaws. The method was able to identify flaws within a region of 1.0 in.
- Both methods were more accurate in locating and identifying small flaws with a damage length of 1.5 in.; when compared to those with damage lengths of 1/2 or 1 in. The MFL method correctly identified the presence of 91.3% of all small flaws with a large damage length of 1.5 in., compared to only 60% correctly identified for those with damage lengths of 1.0 or 0.5 in. The RM method correctly identified the presence of 56.5% of all small flaws with a damage length of 1.5 in., compared to only 30% correctly identified for those with damage lengths of 1.0 or 1/2 in.
- As the clear cover varied, both magnetic methods had a somewhat consistent flaw identification rate with respect to small flaws. The MFL method successfully detected 73.3% of small flaws with 1 inch of clear cover, 78.6% of small flaws with 1.5 inches of clear cover, and 71.4% of small flaws with 2 inches of clear cover. The RM method successfully detected 40% of small flaws with 1 inch of clear cover, 42.9% of small flaws with 1.5 inches of clear cover, and 50% of small flaws with 2 inches of clear cover.
- Although both methods did not successfully identify all of the small flaws, the strength reduction would not be severe for these cases. The 10% reduction in area, which simulates pitting due to corrosion, would correlate with approximately a 20% loss of strength for that piece of reinforcement. Both methods have been found to be highly accurate in detecting the larger flaws which correlate to strength losses from approximately 30% to 100%.
- Both MFL and RM identified 100% of all complete fractures.
- Both methods were slightly more accurate in correctly identifying flaws in the steel strand versus flaws in the conventional rebar. The MFL method accurately identified 88.3% of flaws in slabs with conventional steel reinforcing; compared to 91.8% of flaws in slabs reinforced with 7-wire strand. The RM method accurately identified 70.7% of flaws in slabs with conventional steel reinforcing; compared to 73.2% of flaws in slabs reinforced with 7-wire strand.

8. References

Naito, C., Hodgson, I., Jones, L., “Inspection Methods & Techniques to Determine Non Visible Corrosion of Prestressing Strands in Concrete Bridge Components – Task 3 – Forensic Evaluation,” ATLSS Report 09-10, Lehigh University, June 2010.

Naito, C., Sause, R., Hodgson, I., Pessiki, S., Desai, C., “Forensic Evaluation of Prestressed Box Beams from the Lake View Drive Bridge over I-70 – Final Report,” ATLSS Report No.06-13 and FHWA-PA-2006-017-EMG002, ATLSS Center, Lehigh University, September, 2006, 62 pages.

9. Appendix

Reports from the six NDT contractors are included in their entirety. The reports are as follows:

- Contractor #1: Dr. Al Ghorbanpoor and Mr. Emad Abdelsalam
 - Method: Magnetic Flux Leakage (MFL)
- Contractor #2: Infrasense, Inc.
 - Method: Ground Penetrating Radar (GPR)
- Contractor #3: Prof. Bernd Hillemeier and Andri Walther of Technische Universitat Berlin Institute for Civil Engineering in association with Vector Corrosion Technologies
 - Method: Remanent Magnetization (RM)
- Contractor #4: Physical Acoustics Corporation (PAC)
 - Method: Line Scanning Thermography (LST)
- Contractor #5: LIMCMT, Inc. & David L. Gress & Associates
 - Method 1: Electromagnetic Corrosion Detection (EMCD)
 - Method 2: Galvanostatic Pulse Corrosion Rate (GPCR)
- Contractor #6: Dynasty Group
 - Method 1: Ultrasonic Impact Echo (IE) Test Method
 - Method 2: Ultrasonic Shear-Wave Test (UST) Method
 - Method 3: Ground Penetrating Radar (GPR)
 - Method 4: 3D Laser Scanning
- Survey of Contractors

Magnetic Flux Leakage NDE of Penn-DOT Prestressed Concrete Box Girders

By

**Al Ghorbanpoor & Emad Abdelsalam
University of Wisconsin-Milwaukee**

November 22, 2008

Magnetic Flux Leakage NDE of Penn-DOT Prestressed Concrete Box Girders

Summary:

On November 22, 2008, Dr. Al Ghorbanpoor and Mr. Emad Abdelsalam of the University of Wisconsin-Milwaukee performed a series of NDE tests of seven prestressed concrete box beams at Lehigh University's ATLSS Research Center in Bethlehem, PA. The test samples had been recently removed from various bridge structures in Pennsylvania and transported to Lehigh University for examination. All tests reported here were performed using the Magnetic Flux Leakage (MFL) system that has been developed by Dr. Al Ghorbanpoor at the University of Wisconsin-Milwaukee. This summary report includes test results for all tests performed on the beams. The report also includes an appendix that provides background information on the MFL system and selected examples of recent applications.

Test Samples:

A total of seven prestressed concrete box beams were transported inside the ATLSS Research Center at Lehigh University and were subjected to magnetic flux leakage tests. The tests included scanning of the lower flanges of these beams on the outside surfaces. Due to the current mechanical configuration of the MFL system, all the box beams were placed on the laboratory's test floor in inverted positions so the MFL tests could be performed by placing the MFL equipment directly above the lower flange of each beam. Some of the beams showed extensive corrosion of the prestressing and reinforcing steel with significant spalling of concrete cover. The remaining beams had little or no evidence of steel corrosion. Figures 1 and 2 show the overall staging layout of the beams in the laboratory and a typical MFL test scan of a beam, respectively.

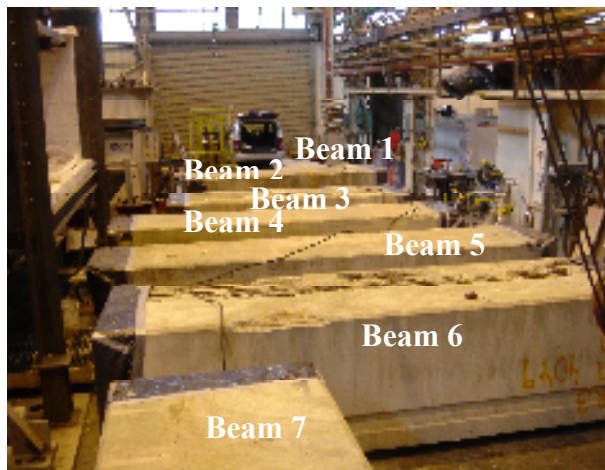


Figure 1 - Beams staging layout in the laboratory

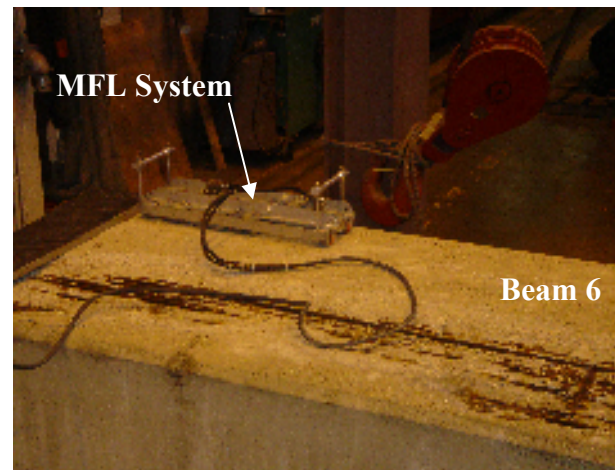


Figure 2 – Typical MFL scan of a box beam (Beam 6)

MFL System and Test Procedure:

The MFL system consists of two strong permanent magnets and a series of Hall-Effect sensors. The MFL magnets and sensors assembly is used to scan a concrete surface at a close distance to detect corrosion of steel embedded in the concrete. Each scan width for the current MFL system is 8 inches. Corrosion of steel within concrete will cause a leakage of the magnetic field in the steel during each MFL scan. The magnetic field leakage will then be detected by the sensors. There are 10 Hall-Effect sensors in the current MFL system. During each MFL scan, the lower surfaces of the magnets and seven of the sensors are positioned near the test surface at about 1/2 inch. These 7 sensors are spaced equally across the 8-inch width of the MFL equipment and these are the sensors that are normally used to report test results. The 3 additional sensors are located 1.0 inch above the other sensors and are used for additional analysis during data post processing. The MFL system includes an encoder device that accurately (within 0.1 inch) measures the traveled distance of the equipment during each test scan. MFL test results are normally shown in the form of graphs of relative magnetic field amplitude and the traveled distance. The relative magnetic field amplitude is proportional to the extent of the loss of section in the steel.

Each MFL tests is performed by rolling the equipment on the concrete surface on a set of wheels that maintain a constant distance of about 1/2 in. between the magnets/sensors assembly and the test surface. As such, the MFL tests could be conducted only on relatively smooth concrete surfaces such as those with normal formwork finish. Concrete surfaces with significant spall and exposed reinforcing or prestressing steel are not suitable for MFL testing. For example, MFL tests were conducted on Beam 6 that had severe concrete spall and exposed corroded prestressing steel only after a 1/2-inch thick wood board was placed on the flange surface. Testing of Beam 6 was done to allow a verification of the capability of the MFL system in detecting known corrosion of the prestressing steel in the beam.

Results from the lowest 7 sensors are used for each scan in this report. Accordingly, multiple scans, or tracks, were made along the length of each beam so the width of each beam could be covered for the MFL testing. Based on the MFL results during each scan a determination was made for the presence or lack of prestressing steel wire breaks or corrosion.

Beam 1:

Beam 1 was located at the north end of the laboratory and it was oriented in the south to north direction. There was extensive damage in the beam including concrete spall, concrete fracture, and steel corrosion. As such, only a relatively small part of the surface of the bottom flange was suitable for the MFL test. In the area that the MFL tests were conducted, there were longitudinal cracks in the concrete but no significant corrosion stain was observed. Four MFL test scans were performed (tracks T1 to T4) for this beam and each test was along the south to north direction. Each test was started at 99 inches and stopped at 39 inches from the north end of the beam. Also, due to the damage, the first track, T1, of the testing had to be performed at approximately 10 inches clear from the east edge and the fourth track, T4, of the testing was at about 6 inches clear from the west edge of the beam. Figure 3 shows the condition of the bottom flange of Beam 1 as well as the centerlines of the MFL test scans or tracks T1 to T4.

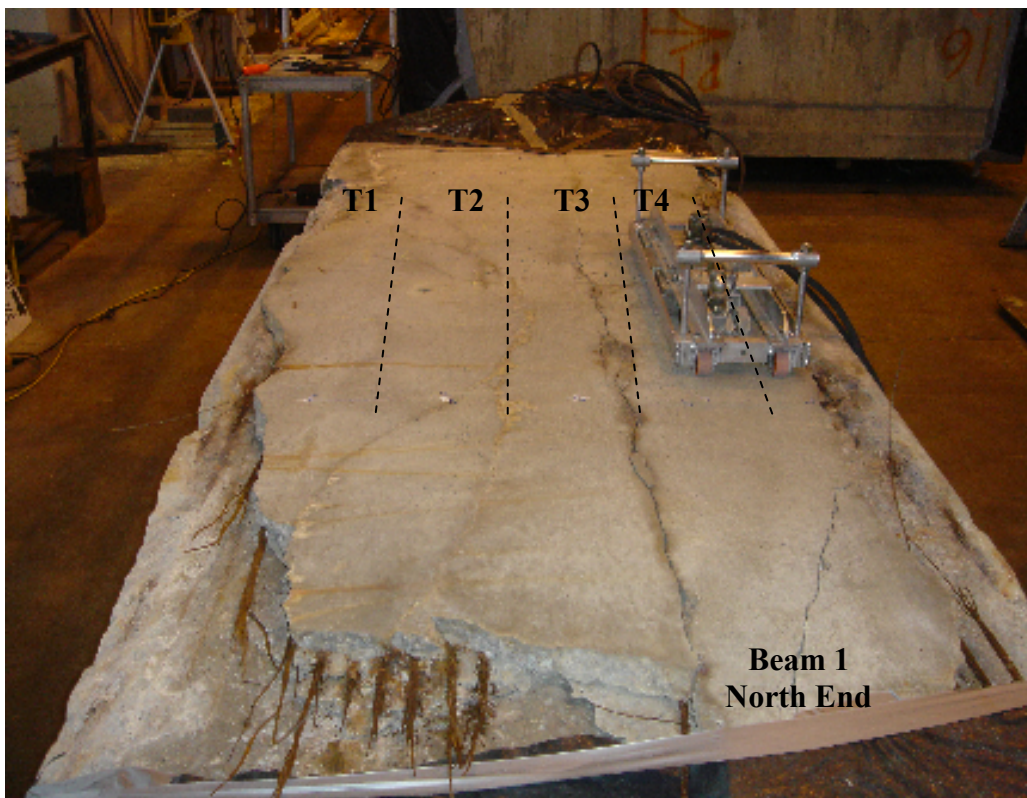


Figure 3 – Appearance of the bottom flange of Beam 1 and the centerlines of MFL tracks T1 to T4

The MFL test results from the four tracks that were taken over the specified surface area of the lower flange for Beam 1 indicated evidence of general surface corrosion of the prestressing steel and the transverse reinforcing bars. No indications of wire breaks or fracture of the strands were observed. Figure 4 shows the side-by-side results from the MFL testing of the 4 tracks in the beam. Please note that the left end of each graph corresponds with the beginning of each test (the south end of the beam). The MFL tests also showed irregularities in the placement/orientation of the transverse reinforcing steel bars in the beam. The large local amplitude variations in the figure (4 indications along the east edge and 3 indications along the west edge of the beam) represent the location of the transverse steel bars in the beam. The red lines in the figure indicate the locations of the transverse reinforcing bars in the beam. It is clear from the figure that the first 2 transverse steel bars are not perpendicular to the sides of the beam and are embedded deeper inside concrete at the west edge.

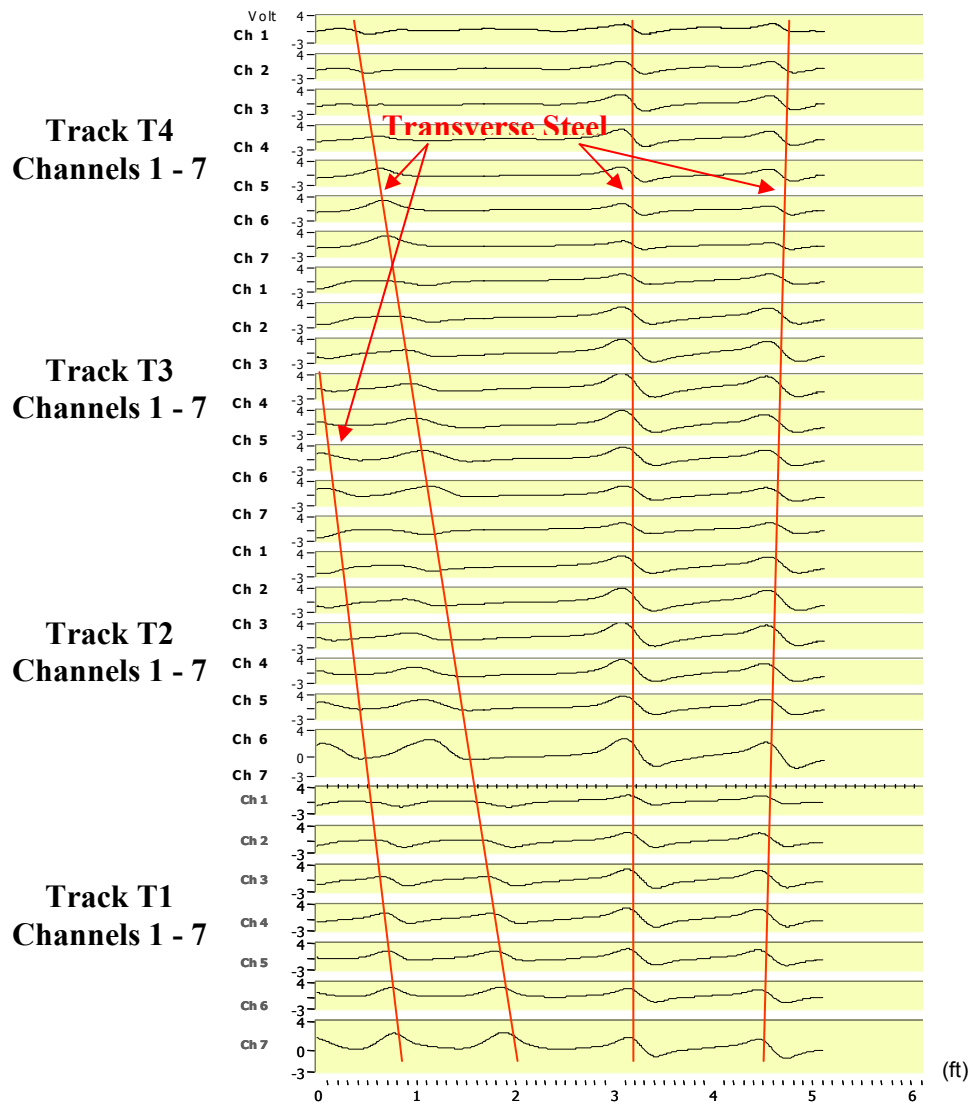


Figure 4 – Longitudinal MFL scans shown for 4 Tracks in Beam 1
(Scan results are laid out side-by-side)

Beam 2:

Beam 2 was located immediately to the south side of Beam 1 but it was oriented in the east to west direction. Three MFL tests were performed (tracks T1 to T3) for this beam and each test was along the east to west direction. A local concrete damaged area was present along the north edge and closer to the west end of the beam. As such, the first scan was performed at a clear distance of 13.5 inches from the north edge of the beam. Each scan length was approximately 8 feet. Each scan was started at a distance of 23.5 inches from the east end of the beam. The MFL test results indicated no prestressing steel wire breaks or significant corrosion in the area of the beam that was scanned. The MFL scan for track T1, however, indicated the presence of a local anomaly (i.e., additional steel, or a ferromagnetic material) at 6.3 feet from the start of the scan or 8.25 feet from the east end of the beam. The anomaly is estimated to be located within a circular area with a diameter of 8 inches located at 8.25 feet from the east end and 16 inches from the north edge of the beam. Figure 5 shows the MFL scans from tracks, T1, T2, and T3 laid out side-by-side and with the beam's transverse reinforcing steels and the local anomaly marked on the figure.

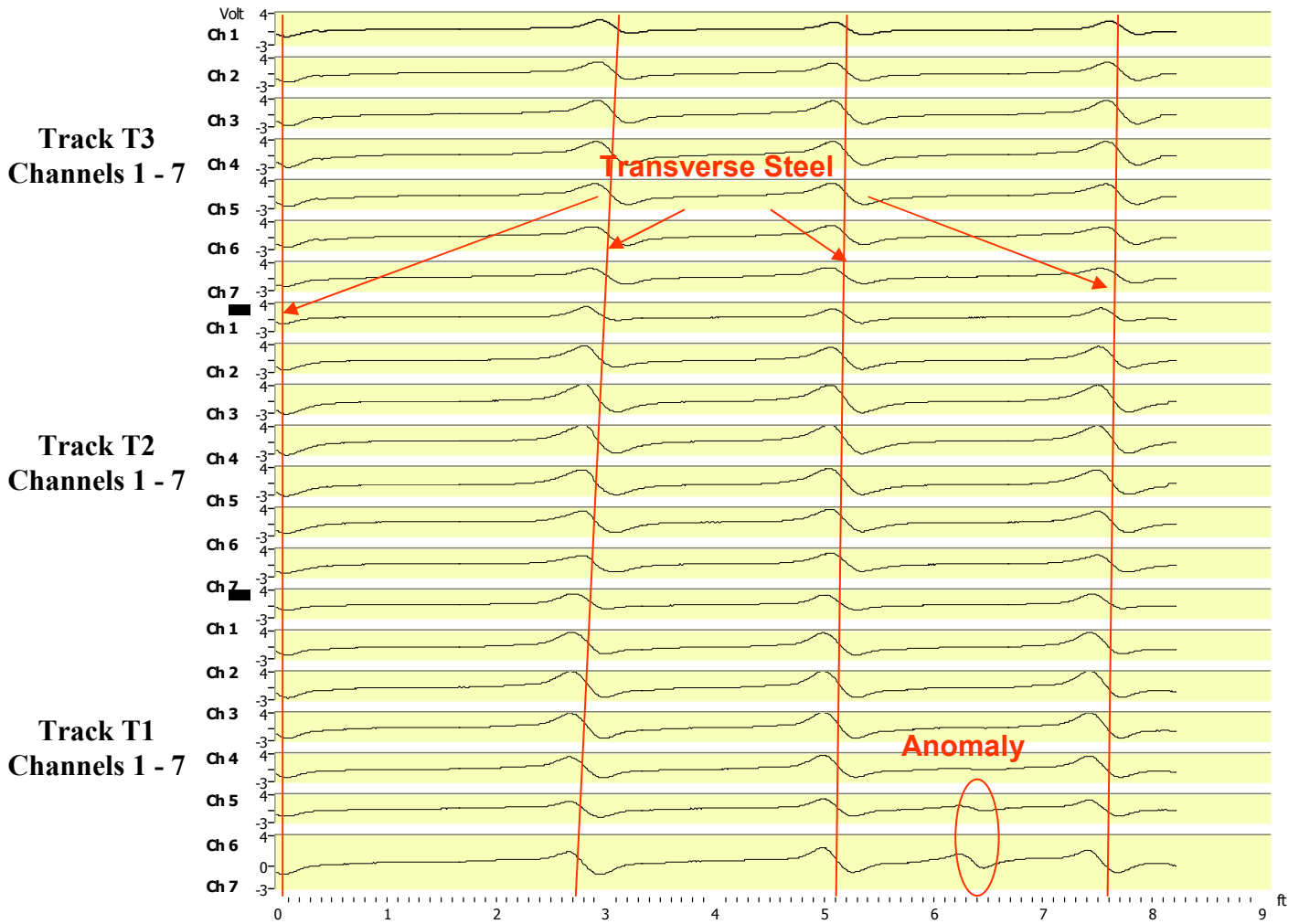


Figure 5 – Side-by-side longitudinal MFL scans shown for 3 Tracks in Beam 2

Beam 3:

Beam 3 was located immediately to the south side of Beam 2 also oriented in the east to west direction. No significant evidence of corrosion (i.e, corrosion stain or concrete spall) was observed on the surface of the concrete that was scanned by the MFL system. Five MFL tests were performed (tracks T1 to T5) for this beam and each test was along the east to west direction. Because of the edge chamfers, MFL scans were made with 3.5 inches clear of each edge of the beam. Each scan length was approximately 7 feet. Each scan was started at a distance of about 22 inches from the east end of the beam. The MFL results indicated no prestressing steel wire breaks or significant corrosion in most of the area of the beam that was scanned except in an area under track T2. Indications of corrosion of prestressing steel were observed along the length of the scan for the northern one half of the width of the MFL system (Channels 4, 5, 6, and 7) for track T2. The area of the corroded prestressing steel is bound by a band width between 12 to 18 inches from the north edge of the beam. Figure 6 shows MFL scans from Tracks, T1 to T5 laid out side-by-side and with the beam's transverse reinforcing steels and the corroded prestressing steel region marked on the figure. Figure 7 shows close up MFL test graphs for tracks T1 and T2. Evidence of corrosion can be seen easily in the data from track T2 in comparison with the graph from track T1 that showed no corrosion indications.

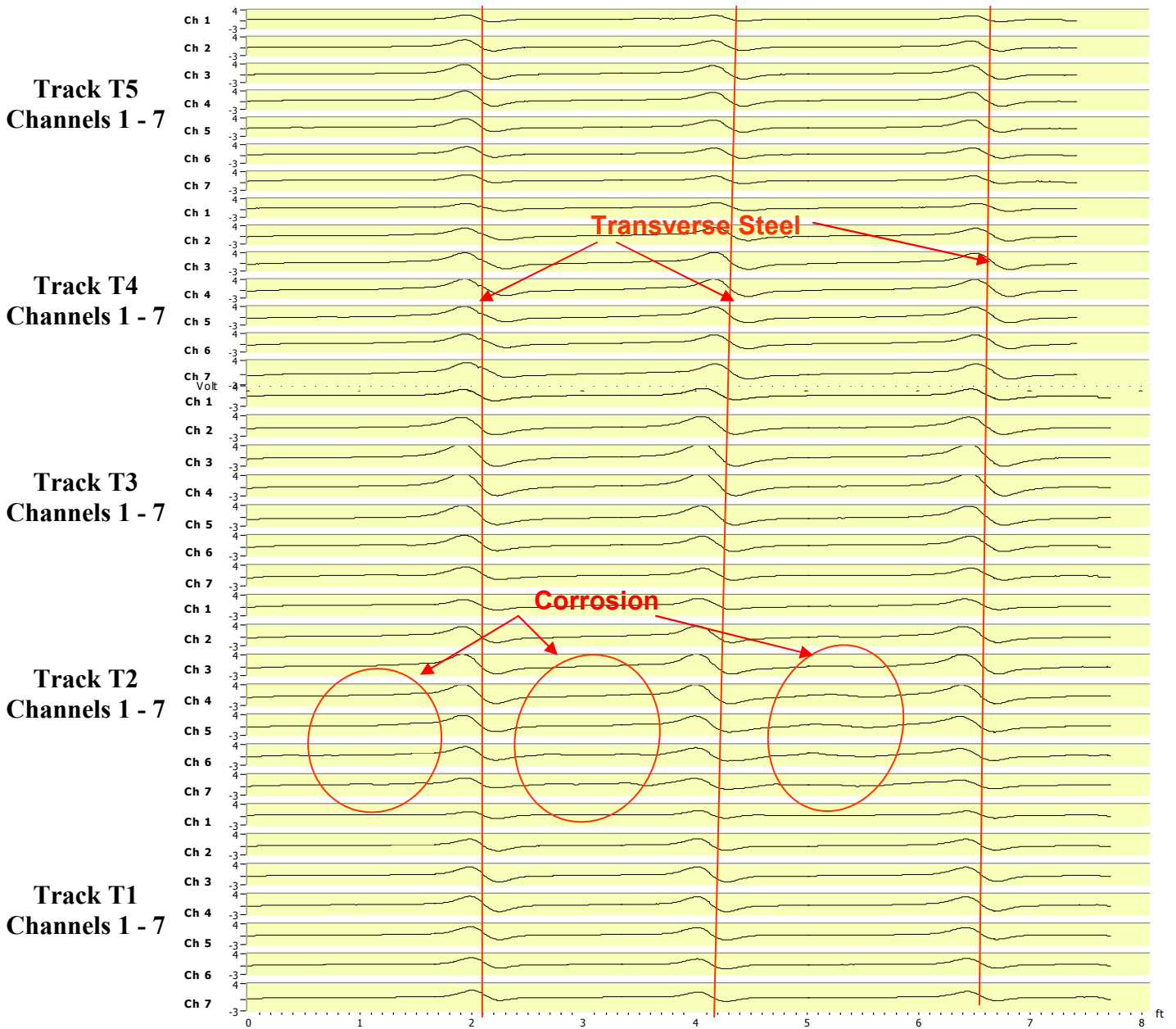


Figure 6 – Side-by-side longitudinal MFL scans shown for 5 Tracks in Beam 3

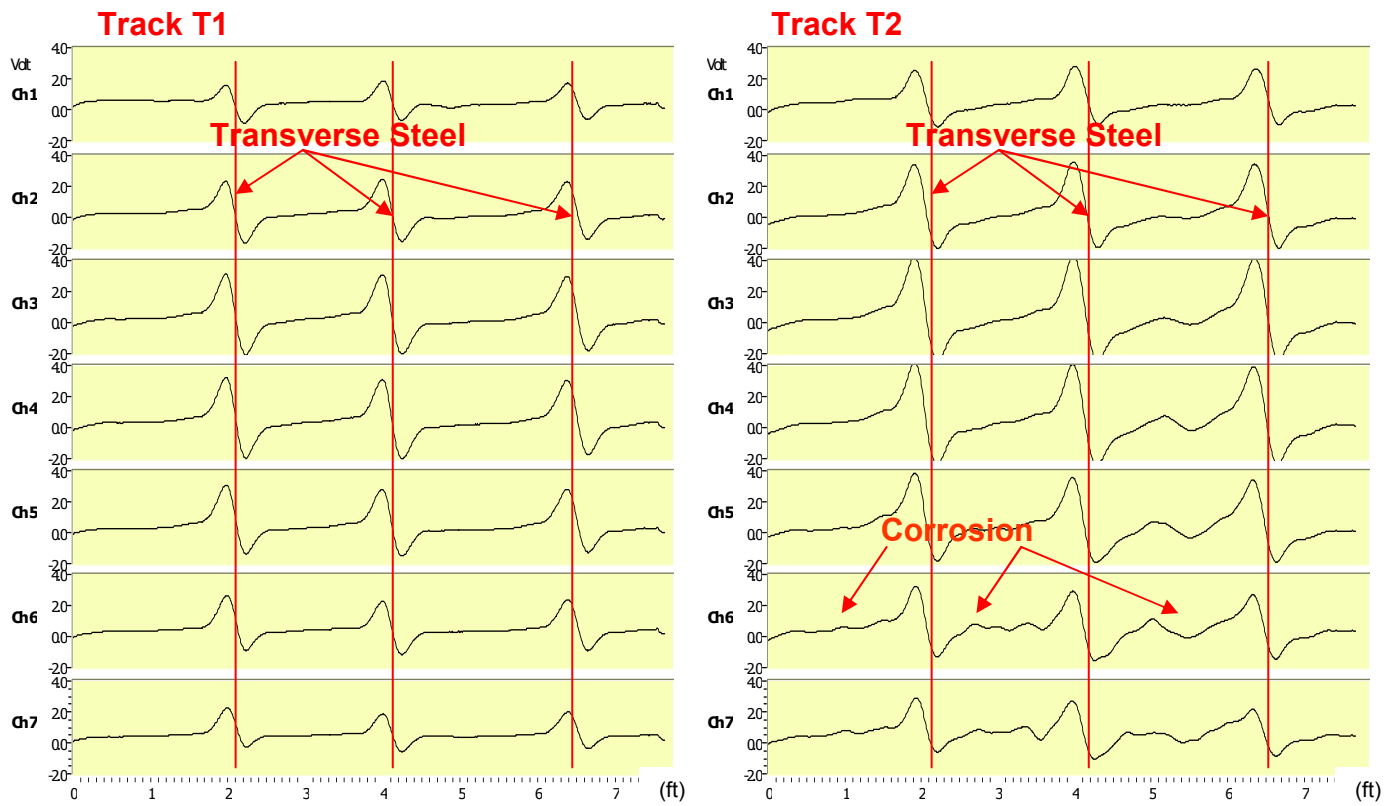


Figure 7 – Longitudinal MFL scans shown for Tracks T1 (left) and T2 (right) in Beam 3 (Indications of corrosion can be seen in the data between transverse steel bars in track T2)

Beam 4:

Beam 4 was located immediately to the south side of Beam 3 also oriented in the east to west direction. No significant evidence of corrosion (i.e, corrosion stain or concrete spall) was observed on the surface of the concrete that was scanned by the MFL system. Four MFL tests were performed (tracks T1 to T4) for this beam and each test was along the east to west direction. Because of the edge chamfers, MFL scans were made with 1.5 inches clear of the north edge and 2.5 inches clear of the south edge of the beam. Each track scan was about 11.5 feet long and started at 17.5 inches from the east end of the beam. Based on the results of the MFL tests, there were no indications of prestressing steel wire breaks or major corrosion in the bottom flange of the beam. Figure 8 shows side-by-side MFL longitudinal scans for 4 tracks, T1 to T4, for Beam 4. As shown in the figure, there are no transverse reinforcing steel bars in the bottom flange of the beam. Please note the MFL signals from the near side sensors indicating the presence of tips of vertical bars in the webs (stirrups) on both sides of the beam.

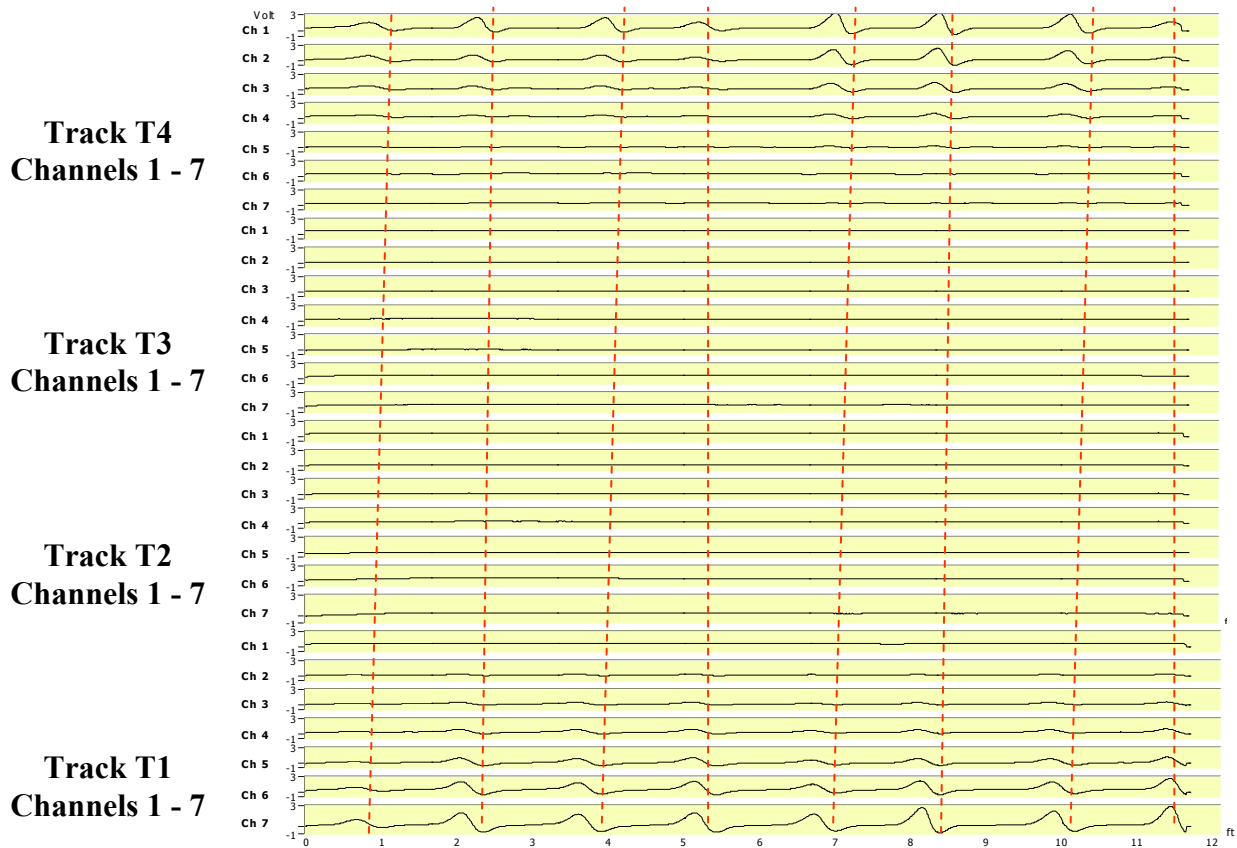


Figure 8 - Side-by-side MFL longitudinal scans for 4 tracks in Beam 4

Beam B5:

Beam B5 was located immediately to the south side of beam B4 also oriented in the east to west direction. No significant evidence of corrosion (i.e, corrosion stain or concrete spall) was observed on the surface of the concrete that was scanned by the MFL system. Four MFL tests were performed (Tracks T1 to T4) for this beam and each test was along the east to west direction. Because of the edge chamfers, MFL scans were made with 2.0 inches clear of the north and south edges of the beam. Each track scan was about 12 feet long and it started at 24.0 inches from the east end of the beam. Based on the results of the MFL tests, there were no indications of prestressing steel wire breaks or major corrosion in the bottom flange of the beam. Figure 9 shows side-by-side MFL longitudinal scans for 4 tracks for the beam. As shown in the figure, there are no transverse reinforcing steel bars in the bottom flange of the beam. Please note the MFL signals from the near side sensors indicating the presence of tips of vertical bars in the webs (stirrups) on both sides of the beam. Also, please note the MFL data indications from track T3 at locations between 5 ft to 8 ft from the start of the test (7 ft to 10 ft from the east end of the beam). The MFL amplitude variations in this region are related to the presence of local steel elements such as chairs, couplers, etc. They do not indicate the presence of prestressing steel wire breaks or major corrosion.

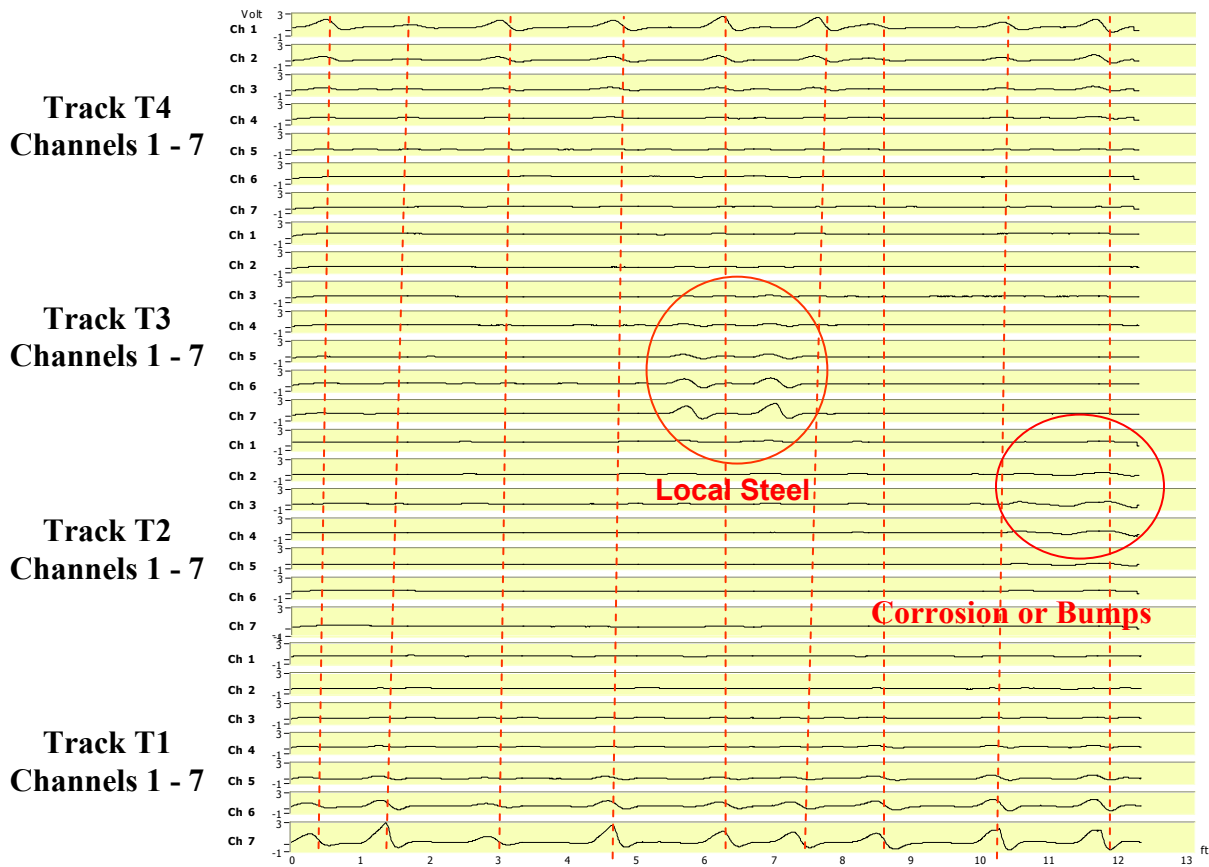


Figure 9 - Side-by-side MFL longitudinal scans for 4 tracks in Beam 5

Beam 6:

Beam 6 was located immediately to the south side of beam 5 and it was oriented in the east to west direction. Significant steel corrosion including prestressing steel wire breaks existed in the beam particularly along the north half width of the beam. Figure 10 shows a photograph of Beam 6. The photo shows the condition of the lower flange of the beam including prestressing corrosion and concrete spall. The figure also shows a local area (covered with gray plastic tape) with corroded prestressing steel that is located close to the south-west corner of the beam. On the figure, the centerlines of the MFL test scans for tracks T1 to T7 are shown. Track T7 was taken for the locally spalled area of the lower flange that was covered with the plastic tape. The small photo on the top shows the corroded prestressing steel area that was initially covered with the plastic tape to allow conducting the MFL testing over that area.

Because of the extensive concrete spall and unevenness in a large surface area of the lower flange, the MFL test could not be performed directly on the flange surface. To achieve a relatively smooth test surface for conducting the MFL scan for track T7, the local concrete spalled area close to the south-west corner of the beam was filled with wood chips and covered with plastic tape. The MFL testing for the entire surface of the lower flange (scan tracks T1 to T6) was then performed after a ½-in. thick wood board was placed on the flange surface. The introduction of the wood board on the test surface caused an increase in the distance between the MFL system and the prestressing steel in the flange. This resulted in lowering of the system's sensitivity for corrosion detection but made it possible to conduct the MFL tests on a smooth surface.

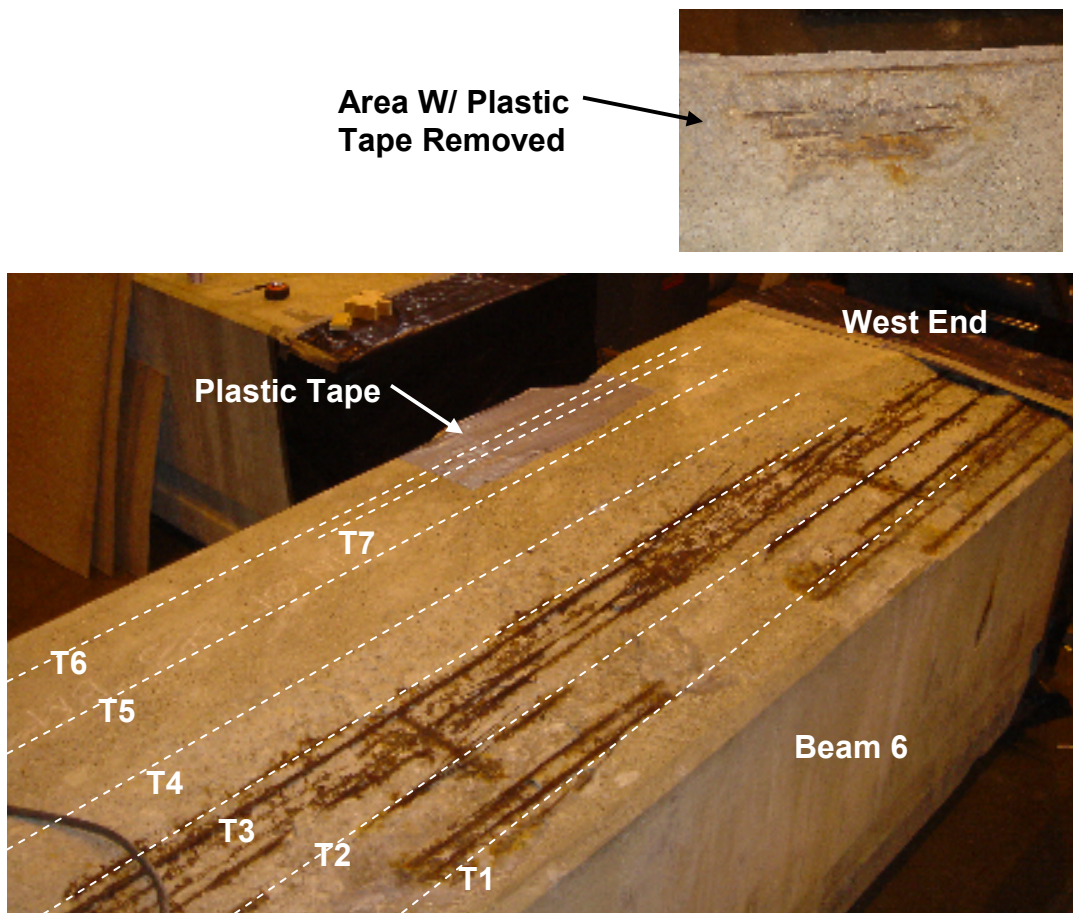


Figure 10 – Photo showing extensive corroded steel and the centerlines of the MFL test tracks in Beam 6

Figure 11 shows the MFL test results for track T7 in Beam 6. As shown in the figure, test track T7 was conducted for a scan length of about 5.5 feet and it was taken in the east to west direction. The figure on the left side (a) shows the test results when the MFL system was placed directly on the concrete and the plastic-tape-covered surfaces. The figure on the right side (b) shows the MFL results from the same test except with a ½-in. wood board that was placed on the lower flange surface. In both figures (a) and (b), indications of transverse steel and prestressing corrosion can be seen. While corrosion indications can be seen clearly from both figures, it should be noted that the placement of the ½-in. wood board on the concrete surface caused a reduction in the MFL signal amplitudes and a diminishing of some of the MFL signal details related to the steel corrosion.

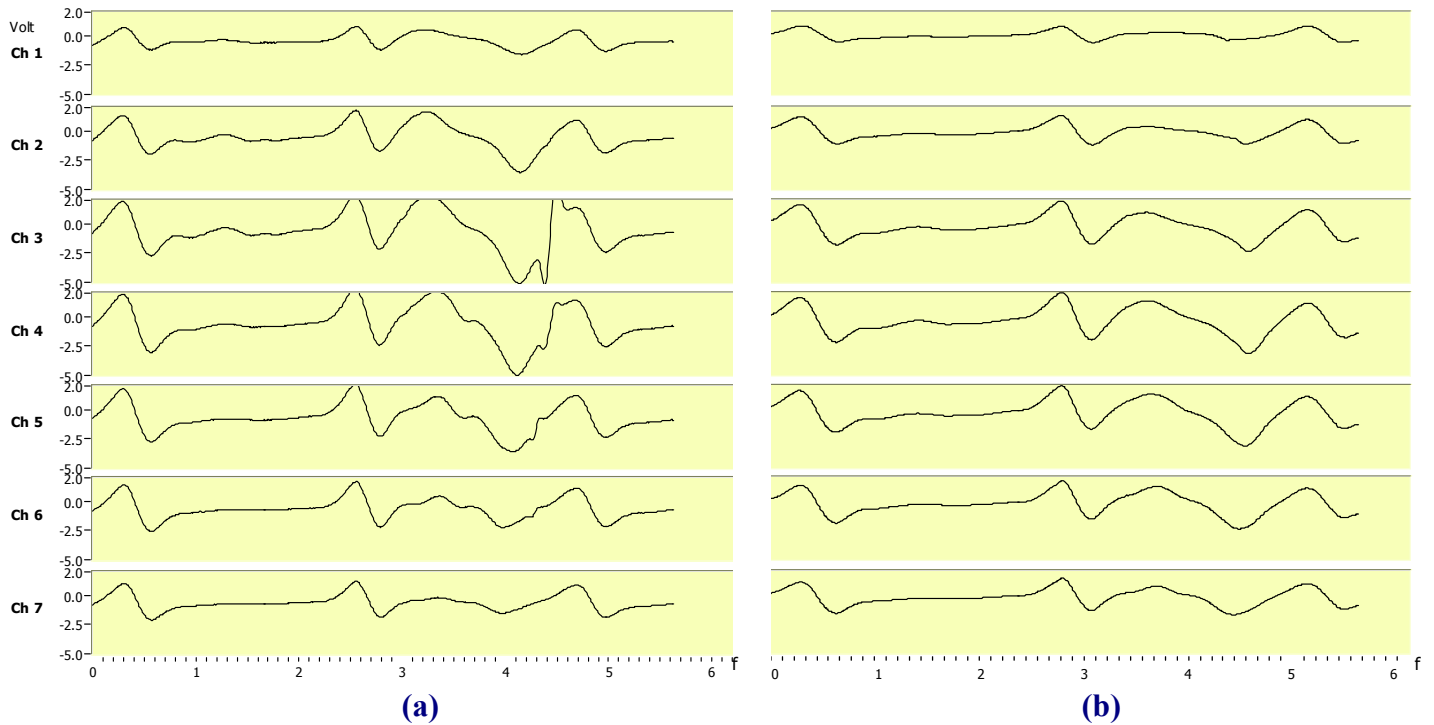


Figure 11 – MFL test results for track T7 in Beam 6
 (a) MFL scan without the ½-in. wood board, (b) MFL scan with the ½-in. wood board

After the ½-in. thick wood board was placed on the surface of the lower flange of Beam 6, a total of six MFL tests (scans) were performed, Figure 10. Each test was performed along the east to west direction. Each test scan was about 10 feet long and it started at about 24 inches from the east end of the beam. Because of the edge chamfers, the MFL scans for tracks T1 and T6 were made at a distance of about 2.0 inches and 0.5 inches clear from the north and south edges of the beam, respectively. Based on the results of the MFL tests, indications of significant corrosion and wire breaks in prestressing steel were noted. Figure 12 shows side-by-side MFL longitudinal scans for 6 tracks in Beam 6. Figure 12(a) shows the MFL data for tracks T1, T2, and T3 and Figure 12(b) shows the data for tracks T4, T5, and T6. Scan tracks T1, T2, and T3 indicated the presence of corrosion throughout the scan lengths. For tracks T4, T5, and T6 corrosion was detected primarily at locations closer to the end of each scan (7.5 to 11 feet from the east end of the beam). The magnetic field variations due to the presence of steel corrosion in Beam 6 can be seen easier if the MFL scans are shown separately for each track as presented in Figure 13. For comparison, the MFL data without any indications of steel corrosion from the test scan for track T5 is also shown in Figure 14.

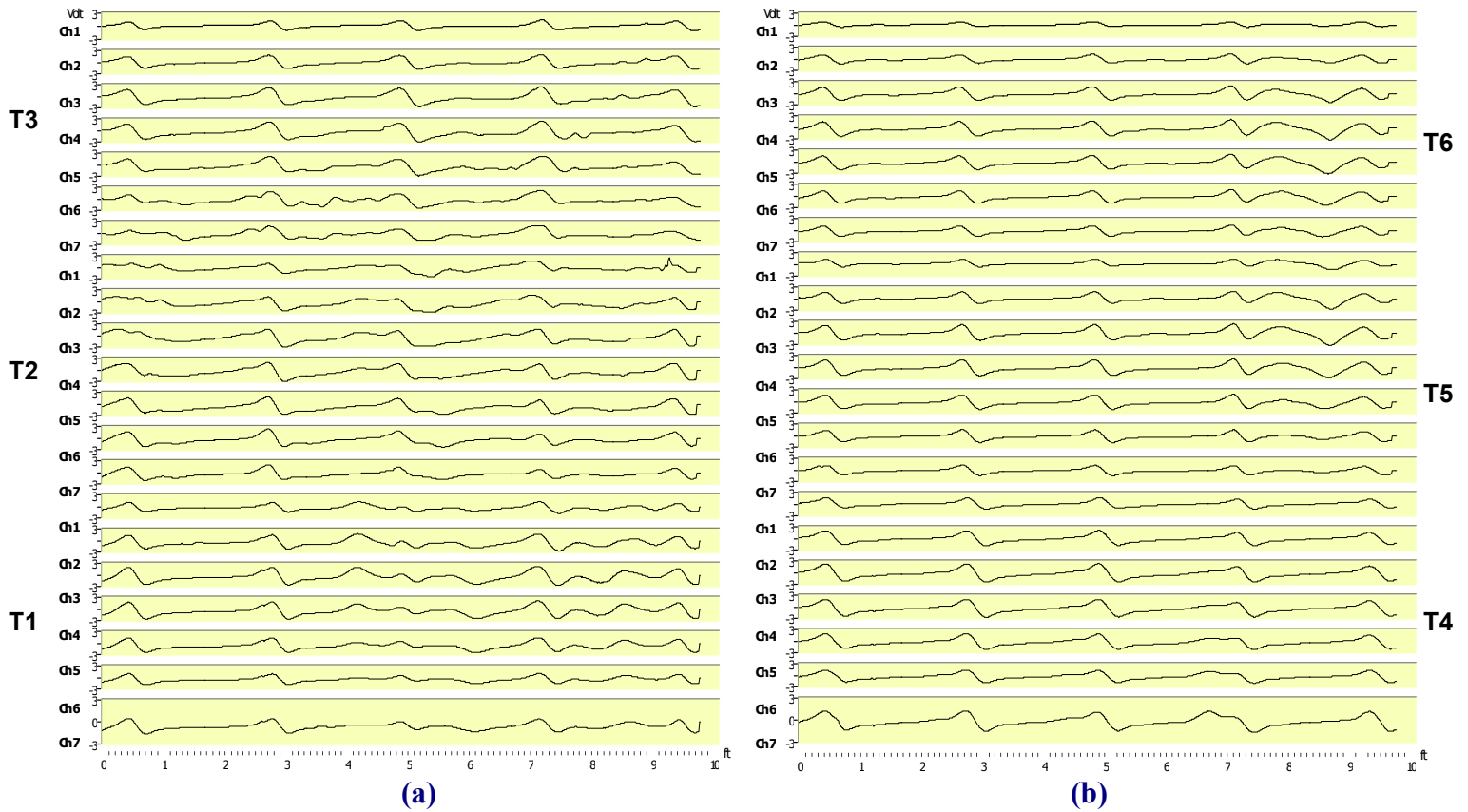


Figure 12 - Side-by-side MFL longitudinal scans for 6 tracks in Beam 6 (w/ 1/2" thick plank)
 (a) Tracks T1 to T3, (b) Tracks T4 to T6

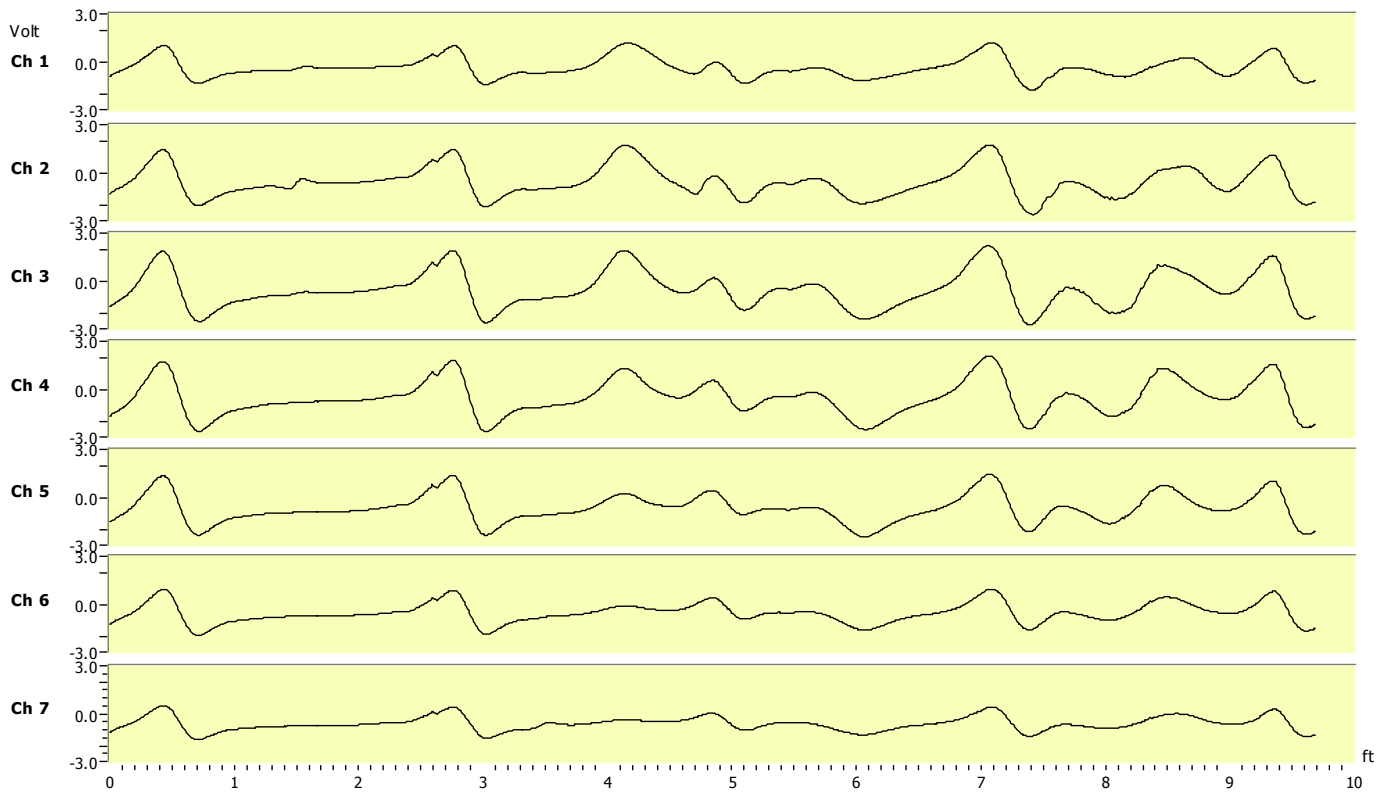


Figure 13 - MFL scan data for track T1 in Beam 6 (w/ 1/2" thick plank)

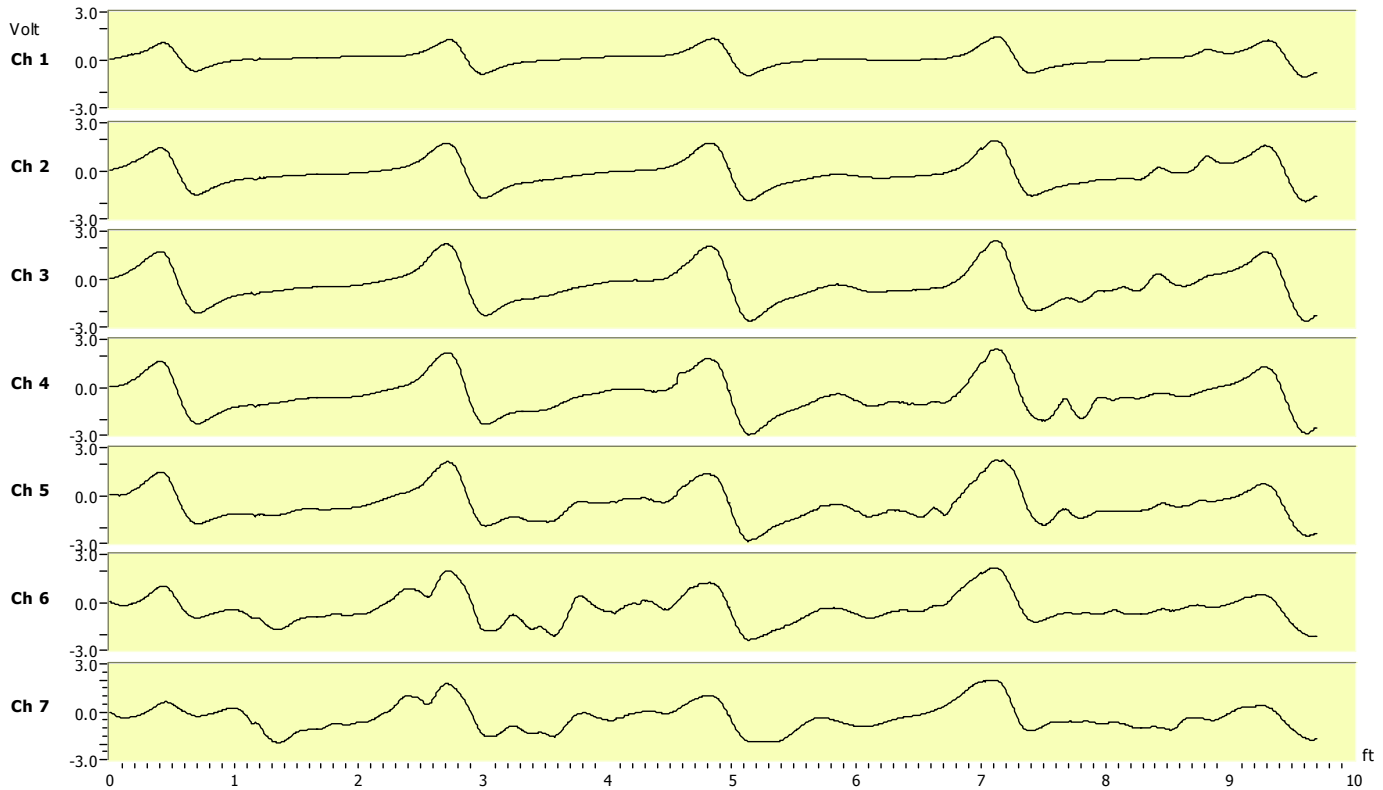


Figure 14 - MFL scan data for track T3 in Beam 6 (w/ 1/2" thick plank)

Beam 7:

Beam 7 was located at the far south side of the area where the test beams were placed in the laboratory. This beam was oriented in the south to north direction. The beam's lower flange contained isolated longitudinal cracks, concrete splitting, and exposed corroded strands. Figure 15 is a photograph showing the surface condition for the lower flange of Beam 7 and the locations of the centerlines of all the MFL scans (tracks T1 to T6) taken for the beam. A total of six MFL tests (scans) were performed for this beam. Each test was performed along the south to north direction. Each test scan was about 10 feet long and it started at about 29 inches from the south end of the beam. Because of the edge chamfers, the MFL scans for tracks T1 and T6 were made at a distance of 2.0 inches clear from the east and west edges of the beam. Due to the location of concrete splitting on the flange surface, the MFL test scans for tracks T4 and T5 had an overlap of about 4 inches. As such, the data from channels 1, 2, and 3 of track T4 are duplicates of those from channels 5, 6, and 7 of track T5. Based on the results of the MFL tests, no evidence of prestressing wire breaks or major corrosion was noted for tests performed along tracks T1, T2, T3, and T6. Test results performed along tracks T4 and T5 showed indications of corrosion of prestressing steel along the longitudinal cracked area and where there was concrete splitting and exposed corroded prestressing steel. Figure 16 shows side-by-side MFL longitudinal scans for 6 tracks in Beam 7. Figure 16(a) shows the MFL data for tracks T1, T2, and T3 and Figure 16(b) shows the data for tracks T4, T5, and T6. Evidence of steel corrosion can be seen in the test scans for tracks T4 and T5 as marked on the figure. Steel corrosion is detected along the beginning part of the scan for track T4 and along most part of the scan for track T5. The magnetic field variations due to the presence of steel corrosion in Beam 7 can be seen easier if the MFL test graphs are shown separately for tracks T4 and T5 as presented in Figure 17. For comparison, the MFL graph for a test scan with no indications of steel corrosion (for track T2) is also shown in Figure 18.

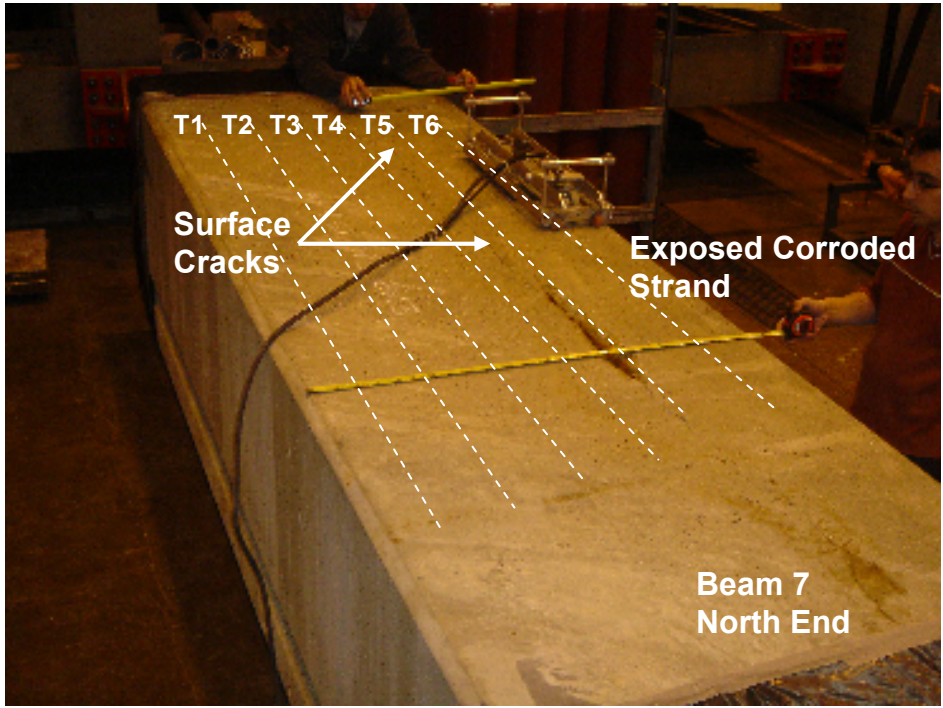


Figure 15 – Surface condition for the lower flange of Beam 7

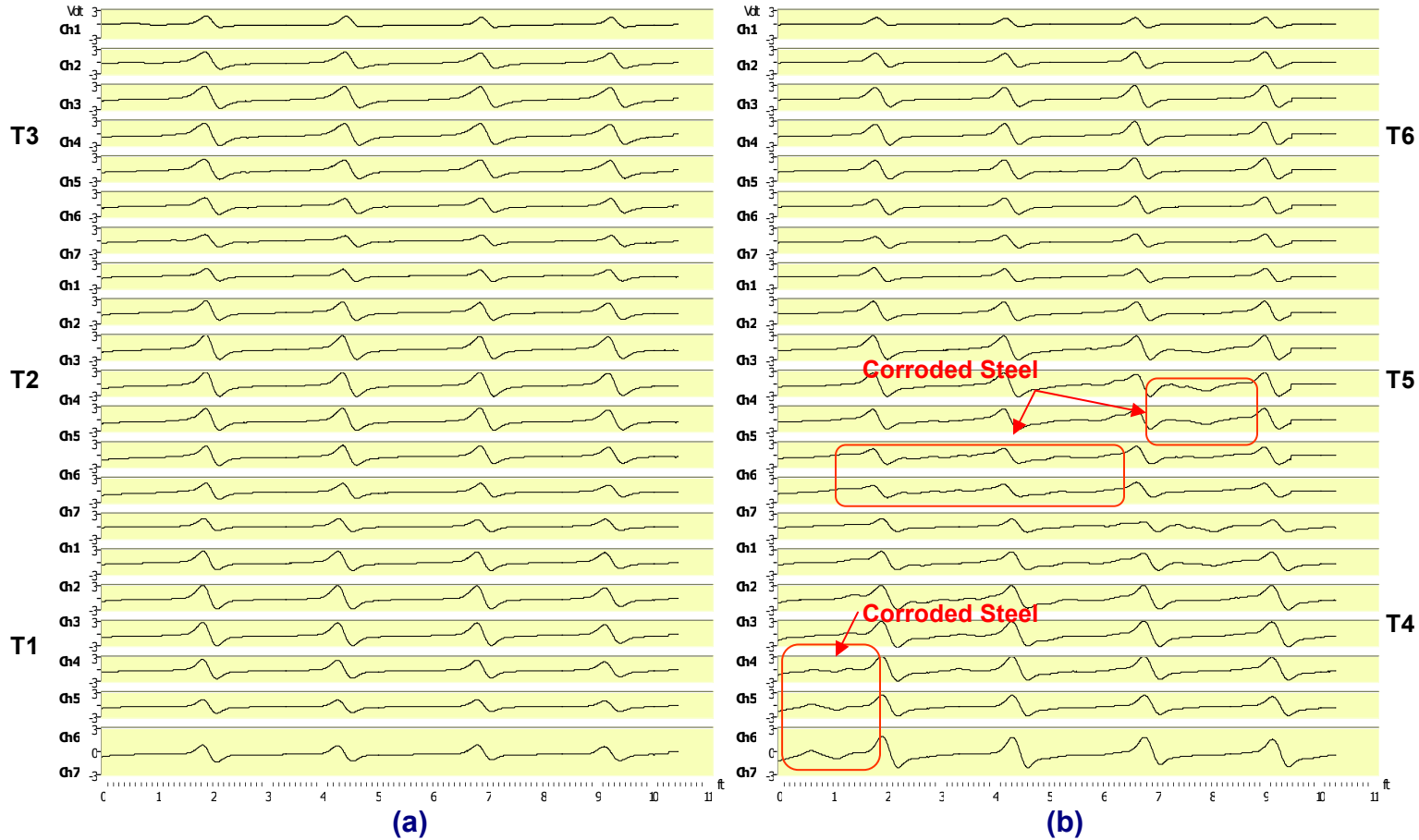


Figure 16 - Side-by-side MFL longitudinal scans for 6 tracks in beam B7
 (a) Tracks T1 to T3, (b) Tracks T4 to T6 (5" overlap of T4 & T5)

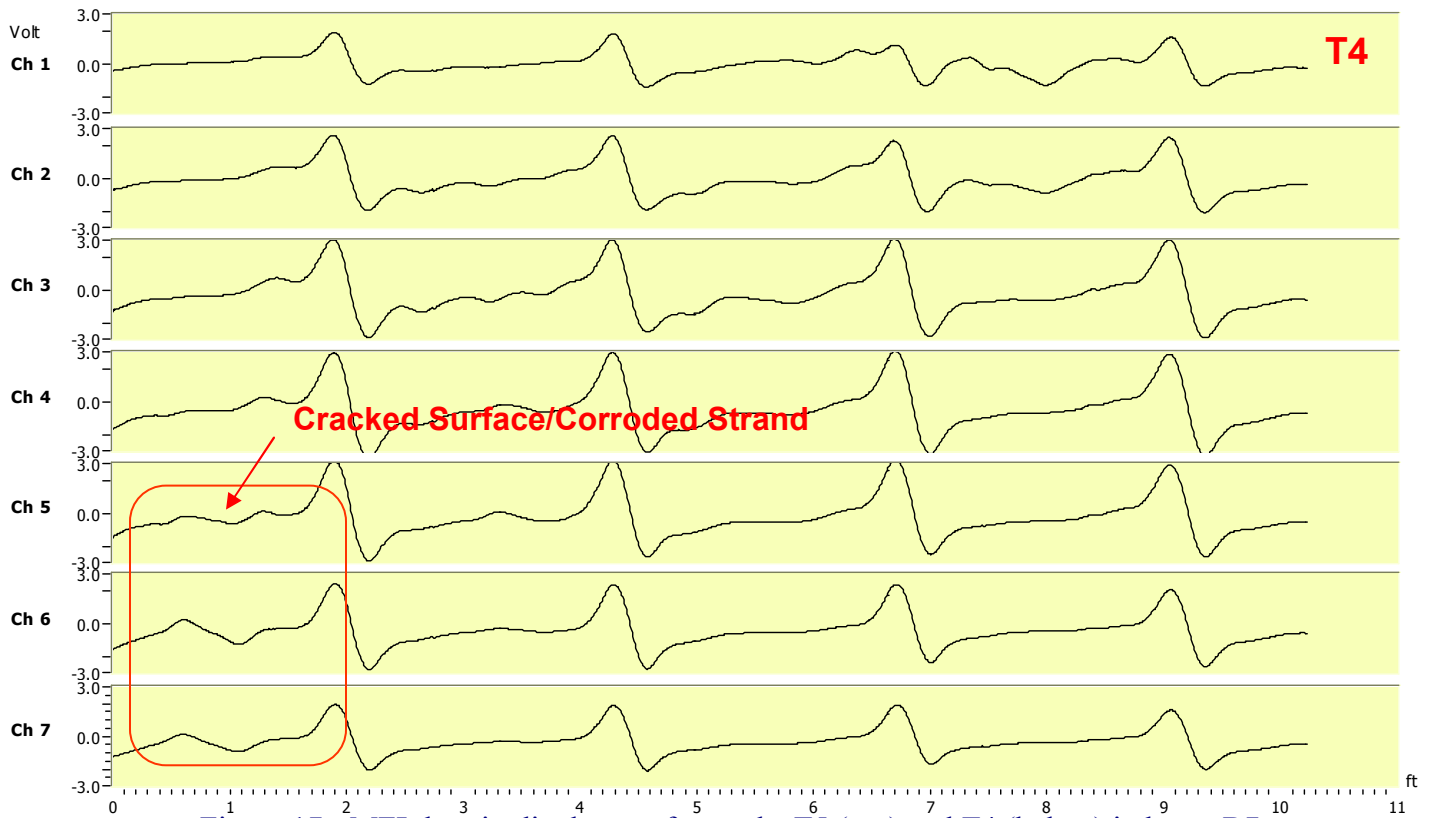
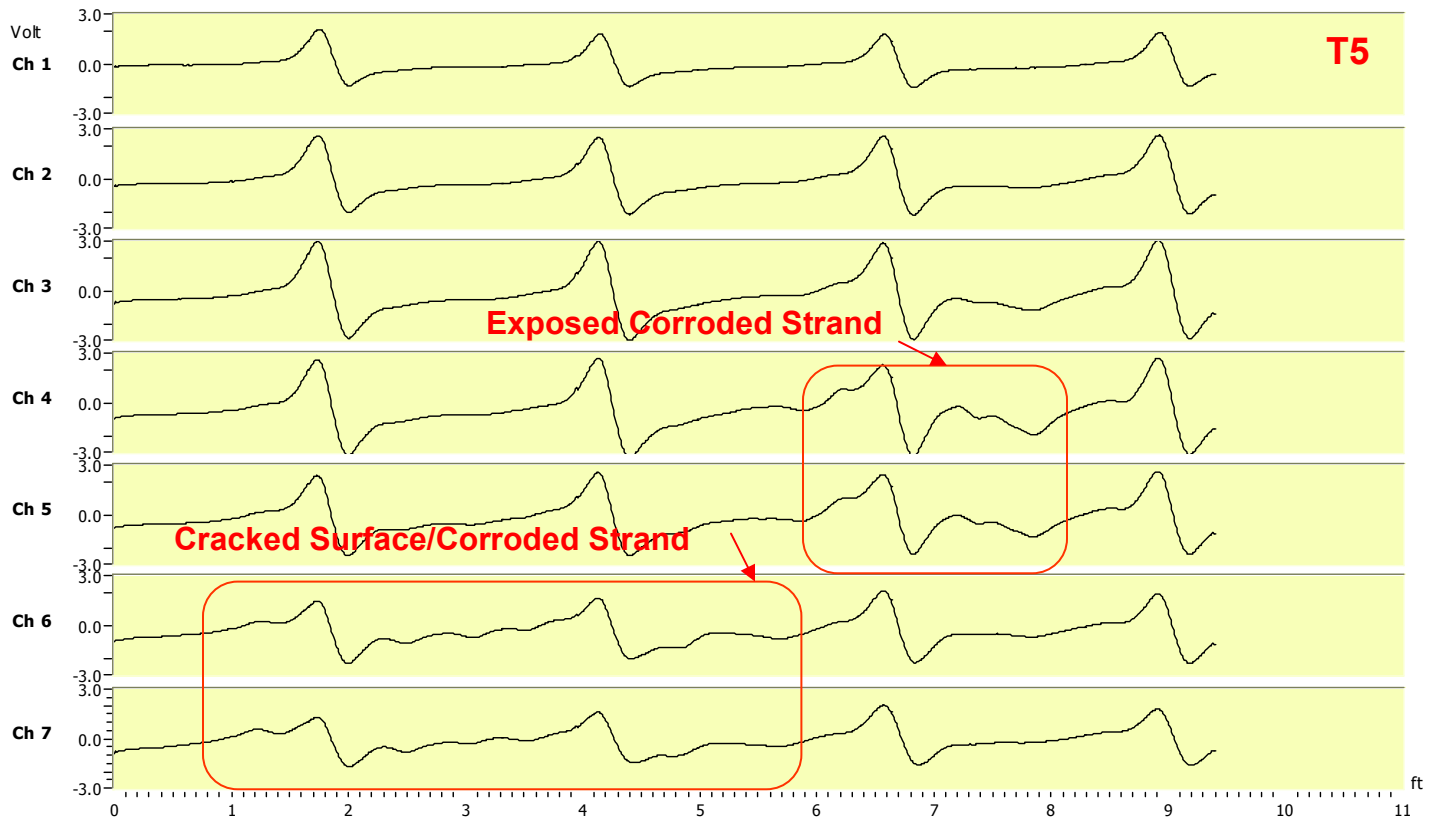


Figure 17 - MFL longitudinal scans for tracks T5 (top) and T4 (below) in beam B7
 (Note: Scan overlap resulting duplicate data in Ch. 5, 6, and 7 of track T5 and Ch. 1, 2, and 3 of track T4)

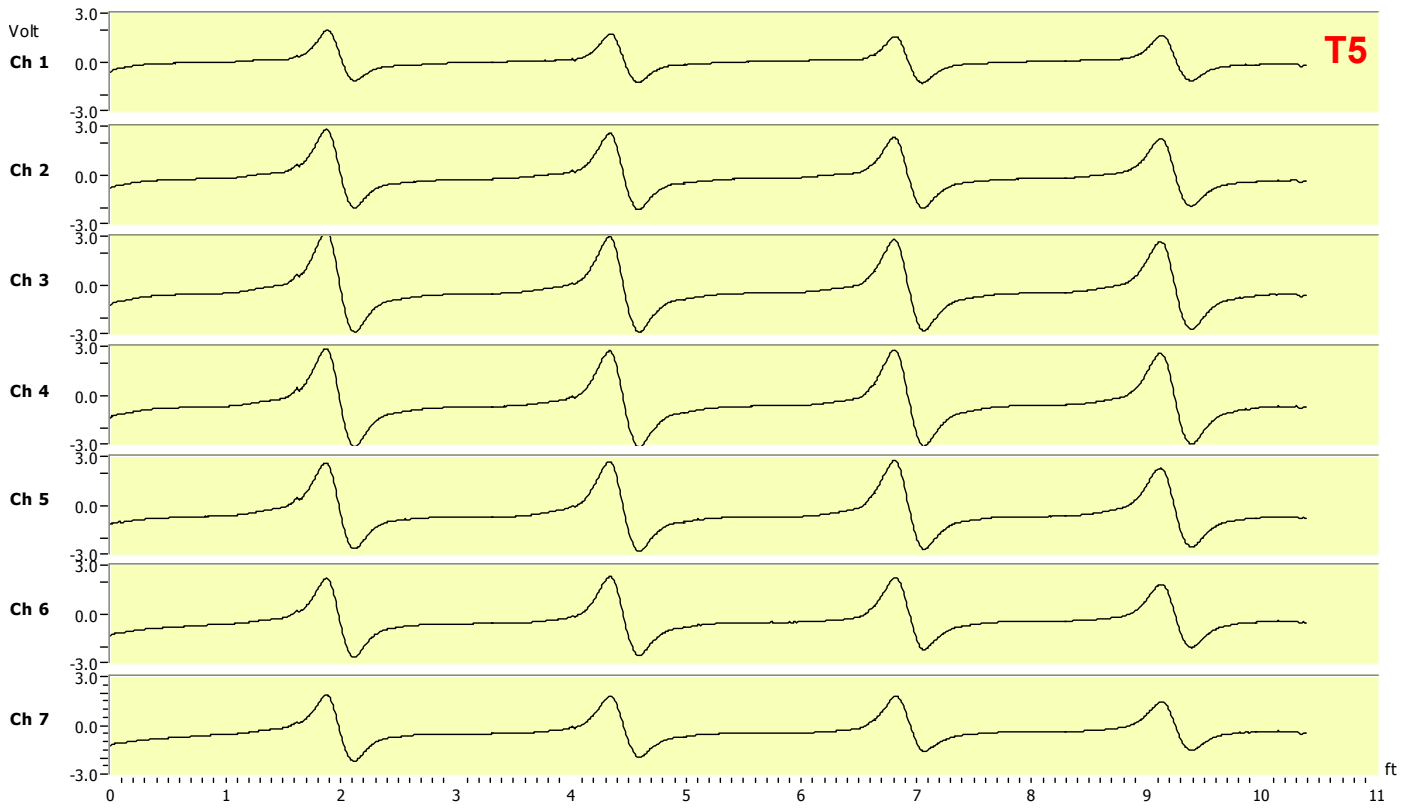


Figure 18 - MFL data for track T2 where there are no indications of steel corrosion in Beam B7

Laboratory Evaluation of Subsurface Corrosion in Box Beam Prestressing Strands using Ground Penetrating Radar



Report Submitted to

Lehigh University, Fritz Laboratory
Department of Civil and Environmental Engineering
13 East Packer Avenue
Bethlehem, PA 18015

by

Infrasense, Inc
14 Kensington Road
Arlington, MA 02476

September 10, 2009

Executive Summary

GPR data was collected on six box girder sections removed from decommissioned beams from 3 bridges and staged in the ATLSS Engineering Research Center test facility at Lehigh University. The data was collected using a 2.6 GHz antenna, and the collection included a series of transverse and longitudinal scans on the bottom flange of each box section. The GPR data clearly revealed the internal geometry of the prestressed concrete flange, including location, number and depth of prestressing strands and reinforcing steel, and the thickness of the flange. A detailed reflection amplitude analysis was carried out on the transverse scan data to reveal areas of corrosion. The result of this analysis was a contour plot for each girder section showing possible areas of corrosion. The methodology implemented in this laboratory could be enhanced under actual field conditions, and the equipment can be readily adapted to field use

1. Objective

The objective of this work is to identify and develop inspection methods and techniques to detect and quantify non-visible corrosion of prestressing strands in adjacent box beam bridges. The research is motivated by recent catastrophic failures of prestressed precast box beam bridges that have occurred in a number of states in the north east region of the United States.

The work seeks to identify nondestructive inspection methods, techniques and equipment to detect and evaluate corrosion that is otherwise undetectable by visible inspection methods. The work has involved testing of sections of actual corroded bridge girders that have been brought to the ATLSS laboratory for testing. Lehigh University has solicited outside experts in NDE methods to participate in this study, and Infrasense has responded with the test program and results described in this report.

2. Description of Girder Sections

The girder sections were obtained from decommissioned beams from three adjacent non-composite prestressed precast concrete bridges at set up for testing at the ATLSS Research Center. A description of the beams is provided in Table 1. Detailed bridge design drawings were also provided for each bridge, showing prestressing detail for the girders. The layout of the test samples in the laboratory is shown in Figure 1. The girders were positioned so that the bottom flange was in the "up" position. Therefore, all testing could be carried out directly on the bottom surface of the box girder.

3. GPR Background and Methodology

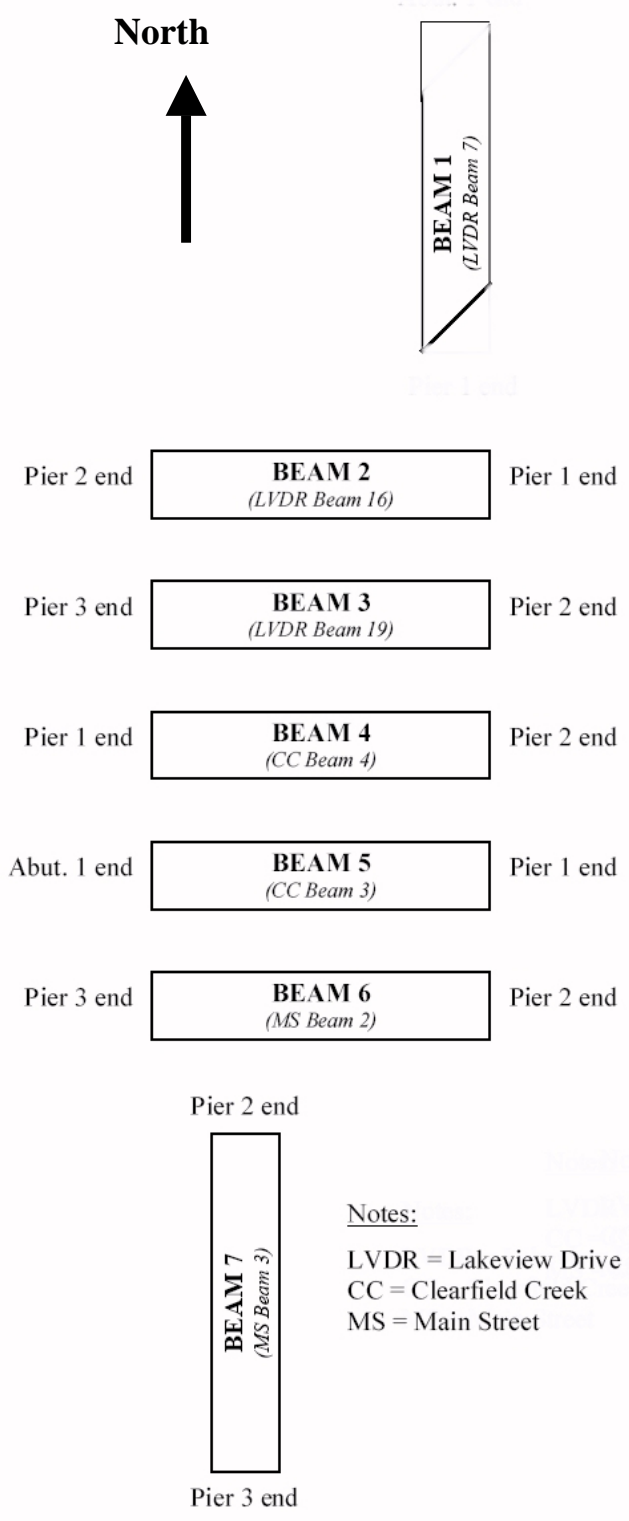
Ground penetrating radar (GPR) uses an antenna to transmit short pulses of radio waves into concrete. These pulses reflect off of dielectric discontinuities such as the reinforcing steel and the bottom of the slab. The reflections are transmitted back to the antenna, received, recorded, and stored for subsequent analysis. GPR is routinely used for locating reinforcing steel in

Table 1 – Girder Samples

Section No.	ID from Design Dwgs.			Section Length	Cross Section	Condition Description
	Bridge	Orig. Beam #	Span			
1	Lakeview	7	1	15ft	48x27 Box	Heavily damaged section with spalls and cracks. The section was full of water. Examine potential for delamination
2	Lakeview	16	2	12ft	48x42 Box	No cracking or corrosion visible on section however other areas of beam have significant corrosion.
3	Lakeview	19	3	12ft	48x42 Box	Longitudinal crack with heavier corrosion. Hairline and larger distributed cracks Use for visual assessment
4	Clearfield	4	2	15ft	42x36 Box	Large longitudinal crack with spalling visible.
5	Clearfield	3	1	15ft	42x36 Box	Longitudinal cracking with rust staining.
6	Main St	2	3	15ft	48x42 Box	Heavy corrosion on bottom flange without longitudinal cracking. Large patches. Determine if corrosion adjacent to patch exists using NDE methods.
7	Main St	3	3	15ft	48x42 Box	Longitudinal crack with heavy splitting. Examine damage formation and NDE study.

concrete. The reinforcing shows up very clearly in the GPR scan. The rebar grid can be mapped in 2- and 3- dimensions by a field technician using standard software. GPR is also used to detect deterioration and delamination in reinforced concrete bridge decks. In this application, the amplitude of the reflection from the rebar is analyzed, and areas with higher attenuation (weaker reflections) are identified as delaminated and possibly corroded. The principle is that the moisture, chloride, and cracking that accompany the corrosion/delamination process attenuate the GPR signal. This is a more complex application than rebar locating.

The principle used to investigate corrosion in this study is that (a) corroded prestressing will produce a decreased GPR reflection; and (b) the concrete condition producing the corruptions (moisture, chloride) will also attenuate the GPR reflection. Unfortunately, in the laboratory environment, factor (b) will be absent, since the girders are dried out there will be no moisture related effects detected with GPR.



a) Schematic



b) Overhead Photo

Notes:
 LVDR = Lakeview Drive
 CC = Clearfield Creek
 MS = Main Street

Figure 1 – Layout of Beams for Testing

In a prestressed box girder, the prestressing strands are smaller in diameter, and more closely spaced, than the bars in reinforced concrete. Therefore, in order to clearly distinguish the reflections from the prestressing strands, a high frequency 2.6 GHz GPR antenna was used for data collection in this study. This is the highest antenna frequency available in commercial GPR antennas. The short wavelength associated with this high frequency maximizes the resolution of the prestressing.

The 2.6 GHz antenna was operated with a SIR-20 control and data acquisition system, both systems are manufactured by Geophysical Survey Systems, Inc. of Salem, NH. The antenna is supported by a small carrier with four rolling wheels, allowing the antenna to maintain close proximity to the tested surface without dragging. One of the four wheels has a rotary encoder allowing the GPR data collection to trigger on distance. Figure 2 shows the antenna and carrier, and Figure 3 shows the complete instrumentation arrangement with the SIR-20.



Figure 2 –2.6 GHz GPR Antenna and Carrier

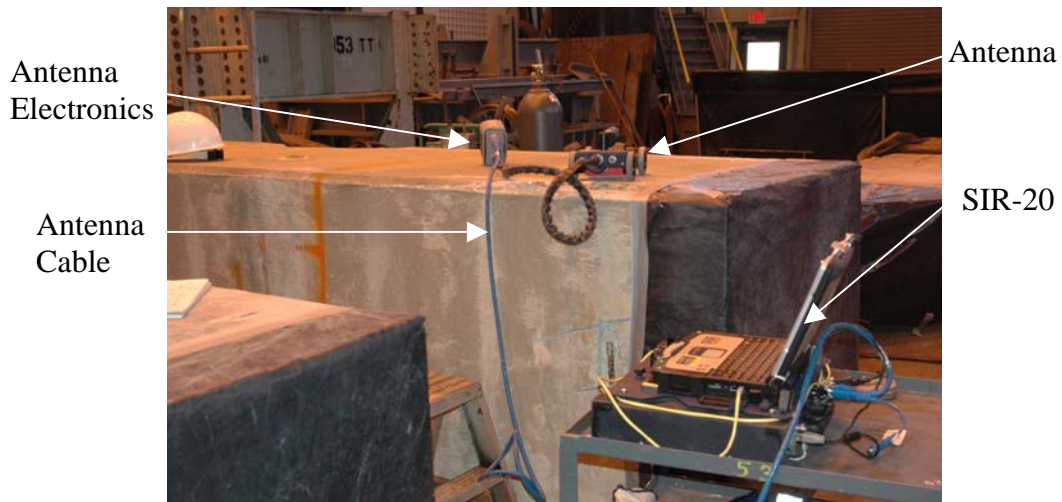


Figure 3 – Complete GPR Instrumentation Arrangement

4. Data Collection

GPR data collection took place on December 29, 2009, and covered six of the seven girders. Girder #6 was extensively spalled with areas of exposed steel, a condition that was not suitable for GPR scanning. Data collection for each of the six tested girders was carried out in two directions (a) as a series of parallel scans transverse to the long axis of the girder spaced at one-foot offsets, starting at one foot from the edge of the girder, and (b) as a series of scans parallel to the long axis of the girder, spaced at 9" or 12", depending on the girder width. Figure 4 shows the survey pattern. The offset from the edge of the girder was required to avoid the plastic covering that had been placed on the ends of the girders.

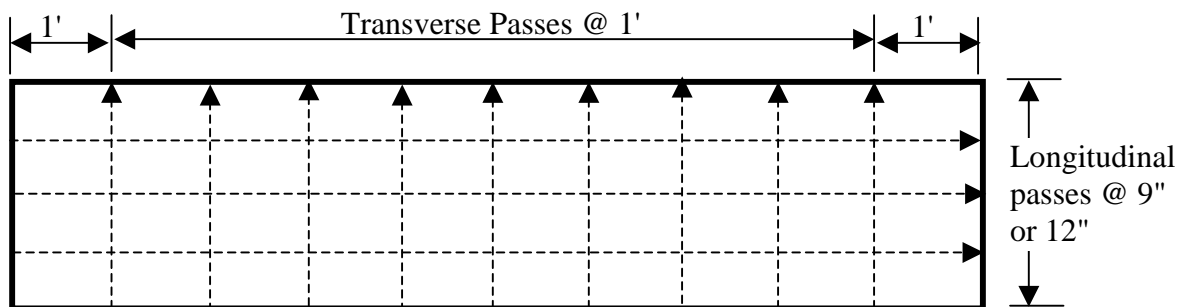


Figure 4 – Layout and Direction of GPR Scans

Figure 5 shows the data being collected in the transverse direction. With the antenna orientation shown, the polarization of the antenna is transverse to the direction of the scan, and thus is optimized to detect the tendons. Using this setup for the longitudinal passes results in an antenna orientation that perpendicular to the tendons, and thus the tendons are unlikely to be detected. As an alternative, a separate set of longitudinal scans were collected with the antenna repositioned to be parallel to the direction of the tendons.

Initial testing was carried out to establish the GPR data collection parameters. Based on this initial testing, the following parameters were established for the remainder of the study:

- Scans per foot = 144
- Total time range = 4.0 nanoseconds
- Feet per mark = 0.5



Figure 5 –Transverse Scanning.

(antenna polarization is perpendicular to direction of scan, parallel to strands)

All of the transverse scans for a given girder were collected as a single data file, with marks placed at the end of each scan to denote the end of that scan and the beginning of the next. Later in the analysis these scans would be sorted and separated as needed. The longitudinal scans were each collected as a single file. Each transverse pass began with the center of the antenna approximately 4 inches from the edge of the girder, so that the antenna would be in full contact with the concrete. Thus, the length of each transverse pass was approximately 8 inches less than the width of the girder.

Figure 6 shows a sample of the transverse raw GPR data collected on girder #4. Note that the reflection from each tendon alone would appear as a hyperbolic pattern, so the group of tendons appears as a cluster of hyperbolas, with the apex of each hyperbola representing the location of the individual tendon. The Figure shows clusters of strands, each cluster appearing to have 5 strands. Figure 7 shows the layout of the strands as they appear in the design details. The design data shows a similar pattern.

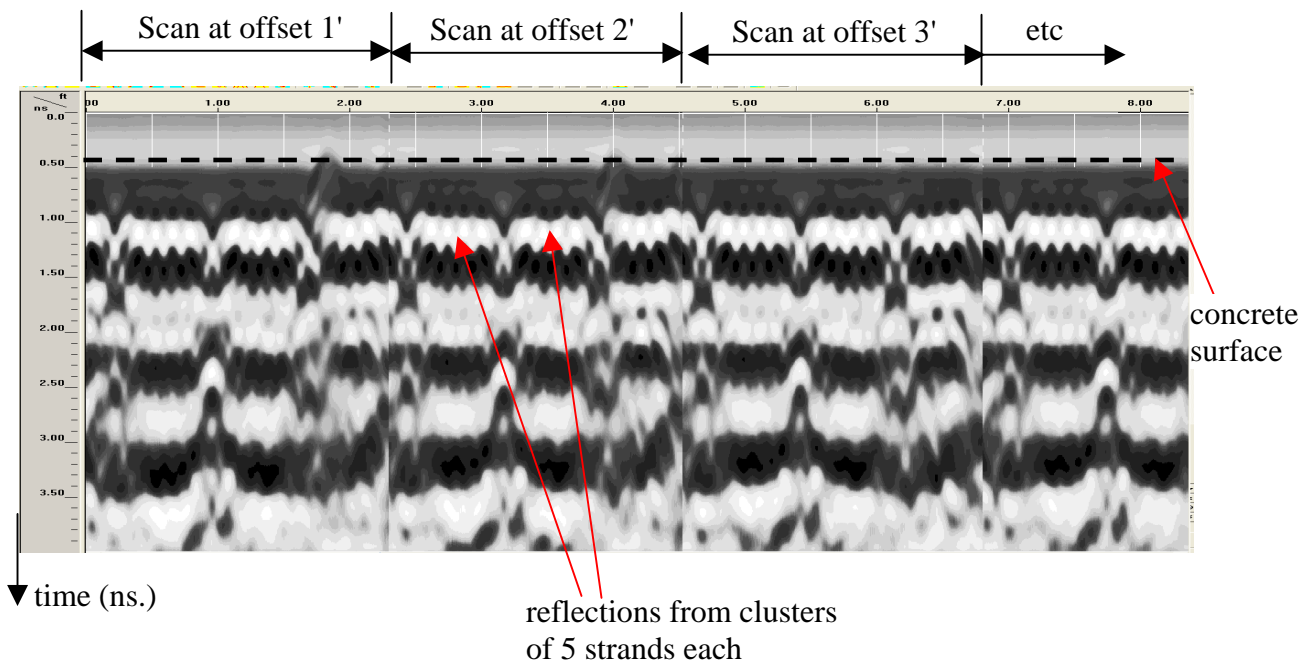


Figure 6 – Sample GPR Data from Transverse Scan, Girder #4

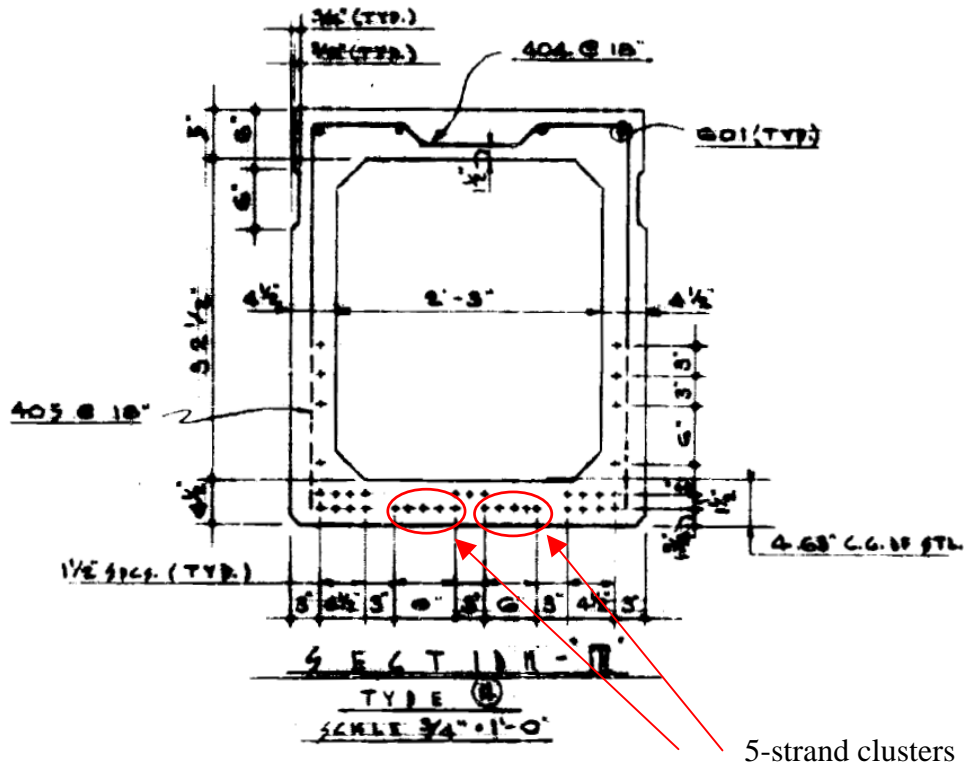


Figure 7 – Girder #4 Bridge Plan Detail showing Prestressing Strands

Figure 8 shows a sample of the longitudinal raw GPR data collected along the centerline of girder #2. The strands do not appear as they did in the transverse scans because the antenna is polarized perpendicular to the strands, and the direction of the scan is parallel to the strands. With the absence of the numerous reflections from the strands, the data now reveals the interior surface of the bottom flange of the box beam. The time scale has been converted to depth using an estimated concrete dielectric constant, yielding a flange thickness of 4.5 inches coinciding with that specified in the bridge plans. Also appearing is transverse reinforcing spaced at approximately 2.5 feet (vs. 24 inches specified in the bridge plans). Note the local disappearance of the interior surface reflection at 3 feet into the scan. This is most likely due to the presence of a diaphragm in the box.

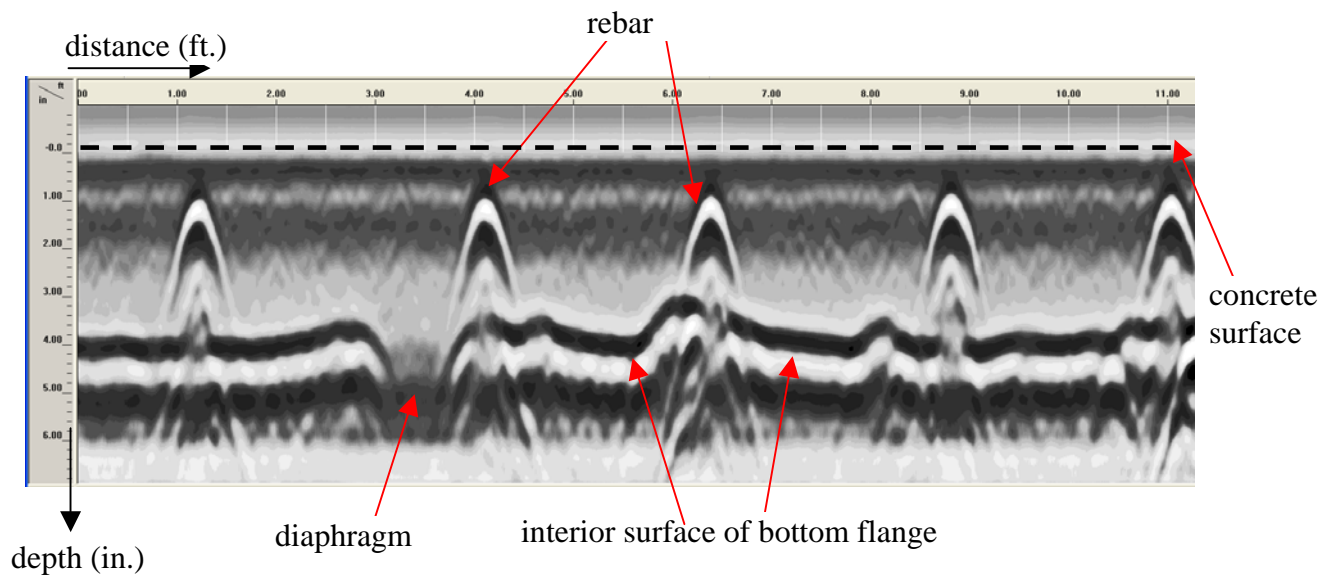


Figure 8 – Longitudinal Scan, Centerline of Girder #2

5. Data Analysis

The discussion above shows how the raw GPR data reveals the internal geometric features of the bottom flange of the box beam, including the location and number of prestressing strands, the location and spacing of reinforcing steel, and the thickness of the flange. The detection of corrosion requires a more detailed analysis, as discussed below.

The fundamental principle applied in this work is that the reflections from corroded strands will be less than that from intact scans due to the loss of section and the presence of moisture, chloride, and corrosion products in the concrete surrounding the corroded scans. The effect of the latter is diminished in the laboratory due to the dry environment, but the loss of section should still be present and possibly detectable. This analysis principle can be observed visually in Figure 9. This figure shows a transverse scan at offset 5 feet on girder #3. The reflection amplitude is proportional to the intensity of the color in the display. Note that the reflection amplitudes in the strand group on the right side of the figure is diminished compared to the group on the left side of the figure. This reduction in amplitude could be due to corrosion.

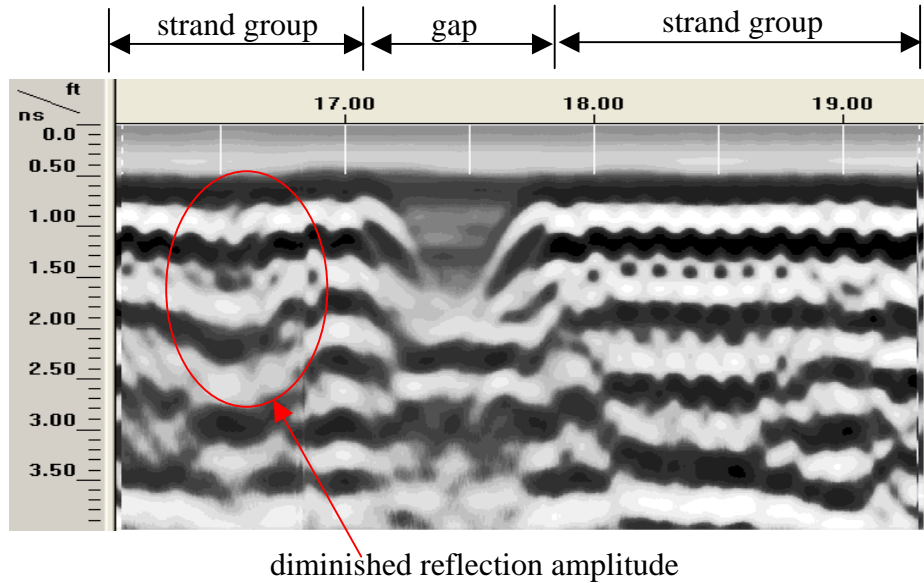


Figure 9 – Transverse Scan, Girder #3, at 5 Feet from E end, Scanning N-S

The qualitative observation described above was converted into a quantitative analysis using Infrasense's automated GPR analysis software, *winDecar*. The software was used to track the reflection amplitude from the prestressing strands as they appeared in the transverse scans. These amplitudes were then contour plotted to graphically display areas with diminished reflection amplitude. These areas are identified as areas of potential corrosion. A sample contour map is shown in Figure 10.

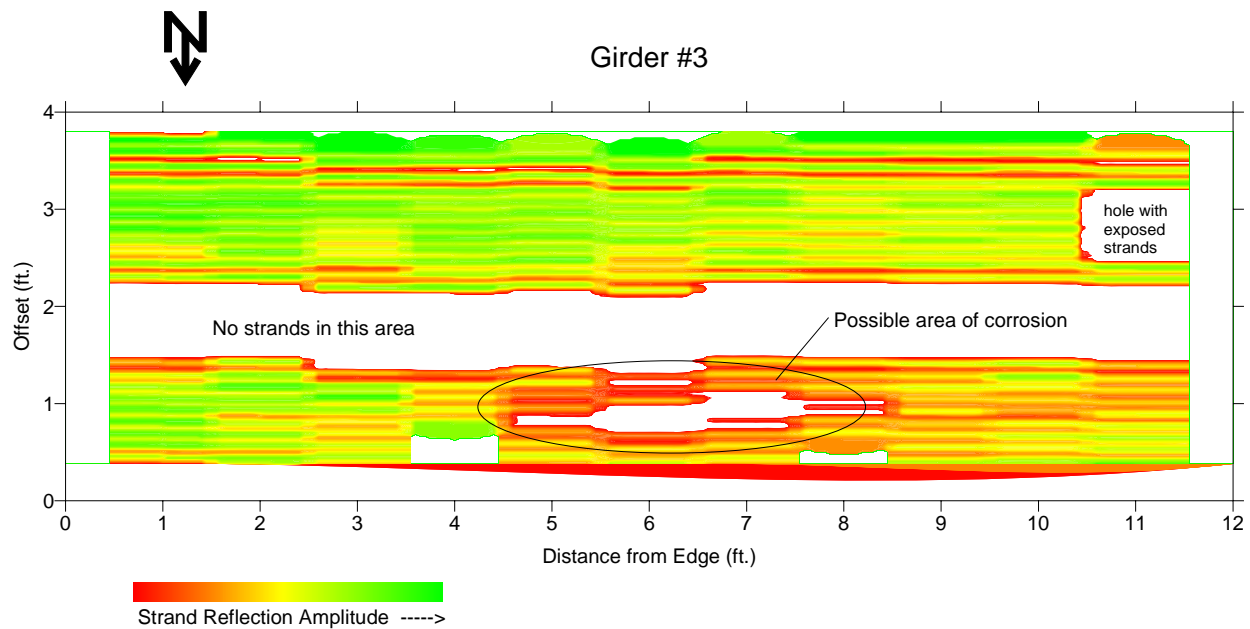


Figure 10 – Sample Contour Plot of Strand Reflection Amplitude, Girder #3

In order to generate the contour plot of Figure 10, a color scale was established ranging from red for low amplitude reflections to green for high amplitude reflections. Below a certain threshold, the color was set to white. This was done to distinguish the areas where there are no strands from the areas where the strands exist. The horizontal striations in the contour map represent the alignment of the individual strands. These are not perfectly horizontal, due to slight discrepancies in the start location of each transverse scan.

Attachment A to this report includes the contour plots for girders 2, 3, 4, 5, and 7. Data was collected on slab #1, but the available surface area for analysis was limited due to the geometry and the extensive damage along the edges.

Discussion of Results

The contoured data for girders 2 and 3 show a similar prestressing pattern, which is expected since both girders come from the same bridge. In each case, there is an area that shows diminished reflection amplitude. In girder 2, this area surrounds an existing spall, and is very likely showing the expansion of the corrosion that created the spall. In girder 3, the area identified in the contour map does not coincide with any surface distress.

The contoured data for girder 4 also shows a regular prestressing pattern, but one that is different than girders 2 and 3. This is to be expected, since girder 4 comes from a different bridge. There are no large areas of diminished reflection amplitude, but there appear to be individual strands that show low amplitude, and these individual strands may be corroded. While girder 4 is from the center span of the Clearfield bridge, girder 5 is from the end span, and shows an entirely different, and somewhat irregular pattern of prestressing. Figure 11 shows the raw GPR data for these two girders, and the difference is readily apparent. Reference to the design drawings does not explain the irregular pattern observed in girder 5. The irregular pattern makes it difficult to identify possible areas of corrosion with this type of contour plot.

The contour plot for girder #7 shows three strand groups plus individual strands at offsets 0.75 and 3.8 feet. The map shows that the amplitude analysis is easier to interpret when there is a group of strands. Nevertheless, two areas with diminished reflection amplitude appear in the map, and these are identified.

Field Implementation of the GPR Method

The method employed in the lab can be implemented in the field using a snooper or platform truck. The GPR antenna can be deployed using a mounting arrangement shown in Figure 12, so the operator does not have to be directly in contact with the bottom of the girder. Since the box girders are adjacent to one another, the transverse data collection can be carried out on multiple girders covering the full width of the bridge, and the edge effects encountered in the lab would be minimized. Also, the environmental conditions, including moisture inside the box girder, would add to the attenuation in the concrete in corroded areas, and would thus would make these areas more likely to be detected.

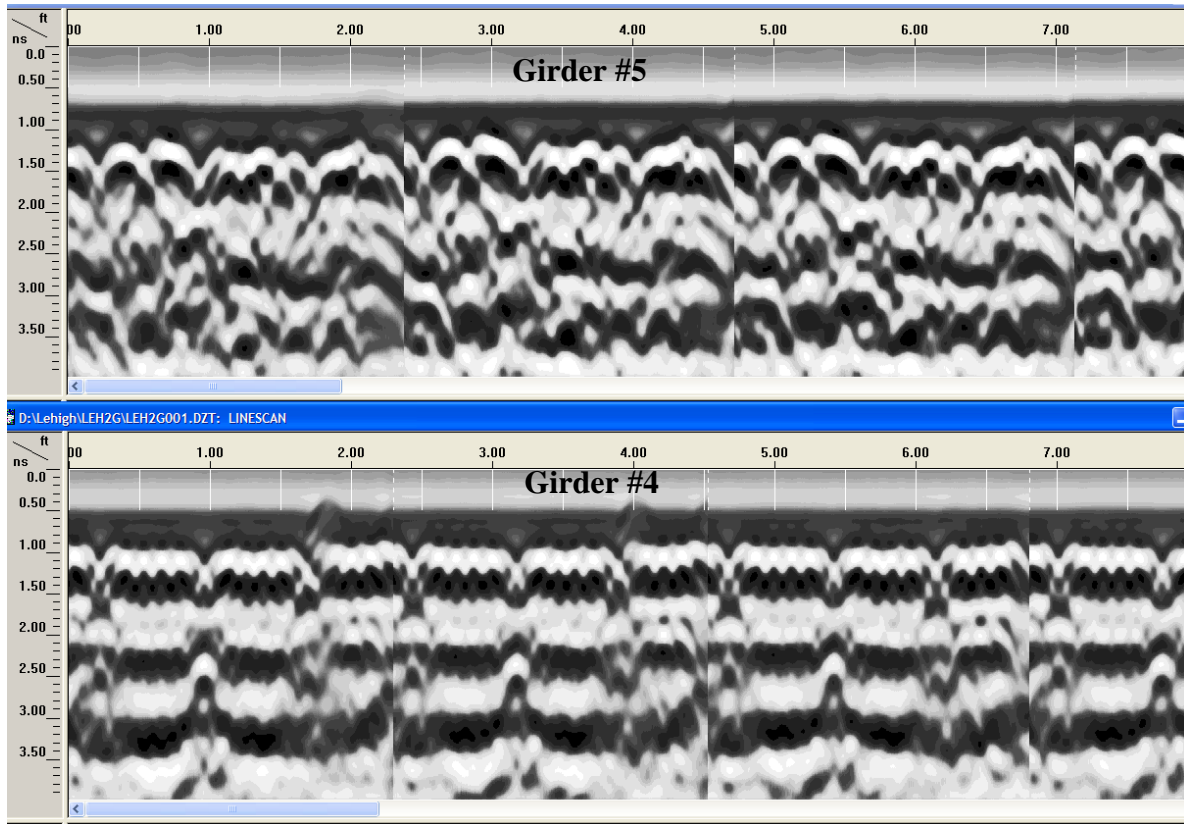


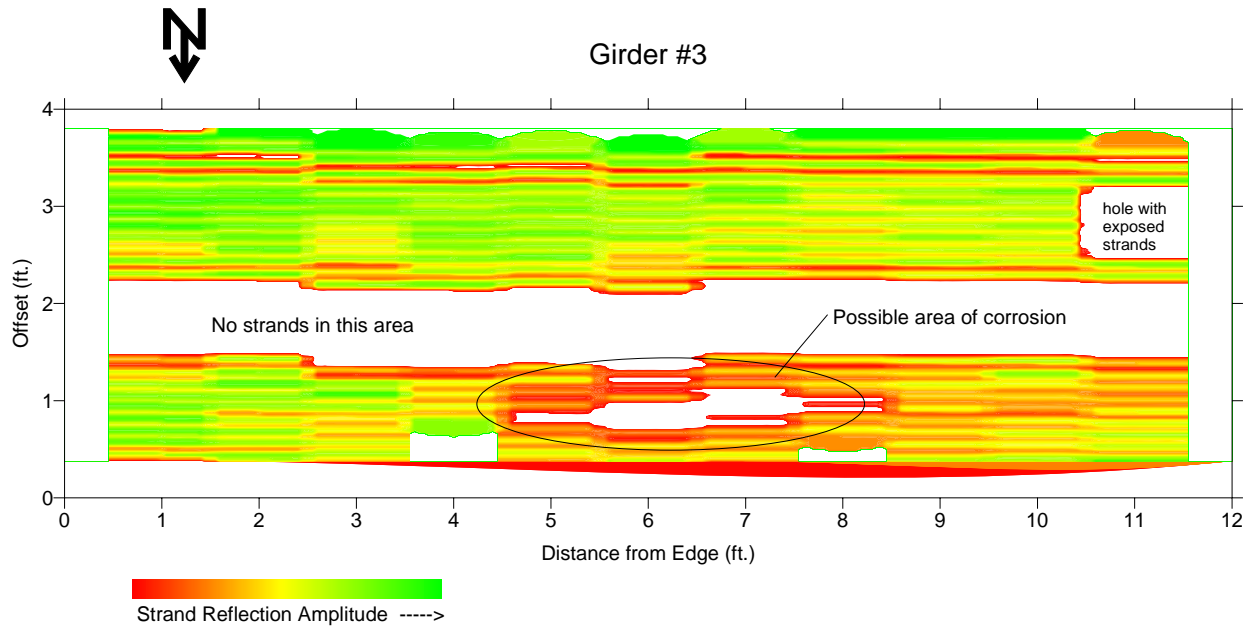
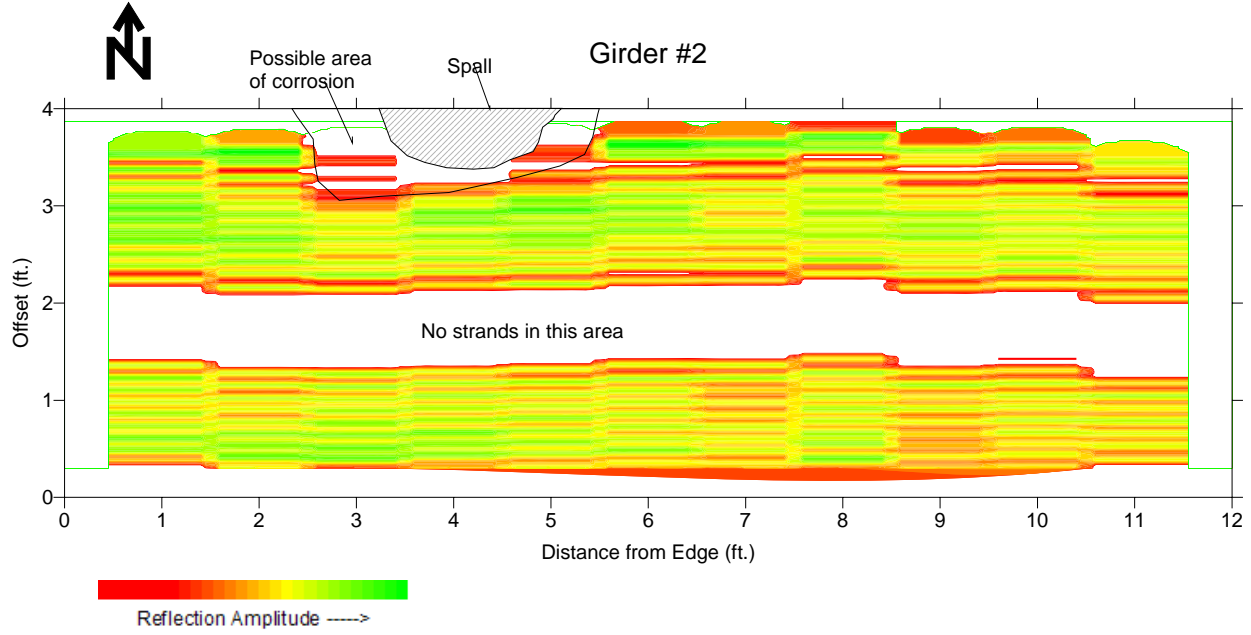
Figure 11 – GPR Data Showing Prestressing Patterns of Girders #5 and #4

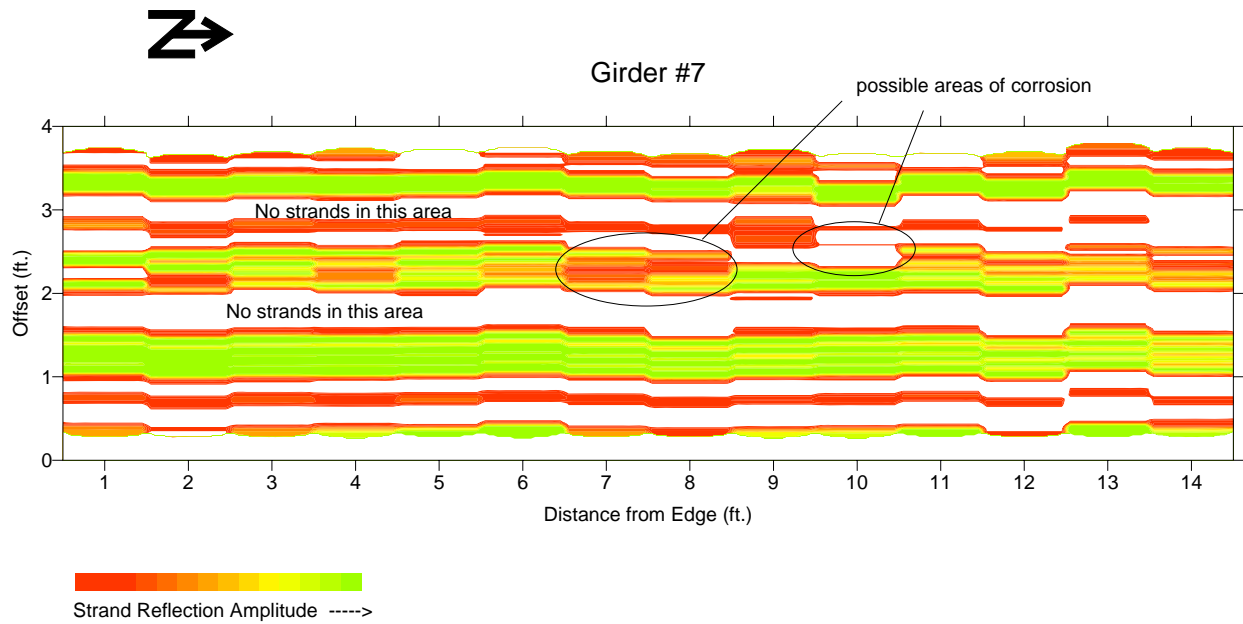
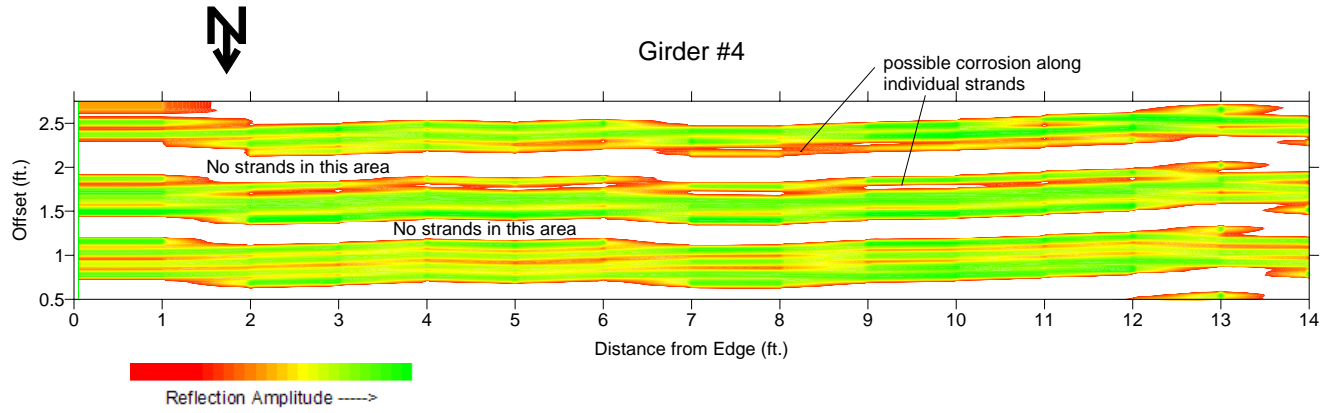


Figure 12 – GPR Antenna Deployment under a Structure

Attachment A

Strand Reflection Amplitude Contour Plots





The Remanent Magnetization Method (RM-Method) Applied for the
Localization of Fractures in Pretensioned Strands in Box Girders of 3
Bridges at Lehigh University, Bethlehem, PA

Univ.-Prof. Dr.-Ing. Bernd Hillemeier

Dipl.-Ing. Andrei Walther

Technische Universität Berlin

Institute for Civil Engineering

Department of building materials and building material examination

In association with Vector Corrosion Technologies Ltd

Vector Corrosion Technologies commissioned the University of Berlin with the investigation of six prestressed box girders from three different bridges in the Pennsylvania area. The girders were taken during the dismantling of the bridges and brought to Lehigh University in Bethlehem, Pennsylvania for investigation. In the frame of a research program, several methods were to be tested for their suitability to locate breaks in prestressing tendons reinforcing the girders. Vector was asked to participate because of its expertise in this area none the least due to its activities in 2008 in Canada, when TU Berlin together with Vector inspected a parking garage in Toronto, Canada and part of the Champlain Bridge Montreal, Canada with the same objective.

Vector therefore asked TU Berlin again to cooperate in the above mentioned study. Vector used ground penetrating radar to locate the transverse reinforcement (stirrups) It might be stated that at the present time there is no better suited and faster procedure to detect breaks in tendons than the magnetic flux density method.

The measurements took place at Lehigh University on Tuesday, the 17th of March 2009. The measurements on all six girders were completed in one day. The method and the measurements are presented below.

1. The Phenomenon and the Causes of Steel Fractures

There are various reasons for fractures in prestressing steel tendons; some of them have led to structural collapses. All types of prestressing steel are at risk of breaking if they come in contact with corrosive media. In bonded prestressed structures this happens if the top surface of bridge or parking deck is not adequately waterproofed and chlorides reach and depassivate the prestressing steel wires. In unbonded prestressing, or poorly grouted bonded prestressing, only water is needed to cause corrosion [1]. Sometimes grouting mortars have high chloride content. In the past, chlorides were admixed to prevent the fresh grouting mortar from freezing. In this case, penetration of moisture may greatly accelerate the corrosion process.

A further reason for fractures may be that corrosion had already started prior to grouting work, during shipping and storage of the steel. Exposure to water between placement in the ducts and grouting work is likely the main reason for the fractures of the prestressing steel wires [2]. Many heat-treated prestressing steels are so sensitive to stress-induced corrosion that steel fractures have been found even if the wires had been embedded in alkaline mortar in high quality grouted ducts [3].

In almost every case there are no visible signs of failed wires at the concrete surface. The failure of prestressed concrete members often happens abruptly.

Shown below are sections of box girders tested at Lehigh. The pictures show the condition of the girders, as they were positioned in Lehigh's ATLSS Research Center.



Figure 1: Box Girder Main Street Bridge (MS)



Figure 2: Box Girder Lakeview Drive Bridge (LV)



Figure 3: Box Girder Clearfield Creek Bridge (CC)

Figure 4 shows a highly deteriorated concrete surface where the concrete above the corrosion of the reinforcement has already spalled of. In Figure 5 the magnetic signal is shown. It becomes obvious to the viewer, how breaks in the strands present themselves as an inflection point of the magnetic signal along the X-axis. In this ideal case a photo of the real specimen (Figure 4) and a graph of the corresponding magnetic flux density (Figure 5) measurement are displayed alongside each other.



Figure 4: Corroded section of a box girder (MS2, line 1) with destruction of the tension wires over a length of 20cm.

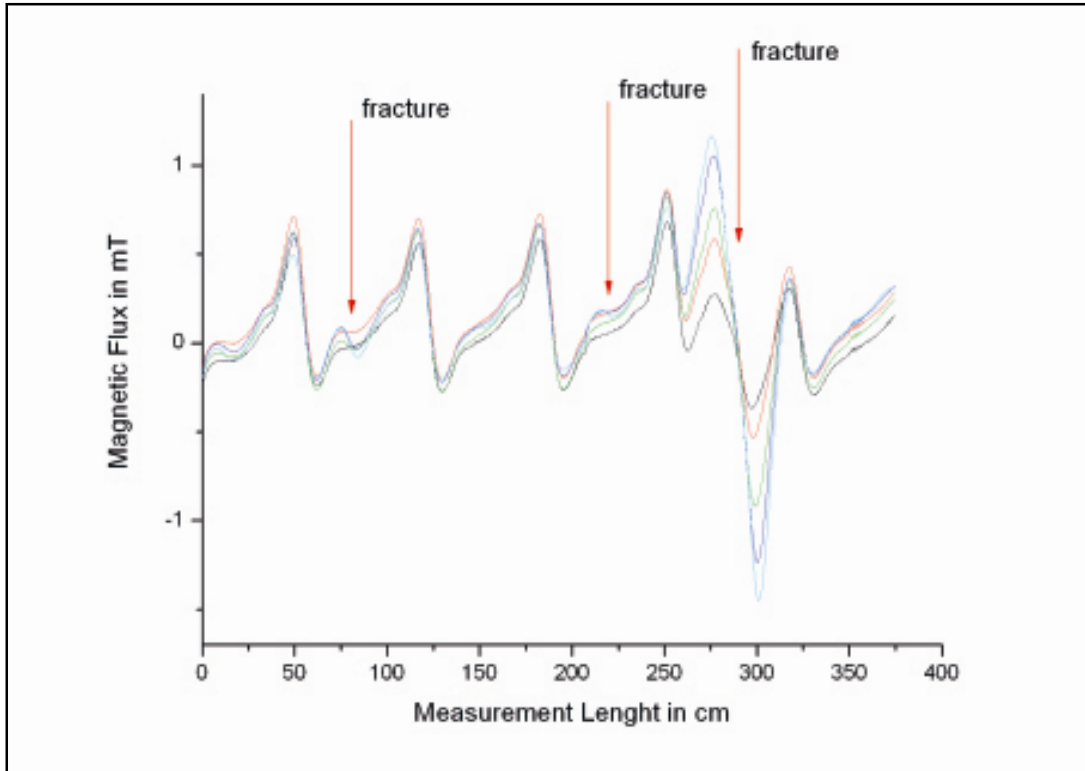


Figure 5: Measurement of the total length of the tension wires of the box with a strong fracture signal at 270cm. This signal is from the fracture, as shown in Figure 4.

With this demonstration of the performance of the method, it is now possible to evaluate the condition of the tendons under those concrete surfaces where no specific indications for breaks in the tension wires can be seen by visual inspection.

2. The Method

The Remanent Magnetism Method (RM-method) allows the identification of potentially unsafe conditions in pretensioned and post tensioned concrete structures by locating fractures in the prestressing steel. This non-destructive method identifies fractures in single wires, even when they are bundled with intact wires. The magnetic field of tendons is measured at the concrete surface, once they have been pre-magnetized with an electromagnet. Fractures produce characteristic magnetic leakage fields, which can be measured with appropriate sensors at the concrete surface.

The parameters associated with fractured wires have been quantitatively identified in the laboratory and have been confirmed in the field. The knowledge of these parameters allows us to draw conclusions about the reduction of the cross-sectional area or the number of fractured wires in a tendon.

The location of prestressing wire breaks with an extraordinarily dense arrangement of reinforcement requires a more powerful electromagnet, specifically adapted to the high

degree of reinforcement in order to magnetize the tendon behind a dense mild reinforcement. After a multi-level processing of measuring data, which represent certain magnetic states of the entire concrete unit, clear fracture signals result at the locations of built-in breaks.

When testing the tendons from the upper surface, like in bridge decks or parking decks, the measuring speed of the RM-Method can be significantly enhanced by replacing the time-consuming multi-step-magnetization by a single-step-magnetization. Large yoke-shaped magnets have been constructed to magnetize transverse tendons over lengths of up to 3.5 m in a single process. Measuring the magnetic flux density of an entire bridge deck simplifies the comparison of data from measurements at different times, which would be helpful for monitoring the long time behavior of the structure.

3. The Detection of Fractures of Prestressing Steel

3.1 The Different Detection Methods

Until now three possibilities have been available to detect fractures of prestressing steel wires. These are:

- Visual inspection after opening the concrete
- Application of the X-ray-method
- Application of the Remanent-Magnetism-Method
- Application of Magnetic Measurement in the Active Field (Magnetic Flux Method)
- Another method detects the breaking of a steel wire as it occurs by detecting its short characteristic acoustic emission. The system is called the SoundPrint acoustic monitoring system.

3.2 Visual Inspection

The main disadvantage of the visual inspection in a short opening in the concrete is its local nature. Only in unbonded tendons, the local opening may give information about the condition of the entire tendon by applying the so-called screw-driver-test: testing the state of a tendon by trying to wedge a flat-head screw driver between its wires [4]. If the steel wires of a tendon are arranged in a bundle, a further disadvantage lies in the fact that after the sheathing has been cut, only a part of the surface of the wires in the outer layer, perhaps three or four wires of a strand containing 16 up to 48 wires, can be inspected visually.

After this destructive examination the hole needs to be repaired. The repair could become the starting point for a corrosive attack.

3.3 The X-Ray-Method

The X-ray-method requires a detectable wire separation to be able to locate fractures in prestressing steel. The fracture is not detectable with the X-ray-method if it is covered by other steel wires. As concrete is a shielding material against x-rays, the method needs high x-ray-energy, long exposure time and focusing on small areas [5].

3.4 The Remanent-Magnetism-Method (RM-Method)

The magnetic method solves the above mentioned difficulties. Tendons can typically be tested along their full length. The characteristic magnetic flux leakage field can be detected even if the fractured wire is screened by other wires or by the metal sheathing. The magnetic leakage field occurs even if the fracture width is negligible.

Important results of laboratory and field work are presented in this paper. More details are reported in [6] and [7].

3.5 Magnetic Measurement in the Active Field

A particular advantage of the magnetic measuring method is demonstrated in the measurement in the continuous field. If this information is available, the information that is not related to wire breaks can be filtered out using a special magnetizing method. This method is similar to the so-called MFL (Magnetic Flux Leakage). When measuring in the active field, the signals, for example of the stirrups, show very clearly. An example for this is shown in figure 6.

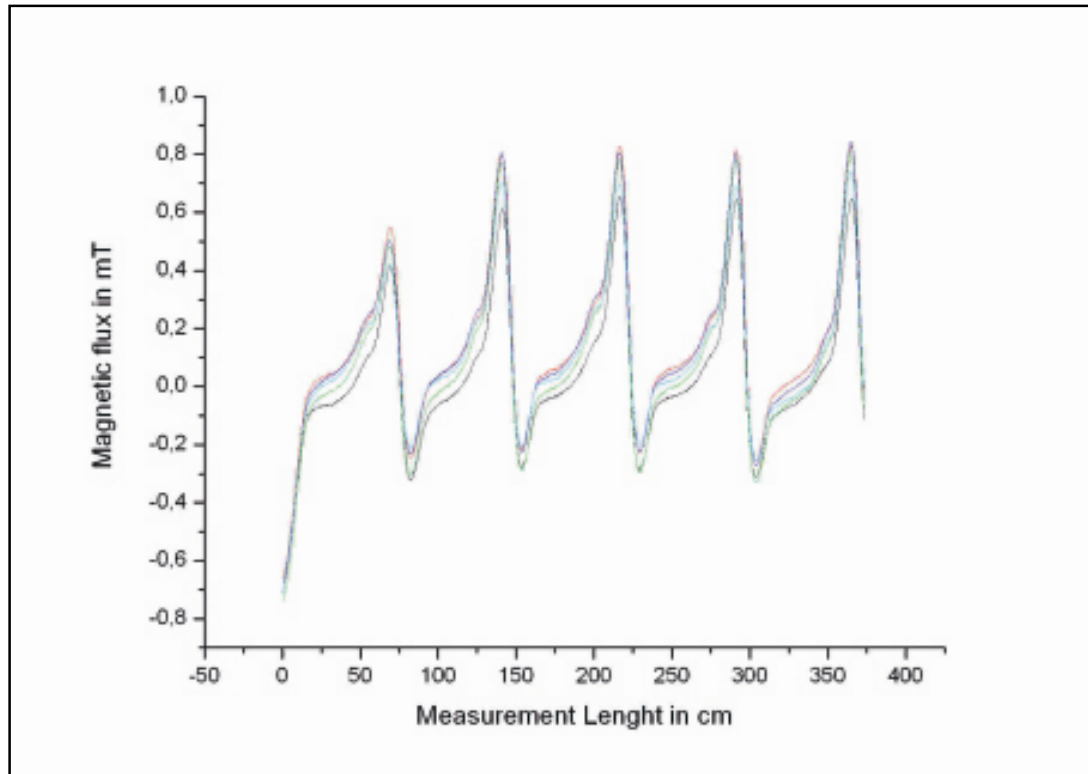


Figure 6: Measured signal along the course of the tension wire of box girder MS 3 with typical signals from stirrups

3.6 Sound Print – Acoustic monitoring system

The failure of a prestressing steel wire is characterized by the sudden release of energy at the moment of fracture. This energy is dissipated through the structure in the form of sound waves, which can be detected by acoustic sensors. The different arrival times of the sound waves at several sensors allow the calculation of the location of the fracture. The system requires a permanent data acquisition with a sufficiently high sampling rate. The technology does not provide any information on failures that occurred before its implementation [4].

4 The Physical Principle of the RM-Method

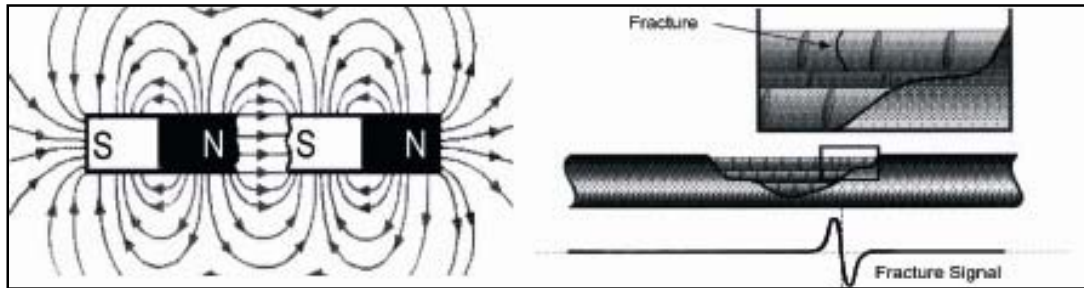


Figure 7: A magnetized prestressing steel wire has a magnetic field comparable with the field of a bar magnet (above). The transverse component of the leakage field is shown on the right, named “Fracture Signal”. From this, conclusions regarding fractures of single prestressing steel wires inside the duct may be drawn.

The magnetic field resulting from a magnetized tendon or a magnetized steel wire is comparable to the magnetic field of a bar magnet. In the vicinity of a fracture, a magnetic dipole-distribution is formed and, accordingly, a magnetic leakage field in the surrounding region. The transverse component of the magnetic flux density, measured at the concrete surface, is shown in fig. 7. The characteristic leakage field allows for the detection of the fracture of a single prestressing steel wire.

4.1 Applications

4.1.1 Standard Applications on Full Size Structures

The examples in nature show that it is possible to perform the measurements with the RM-Method under different boundary conditions.

In practice, the limitations of the method depend mainly on the density and regularity of mild reinforcement and on the minimum degree of damage that is to be detected. It does not depend on the type of magnetic sensors. The applied magnetization technique allows remanent magnetization of the tendons up to a concrete cover of 30 cm. In the case of a tendon that consists of only one steel wire with sufficiently large cross-section and if the distances between the installed mild reinforcement bars do not vary too much, a wire fracture can also be detected up to a concrete cover of 30 cm. In the case where a tendon consists of 40 single wires with a small cross-section (about 20 mm²) with dense mild reinforcement, the detectability of single steel fractures (one fracture in a cross-section) might be restricted to a concrete cover of 10 cm or less. In cases of more than one broken wire the detectability increases with the increasing peak-peak-amplitude (fig.8).

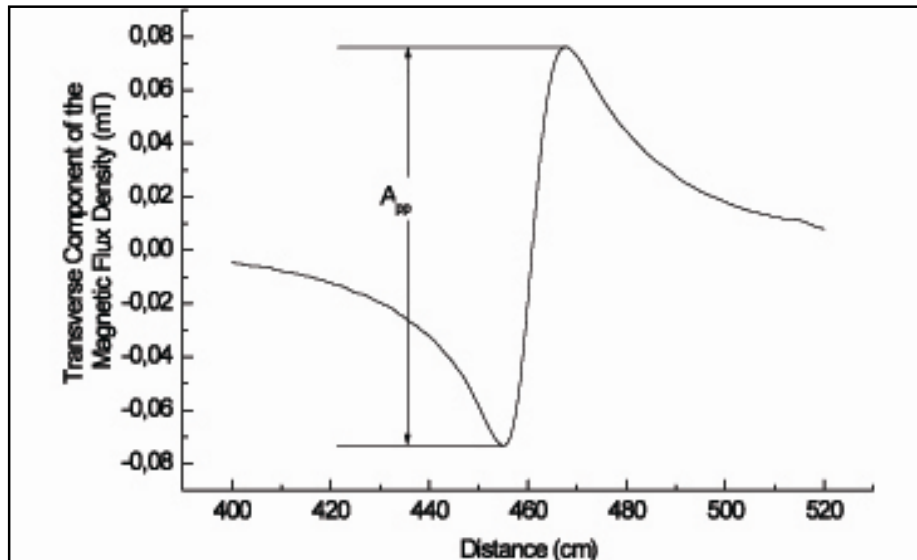


Figure 8: The peak-peak-Amplitude is important to estimate the degree of damage concerning fractures of prestressing steel wires in tendons.

The method has been applied on structures for several years. The installed measurement device is shown in Fig. 9 under a beam. This device is used to inspect tendons from the bottom surface of structural elements.



Figure 9: Measurement devices fixed under a girder for inspection.

The testing of tendons can also be performed from the vertical surface (fig. 10 left) or from the top surface (fig. 10 right). Bridge beams, factories and indoor pools, post tensioned bridge slabs, prestressed parking decks and circumferential tendons of oil tanks have been inspected.



Figure 10: *Left:* Testing of a tendon performed from the vertical surface.
Right: Testing of transverse tendons in a bridge deck from the upper surface.

The method has been independently evaluated by the German Federal Highway Research Institute (Bundesanstalt für Straßenwesen, BASt). The evaluation consisted of two parts: Application of the system on an existing structure (bridge deck of a federal highway bridge) and on a prestressed concrete test specimen in the BASt-laboratory. In both cases, the number and location of the fractures had not been disclosed to the measuring team. On the bridge deck, all known fractures were detected. In the laboratory, some fractures could not be found because of special difficulties like short tendon length (5 m) in combination with large diameter (10 cm) and large concrete cover of the tendon. Nevertheless, the RM-Method gave the best results of all tested systems [8].

In 2002 there was a successful trial on the prestressed parking decks of a shopping mall in Toronto under the initiative of Halsall Associates Limited, Canada. The parking decks concerned are prestressed with post-tensioned cables that consist of an unbounded 7-wire cold-drawn strand. All the fracture locations that were found by RM-method could be confirmed physically.

4.1.2 Location of Prestressing Steel Fractures in Highly Reinforced Prestressed Concrete Components

One of the main research topics concerning the RM-Method was its application to tendons located behind densely spaced mild reinforcement.

In the course of a research project, a test stand with tendons and a highly dense arrangement of mild reinforcement was constructed. The arrangement is similar to the arrangement of highly reinforced containments or the anchorage zone of larg post-tensioned concrete beams. In the lab test we used a tendon with 20 cold-drawn wires with a diameter of 9.6 mm each and a simulated concrete cover of 15 cm. Wires contained intentionally induced fractures at three locations (fig. 11). Between the tendon and the surface of the component dense mild reinforcement was arranged in the following way:

Orthogonal to the tendons: Steel bars of $\varnothing 28$ mm are located at a spacing of 12.5 cm. The average concrete cover is approximately 4.5 cm.

Parallel to the tendons, steel bars of $\varnothing 16$ mm are located at a spacing of 12.5 cm. The average concrete cover is approximately 3 cm.

After the construction of a larger electromagnet specifically designed to adapt to the high degree of reinforcement, magnetization of the tendon behind the dense mild reinforcement was successful. After multi-level processing of the measurement data, which represent certain magnetic states of the entire reinforced concrete unit, fracture signals can be clearly identified and the corresponding wire breaks are thereby clearly identifiable (fig. 11).

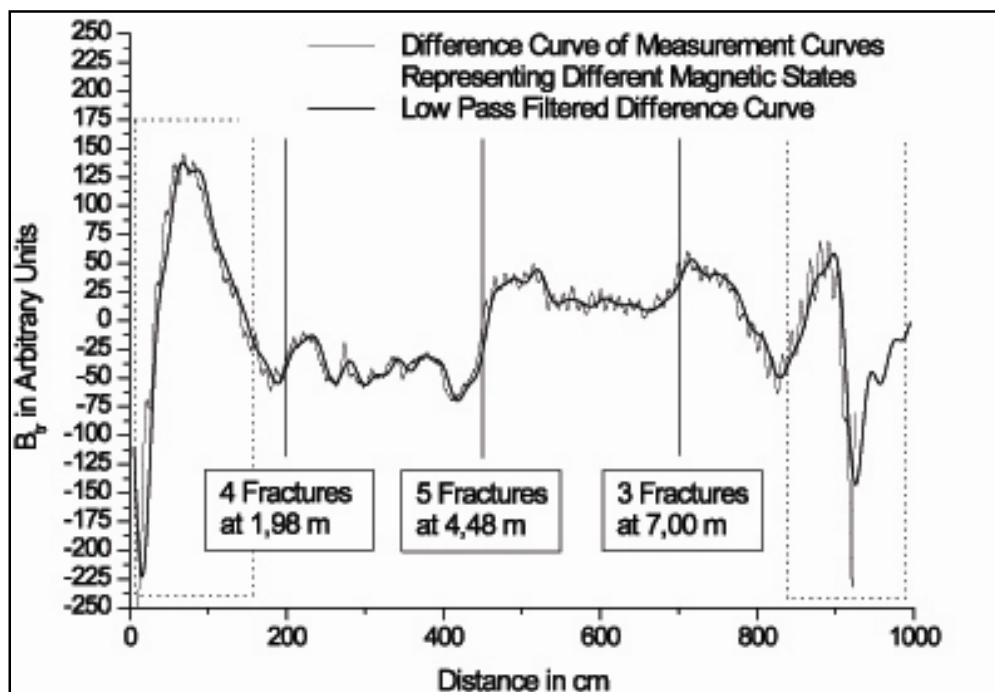


Figure 11: The shown curve is the result of the difference between two experimentally obtained curves, representing different magnetic states. The bold line is the low-pass-filtered difference-curve, in which signals of widths significantly smaller than the width of a fracture signal have been suppressed. It almost exclusively contains signals originating from inhomogeneities (particularly fractures of single wires) of the tendons. Interference content is minimal. Due to edge-effects in data processing, either end of the curve (encased with dashed lines) cannot be interpreted. Signals corresponding to fracture can clearly be identified. Degrees of damage and signal amplitude are correlated.

4.1.3 Testing of Prestressed Concrete Bridge Decks and Parking Structures Concerning Prestressing Steel Fractures

4.1.3.1 Introduction

Location of prestressing steel fractures in bridge decks and parking structures involves the following four processes:

- Magnetization of the prestressing steel
- Scanning of the magnetic flux density
- Data acquisition and processing
- Data interpretation

Each of these steps has to be optimized in order to speed-up the testing of these structures.

4.1.3.2 The Technique of Magnetization

Necessity of Magnetization

In order to assess potential fractures from the magnetic flux density measured at the concrete surface, external magnetization of the prestressing steel has to generate a magnetic state where all irreversible magnetization processes in the prestressing steel have been completed. This is necessary in order to erase the unknown magnetic history of the steel. Magnetization of the tendons is performed from the concrete surface using an electromagnet. A remanent magnetization of the tendons is achieved up to a concrete cover of 30 cm [7], when yoke-shaped electromagnets with a length of approximately 40 cm and a mass between 35 kg and 65 kg are used. The disadvantage of using these comparably small magnets is the time consuming magnetization procedure, because the magnets have to be moved several times along the tendons until the sufficient magnetization is achieved [7].

The position of the tendon has to be known along the entire magnetized length within a tolerance of about 10 cm. Consequently, it is often necessary to locate the tendons using ground penetrating radar before the magnetization may begin.

The New Single-Step-Magnetization

In cases where measurements can be performed from the top surface of the concrete component, use of larger magnets is feasible. The first idea was to construct a separable electromagnetic yoke that could reach from one end of a transverse tendon in a bridge deck to the opposite end. For German standard conditions this translates into a length of the yoke of up to 18 m. Numerical simulations have shown the possibility to magnetically saturate tendons of this length using an equally-long electromagnetic yoke. Laboratory tests showed that a magnetization length of 10 m was no problem for standard mild steel, however, prestressing steel could not be magnetized over such distances. This is due to the higher coercivity of prestressing steel compared to mild steel. Prestressing steel is not only mechanically but also magnetically harder than mild steel.

This method is applied primarily on bridge decks, multi-story parking garages and other large inspection areas. In the present case of the relatively small box girders, this method was not applied. Rather, each individual tendon was longitudinally magnetized by rolling along a small magnet along the concrete surface.

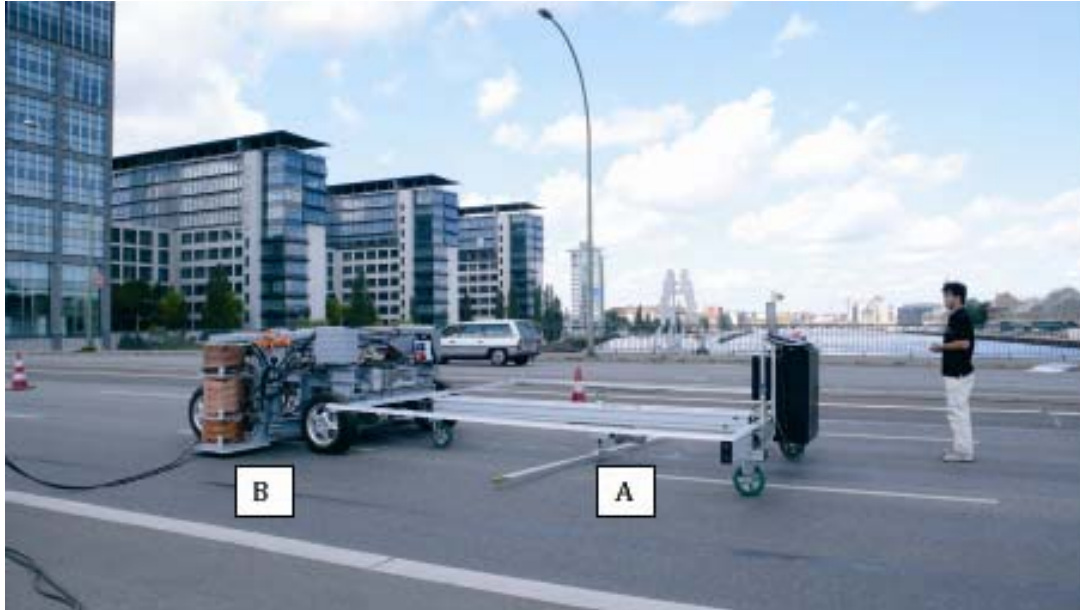


Figure 12: The Vehicle on a bridge deck with the rotation sensor (A) and the driveable magnet (B) to locate pre-stressing steel fractures in bridge decks

The magnetic flow density is scanned by an attached rotation sensor in a raster of approximately 1 cm x 1 cm. The rotating sensor heads contain sensors on the top side, as shown in Fig 12.1

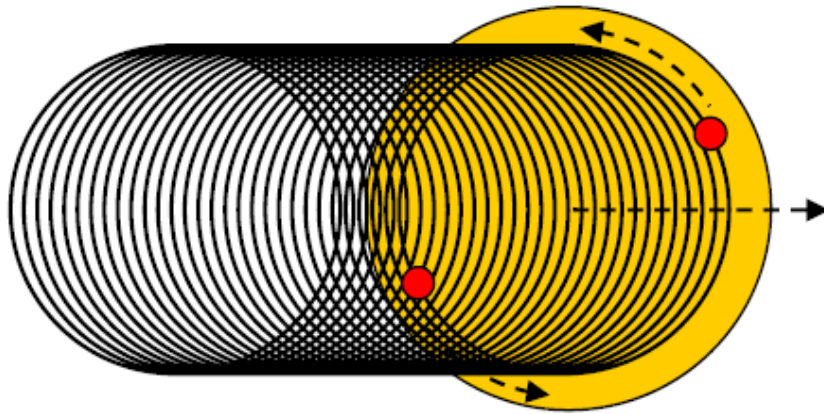


Figure 12.1: Top view of rotating sensor head (orange) with two sensor elements (red) on top; approximate representation of scanned paths (black) under linear translation across a flat surface [9].

A software solution was developed for the reconstruction of magnetic field images in Cartesian coordinates, based on the measured signals and clock pulses from wheels and rotor. This software also included a calibration algorithm.

References

Assessment of the structural safety of the Champlain Bridge in Montreal, Canada

The Champlain-bridge is one of the busiest bridges in North America. The bridge is crossed by approximately 50 million cars per year. The bridge has been examined on a part of one lane on Monday 15.09.2008 during a night session, from 9:00 pm until 4:00 am with the big magnet and the rotation-scanner into the direction south shore (SS). The girder length is 53.8 m. 7 girders run parallel. The depth of each girder is 3.0 m. The spacing between girders is approximately 3.10 m. [11]

The Spandauer Damm Bridge in Berlin, Germany

The Spandauer Damm Bridge, built in Berlin around 1960, is at present being replaced by a new one. It showed damages, which were ascribed not the least to tension wire breaks and corrosion, and made a renewal necessary. In a research project with the Federal Institute for Materials Research and Testing (BAM), the REM method was applied. The usage of the large magnet and the rotor scanner, as well as a magnetic image of a tension wire fracture are shown in figures 13 to 14.1.



Figure 13: Mobile measuring system used in the measurement campaign at the Spandauer Damm Bridge

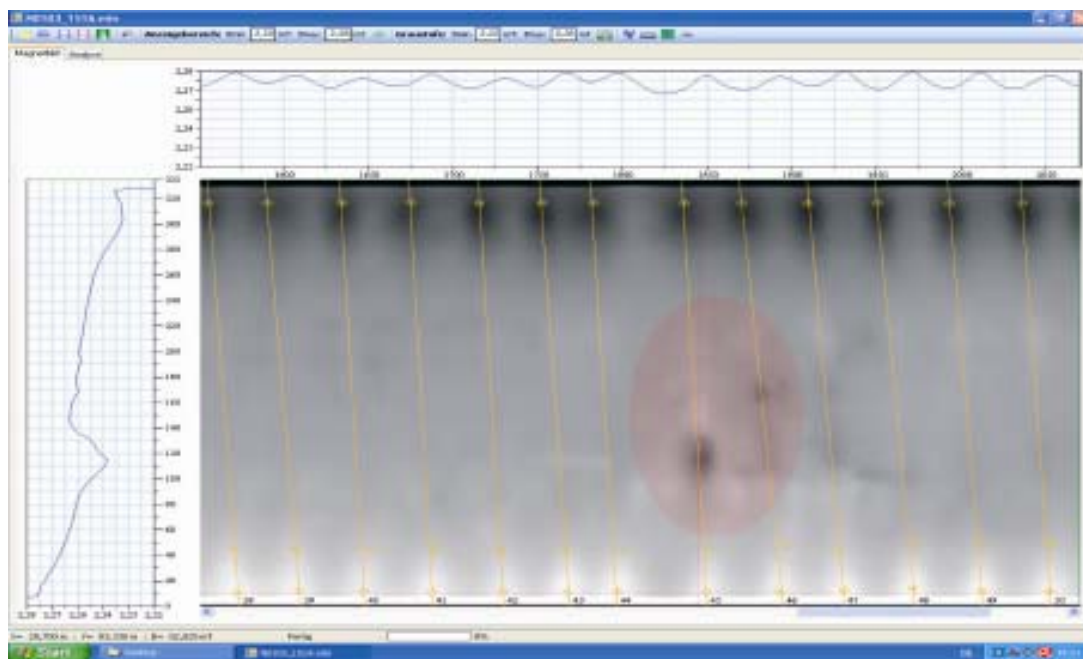


Figure 14: Screenshot of the stray magnetic field as a grayscale image of a road section with the marked range of a fracture



Figure 14.1: Located shear tendon break in the bridge deck

5 The Physical Principle of the Magnetic Measurement in the Active Field

5.1 Application

With this type of magnetization, the sensors are located in the middle of the two poles of the magnets. Figure 15 shows the principle structure of the small measuring unit.

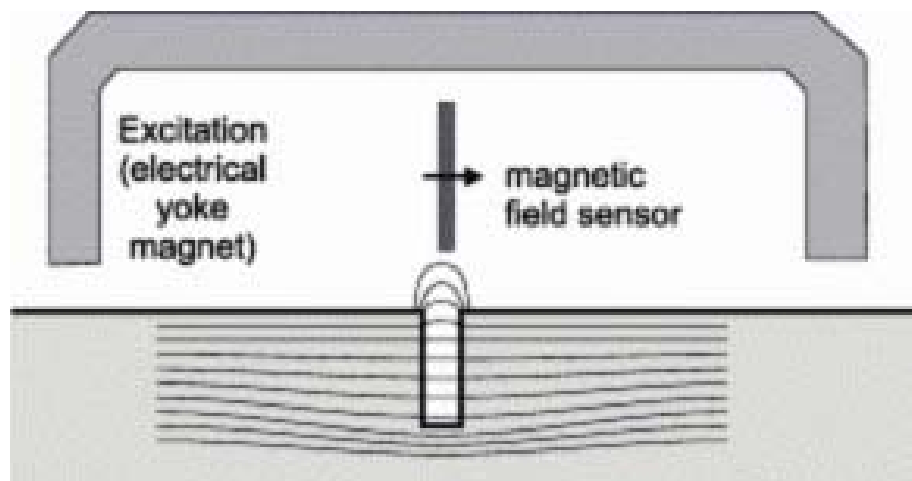


Figure 15: Principle structure of the small measuring unit

The principle can be most impressively demonstrated by showing the results of both methods of one inspection area comparative side by side (figures 16 and 17).

Both images have their typical significance. The expert immediately gains more information about the real situation than one method alone could provide.

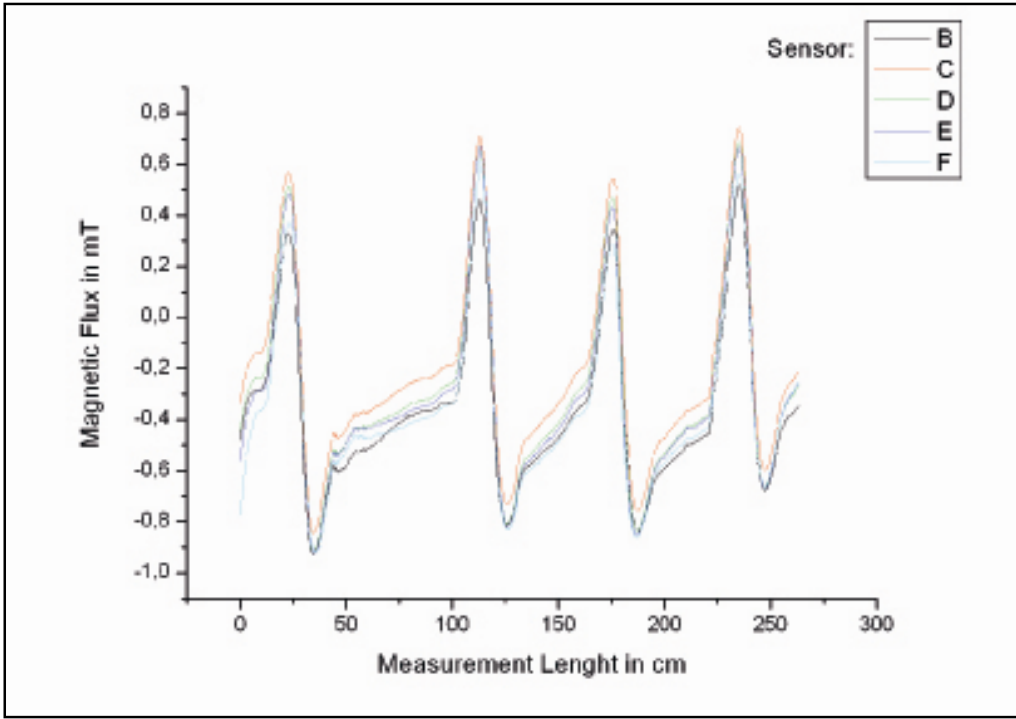


Figure 16: Measurement in the active field (LV16, line 1) without breaks

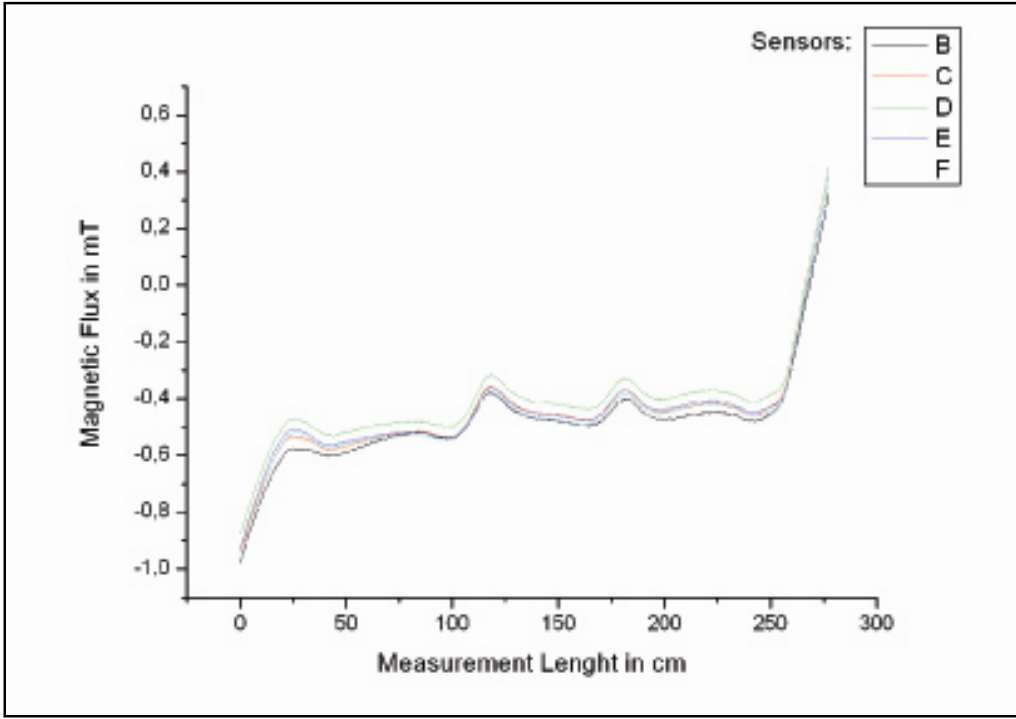


Figure 17: Measurement of the tension wires in the same remanent field (box girder LV16, line 1) without breaks

6 The Measurements at Lehigh University

6.1 Markings

The bridge members are marked with abbreviations. These were partly recorded during the measurements to simplify the allocation later on. The investigated box girders originally belonged to these three bridges:

- Clearfield Creek (CC)
- Lakeview Drive (LV)
- Main Street (MS)

The measurements started with girder LV16. The measuring lines run parallel on the surface of the girder from left to right. Figure 18 shows the arrangement of strands and the measurement lines.

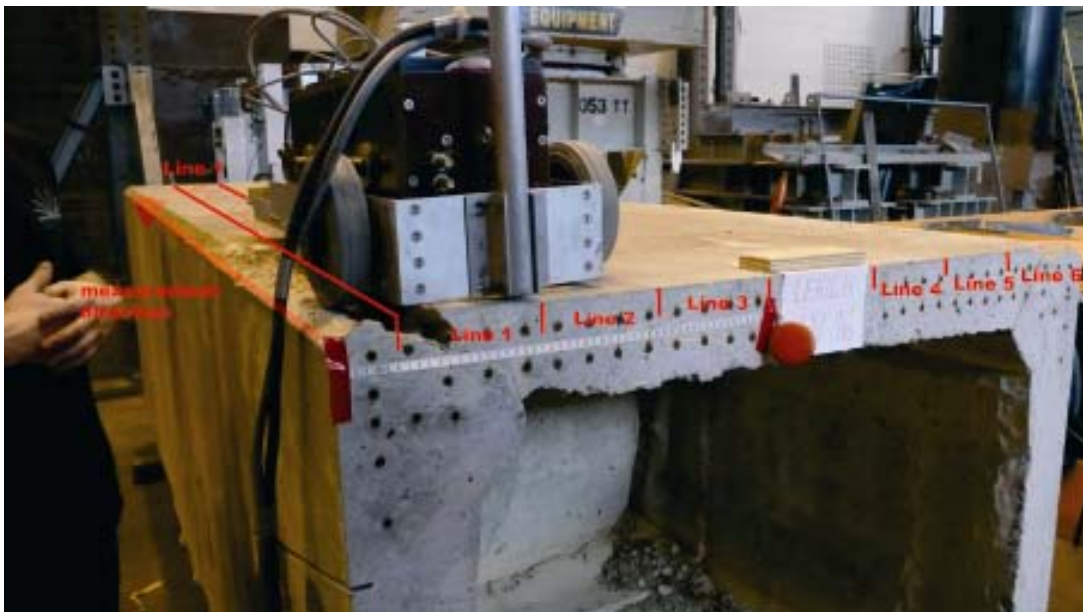


Figure 18: Arrangement of the strands and measuring lines of the box girder

While scanning track line 4, sensor one (the sensor arranged on the far right of the measuring unit) detected the clear evidence of a fracture (Figure 19). This break shows itself in the active field as shown in Figure 20.

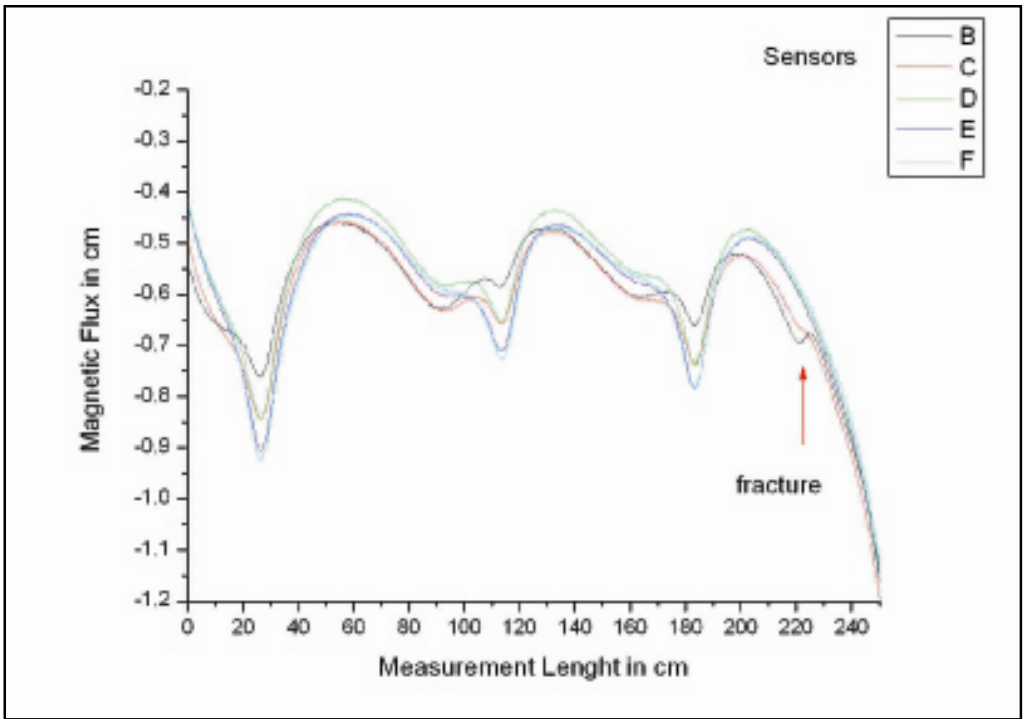


Figure 19: Box girder LV16, line 4; fracture signal by measuring the stray magnetic field of the tension wires

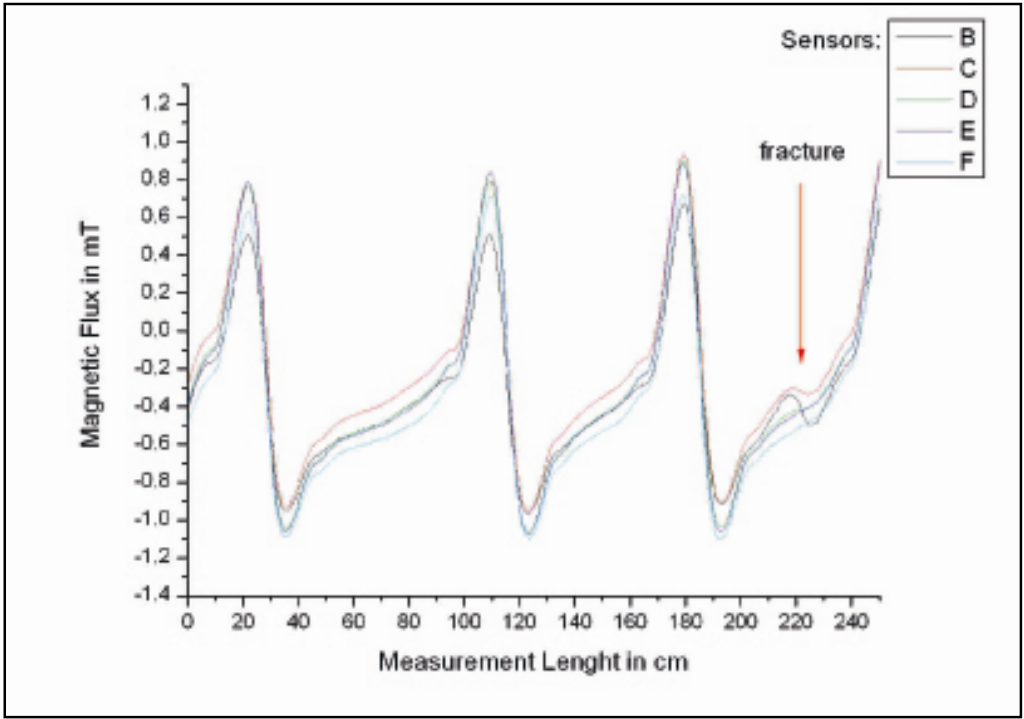


Figure 20: Box girder LV16, line 4; fracture signal measured in the active magnetic field

While measuring line 5 a clear fracture signal shows itself. Both adjacent sensors, F (sensor five) and E (sensor four), show that signal. Thus not only the exact space of the fracture (to the left of line 5) is shown, but even the individual tendon can be determined. Figure 21 shows the situation.

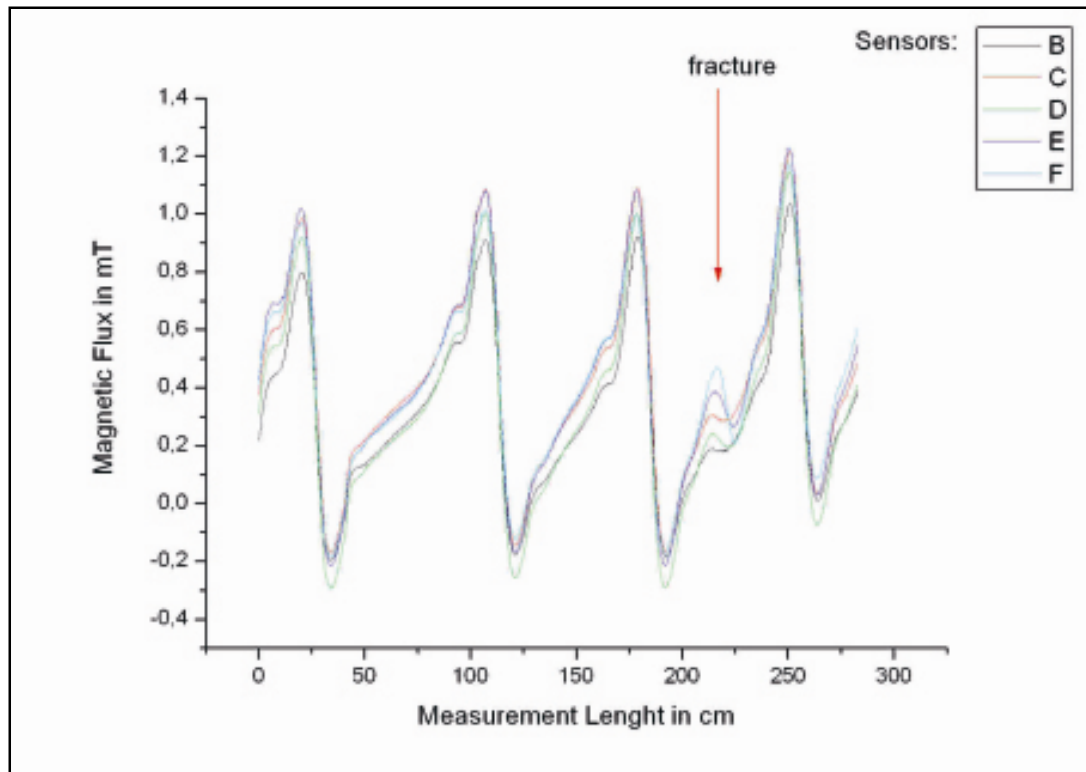


Figure 21: Box Girder LV16, line 5; fracture signal (at about 225cm) measured in the active magnetic field

While measuring a certain area of line 6 the tendons lie blank. In this area, the tendons are corroded (Figure 22). This situation becomes apparent by the stronger scattering in the magnetic image. (Figure 23)

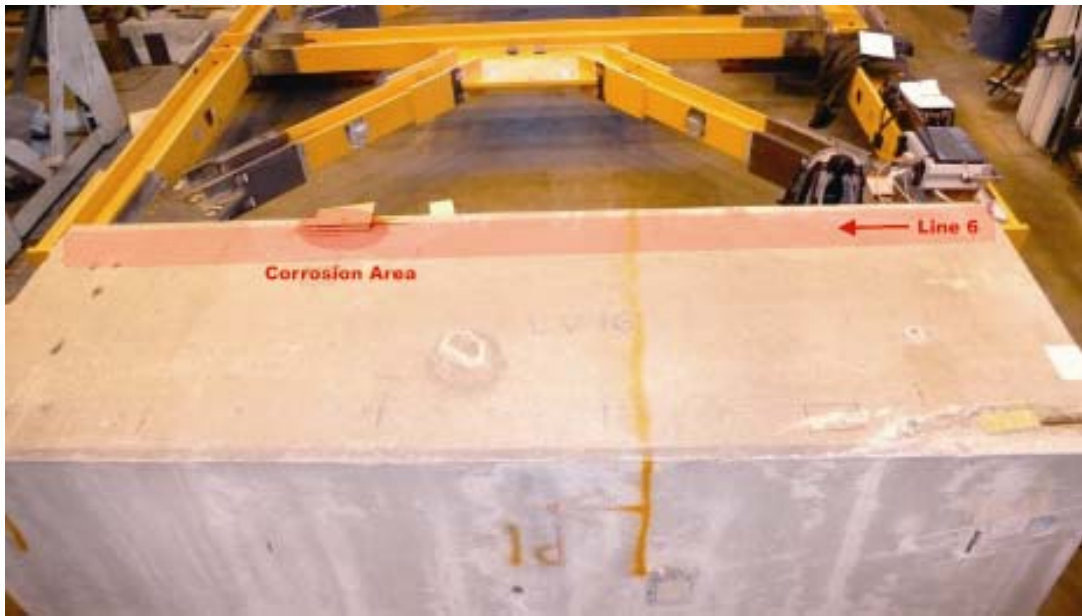


Figure 22: Box girder LV16 with markers of line 6 and open lying corroded prestressing wires

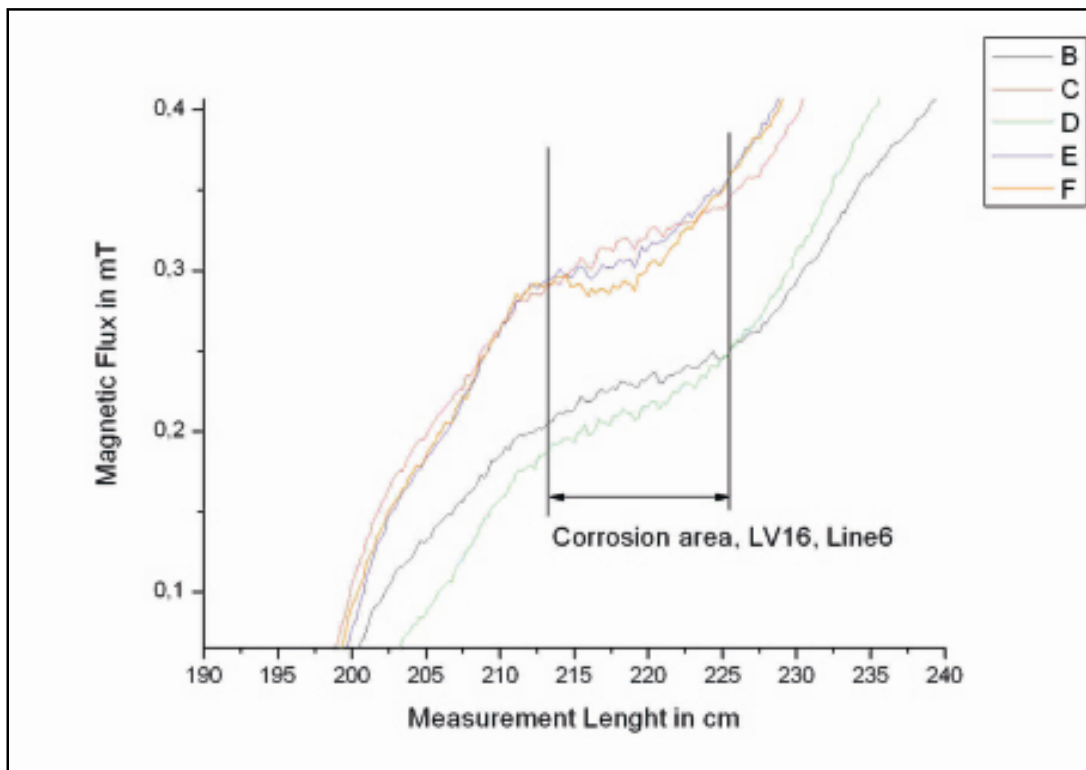


Figure 23: Box girder LV16, line 6; signal scattering in the area of corroded wires at measurement in the active magnetic field

Box Girder CC4

This girder has stirrups only in the webs. These stirrups do not extend into the lower flange of the girder. (note – girders were positioned upside down for ease of measurement)

This girder shows no fractures in the magnetic images / measuring results.

Box Girder CC3

This girder has also no stirrups in the lower flange. Stirrups were present only in the side webs, which could be identified in the measuring signal.

Box Girder MS 2

This girder shows the most damages that are already visible on the outside of one half of the binder. Despite the obvious damages of this girder it was completely measured. While measuring line 1, three fracture zones could be located. Only one breaking point (at about 270cm) could be visually identified. (compare Figure 4 to 5).

6.2 Summary of the detected breaks

Girder	Total measurement length from start to end (m)	Line of measurement (from left to right - see Fig. 18 for layout)	Distance from starting line to location of damage	Suspected Condition
LV16	2.65	Line 1 Line 2 Line 3 Line 4 Line 5 Line 6	0.4-0.5m 0.2 m – 0.3 m 2.15 m – 2.25 m 2.15 m – 2.25 m 2.15 m – 2.25 m	only corrosion nothing possible fracture fracture in strand 17/18 fracture in strand 17/18 only corrosion
LV19	2.65	Line 1 Line 2 Line 3 Line 4 Line 5 Line 6	 1.75 m – 1.85 m 0.9 m - 1.20 m 1.75 m – 1.85 m	nothing nothing nothing fracture in strand 15 possible fracture fracture nothing
CC3	3.75	Line 1 Line 2 Line 3 Line 4	 2.6 m – 2.7 m	nothing nothing nothing possible fracture

Girder	Total measurement length from start to end (m)	Line of measurement (from left to right - see Fig. 18 for layout)	Distance from starting line to location of damage	Suspected Condition
CC4	3.65	Line 1 Line 2 Line 3 Line 4 Line 5		nothing nothing nothing nothing nothing
MS2	3.65	Line 1 Line 2 Line 4	0.75 m – 0.85 m 2.15 m – 2.25 m 2.85 m – 2.95 m 2.20 m -2.40m 0.65 m – 0.75 m 1.45 m – 1.55 m 1.95 m – 2.05 m	fracture possible fracture fracture possible fracture fracture fracture fracture and many more
MS3	3.75	Line 1 Line 2 Line 3 Line 4 Line 5 Line 6	2.1 m – 2.2 m 2.35 m – 2.45 m 2.85 m – 2.95 m 1.05 m – 1.15 m 1.75 m – 1.85 m	nothing nothing nothing possible fracture fracture possible fracture fracture possible fracture nothing

7 Conclusions

In prestressed bridge decks and parking structures, fractures of prestressing steel wires are common. In most cases, the reason for the fracture is chloride-induced corrosion. Application of the RM-Method to detect potential prestressing steel fracture has increased the measurement speed by magnetizing the tendons in one step using a larger mobile magnet and by scanning the magnetic flux density over the entire surface of the bridge deck.

8 Literature

- [1] Nürnberger, U., Mehr Sicherheit im Spannbetonbau; Chloridgehalte und Feuchte beachten; Korrosion behindern. Maschinenmarkt 95 (1989) 30-40, 68-72 and 128-134
- [2] Nürnberger, U., Special corrosion problems in post-tensioned Structures, Otto Graf Journal (FMPA Baden Württemberg) 3 (1992) 148-163
- [3] Hillemeier, B., Assessment of Structural Stability of Prestressed Concrete by Non-Destructive Detection of Steel Fractures, Proceedings Vol. 1 of the International Symposium Non-Destructive Testing in Civil Engineering (NDT-CE). Ed. by G. Schickert, H. Wiggenhauser, Deutsche Gesellschaft für zerstörungsfreie Prüfung e. V.(1995) 23-29
- [4] Halsall, A. P.; Welch, W. E.; Trépanier, S. M., Acoustic Monitoring Technology for Post-tensioned Structures, Symposium Papers of the FIP Symposium 1996 on Post-Tensioned Concrete Structures (9196) 521-527
- [5] Bligh, R. P.; Nakirekanti, S.; Bray, D. E.; James, R. W., Evaluation of NDE Techniques for Detecting Grout Defects in Cable Stays, Materials Evaluation (1994) 508-514
- [6] Hillemeier, B.; Scheel, H., Ortung von Spannstahlbrüchen in metallischen Hüllrohren, Abschlußbericht zum Forschungsauftrag des Deutschen Instituts für Bautechnik AZ.: IV 1-5-672/92 (1996)
- [7] Scheel, H. and Hillemeier B., Capacity of the remanent magnetism method to detect fractures of steel in tendons embedded in prestressed concrete, NDT&E International, Vol. 30, No. 4 (1997) 211-216, Elsevier Science Ltd.
- [8] Krieger, J., Einsatz von SQUID-Systemen bei der zerstörungsfreien Prüfung von Spannbetonbauwerken, Final report of the BAST-project 97 242/B4, Bergisch-Gladbach 2000 (not published), copies available (contact the authors of this paper)
- [9] Szielasko, K; Kloster, A.; Dobmann, G.; Scheel H. and Hillemeier, B; High-Speed, High-Resolution Magnetic Flux Leakage Inspection of Large Flat Surfaces; European Conference on Nondestructive Testing 2006
- [10] Walther, A., Schnelle zerstörungsfreie Ortung von Spannstahlrissen in Querspanngliedern von Spannbetonbrücken; Verstärken und Instandsetzen von Betonkonstruktionen; Innsbruck 2007
- [11] Report about the magnetic measurements in order to check the structural safety of the Champlain bridge in Montreal (Internal Report with Vector by TU-Berlin)

Feasibility of using Line Scanning Thermography for the inspection of concrete structures with embedded rebar

Prepared for: Prof. S.P. Pessiki
P. C. Rossin Professor and Department Chair
Civil & Environmental Engineering,
Lehigh University
Bethlehem PA 18015

Prepared by: _____
Obdulia Ley, Ph.D.
Research Scientist
Research Contracts & Applications
Physical Acoustics Corporation

Prepared by: _____
Valery Godinez, Ph.D.
Manager
Research Contracts & Applications
Physical Acoustics Corporation

August 31, 2009



Feasibility of using Line Scanning Thermography for the inspection of concrete structures with embedded rebar

Thermal imaging techniques have the potential of detecting subsurface features or structures; however, the depth at which these occur has a crucial influence on their detectability (Almond & Peng, 2000). Most dynamic thermography techniques are able to detect defects larger or equal to its depth. Line Scanning Thermography (LST) provides the capability of detecting regional alterations in the thermal properties of the material inspected, and in the case of boiler tubes, LST has been observed to effectively detect thinning in carbon steel samples (Cramer and Winfree et al, 1999).

The LST technique has been used to successfully inspect metallic and composite samples. In metallic samples, LST was applied to detect thickness variation of plates; in laminate composites LST has been used to determine the presence of different types of disbonds. The success of LST in different applications strongly depends on the selection of the scanning parameters.

The present study intended to determine the feasibility of using LST for concrete inspection, particularly the identification of the presence of embedded rebar in a structure and the determination of the presence of corrosion. The LST system used (THELIS) is able to deposit up to 180W/in through a width of 10 inches and can scan a surface at speeds ranging from 0.1in/s to 4.25in/s. The power deposition and scanning velocities attainable by the portable LST system used were selected to meet the requirements to inspect the bonding between two composites of up to 1-inch in thickness.

In the scans performed in the concrete samples it was observed that the amount of heat delivered was not sufficient to clearly observed the embedded rebar and wire structures. The scans provided indication of some cracks that were not clearly visible, as well as regions with different porosities.

In this report, the LST technique is introduced, followed by a description of the procedure used to scan the concrete structures and a summary of the observations and modifications suggested for the system to be used in the inspection of concrete structures.

I. Introduction to LST

In LST, a line heat source of finite width moves across the sample's surface at a constant speed; an infrared camera is used to record the temperature changes in the surface during the heating protocol. The IR detector moves in tandem with the heating line, and its field of view is set to contain a region above and below the location of the heat source as seen in Fig. 1.

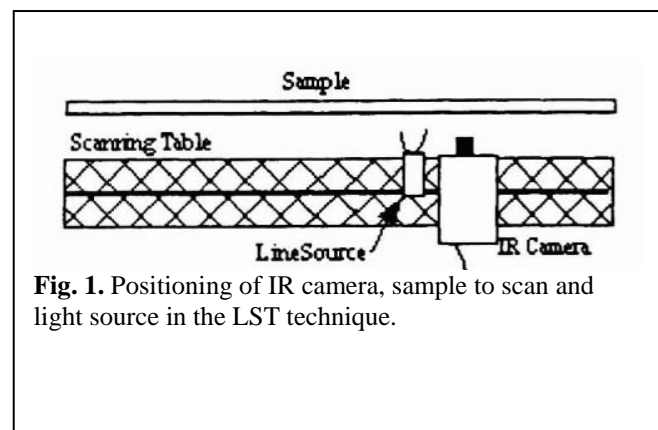


Fig. 1. Positioning of IR camera, sample to scan and light source in the LST technique.

The set up configuration of LST concentrates the camera's field of view around a region surrounding the application of heat. The thermal response of the surface during cooling is extracted from the image sequence captured while the thermal imager scans the surface of interest. The image generation and analysis process is done following proprietary and patented algorithms (termed *ThermoWin*) that are performed automatically while the scan is performed, and produces a thermal image of the whole sample scanned at a selected time after heat application once the scan is completed. The observation time selected depends on the system maximal thermal contrast of the system, which need to be properly identified beforehand.

The efficiency of LST when inspecting large areas is achieved by the controlled movement of the thermal camera and line heat source through the surface inspected. The common scanning speed used when inspecting metals such as carbon steel is 2.5 inches per second. This technique has been used successfully in the analysis of boiler tubes to identify thickness reduction and material loss [19-22].

LST image generation procedure

In LST the movement of the heat source and thermal camera in tandem allows the study of large areas ensuring uniform heat deposition throughout the surface, which is something difficult to achieve with other dynamic thermography methods that only analyze a section of a large sample at a time. Large area inspection is achieved thanks to a patented image generation procedure.

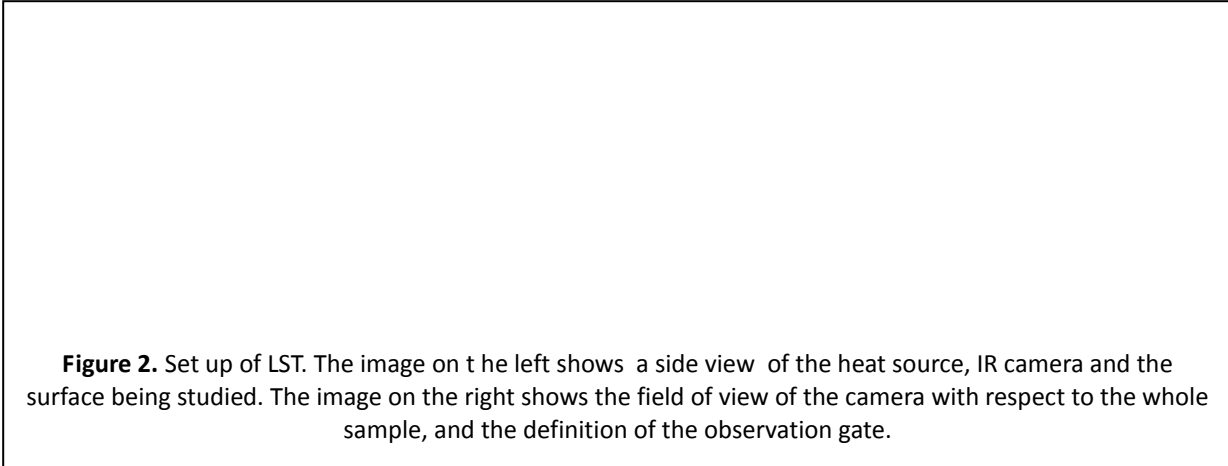


Figure 2. Set up of LST. The image on the left shows a side view of the heat source, IR camera and the surface being studied. The image on the right shows the field of view of the camera with respect to the whole sample, and the definition of the observation gate.

As indicated in Figure 2, in LST the field of view of the thermal camera is restricted to a region of the sample surrounding the heat application region. During the scan (i.e. as the heat source moves through the sample's surface), the temperature of the region swept by the heat source increases, whereas the surface temperature of the region where the heat source has passed.

In the heated region captured by the imager an observation gate G_1 is defined at a distance ℓ_1 from the location of heat application. Since the heat source and camera move at velocity v , time between the heat source was applied at location ℓ_1 and its current location d is given by $\Delta t = \ell_1 / v$, when ℓ_1 is small, the temperature change experienced increases due to its proximity to the heat application location or heat source.

A thermal image of the complete scanned region is constructed by collecting the photon intensity or temperature values at the location or pixel line ℓ_1 of each frame acquired during the scan; this information (pixel line at ℓ_1) is stacked to form the thermal image of the complete sample.

The scanning parameters correspond to scan velocity (v) and intensity (q); their selection with respect to the thermal properties (k , C_p , ρ , α , β) of the plate will change the maximum surface temperature reached during the scan and consequently the thermal contrast reached. Producing a thermal image that shows the presence of subsurface defects depends on the appropriate selection of scanning parameters for a given material (k , C_p , ρ , α , β) with specific thickness and or geometry. ***In the scans performed during this study, the velocity selected ranged between 0.5 in/s and 0.25 in/s.***

The maximum intensity of the heat line or power deposition of the LST system used was 180 W/in; the intensity can be varied from 0 to 100% in a controlled manner. In the scans performed the value selected ranged between 45 and 70% of the maximum lamp power. If the lamp intensity or energy deposition increases and the scanning velocity is reduced, local heat deposition increases; favoring bad heat diffusing samples (smaller α) where heat needs more time to penetrate into the structure.

From published studies using LST for nondestructive evaluation in single layer metallic samples, it has been observed that:

- The minimum detectable feature size increases with the depth of the anomaly or feature, and the time required to detect a feature; in a single layer medium has been experimentally observed to be proportional to the square of its depth.
- The minimum detectable anomaly at any depth is commonly expressed by $l/d \geq 2$, where the ratio l/d is called the anomaly aspect ratio (Maldague, 2002), l is the characteristic size of the defect or defect diameter and d the depth at which it is located with respect to the surface imaged.

In LST, a thermal image of the whole sample scanned is generated for a given time t after heat application. In materials with thermal conductivities lower than metals the time to reach a steady temperature distribution increases, and therefore any thermal indication from the surface will require more time to be visible. In the scans performed in this study, the field of view of the camera was pointed to observe only the region behind the heat source and extended 10.5 inches in length; considering the prototype moved at speed of 0.25 in/s, the times at which the thermographs can be generated ranged from 5 to 42 seconds after heat application.

II. Scans performed

Thermography on concrete structures

Studies showing the utilization of Thermography for the inspection of various concrete structures have been published since 1994. The main problems encountered are the heat intensity required and the depth limitation. Inspection has been limited to small areas using flash thermography and Pulsed Phase Thermography. The heat sources used are infrared lamps, radiofrequency and microwave. Using infrared lamps, the power used is over 2400 W and the exposure time ranges between 3 and 120 minutes. Some of the authors that have used dynamic thermography on concrete are Osiander, and d'Ambrosio.

Details about LST unit used for the Scans

The Thermography Line Inspection System (THELIS) used was designed to scan a particular type of laminate carbon composites where observations of delaminations and kissing bonds can be done during the first 30 to 40 seconds after heat application. The prototype can sustain scanning speeds from 0.1in/s to 4.2in/s, and can deliver up to 180W/in of power, which is focused on a line that is 0.25in thick and 10in wide. The system uses a microbolometer or IR camera that detects long wave infrared radiation (LWIR) with wavelengths between 8 and 13 μm . A microbolometer is a device capable of measuring the energy of incident IR radiation; the radiation striking the detector material heats it and changes its electrical resistance which is processed into temperatures and used to create an image. The camera is placed 24in over the inspection surface. The pixel size of the thermograph generated using the LST technique is given by the horizontal number of pixels that the camera can display times the number of frames acquired during the scan.

Scan Optimization

The scan velocity as well as heating intensity was selected and maintained constant throughout the study. To select the scanning parameters 3 scans were performed at the same region and the contrast attained in the images was compared. Fig. 4 shows a thermal image corresponding to the best thermal contrast observed among the 3 runs performed. The scanning speed selected was 0.25 in/s and the heating intensity was 50% of the maximum power of the lamp (180W/in).



LST images generated using different scanning parameters

V=0.5 in/s, I=70%

V=0.25 in/s, I=50%

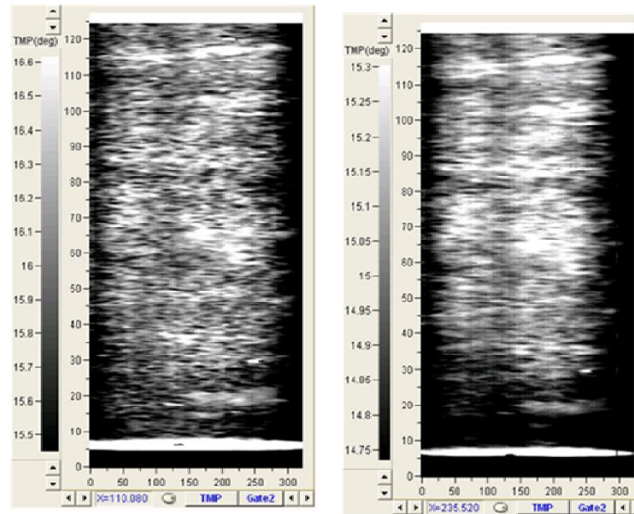


Figure 4. Thermal images of Beam 3. The scans cover 128in in length and the external edge of the prototype wheels were placed 4.5in from the edge of the structure. Direction of scanning in indicated in Fig. 3.

A total of 3 structures were scanned, the location of the structures is indicated in Fig. 5. The prototype provides an effective scan of 8 inches wide. The structures inspected had widths ranging between 36 in and 48in. The average length for each scan was of 120 inches, and was started 25 to 35 inches from the edge depending of the structure.

Location and labeling of the samples studied

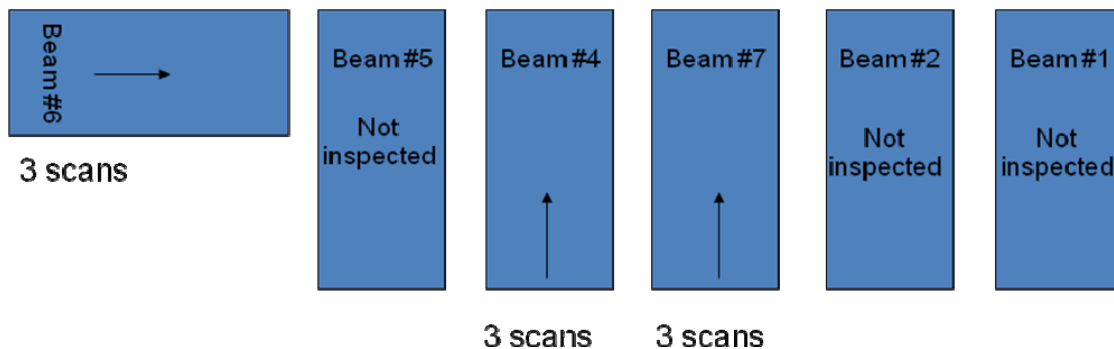


Figure 5. Diagram indicating the location of the samples in the laboratory and the scan direction.

Due to the low thermal conductivity of concrete, thermographs at very short time after heat application cannot be generated because the excess heat available at the inspected surface has not been dissipated towards the interior of the sample, and the images are blurry; on the other hand, the maximum observation time is limited by the size of the field of view if the IR camera. These two are the main limitations of the LST technique. These problems can be partially reduced by modifying the size and configuration of the prototype (camera/heat source configuration).



Results

The present prototype configuration lacks of a cooling system for the heat source, so it was necessary to wait between scans. The time required for completing a scan of the top surface of the concrete structure was 30 minutes per structure, this time does not include the time necessary to reposition the scanner and to allow cooling down of the lamp, which was about 80 minutes per beam.

The thermograms generated from each scan is included in the **Appendix**, which is enclosed as a separate file. In this appendix, thermal images generated at three different times after heat application are presented for each one of the scans performed. Analysis of the dynamic response is important to estimate depth of indications as well as severity of some cracks.

The scans from Beam #6 show a darker region that extends vertically, the local reduction in brightness can be associated to the presence of a highly heat conducting material below the surface, such as wire bundles or rebar. The spacing between the rebars currently cannot be identified due to lateral diffusion and the need for higher heat deposition. The first scan shows a circular indication around $y=22$ in from the locations where the scan started. The region at $y=60$ in and $x>170$ pixels shows a resistance to heat flow and a region of increased brightness. Another region of increased heat resistance is observed at $y=117$; this region is brighter on the right hand of the scan and the intensity increases as time passes indicating that the indication takes place superficially.

The second scan performed in Beam #6 showed a bright spot covering the region $100\text{in} < y < 90$ in and 200 pixels $< x < 250$ pixels. The third scan covered a large exposed crack, where the rebar was exposed, the thermal image is able to show the regions of the crack where significant separation exists as they show increased brightness short times after heat application. The heat application revealed cracks growing horizontally; and 3 bright spots are observed centered at

- 1) $x=198$ pixels and $y=37$ in,
- 2) $x=102$ pixels and $y=67$ in and
- 3) 122 pixels and $y=125$ in.

The first scan in Beam #4 showed two regions of high brightness growing laterally to a small crack that did not show significant depth or separation. These indications are found around 30 to 40 in from the location the scan started. This scan also shows one bright spot centered at $y=95$ in and $x=192$ pixels.

This scan covered part of a crack, as well as two indications associated to increased brightness in the thermal image which are centered at

- 1) $y=70$ in and $x=145$ pixels, and
- 2) $y=115$ in and $x=193$ pixels.

These two indications light up at different times indicating that they are located at different depths. Currently information about the depth cannot be extracted, but using modeling and experimentation the information can be determined.

In Beam #7, The first scan showed a bright spot around $y=100$ in and $x=195$; the second scan showed a region where the thermal images acquired at different times consistently showed a



darker region, which might indicate the presence of humidity or different porosity of the material. In scan #3 of Beam #7 there is a vertical band showing increased intensity.

As protocol before starting the inspection of each beam, NUC was performed on the camera. The images acquired from Beam #7 showed lower quality than the images acquired with the other two beams, this might be due to a faulty non uniform calibration (NUC) performed on the camera before the test. This problem can be avoided by using a microbolometer that has built-in black body surface that rotates in front of the sensor to perform the NUC and the procedure can be programmed to be performed before the scan.

Suggestions for future study

Due to the need to see deep into the structure, it is necessary to increase the heating power of the lamp. However this will increase the observation time necessary to generate the images using the LST procedure. A possibility to increase heat deposition to have a larger signal coming from the rebar or any metallic structure is to use microwaves as the heating source and generate a beam that can be focused at the depth of the rebar. This will limit surface heat, will improve the contrast in the thermal image, will reduce the transit time of the thermal front, and will provide the best possibility to detect changes in the rebar or embedded metallic structures. At this moment, we have not been able to find a commercial microwave source that can be used easily for this purpose.

We are currently working of implementation of further image processing capabilities in our ThermoWin software, used to control the scanning and to generate the thermal images using the LST algorithm. These image analysis tools will provide the capability of calculating spatial and temporal derivatives with the thermal images improving thermal contrast.

Perform some numerical modeling and sensitivity analysis to determine the optimal scanning parameter combination that can be used to obtain maximum thermal contrast between the concrete and the embedded metallic structures. In these analysis the possibility of multiple passes of heating can be analyzed. The equations and boundary conditions needed for this analysis of finding the transient temperature distribution in a concrete block with finite thickness and with embedded structures that can be rebar, water or voids is described in the Appendix.



Bibliographic search in the area of thermography of composites.

- [1] Almond, D. P., Delpech, P., Beheshtey, M. H., and Wen, P., 1996, "Quantitative determination of impact damage and other defects in carbon fiber composites by transient thermography," SPIE, pp. 256-264.
- [2] Avdelidis, N. P., and Almond, D. P., 2004, "Transient thermography as a through skin imaging technique for aircraft assembly: modelling and experimental results," *Infrared Physics & Technology*, 45, pp. 103-114.
- [3] Avdelidis, N. P., Almond, D. P., Moropoulou, A., and Marioli-Riga, Z. P., 2003, "Transient thermography in the assessment of various defects under composite aircraft repair patching," SPIE, K. E. Cramer, and X. P. Maldague, eds., *Thermosense XXV*, pp. 356-362.
- [4] Avdelidis, N. P., Ibarra-Castanedo, C., Marioli-Riga, Z. P., Bendada, A., and Maldague, X. P. V., 2008, "A study of active thermography approaches for the non-destructive testing and evaluation of aerospace structures," SPIE, V. P. Vavilov, and D. D. Burleigh, eds., *Thermosense XXX*, pp. 1-6.
- [5] Badghaisha, A. A., and Fleming, D. C., 2008, "Quantitative characterization of resistive defects in thick composites using step heating thermography," SPIE, V. P. Vavilov, and D. D. Burleigh, eds., *Thermosense XXX*, pp. 1-12.
- [6] Bates, D., Lu, D., Smith, G., and Hewitt, J., 2000, "Rapid NDT of composite aircraft components using lock-in ultrasonic and halogen lamp thermography," SPIE, G. Y. Baaklini, C. A. Lebowitz, and E. S. Boltz, eds., *Nondestructive Evaluation of Aging Materials and Composites IV*, pp. 277-786.
- [7] Bates, D., Smith, G., Lu, D., and Hewitt, J., 2000, "Rapid thermal non-destructive testing of aircraft components," *Composites, Part B* 31, pp. 175-185.
- [8] Baughman, S. R., 1998, "Applications for thermal NDT on advanced composites in aerospace structures," SPIE, pp. 277-786.
- [9] Bendada, A., Erchiqui, F., and Lamontagne, M., 2005, "Pulsed thermography in the evaluation of an aircraft composite using 3D thermal quadrupoles and mathematical perturbations," *Inverse Problems*, 21, pp. 857-877.
- [10] Boras, I., and Svaic, S., 1998, "Determination of defect parameters in specimen by means of thermography and numerical methods," SPIE, pp. 277-768.
- [11] Brown, J., Baker, R., Kallemeyn, L., and Zandler, A., 2008, "Crack detection and fatigue related delamination in FRP composites applied to concrete," SPIE, V. P. Vavilov, and D. D. Burleigh, eds., *Thermosense XXX*, pp. 1-10.
- [12] Cobble, M. H., 1968, "Finite transform solution of the temperature of a plate heated by a moving source," *International Journal of Heat Mass Transfer*, 10, pp. 1281-1289.
- [13] Cramer, K. E., and Winfree, W. P., 2000, "Application of the Thermal Line Scanner to Quantify Material Loss Due to Corrosion," SPIE, R. B. Dinwiddie, and D. H. LeMieux, eds., *Thermosense XXII*, pp. 210-219.
- [14] Cramer, K. E., and Winfree, W. P., 2001, "Thermographic Detection and Quantitative Characterization of Corrosion by Application of Thermal Line Source," SPIE.
- [15] Cramer, K. E., Winfree, W. P., Reid, D., and Johnson, J., 1999, "Thermographic Detection and Quantitative Characterization of Corrosion by Application of Thermal Line Source," SPIE Conference on Nondestructive Evaluation of Utilities and Pipelines III, pp. 277-768.



- [16] Galietti, U., Ladisa, S., Pappalettere, C., and Spagnolo, L., 2002, "Hybrid procedure to characterize hidden defects in composite materials," SPIE, X. P. Maldague, and A. E. Rozlosnik, eds., Thermosense XXIV, pp. 599-609.
- [17] Galmiche, F., Maldague, X., Vallerand, S., and Couturier, J.-P., 2000, "Pulsed Phased Thermography With The Wavelet Transform," Review of Progress in Quantitative Nondestructive Evaluation, D. O. Thompson, and D. E. Chimenti, eds., American Institute of Physics.
- [18] Hendorfer, G., Mayr, G., Zauner, G., Haslhofer, M., and Pree, R., 2007, "Quantitative determination of porosity by active thermography," Review of Quantitative Nondestructive Evaluation, D. O. Thompson, and D. E. Chimenti, eds., American Institute of Physics, pp. 702-708.
- [19] Ibarra-Castanedo, C., Genest, M., Servais, P., Maldague, X. P. V., and Bendada, A., 2007, "Qualitative and quantitative assessment of aerospace structures by pulsed thermography," Nondestructive Testing and Evaluation, 22, pp. 199-215.
- [20] Ibarra-Castanedo, C., and Maldague, X., 2005, "Pulsed Phase Thermography Inversion Procedure using Normalized Parameters to Account for Defect Size Variations," SPIE, G. R. Peacock, D. D. Burleigh, and J. J. Miles, eds., Thermosense XXVII, pp. 334-341.
- [21] Kidawa-Kukla, J., 2008, "Temperature distribution in a rectangular plate heated by a moving heat source," International Journal of Heat and Mass Transfer, 51, pp. 865-872.
- [22] Krishnapillai, M., Jones, R., Marshall, I. H., Bannister, M., and c, N. R., 2006, "NDTE using pulse thermography: Numerical modeling of composite subsurface defects," Composite Structures, 75, pp. 241-249.
- [23] Kulowitch, P., Perez, I., and Granata, D., 1995, "Flash infrared thermography for NDT/I/E of Naval aircraft," SPIE, pp. 252-260.
- [24] Leung, M., 2001, "Phase-change heat transfer in laser transformation hardening by moving Gaussian rectangular heat source," JOURNAL OF PHYSICS D: APPLIED PHYSICS, 34, pp. 3434-3441.
- [25] Maierhofer, C., Arndt, R., Rollig, M., Rieck, C., Walther, A., Scheel, H., and Hillemeier, B., 2006, "Application of impulse-thermography for non-destructive assesement of concrete structures," Cement & Concrete Composites, 28, pp. 393-401.
- [26] Maldague, X., and Marinetti, S., 1996, "Pulse phase infrared thermography," Journal of Applied Physics, 79, pp. 2694-2698.
- [27] Marinetti, S., Muscio, A., Giulio, P., and Grinzatoa, E., 2000, "Modeling of thermal non-destructive evaluation techniques for composite materials," SPIE, R. B. Dinwiddie, and D. H. LeMieux, eds., Thermosense XXII, pp. 164-173.
- [28] Meola, C., 2007, "A new approach for estimation of defects detection with infrared thermography," Materials Letters, 61, pp. 747-750.
- [29] Micelia, M., Horneb, M. R., and John C. Duke, J., 2001, "Health monitoring of FRP bridge decks," SPIE, T. Kundu, ed., Advanced Nondestructive Evaluation for Structural and Biological Health Monitoring, pp. 100-105.
- [30] Mulaveesalaa, R., and Tuli, S., 2006, "Theory of frequency modulated thermal wave imaging for nondestructive subsurface defect detection," Applied Physics Letters, 89, pp. 1-3.





October 02, 2009

Dr. Stephen Pessiki, Ph.D.
Lehigh University
Chairperson, Department of Civil and Environmental Engineering
P.C. Rossin College of Engineering & Applied Science
Civil & Environmental Engineering
13. E. Packer Avenue, Fritz Engineering Laboratory,
Bethlehem, PA 18015

Re: Report for the Nondestructive Testing of Prestressed Precast Box-Beams
Dynasty No. 09-146

Dear Dr. Pessiki:

Thank you for allowing Dynasty Group, Inc. (Dynasty) to perform a nondestructive evaluation of six prestressed precast box-beams at the Lehigh University's ATLSS Research Center Facility in Bethlehem, Pennsylvania and contribute to the research knowledge base of your project. The purpose of these evaluations was to nondestructively assess each of the beams in your study to determine the presence of corrosion of the embedded reinforcing steel and their potential deterioration effects.

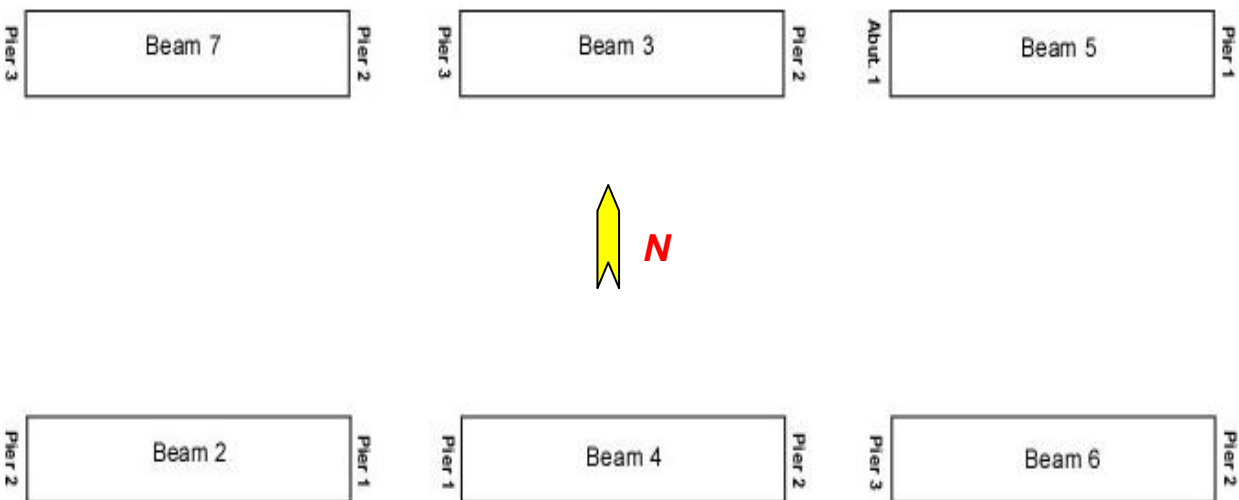
Background

We understand that the beams in this study were parts of bridges decommissioned by the Pennsylvania Department of Transportation (PennDOT). Three non-composite prestressed precast concrete box girder bridges were part of a global corrosion study. The beams were removed from the following bridges in counties within the State of Pennsylvania:

- Clearfield Creek Bridge, Cambria County, PA
Sample Beams 4 and 5
- Lakeview Drive Bridge, Washington County, PA
Sample Beams 2 and 3
- Main Street Bridge, Washington County, PA
Sample Beams 6 and 7



Beam 1, also removed from the Lakeview Drive Bridge, was not evaluated by in our study. The beams were staged outdoors, adjacent to the ATLSS Research Center Facility. Figure 1 below shows the beam staging layout. All beams were supported on wood blocks, and were positioned with the bottom flange facing up. For identification purposes, each beam was numbered consecutively by Lehigh University (Lehigh) staff. Additional labels denoting the corresponding bridge designation was also marked on each of the beams. Eventually, these samples will be demolished to make visual observations of the embedded prestressing and reinforcing steel.



Beam Staging Layout (beams are inverted and supported on top flange)

Figure 1 - Beam staging layout

Description of the beams and noted conditions

A cursory visual inspection of each of the beams was conducted. Only the accessible sides of the beams (bottom flange and webs) were documented. Based on our brief review of the submitted documents and visual observations, we understand the following:

Beams 2 and 3 - Beams 2 and 3 were removed from the Lakeview Drive Bridge in Washington County, Pennsylvania. The beams are about 49 years old, with a nominal 48 in. width by 42 in. depth rectangular cross-section and about 12 ft long.

The visual inspection of Beam 2 showed an approximately 3 ft long longitudinal crack at the edge of the beam and some concrete spalls. Three 4-in. diameter cores and a 2-in. diameter core had been extracted from the bottom flange. Cracks in the webs were noted at the ends of the beam segment.



Similarly, Beam 3 showed a longitudinal crack with some corrosion staining spanning almost the full length of the bottom flange. In addition, a large concrete opening was also noted near one of the corners of the beam (see Figure 3). A total of four 4-in. diameter cores had been extracted from the bottom flange. Cracks in the webs were noted at the ends of the beam. Figures 2 and 3 are views of the Beams 2 and 3, respectively. Also, the documented visual deterioration for beams 2 and 3 is shown in the appendix section of this report (See Figures 2V and 3V).

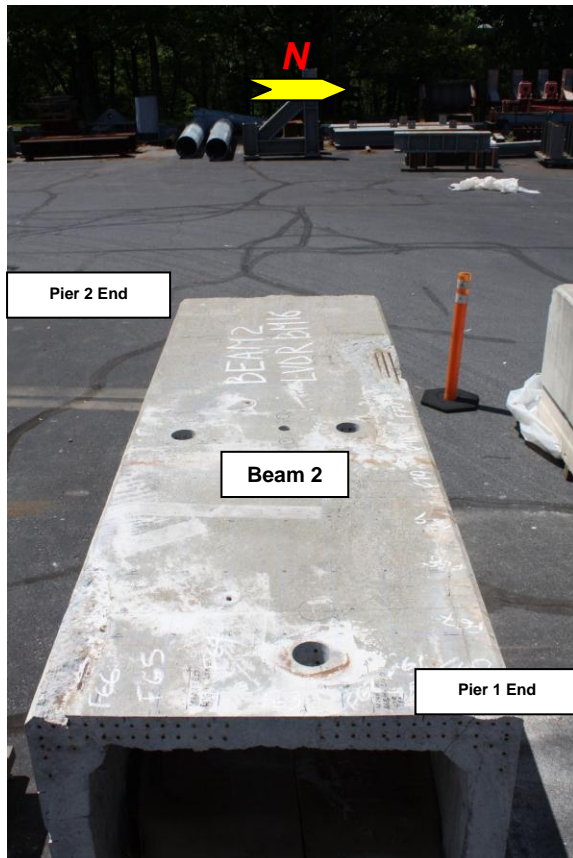


Figure 2 - Beam 2

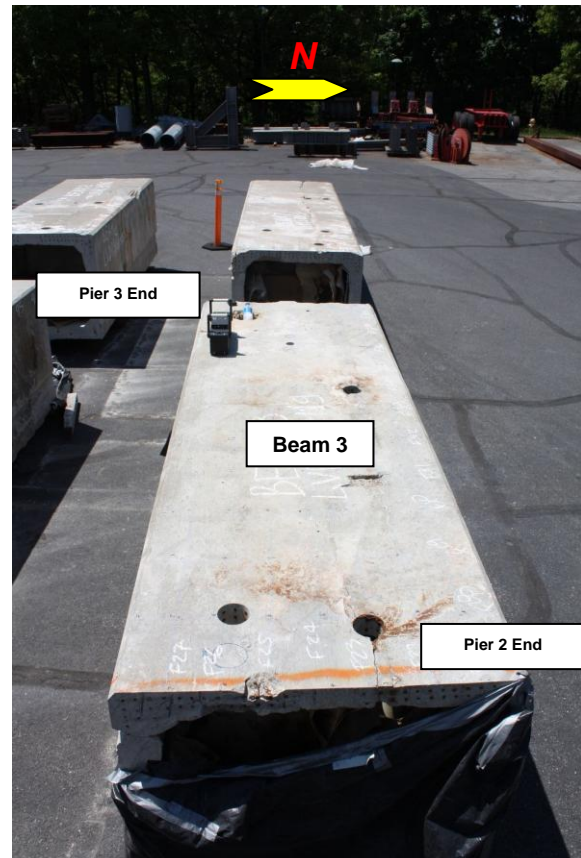


Figure 3 - Beam 3

Beams 4 and 5- Beams 4 and 5 were removed from the Clearfield Creek Bridge in Cambria County, Pennsylvania. The beams are about 56 years old, with a nominal 48 in. width x 36 in. depth rectangular cross-section and about 15ft. long.

The visual inspection of Beam 4 showed a longitudinal crack near one side of the beam, spanning almost the full length of the beam (see Figure 4). Some concrete spalling was also noted. A total of three 4-in. diameter cores had been extracted from the bottom flange. Cracks in the webs were also noted (see Figure 4).



Beam 5 showed a longitudinal crack with some corrosion staining spanning the full length of the beam. A total of five 4-in. diameter cores had been extracted from the bottom flange (see Figure 5). Figures 4 and 5 are views of the Beams 4 and 5, respectively. Cracks in the webs were noted at the ends of the beam. Also, the documented visual deterioration for Beams 4 and 5 is shown in the appendix section of this report (See Figures 4V and 5V).

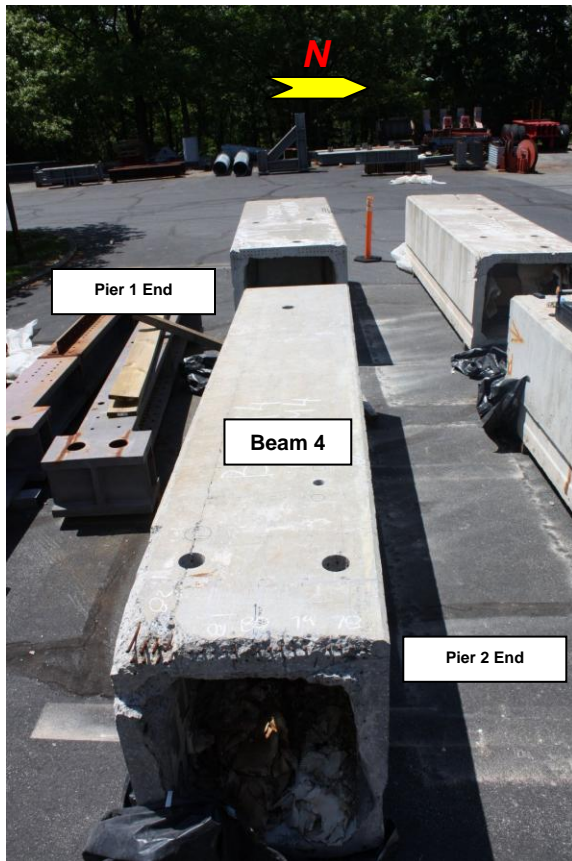


Figure 4 - Beam 4

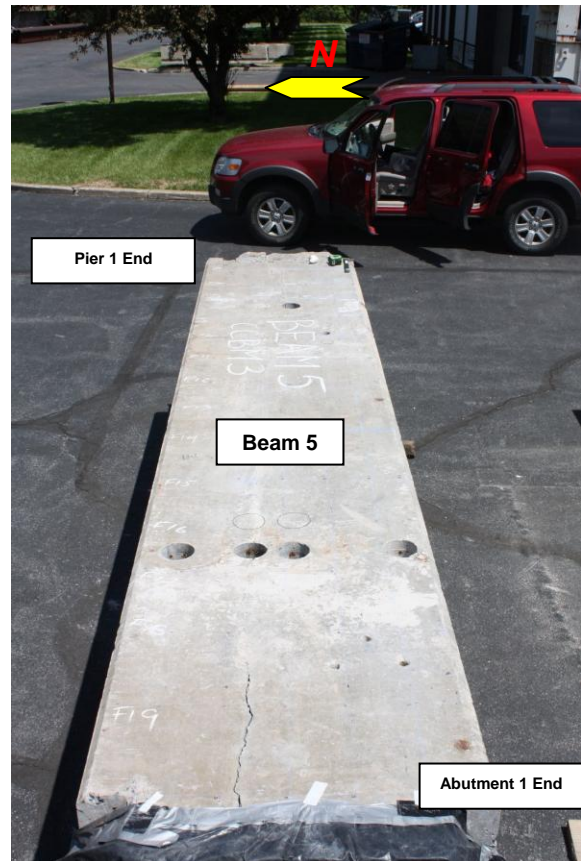


Figure 5 - Beam 5

Beams 6 and 7- Beams 6 and 7 were removed from the Main Street Bridge in Washington County, Pennsylvania. The beams are about 48 years old, with a nominal 48 in. width x 42 in. depth rectangular cross-section and about 15ft. long.

The visual inspection of Beam 6 showed a severe deterioration on at least half of the bottom flange surface, where the concrete had spalled, exposing the prestressing strands. A total of three 4-in. diameter cores and a 2-in. diameter core had been extracted from the bottom flange. Web cracks at the ends of the beams were also noted (see Figure 6).

Beam 7 showed a wide longitudinal crack with some corrosion staining spanning the full length of the beam segment. Some of the concrete had spalled around the edges of the cracks. A total of five 4-in. diameter cores and a 2-in. diameter core had been extracted from the bottom flange (see Figure 7). Figures 6 and 7 below are views of the Beams 6 and 7, respectively. Also, the



documented visual deterioration for Beams 6 and 7 is shown in the appendix section of this report (See Figures 6V and 7V).

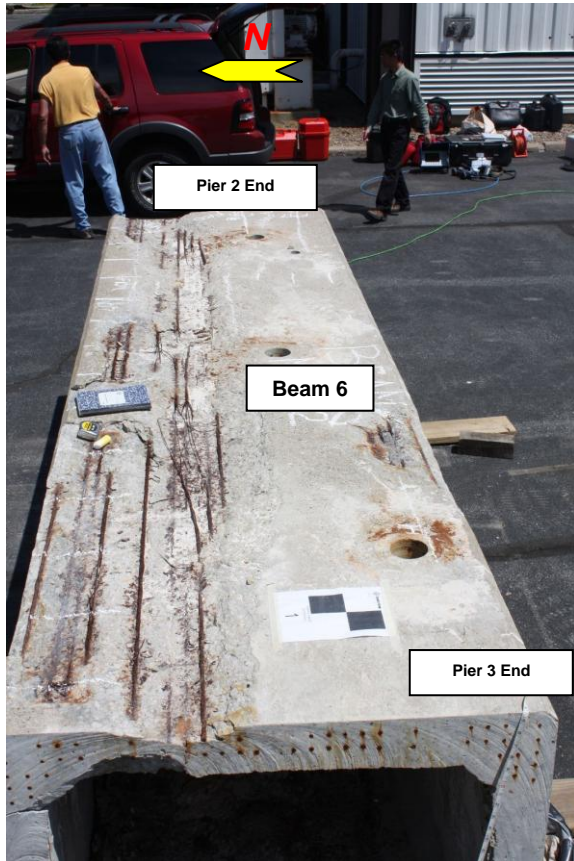


Figure 6 - Beam 6

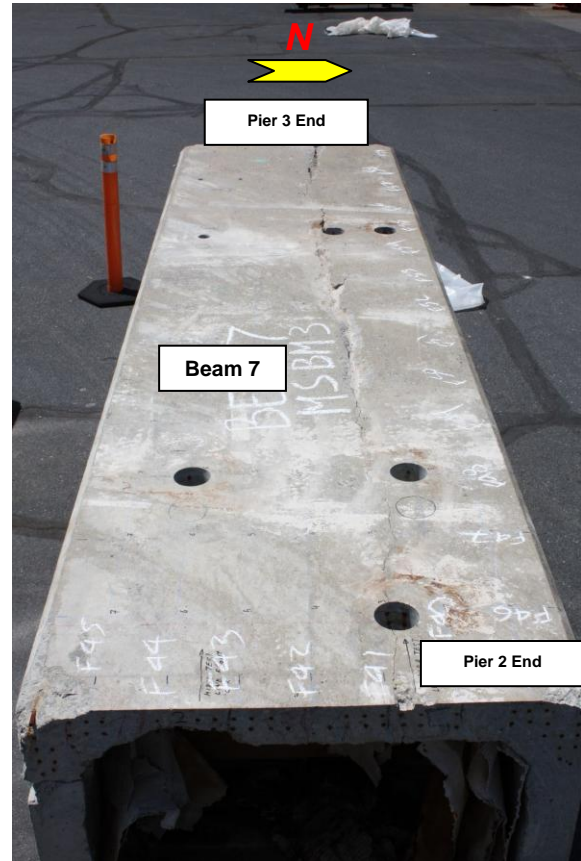


Figure 7 - Beam 7

Nondestructive Test Methods

During the course of the investigation, a combination of nondestructive test methods were utilized, including the Impact-echo (IE) test method, the Ultrasonic shear wave test method (UST) using the Polygon and Monolith devices, and the Ground-penetrating Radar (GPR) test method. In addition, the overall geometric characteristics and some of the cracking pattern were documented using a 3D laser scanner.

Ultrasonic Impact-echo (IE) Test Method - Impact-echo testing is a nondestructive testing technique used to detect internal flaws within materials such as concrete, stone, masonry, and other construction materials. The IE method involves introducing mechanical energy, in the form of a brief impact, to the structure. When a material, such as concrete, is subject to a surface impact, stress waves propagate through the material at a finite speed. The velocity of these waves is a characteristic of the material through which the waves propagate. Typically, the higher the velocity the more dense i.e., fewer internal discontinuities, the material can be characterized. When the concrete surface is impacted, a transducer acoustically mounted on the same surface receives the primary or P-wave energy reflections from discontinuities within



the pier. Therefore, with the knowledge of the propagation velocity through the material, the amplitude spectrum can be evaluated to determine the location of discontinuities or flaws within the concrete section. One of the advantages of the impact-echo method is that it requires access to only one side of the structure. This method can be used to detect internal voids, cracks, freezing and thawing deterioration, alkali silica reaction (ASR) damage, and locate internal honeycombing and delaminations in concrete due to the corrosion of the embedded reinforcement. The IE test method is limited to a maximum depth of about 1 meter. Figure 8 and 9 below shows a schematic representation of the test method and an impact-echo test in progress, respectively.

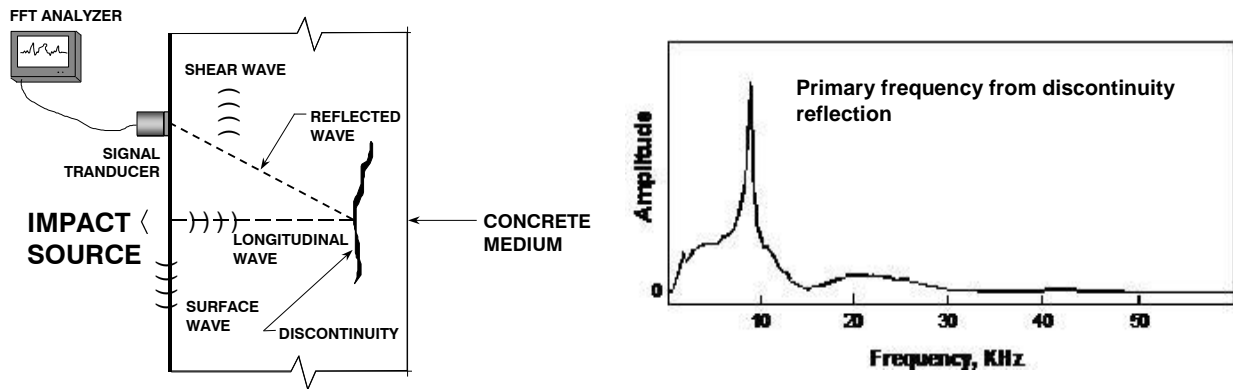


Figure 8 - Conceptual representation of the impact-echo test method



Figure 9 - View of an IE test in progress



Ultrasonic Shear-Wave Test Method (Polygon Device) – The ultrasonic shear-wave test method, commercially known as *Polygon*, is a concrete flaw detection system capable of generating a 2D or 3D tomographic image of concrete elements. The basic system consists of a phased array console with 10 modules; each module contains 4 shear wave transducers. The transducers are spring-loaded, dry point contact (DPC) piezoelectric sensors with a center natural frequency of 50 kHz. Each transducer is built with a ceramic tip, which allows testing even on very rough or uneven surfaces. When the ultrasonic shear-wave signals are emitted; the received signals are processed by the controlling console and then transferred to a laptop computer for analysis by proprietary software. A Synthetic Aperture Focusing Technique (SAFT) data processing method is then performed to generate the 2D or 3D images of the concrete element. The reconstructed images are displayed on the computer screen as a plan view, cross-section, or isometric view. In addition, Polygon test results can also be shown as single reading at a discrete location. For example, Figure 10 represents a cross-section image of a single Polygon test result. The bright image in the middle of the graph represents a shear-wave ultrasonic reflection from the bottom of the concrete element or internal discontinuities. In Figure 10, the x-axis represents distance, where the zero mark indicates the centerline of the antenna array. The y-axis shows from the top surface of the concrete. Figure 10 indicates a shear-wave reflection from the bottom flange with a nominal thickness of 5 in. Figure 11 shows a view of a Polygon test in progress on Beam 5.

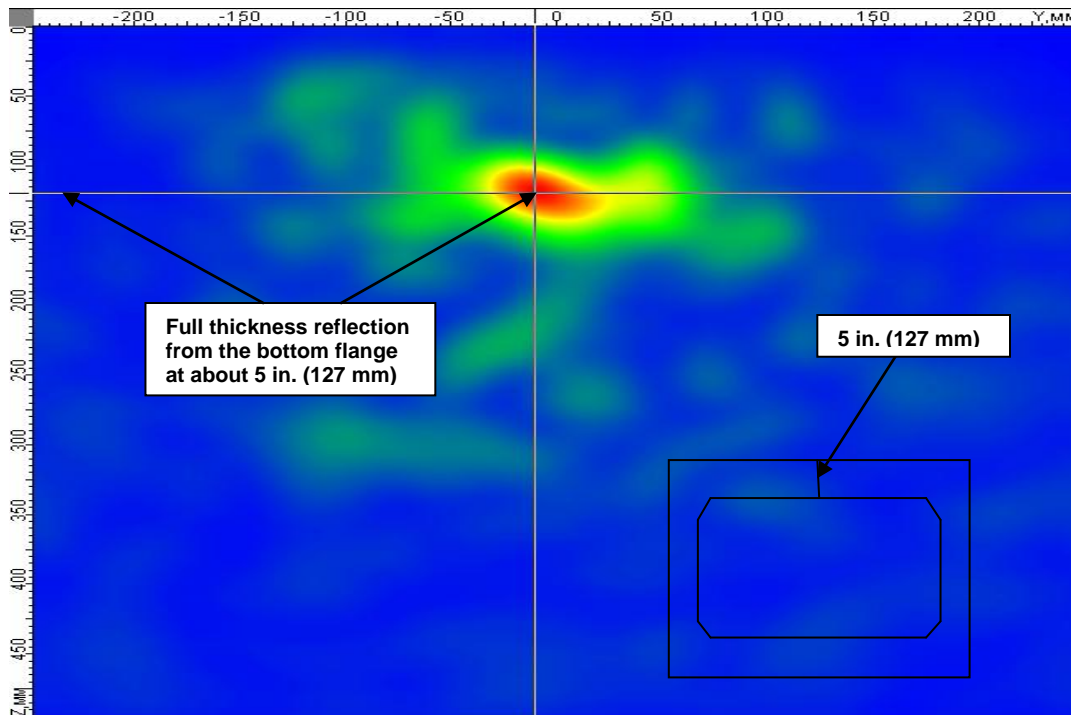


Figure 10- Polygon test result showing a bottom flange thickness of about 5 in.



Figure 11 - View of a Polygon test in progress – Beam 5

Ultrasonic Shear-Wave Test Method (Monolith Device) – The ultrasonic shear-wave test method, commercially known as A1220 Monolith, is a portable ultrasonic low-frequency flaw detection instrument for testing concrete and other materials. The basic system consists of an electronic control unit connected to an array console with 24 shear-wave transducers. The transducers are wideband, spring-loaded, dry point contact (DPC) piezoelectric sensors with a center frequency of 50 kHz. Each transducer is built with a ceramic tip, which allows testing even on very rough and uneven surfaces.

The transducers are divided into two sets of 12 transducers each, which are electronically connected to act as a single transmitting and receiving transducer. The Monolith test equipment functions are founded in ultrasonic pulse-echo principles; therefore access to only one side of the concrete surface is needed.

The Monolith system is commonly used in concrete, stone, and masonry structures to detect internal flaws such as delaminations, cracks, poorly consolidated or honeycombed concrete and to measure the thickness of the materials, as well as voids in grouted tendon ducts systems. Figure 12 shows a typical signal from a monolith test result at a grid point indicating a bottom flange thickness of about 4.8 in. Figure 12 is a time-decay graph of the shear-waves reflecting within the beam's flange. The x-axis denotes the two-way travel time of the shear-wave shown in units of micro-seconds. The y-axis denotes the amplitude or strength of the shear-wave reflections in units of decibels. The resulting depth is then calculated based on the inputted velocity. Figure 13 is a view of a monolith test in progress on Beam 5.

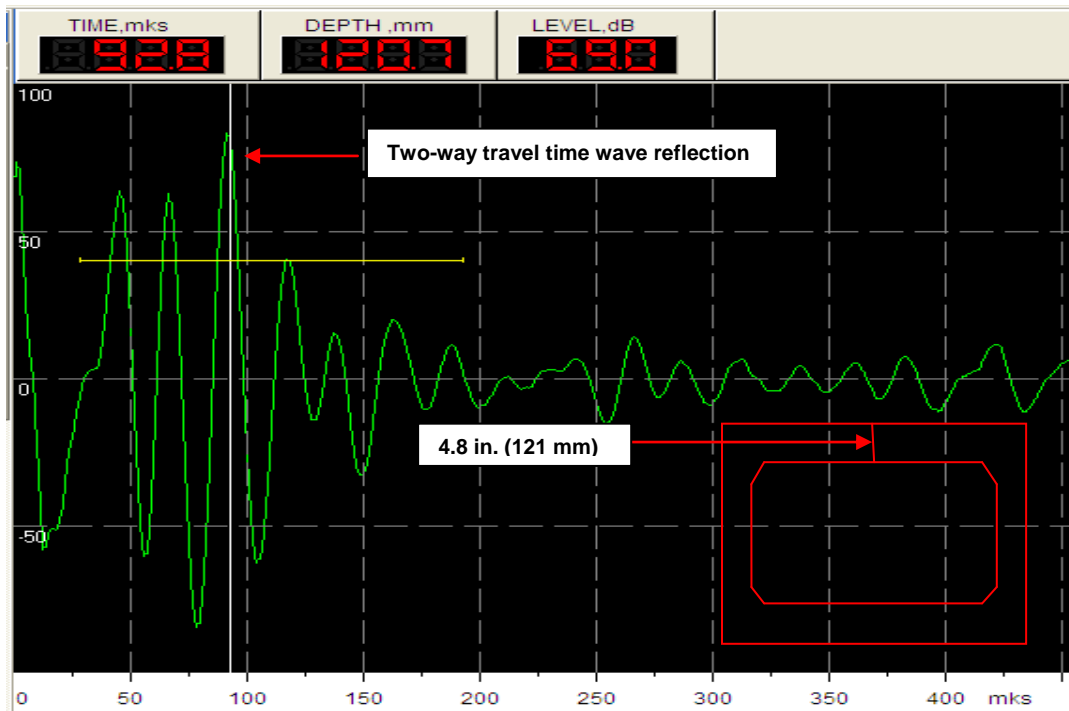


Figure 12- Monolith test result showing a nominal bottom flange thickness of 4.8 in thick.

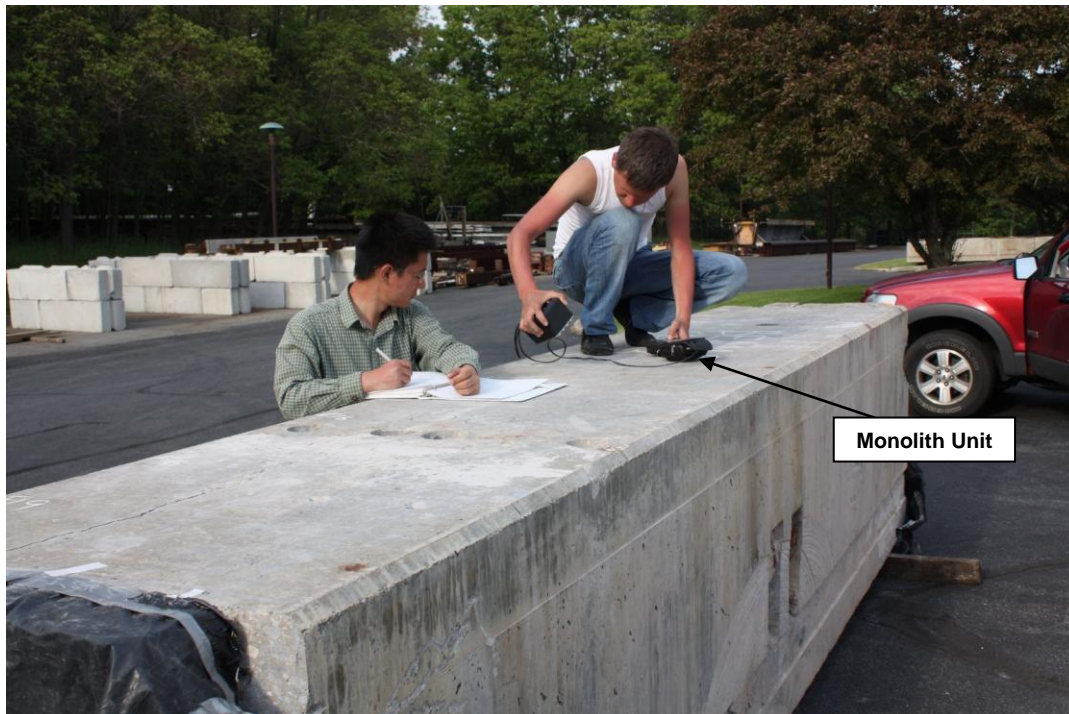


Figure 13- View of an ultrasonic shear wave monolith test in progress – Beam 5



Ground Penetrating Radar (GPR) – The GPR test method involves using electromagnetic waves to assess the internal characteristics of a material. For concrete or cementitious materials, GPR is used almost exclusively in the reflection mode, where transmitting and receiving antennas, a small fixed distance apart, traverse the inspected surface. The transmitting antenna sends a diverging short pulse of energy between 1 to 3 nanoseconds (ns) duration. The receiving antenna collects the energy reflected from dielectric interfaces between materials of differing dielectric properties and then is processed by the radar unit and displayed on the screen of the instrument. The reflected energy is recorded as a pattern. A high frequency GPR antenna of 2.6 GHz was used to assess the concrete characteristic and to determine the location of embedded reinforcement.

Figure 14 show a typical GPR linescan conducted along the length of Beam 5. The x-axis denotes distance travel in units of feet. The y-axis denotes the two-way travel time of the electromagnetic wave shown in units of nano-seconds. Figure 14 shows the location of the embedded reinforcement as well as the thickness of the bottom flange. Figure 15 shows a view of the high frequency antenna GPR test equipment.

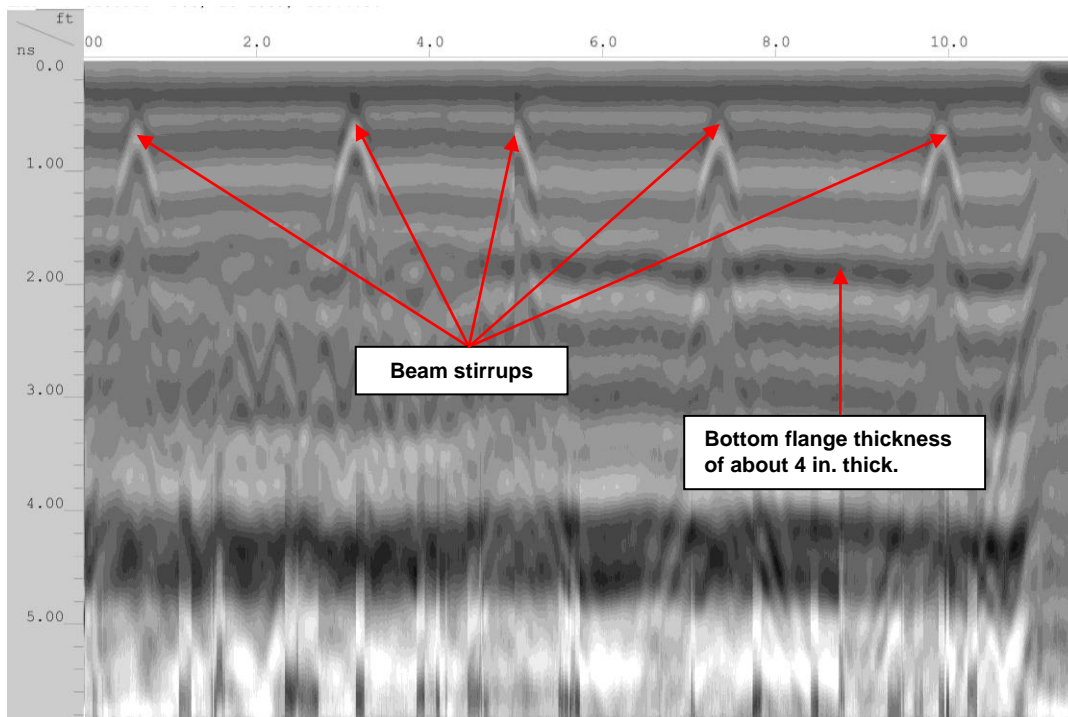


Figure 14- Typical GPR linescan test result

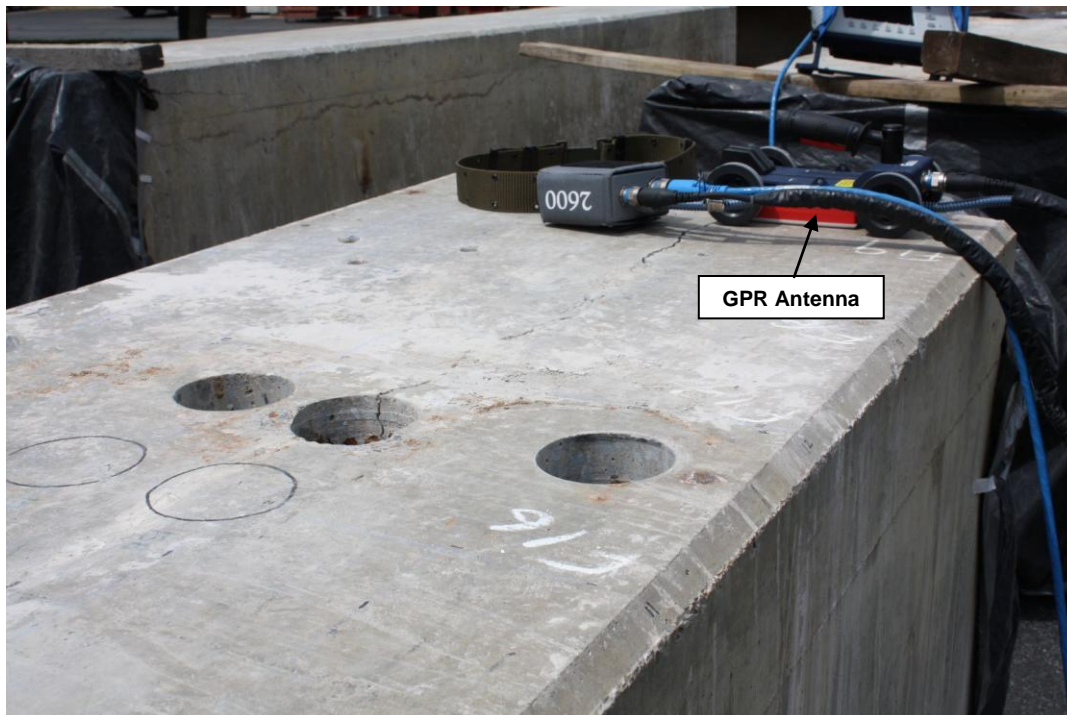


Figure 15- View of the high frequency GPR test equipment

3D Laser Scanning – 3D laser scanning is a high density measurement of the environment surrounding the scanning instrument. Thousands of measurements are taken per second and are visualized as points, each point having a specific x, y, and z coordinate relative to the instrument. A complete scan contains millions of measurements and once visualized is called a point cloud. Multiple scans can be taken at different locations and registered together to create a larger point cloud. Since these points represent specific coordinates, accurate measurements may be taken from the point cloud data. Information obtained from the laser scanning work and nondestructive testing will be used to prepare 2D plots identifying physical features of the structure including core locations, concrete spalls, cracks, etc. Figures 16 and 17 show, respectively, a point cloud plot of the beams' staging layout and the laser scanning equipment.



Figure 16 - Point cloud plot of the beams' staging layout

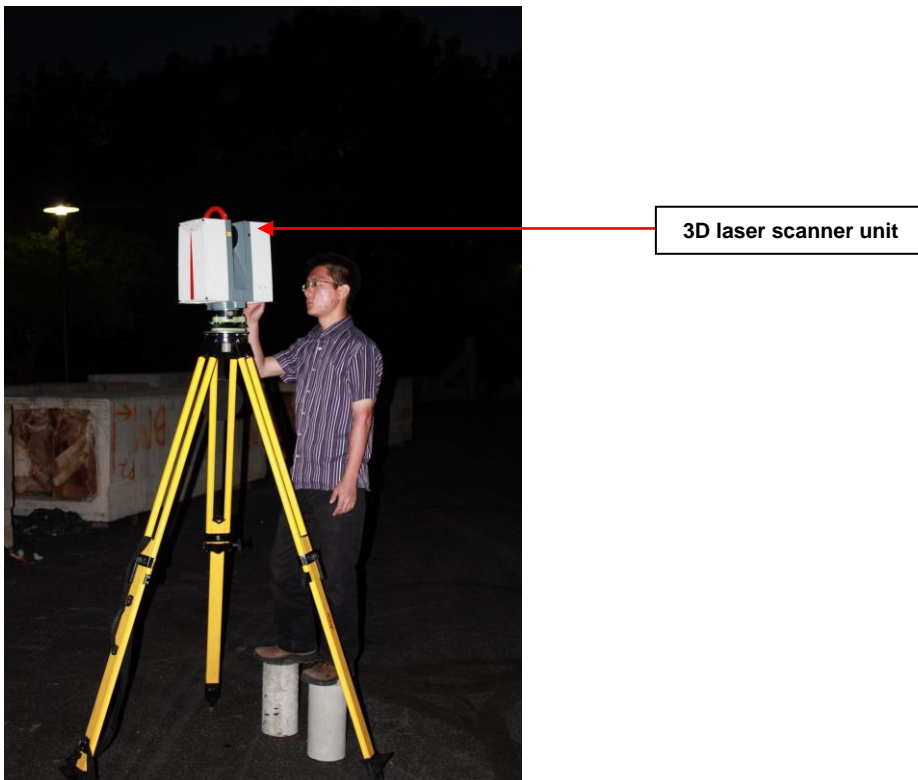


Figure 17- 3D laser scanner equipment



Field Investigation

The following tasks were performed during the nondestructive evaluation of the selected box-beams:

- A test grid was layout on the bottom flange surface of each of the beams. The test grid consisted of longitudinal lines spaced 6 in. apart and transverse lines spaced at 1 ft apart.
- A 3D laser scanner was used to electronically document the geometric characteristic and physical features of the beams.
- Test measurements were made with Impact-echo testing equipment on beams 2-5 and 7 at each of the test grid points.
- Test measurements were made with Ultrasonic Shear wave testing equipment (Polygon Device) on beams 2-5 and 7.
- Test measurements were made with Ultrasonic Shear wave testing equipment (Monolith Device) on beams 5 and 7.
- Test measurement were made with Ground-penetrating radar (GPR) equipment to survey Beams 2-7 to determine the location of the embedded reinforcing steel and assess the potential for corrosion deterioration. GPR testing was conducted along each of the test gridlines.

Test Results and Analysis

The test results for each of the nondestructive test methods used in this investigation are summarized in the Appendix section of this report. In addition, comparisons between the different test methods results have been made to determine any correlation between techniques. Finally, the test results for each of the test methods have been superimposed on a superimposed summary plot for each of the beams (see Sheets 2S through 7S).

Visual Documentation - The results of the visual documentation are summarized in the Appendix section of this report (see Sheets 2V through 7V). Sheets 2V – 7V were prepared using a combination of our visual observations and the laser scanning point cloud data. The visual survey sheets summarize the general geometrical and physical features for each of the beams, including the core locations, concrete spalls, cracks in the bottom flange and webs etc. In addition, the test grid for each of the beams has been added to the plots to provide a reference scale.

Impact-echo Test Results - Impact-echo testing was performed on each of the test grid points for each of the beams, except Beam 6. IE testing on Beam 6 was not performed because of the observed uneven surface from the severe concrete deterioration. The results for each of



the beams have been graphically summarized in Appendix section of this report (see Sheets 2IE through 7IE). The results of the IE testing Sheets 2IE – 7IE show color coded dots at each of the test grid points. A green color denotes an IE test result indicative of a full thickness reflection from the bottom flange section. Similarly, a red dot denotes an IE test result indicative of either a delaminations due to corrosion of the embedded reinforcement or other anomalies such as honeycombing, additional reflections from internal cracks, etc. Figure 18 shows a typical IE test result conducted on Beam 3, on test grid point D5. Test Grid Point D5 has been marked with a green dot, which indicates a full thickness reflection without any internal flaws. The upper portion of the graph shown in Figure 18 is a time domain plot, which shows the reflections of the longitudinal P-waves, and the decay of the signal with time. The bottom portion of the graph shows the spectra plot or frequency domain, which represents the Fast Fourier Transform (FFT) analysis of the discrete time domain. The result of the IE testing at Grid Point D5 on Beam 3 shows a nominal concrete thickness of 4.2 in. thick. Analysis of the time and frequency domains provides information on the thickness of the material as well as internal flaws.

Similarly, Figure 19 shows the results of an IE test location at Beam 7, Grid Point D11. The upper portion of the graph shows a time domain with irregular high frequencies content in the signal. Similarly, the frequency domain portion of the signal shows a low frequency, high amplitude response, which is a typical response for shallow delaminations. The results of the impact-echo testing along the Gridline D indicate discrete delaminations adjacent to the longitudinal crack that span the length of the beam. In many cases, the observed longitudinal cracks exhibited corrosion stains from the embedded prestressing strands. The spectra plots for each of the IE test results can interactively be seen on the accompanying CD by clicking on each of the test grid points.

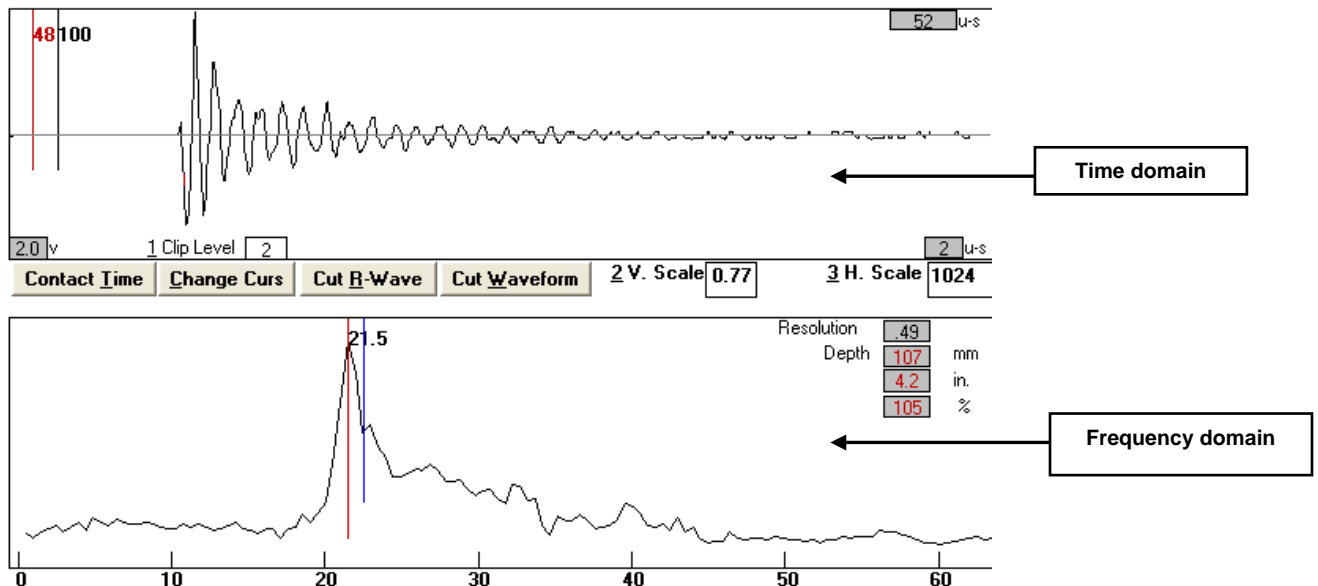


Figure 18- IE test result showing a full thickness reflection at Beam 3, Grid Point D5

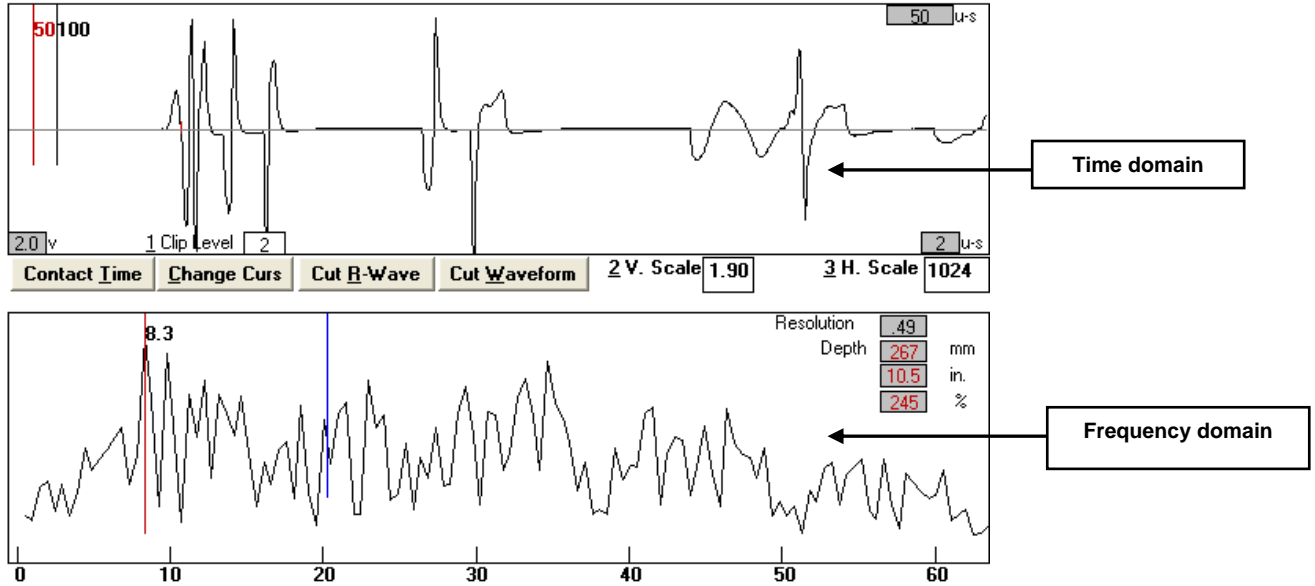


Figure 19- IE test result showing a shallow delamination at Beam 7, Grid Point D11

Figure 20 shows the result of an impact-echo test at Grid Point A1, Beam 3. At this grid point, the IE test indicates a P-wave reflection at about 9 in. A visual inspection of the web side of the beam shows a shear crack at a depth of about 9 in. below the top surface. Note that the point tested is the edge of the beam, which should have additional reflections from the edge conditions and interior chamfer. Figure 21 shows a view of the shear crack on the web side of the beam at depth of about 9 in. In order to correlate the test results from all of the test methods used during this investigation, the results of the IE tests have been integrated into superimposed combined plots for each of the tested beams (see Sheets 2S through 7S).

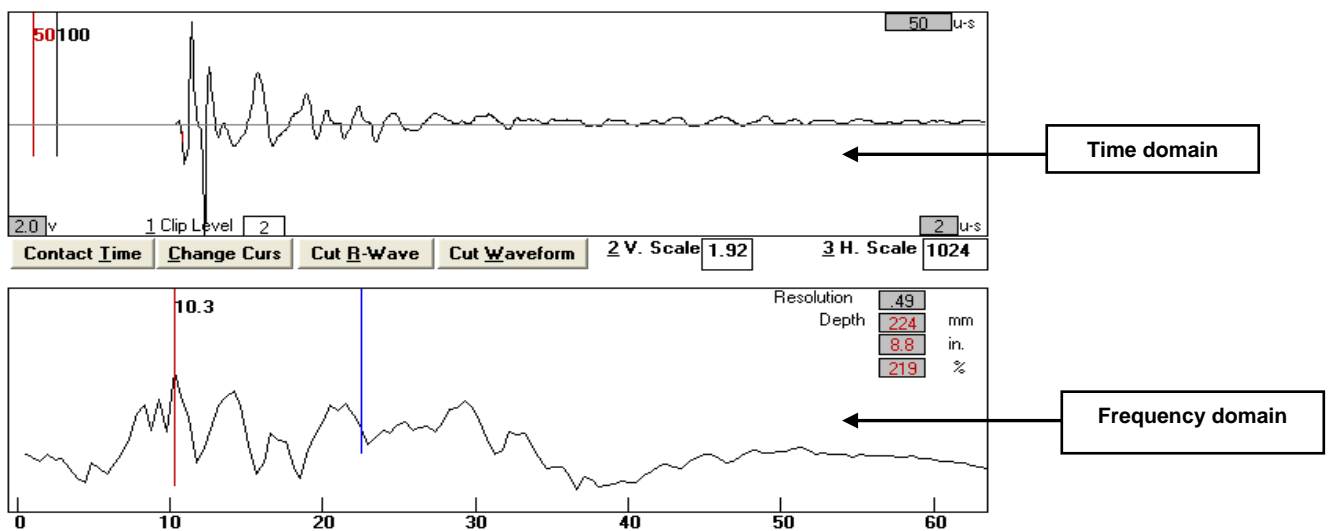


Figure 20- IE test result showing a reflection (10.3 kHz) from a web crack at depth of 9 in. (Beam 3, Grid Point A1).



Figure 21- View of a shear web crack, Beam 3 at about 9 in. below the top surface.

Ultrasonic Shear-Wave Test Results (Polygon Device) – The result from the ultrasonic shear-wave Polygon device are summarized in the Appendix section of the report (see Sheets 2P through 7P). Polygon tests were conducted on every beam, except for Beam 6. Testing on Beam 6 was not performed because of the observed uneven surface from the severe concrete deterioration. Testing was conducted by collecting a series of single readings, 2 in. apart, from one end of the beam to the other. Since the length of the antenna array is about 16 in. long, a minimum of two scans per beam were collected in order to cover the surface area of the beams. Each scan was collected by aligning the side of the antenna array with the centerline of the beam to minimize interference from the interior chamfers and edge of the beams. Once all the readings are collected, the data is then migrated into a single file, which can then be displayed as a 2D and 3D tomography plot showing a top view, longitudinal side view, and cross section view. Figure 22 shows a typical image produced from the Polygon test results conducted on a partial section of Beam 5. Similar to the IE test results, the Polygon tests indicate reflections from potential internal voids, delaminations, or large areas of poorly consolidated concrete. In order to correlate the test results from all of the test methods used during this investigation, the results of the Polygon tests have been integrated into superimposed combined plots for each of the tested beams in the appendix section of the report (see Sheets 2S through 7S).

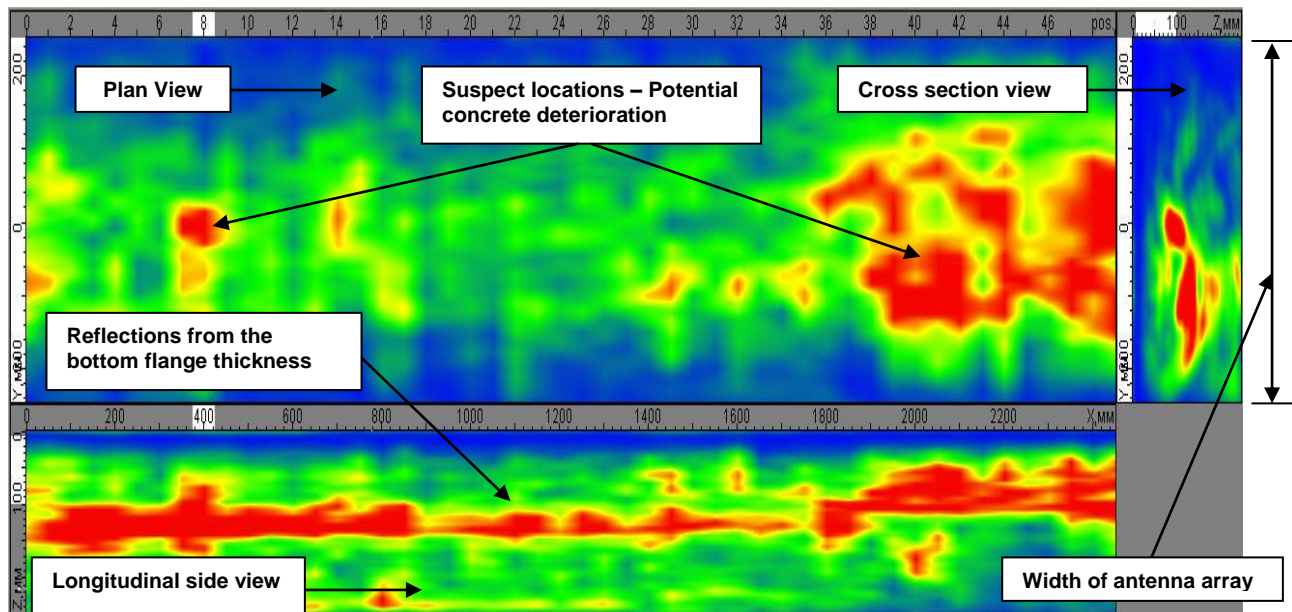


Figure 22- Typical view of a Polygon test result showing a tomographic view of potential concrete deterioration locations (Partial section of Beam 5).

Ultrasonic Shear-Wave Test Results (Monolith Device) – The result of the ultrasonic shear-wave Monolith device are summarized in the Appendix section of the report (see Sheet 2M through 7M). Monolith tests were only conducted on Beams 5 and 7 and on random locations on the other beams. Similar to the IE test results, the results of the Monolith tests (Sheets 2M – 7M) are shown color coded with open triangles at each of the test grid points. A green triangle denotes a Monolith test result indicative of a solid section with a full thickness reflection from the bottom flange section. Similarly, a red triangle denotes a Monolith test result indicative of a potential internal deterioration.

The Monolith instrument was also used to check the crack depth in the concrete webs at the edges of the bottom flange. Figure 23 shows a view of Monolith test at a web crack location showing a nominal crack depth of 4 in. Figure 24 shows the corresponding Monolith time domain plot indicating a concrete reflection at a depth of 4 in (102 mm). Similar to the IE and Polygon test results, the results of the Monolith tests have been integrated into the superimposed combined plots included in the Appendix section of the report (see Sheets 2S through 7S). The time domain spectra plots for each of the monolith test results can interactively be seen on the accompanying CD by clicking on each of the test grid points.

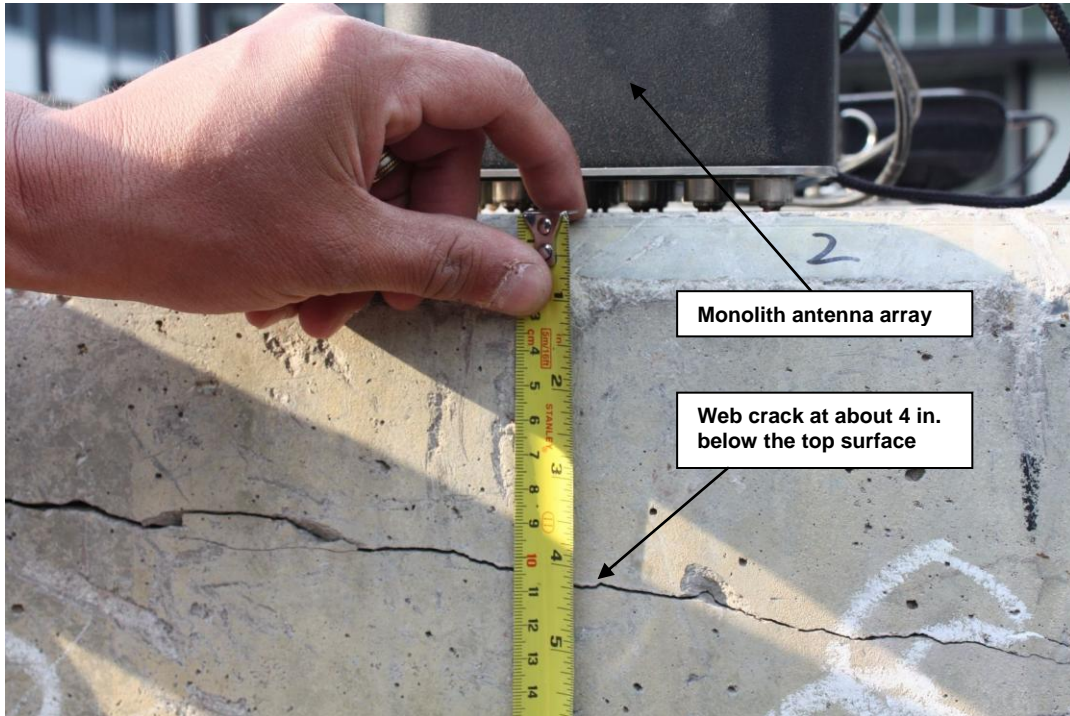


Figure 23 - View of web crack at nominally 4 in. deep.

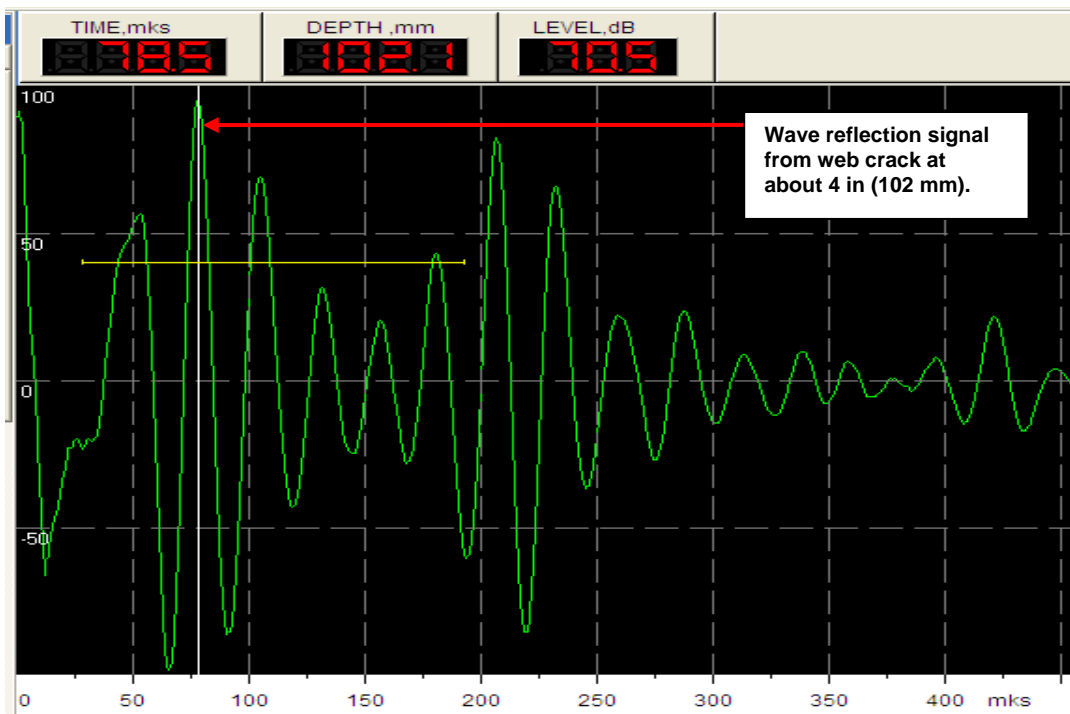


Figure 24 - Monolith test results showing a reflection from a web crack at about 4 in. deep.



Ground Penetrating Radar Test Results – The GPR testing was performed along each of the longitudinal and transverse grid lines. The GPR files were collected on a continuous mode from one end beam to the other. The results are linescans which are analyzed to determine the location of the reinforcement and other embedded objects. In the case of these beams, GPR test results were also analyzed to determine the amplitudes of the electromagnetic reflections and signal attenuation.

GPR testing is commonly used on bridge structures to determine delaminations of the bridge decks due to the corrosion of the reinforcing bars. This is done by assessing the amplitudes of the electromagnetic waves at the reinforcement locations and the attenuation of the signals. This approach was also used in assessing the beams in this study. However, unlike, typical bridge decks where the spacing of the reinforcing bars may be 6 in. apart, or more, in the case of the box beams at the Lehigh ATLSS Laboratory, the closely spaced (about 2 in. apart) prestressing strands makes the interpretation of the collected signals more difficult. Nevertheless, our GPR analysis to determine locations of potential corrosion indicates several suspect locations. Figures 25 and 26 are 3-D views of examples of the closely spaced, longitudinal prestressing strands and transverse stirrups in Beams 2 and 3.

The results of the GPR testing have been summarized in the Appendix section of this report (see Sheet 2G through 7G). Similar to the previous test methods the results of the GPR tests have been integrated into superimposed combined plots for each of the tested beams (see Sheets 2S through 7S) so that a correlation between test methods can be done.

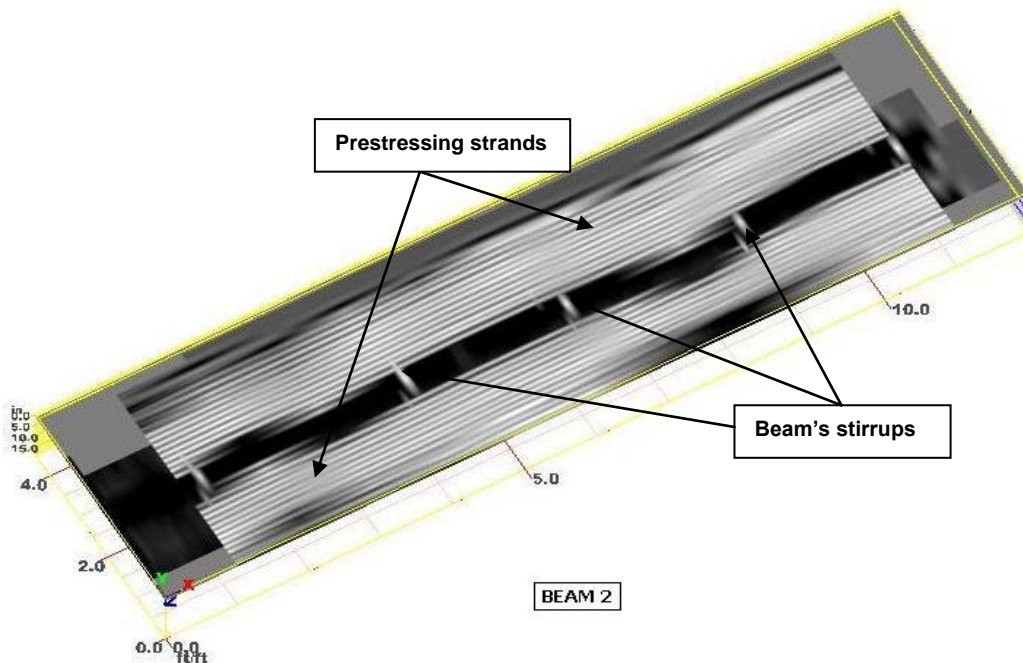


Figure 25 – 3-D view of Beam 2 showing the closely spaced longitudinal prestressing strands and the transverse stirrups.

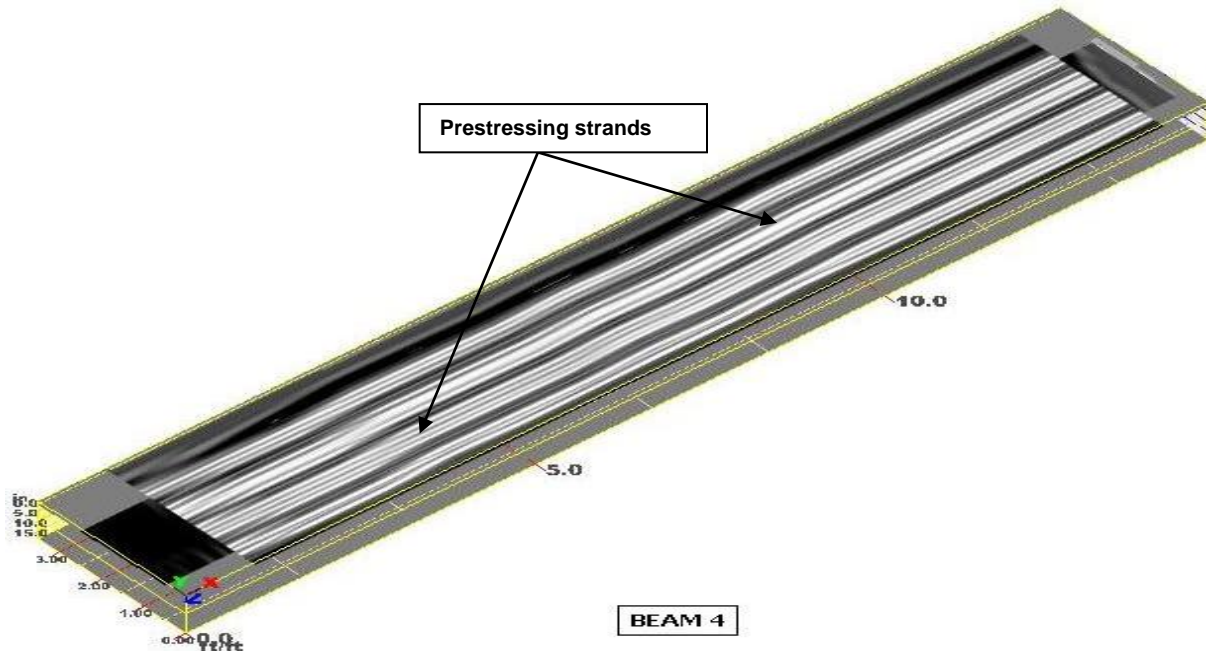


Figure 26 – 3-D view of Beam 4 showing the closely spaced longitudinal prestressing strands.

Figure 27 shows a GPR 3-D view of Beam 3 and a linescan showing some signal attenuation, which may be indicative of delaminations or corrosion of the reinforcing steel.

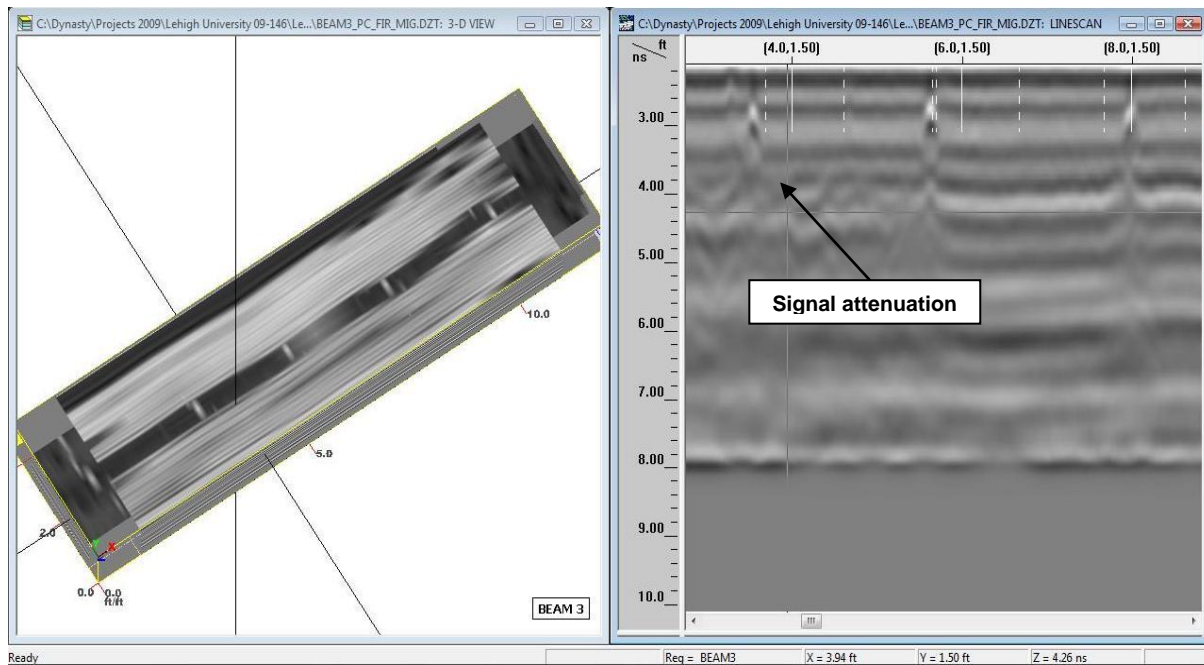


Figure 27 - GPR 3-D view and a linescan view of Beam 3 showing some signal attenuation.



In addition to analyzing the GPR test results to determine locations of potential corrosion, the GPR test results also showed internal features within the concrete such as the location of the embedded reinforcement, and concrete diaphragms. In fact, the results of the GPR testing can clearly locate the concrete diaphragms in Beam 2 and Beam 5. Figure 28 shows a GPR 3-D view and linescan plot identifying the location of the diaphragm and reinforcement in Beam 5. The linescans for each of the GPR test results can interactively be seen on the accompanying CD by clicking on each of the GPR file numbers for each of the tested gridlines.

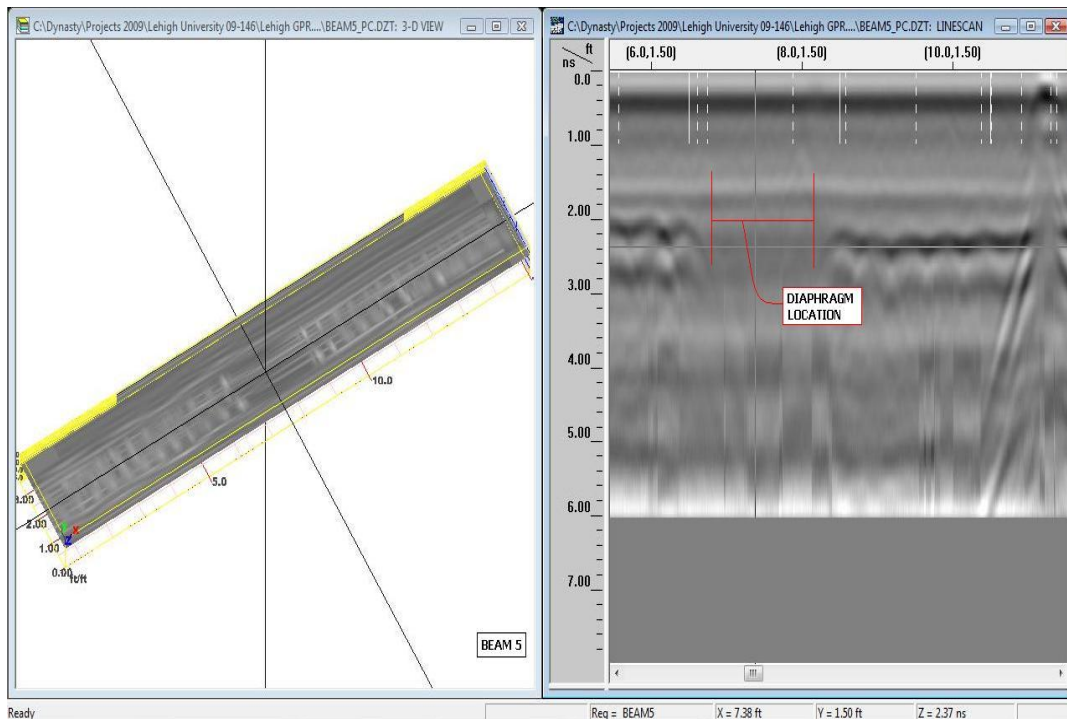


Figure 28 - GPR 3-D view and linescan plot showing the location of the diaphragm in Beam 5.

Analysis of the reflected GPR scans indicate location of potential corrosion in Beams 3, 6, and 7 (see Appendix Sheets 3G, 6G, and 7G). In the case of Beam 3 signal attenuations indicative of locations with potential corrosion were found between Grid lines B/G - 0/4 and also between Grid lines A/E - 4/8, In Beam 6, signal attenuation was found Between Grid lines A/F - 4/9, and between Grid lines A/C - 9/15. Finally in Beam 7, attenuated signals were observed between Grid lines B/E - 1/4, Grid lines C/E - 4.5/7, and Grid lines B/E - 10/11.5.

3D Laser Scanning Data Analysis – A 3D laser scanner was used to produce point cloud plots for each of the tested beams. The point cloud data from the laser scanner system was used in combination with the visual survey to prepare the visual survey plots shown in the Appendix section of the report (see Sheets 2V through 7V). This information was used to prepare 2-D plots identifying physical features of the structure including core locations, concrete spalls, cracks, etc. Figure 30, a view a point cloud plot showing the beam's staging layout and



the laser scanner multiple setups; noted by the yellow triangles. Figure 30, also shows the location of the registering targets, used to correlate and link the data from each of the multiple instrument setups so that a single point cloud file, with all the collected data can be generated. The target locations can be identified by the letter T, followed by the target number. The individual point cloud data for each of the scans (yellow triangles) can be viewed using the *TruView* Leica software, which has been included in the accompanying CD.

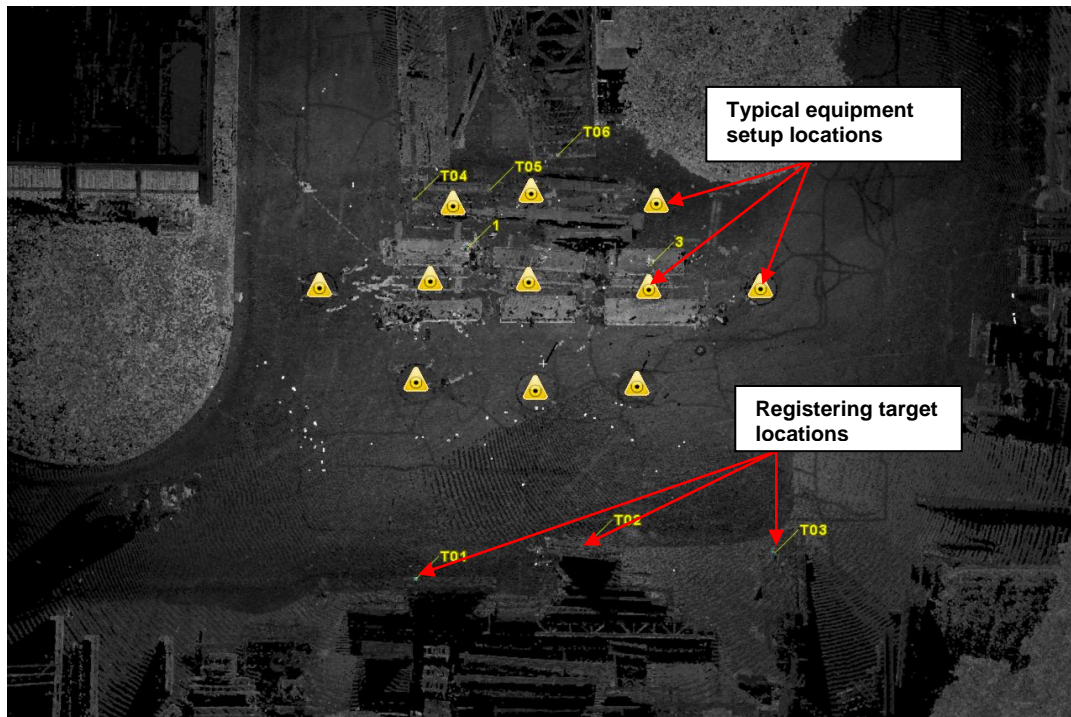


Figure 30 – View of the laser scanner’s instrument setups and the target locations.

Similarly, Figure 31 is a point cloud plot of the box beams. This plot shows a view of the scanned data. The plot shown in Figures 31 is made of thousands of points representing specific coordinates; therefore, accurate measurements may be taken from the point cloud data.

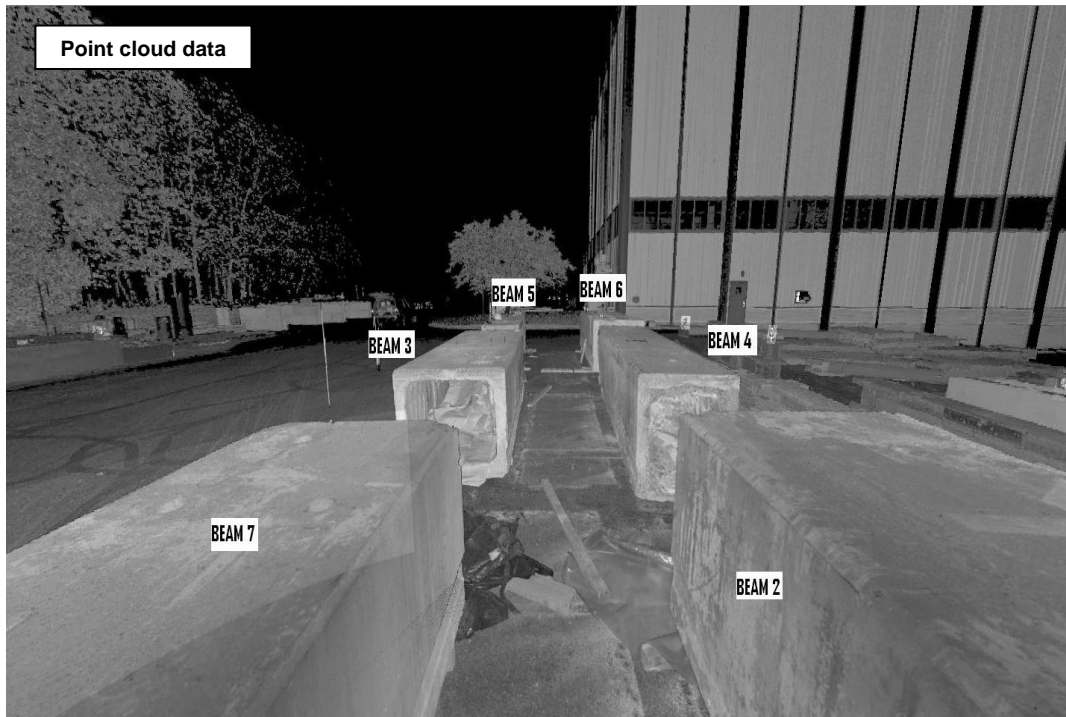


Figure 31- Point cloud plot showing the box beams in the study.

In addition, at selected locations, the point cloud data was used to map and measure the width of the longitudinal cracks. Figure 33 is comparison of a crack width measured using a conventional tape measure and the point cloud data. The actual width of the cracks that can be measured using the laser scanner instrument depends on the amount of points registered in the point cloud data; the greater the amount of points, the finer the crack width that may be measured. Similarly, Figure 34 is a view of longitudinal crack observed in Beam 4 and the corresponding width measurement made using the point cloud data.

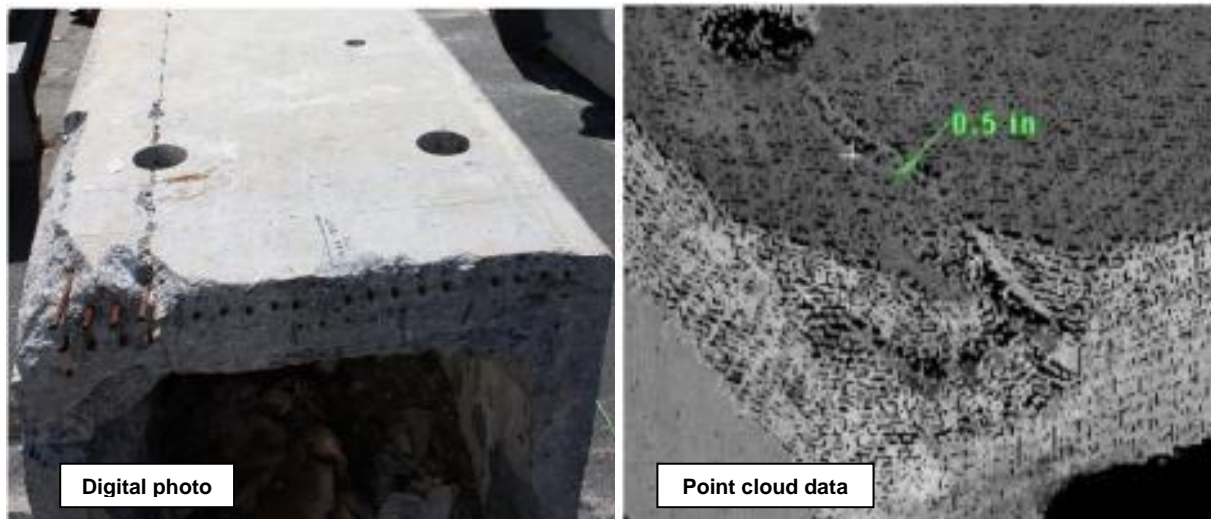


Figure 32 – View of a crack measured with a tape measure and the point cloud data.

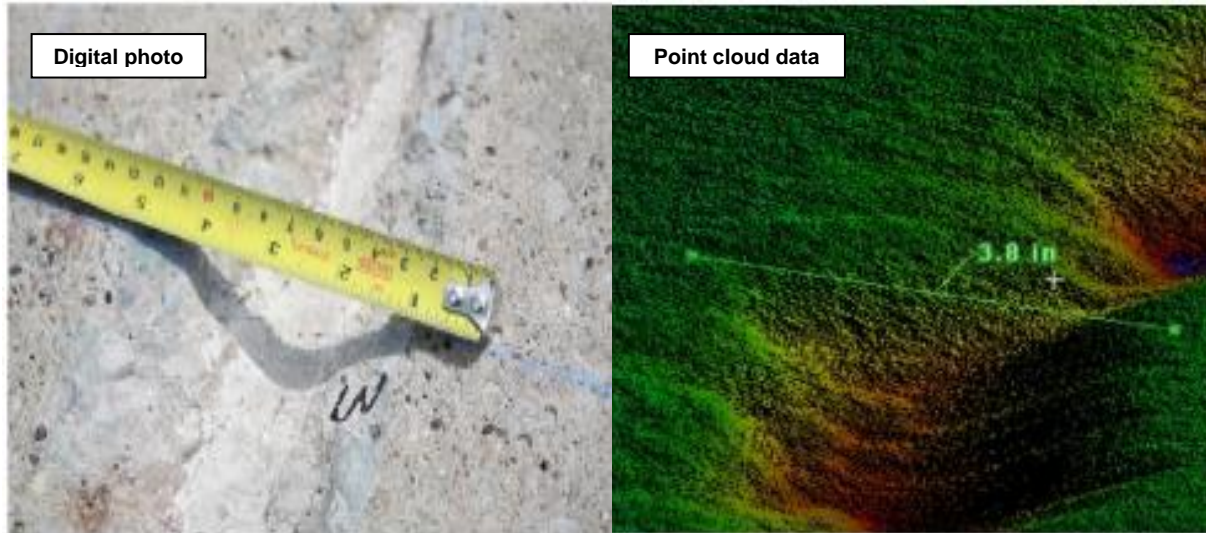


Figure 33 – View of a crack in Beam 4

One of the advantages of collecting laser surveying data is that it can be used as a monitoring system to map out the current state of the structure and then correlate an earlier scan with more up-to-date information. For instance, the growth of cracks, surface deterioration such as spalls and corrosion stains, and geometrical changes can be monitored during time. Figure 34 shows an example of how the point cloud data can be used to document current conditions.

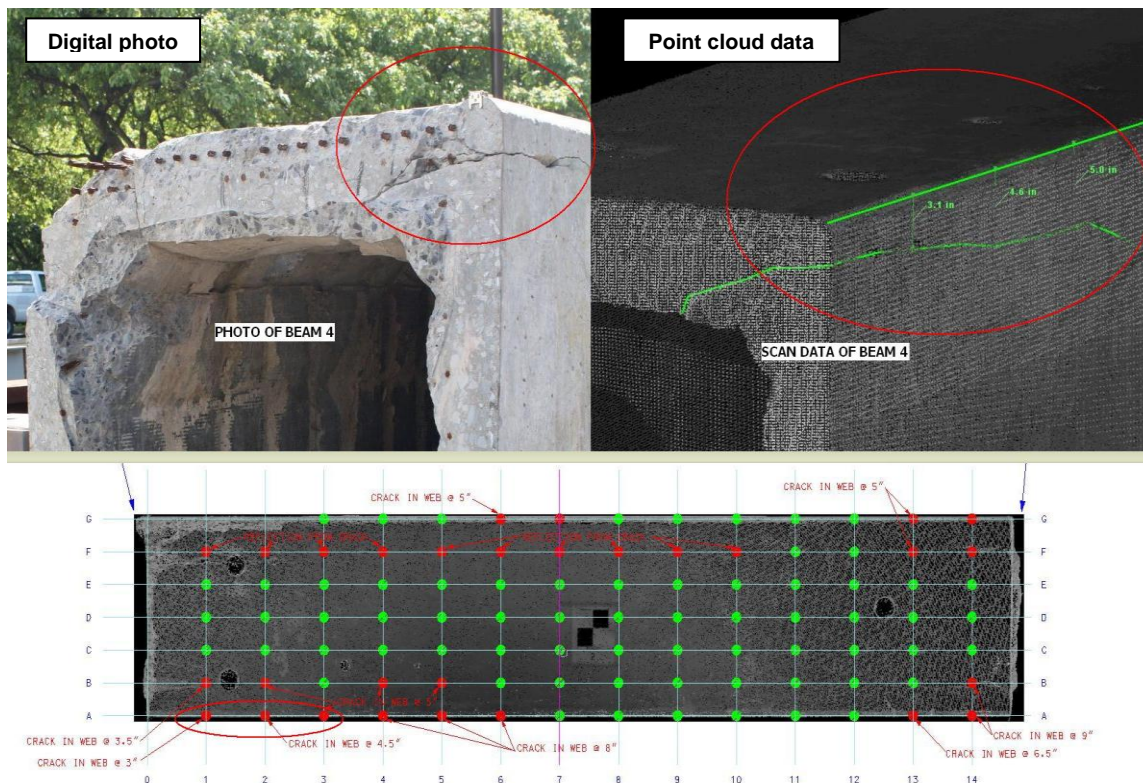


Figure 34 – View of a crack in Beam 4 documented using the 3-D laser scanner



Summary of the Superimposed NDT Plots - The results from the nondestructive testing collected using the impact-echo test method, Ultrasonic shear-wave methods, Ground-penetrating radar, laser scanning, and visual documentation have been integrated into a single plot by superimposing the test results at each grid point (see Appendix Sheets 2S through 7S).

Sheet 2S Beam 2 - The results of the superimposed NDT methods indicate a good correlation with the noted conditions. The result of the IE testing on Beam 2 did not show delaminations along the bottom flange surface. IE tests showed reflections from the web cracks at the edges of the beam. The results of the Polygon testing on this beam correlates well with the IE test results. The majority of the Polygon tomography plot did not show any reflections from internal discontinuities, except for a few locations where reflections from the concrete diaphragm could be seen along Grid Line 4. Similarly, the results of the GPR testing on Beam 2 did not show locations where signal attenuations or corrosion might be found.

Sheet 3S Beam 3 - The results of the superimposed NDT methods indicate a good correlation with the noted conditions. The IE testing on Beam 3 indicated several grid-point locations with shallow isolated delaminations along the length of the longitudinal crack. IE test result also showed reflections from the web cracks at the edges of the beam.

The tomography plot, which summarizes the Polygon test results, shows a good correlation with the internal discontinuities found with the IE test method and the visible crack locations. The majority of the documented deterioration follows the length of the longitudinal crack along Grid Lines C and D. In addition, analysis of the Polygon data shows a suspect location between Grid Lines F through G and Grid Line 11. The tomography test result at this location may be influenced by reflections from the edges of the large concrete opening at Grid Point G11.

Finally, the results of the GPR testing on Beam 3 show several locations where signal attenuations were found. These locations may be indicative of potential corrosion of the embedded reinforcement, which have not cause the concrete cover to delaminate yet. These suspect areas will be correlated by the Lehigh researches with results from the destructive testing. Locations of potential corrosion activity were found between Grid Lines B through G and 0 through 4 and Grid Lines A through E and 4 through 8.

Sheet 4S Beam 4 - The results of the superimposed NDT methods also indicate a good correlation with the noted conditions. IE tests results on Beam 4 indicated several grid point locations with P-wave reflections from the edges of the longitudinal crack along Grid Line F. Also, the IE spectra plots clearly show reflections from the web cracks at the edges of the beam.

The ultrasonic shear-wave Polygon testing on Beam 4 was conducted with a single pass along the centerline of the beam. Consequently, Polygon test results adjacent to the longitudinal crack along Grid line F do not show well on the Polygon tomographic plot. Isolated hot spots near the extracted 4-in. diameter core, between Grid Lines C through E and 12 through 13, showed shear-wave reflections near the surface of the beam. Polygon test results indicate a tomography plot that correlates well with the test results obtained with the IE test method and visual observations. Finally, the results of the GPR testing on Beam 4 did not show locations of signal attenuations.



Sheet 5S Beam 5- The results of the superimposed NDT methods also indicate a good correlation with the noted conditions. The result of the IE testing on Beam 5 indicated several spectra plots with multiple frequency peaks along Grid Line 8, which coincides with the location of the internal concrete diaphragm. The grid points along Grid Line 8 had been marked with red dots in Sheets 5IE and 7S, to denote a potential anomaly. However, the multiple peaks observed in the spectrum plots, may be associated with the small size impactor used to strike the concrete to introduce the propagation wave and the dimensions of the concrete diaphragm. Also, several of the spectra plots along Grid Line D were indicative of a full thickness reflection of the propagation wave. However, additional reflections from the edges of the longitudinal crack were also observed in adjacent grid points.

The ultrasonic shear-wave Polygon testing on Beam 5 was conducted with two passes of the antenna array along the length of the beam surface to produce the composite plot shown in Sheets 5P and 5S. The Polygon tomography plot shown in the Appendix section (see Sheet 5S), correlates well with the IE summary plots and our visual observations. Sheet 5S also shows localized hot spots at the concrete diaphragm location (Grid Line 8). Similarly, tests results from the ultrasonic shear-wave device, Monolith, also correlated well with the IE and Polygon test results. Finally, the results of the GPR testing on Beam 5 did not show locations of signal attenuations.

Sheet 6S Beam 6 – Because of the observed uneven surface from the severe concrete deterioration and time constraints to complete the intended field investigation, testing on Beam 6 was limited to the GPR testing and visual observations. The results of the GPR testing and our visual observations are summarized in Sheet 6S (see Appendix).

GPR testing on Beam 6 show several locations where signal attenuations were found. These locations may be indicative of potential corrosion of the embedded reinforcement, which have not cause the concrete cover to delaminate yet. These suspect areas will be correlated by the Lehigh researches with results from the destructive testing. Locations of potential corrosion activity were found between Grid Lines A through F and 3 through 9 and Grid Lines A through c and 9 through 15.

Sheet 7S Beam 7- The results of the superimposed NDT methods also indicate a good correlation between the ultrasonic test methods and noted conditions. The majority of the IE test results on Beam 5 indicated full thickness reflections from the bottom flange section, except for those test results on grid points adjacent to the longitudinal crack (Grid Line D). IE spectra plots along Grid Line D were indicative of shallow delaminations, potential honeycombing, and reflections from the edges of the crack. In addition, the cracks in the webs near the end of the beams were clearly identified using the IE method.

The ultrasonic shear-wave Polygon testing on Beam 7 was also conducted with two passes of the antenna array along the length of the beam surface to produce the composite plot shown in Sheets 7P and 7S. In general, the Polygon tomography plot shown in the Appendix section (see Sheet 7S), correlates well with the IE summary plots and our visual observations. Sheet 7S also shows some small localized reflections near Grid Points G4, G6, and G8, which do not correlate with any noted conditions.



Test results from the Monolith ultrasonic shear-wave device also correlates well with the IE and Polygon test results.

Finally, GPR testing on Beam 7 show several locations where signal attenuations were found. These locations may be indicative of potential corrosion of the embedded reinforcement, which have not cause the concrete cover to delaminate yet. These suspect areas will be correlated by the Lehigh researches with results from the destructive testing. Locations of potential corrosion activity were found between Grid Lines B through E and 0 through 4, Grid Lines C through E and 4 through 7, and Grid Lines B through E and 9 through 12.

Thank you for giving Dynasty Group, Inc. the opportunity to serve Lehigh University and the Pennsylvania Department of Transportation on this challenging project. Please call if you have any questions regarding the information presented in this report.

Very truly yours,
Dynasty Group, Inc.

A handwritten signature in black ink, appearing to read 'Aldo De La Haza', with a stylized flourish at the end.

Aldo De La Haza
Project Manager